

X-ray spectroscopy of Active Galactic Nuclei

Thesis submitted
for the degree of
Doctor of Philosophy

by
Anastasia Pappa

Astronomy Group
Department of Physics and Astronomy
University of Leicester

December 2000²⁰⁰¹

UMI Number: U148984

All rights reserved

INFORMATION TO ALL USERS

The quality of this reproduction is dependent upon the quality of the copy submitted.

In the unlikely event that the author did not send a complete manuscript and there are missing pages, these will be noted. Also, if material had to be removed, a note will indicate the deletion.



UMI U148984

Published by ProQuest LLC 2013. Copyright in the Dissertation held by the Author.
Microform Edition © ProQuest LLC.

All rights reserved. This work is protected against
unauthorized copying under Title 17, United States Code.



ProQuest LLC
789 East Eisenhower Parkway
P.O. Box 1346
Ann Arbor, MI 48106-1346

Declaration

I hereby declare that no part of this thesis has been previously submitted to this or any other University as part of the requirement for a higher degree. The work described herein was conducted by the undersigned except for contributions from colleagues as acknowledged in the text.

Anastasia Pappa,
December 2000

Acknowledgements

I am obliged to thank my supervisor Gordon Stewart for his guidance during the course of this work. I express gratitude to all the people who have helped me, in many ways, over the years I spent working on this thesis. In particular I thank Ioannis Georgantopoulos for helpful discussions and guidance, Andreas Zezas for helping me when I first came to Leicester, introducing me to the software and for the many after-midnight valuable discussions, Martin Ward for useful discussions and Paulina Lira for being a great friend, for listening and cheering me up as well as for many interesting discussions about all aspects of Astronomy. I would also like to thank Chris Rudge for helping me with all my computing problems and difficulties, Mandy Burston for spending time showing me how to reduce infrared data, and for producing the Mrk609 SED for me and my supervisor in Patras, Prof. C. Goudis for being a great teacher and the inspiration for me to pursue a career in astronomy.

Last but by no means least, my love and thanks go to my wonderful family – all eight of them – for their love and support and all my friends in Greece especially my precious bosom friends Ina and Anna-Maria. In particular, my warmest thanks go to my mother, father and nona. I shall be eternally grateful for their endless love. Above all, I thank Kostas for his unconditional love and support.

X-ray spectroscopy of Active Galactic Nuclei

Anastasia Pappa

Abstract

This thesis was triggered by the question what is the nature of the sources producing the bulk of the X-ray background at hard energies. Of course the pre-Chandra missions did not allow any definite answer to this question. Therefore the approach adopted in this work is to examine whether candidate populations of objects could contribute to the X-ray background significantly. This was achieved by studying spectroscopically a variety of objects. To be more specific, in Chapter 3 it was examined whether broad line quasars, which produce the bulk of the X-ray background at soft energies, contribute significantly to the hard X-ray background as well. In Chapter 4 the X-ray properties of a sample of Seyfert 2 galaxies were examined. The results are examined in the light of the current X-ray background synthesis models. This study revealed two “odd” Seyfert 2 galaxies (NGC3147 and NGC4698). Odd, in the sense that although both galaxies are classified as Seyfert 2 in the optical, their X-ray data do not show evidence for absorption above the Galactic. Possible scenarios explaining the emission from the two galaxies are examined in Chapter 5. Chapter 6 considers the spectral properties of the Ultraluminous infrared galaxy ‘The Superantennae’. In Chapter 7 a study of the composite galaxy Mrk609 is presented. The composite galaxies resemble the narrow-line X-ray galaxies (NLXGs) detected in large numbers in deep *ROSAT* surveys. Thus the study of the spectra of composite galaxies provides an indirect insight into the spectra of the NLXGs. Finally Chapter 8 summarises the results of this work.

Publications

A significant amount of the work contained in this thesis has been published or is due to be published, in scientific journals:

Pappa A., Georgantopoulos I., Stewart G.C., 2000, "X-ray observations of the Ultra-luminous infrared galaxy IRAS19254-7245(The Superantennae)", 2000, MNRAS, 314, 589

Pappa A., Stewart G.C, Georgantopoulos I., 2000. "The X-ray spectrum of $[OIII]\lambda 5007$ selected Sy2 galaxies. Are there any Sy2 with no obscuration?", 2001, MNRAS, 326, 995

Pappa A., Georgantopoulos I., Stewart G.C., et al., 2000, "ASCA observations of Deep ROSAT fields - V. The X-Ray spectrum of hard X-ray selected QSOs.", MNRAS, in press

Pappa A., Georgantopoulos I., Stewart G.C., 2001, Proceedings of the Stellar Endpoints, AGN and the Diffuse Background AIP, in press, "The X-ray spectrum of $[OIII]\lambda 5007$ selected Sy2 galaxies."

Pappa A., Stewart G.C., Georgantopoulos I. et al. 2000, Proceedings of the Stellar Endpoints, AGN and the Diffuse Background, AIP, in press, "The X-Ray spectrum of hard X-ray selected QSOs."

Contents

1	Introduction	1
1.1	A brief History of X-ray astronomy	1
1.2	The AGN phenomenon	2
1.2.1	Seyferts	4
1.2.2	Quasars	6
1.2.3	LINERs	6
1.2.4	NELGs	6
1.2.5	Radio Galaxies	7
1.2.6	Blazars	7
1.3	The Black Hole paradigm	8
1.4	Unification models for AGNs	10
1.4.1	The X-ray spectrum of Seyfert galaxies	13
1.5	The X-ray Background	15
1.5.1	The spectrum of the Cosmic X-ray background	16
1.5.2	The contribution of discrete sources	18
1.5.3	Obscured AGN models for the X-ray background	19
1.6	This thesis	21

2	Instrumentation and Data Reduction	23
2.1	<i>ROSAT</i>	23
2.1.1	Data Screening-Calibration issues	24
2.2	<i>ASCA</i>	24
2.2.1	Data Screening-Calibration issues	28
2.3	<i>BeppoSAX</i>	31
2.3.1	Data screening-Calibration issues	32
2.4	Software-Analysis	34
3	The X-ray spectrum of hard X-ray selected QSOs	36
3.1	Introduction	36
3.2	The sample	37
3.2.1	Radio cross-correlation	38
3.3	Data reduction and analysis	40
3.4	X-ray spectrum	41
3.4.1	Individual source spectra	41
3.4.2	The integrated QSO spectrum	46
3.5	Summary and Conclusions	48
4	The X-ray spectrum of optically selected Sy2 galaxies.	53
4.1	Introduction	53
4.2	The data	56
4.3	Data reduction	57
4.4	Spectral analysis	59

4.4.1	Building the standard model	60
4.4.2	The Compton thick models	68
4.5	Results on single objects	69
4.5.1	<i>NGC 1167</i>	69
4.5.2	<i>NGC 1667</i>	70
4.5.3	<i>NGC 2273</i>	72
4.5.4	<i>NGC 3079</i>	73
4.5.5	<i>NGC 3147</i>	75
4.5.6	<i>NGC 3486</i>	75
4.5.7	<i>NGC 4698</i>	76
4.5.8	<i>M51</i>	76
4.6	Discussion	78
4.6.1	Are most of our objects Compton thick ?	78
4.6.2	The distribution of absorbing columns and its implications for the X-ray background	82
4.6.3	Conclusions	85
5	What are NGC 4698 and NGC 3147?	87
5.1	NGC 4698	87
5.1.1	The <i>ASCA</i> spectrum	88
5.1.2	Variability	91
5.1.3	What lies in the heart of NGC 4698?	93
5.2	NGC 3147	99
5.2.1	The <i>ASCA</i> spectrum	100

5.2.2	Variability	100
5.2.3	What is NGC 3147?	100
5.3	Conclusions	104
6	X-ray observations of the Ultraluminous Infrared Galaxy IRAS19254-7245 (The Superantennae)	106
6.1	IRAS19254-7245	106
6.1.1	An overview of ULIRGs	106
6.1.2	IRAS19254-7245 (The Superantennae)	108
6.1.3	The data	111
6.1.4	Spectral analysis	112
6.1.5	Discussion	118
6.2	Conclusions	123
7	Mrk609 – A composite galaxy with flat X-ray spectrum	124
7.1	Introduction	124
7.1.1	Other composite galaxies observed in X-rays	125
7.1.2	Mrk609	126
7.2	Observations and Data Reduction	127
7.3	Variability	130
7.3.1	Long-term variability	130
7.3.2	Short-term variability	133
7.4	The <i>ROSAT</i> spectrum	137
7.4.1	The AGN models	137

7.4.2	The composite model	138
7.4.3	The starburst models	138
7.5	The <i>BeppoSAX</i> spectrum	141
7.5.1	The AGN models	141
7.5.2	The composite model	142
7.5.3	The pure starburst model	143
7.6	Spectral variability	144
7.6.1	Observation 1	144
7.6.2	Observation 2	145
7.6.3	Observation 3	145
7.6.4	LECS/PSPC spectra comparison	146
7.7	Discussion	147
7.8	Conclusions	151
8	Conclusions	153
8.1	Broad line QSOs	153
8.2	Seyfert 2 galaxies	154
8.3	ULIRGs – The Superantennae	155
8.4	Composite galaxies – Mrk609	155
8.5	Future Prospects	156

List of Figures

1.1	The spectral energy distribution of the Seyfert 1 galaxy NGC 3783 from radio to γ rays. For comparison the SED of a normal galaxy is shown (Peterson 1997).	3
1.2	The optical spectrum of the Seyfert 1 galaxy NGC 5548. The prominent broad and narrow lines are labelled. The FWHM of the broad components is about 5900 km sec^{-1} , and the width of the narrow components is about 400 km sec^{-1} . The lower panel shows the same spectrum as in the upper panel, with the vertical scale expanded to show the weaker features (Peterson 1997).	5
1.3	A schematic view of the central region of a Seyfert galaxy.	11
1.4	The X-ray reflection model.	14
1.5	Spectrum of the extragalactic sky from the radio to γ rays. The bulk of the energy density at X-rays is emitted at around 30 keV (Fabian and Barcons, 1992).	16
1.6	The spectrum of the X-ray background. The thin line is the empirical fit discussed in the text (taken from Charles And Seward 1995).	17
2.1	The effective on-axis area of the <i>ROSAT</i> XMA+PSPC combination with (dashed line) and without (solid line) the boron filter.	25
2.2	The effective area of one XRT, as derived from in-flight calibration. The absorption features between 2-4 keV are the M edges of gold, the reflecting surface of the mirrors. Also shown is the dependence of the effective area on off-axis angle and on azimuthal angle.	26
2.3	The decrease of XRT effective area as a function of off-axis angle for two energies, 1 keV and 7 keV.	27

2.4	The effective area of a single GIS combined with a single XRT for five off-axis angles (0, 5, 10, 15, 20 arcmin).	29
2.5	The effective area of a single SIS and XRT combined for three off-axis angles (0, 5, 10 arcmin).	30
2.6	The effective area of the MECS at different off-axis angles.	33
2.7	The ratio between the off-axis effective area to the on-axis. The curves correspond to the effective area at off-axis angles (0, 4, 6, 8, 12, 16 and 20 arcmin).	34
3.1	The derived integral logN-logS in the 2-10 keV band from our survey; see text for details	38
3.2	Probability of finding an NVSS source within a given radius of an arbitrary position	39
3.3	The hardness ratio (HR) versus flux for our QSOs with predicted HRs for various power-law indices(left hand scale) and for a power-law with $\Gamma = 1.9$ and a range of absorption (right hand scale). The two with possible radio counterparts are shown (stars). Arrows indicate lower limits.	44
3.4	The HR versus the redshift of the sources.	45
3.5	The HR versus the 2-10 keV luminosity.	45
3.6	The <i>ROSAT</i> model to data ratio for the single power-law model over the 0.1-2 keV band, as discussed in the text.	47
3.7	The unfolded spectrum for the power-law model for (a) the <i>ASCA</i> data over the 0.8-8.0 keV; (b) the <i>ROSAT</i> data over the 0.1-2.0 keV; (c) <i>ROSAT</i> data over the 0.5-2.0 keV and (d) the joint data over the 0.5-8.0 keV. The model fits are shown by solid histogram.	49
3.8	The <i>ROSAT</i> 1-2 keV count rate versus the <i>ASCA</i> count rate in the same band. The dotted line corresponds to equal <i>ROSAT</i> and <i>ASCA</i> counts.	51
4.1	The single power-law model for NGC 2273 with $\Gamma = -0.55^{+0.11}_{-0.11}$, $\chi^2(\text{dof})=82.92(22)$. The top panel shows the data with the model and the bottom panel shows the data/model ratio. Data from the two GIS and two SIS have been combined for clarity. The stars represents the GIS data points and open squares the SIS points.	61

4.2 The single power-law model with $\Gamma=1.9$ for NGC 2273, $\chi^2(\text{dof})=117.47(22)$. The top panel shows the data with the model and the bottom panel shows the data/model ratio. Data from the two GIS and two SIS have been combined for clarity. The stars represents the GIS data points and open squares the SIS points. 61

4.3 The single power-law model for NGC 3079 with $\Gamma = 1.93_{-0.12}^{+0.12}$, $\chi^2(\text{dof})=228.06(143)$. The top panel shows the data with the model and the bottom panel shows the data/model ratio. Data from the two GIS and two SIS have been combined for clarity. The stars represents the GIS data points and open squares the SIS points. 62

4.4 The single power-law model for NGC 3147 with $\Gamma = 1.82_{-0.06}^{+0.05}$, $\chi^2(\text{dof})=289.22(285)$. The top panel shows the data with the model and the bottom panel shows the data/model ratio. Data from the two GIS and two SIS have been combined for clarity. The stars represents the GIS data points and open squares the SIS points. 62

4.5 The single power-law model for NGC 4698 with $\Gamma = 1.91_{-0.14}^{+0.14}$, $\chi^2(\text{dof})=243.90(250)$. The top panel shows the data with the model and the bottom panel shows the data/model ratio. Data from the two GIS and two SIS have been combined for clarity. The stars represents the GIS data points and open squares the SIS points. 63

4.6 The single power-law mode for M51 with $\Gamma = 3.07_{-0.06}^{+0.06}$, $\chi^2(\text{dof})=568.88(178)$. . The top panel shows the data with the model and the bottom panel shows the data/model ratio. Data from the two GIS and two SIS have been combined for clarity. The stars represents the GIS data points and open squares the SIS points. 63

4.7 The single power-law model with $\Gamma=1.9$, $\chi^2(\text{dof})=848.21(179)$ for M51. The top panel shows the data with the model and the bottom panel shows the data/model ratio. Data from the two GIS and two SIS have been combined for clarity. The stars represents the GIS data points and open squares the SIS points. 64

4.8 The scattering model for NGC 2273. The top panel shows the data with the model and the bottom panel shows the data/model ratio. Data from the two GIS and two SIS have been combined for clarity. The stars represents the GIS data points and open squares the SIS points. 73

4.9 The composite model for NGC 3079. The top panel shows the data with the model and the bottom panel shows the data/model ratio. Data from the two GIS and two SIS have been combined for clarity. The stars represents the GIS data points and open squares the SIS points. 74

4.10	The composite model for M51. The top panel shows the data with the model and the bottom panel shows the data/model ratio. Data from the two GIS and two SIS have been combined for clarity. The stars represents the GIS data points and open squares the SIS points.	78
4.11	The $f_{HX}/f_{[OIII]}$ versus the column density obscuring the primary X-ray emission.	80
4.12	The column density distribution of all the Seyfert 2 galaxies from the Risaliti sample. The light grey part in the fifth column includes all the sources for which only a lower limit of 10^{24}cm^{-2} is available. The white part represents the objects presented in this Chapter.	85
5.1	Optical spectrum from the nucleus of NGC 4698. No trace of broad H_{α} is visible.	88
5.2	The diagnostic emission line ratios adopted by Veron <i>et al.</i> (1997) for HII regions (crosses), Liners (squares) and Seyfert 2 (circles). The three classes of objects are well defined in these diagrams. NGC 4698 position in the diagrams is marked as a thick cross, whereas NGC 3147 position as a thick star.	89
5.3	The power-law plus warm absorber unfolded spectrum for NGC 4698. The hard component is fitted with a power-law, whereas the soft component is represented by a warm absorbed power-law continuum. The solid line represents the integrated model.	91
5.4	The GIS2+GIS3 light curve for NGC 4698 in the 2-10 keV band.	92
5.5	The GIS2+GIS3 light curve for NGC 4698 in the 0.5-2 keV.	92
5.6	The NGC 4698 spectral energy distribution (stars). The fluxes are taken from NED. Where there are multiple observations, data obtained using the smallest aperture were used. Specifically, V band magnitude 11.39(64.9" aperture), I band magnitude 10.54 (36" aperture) and H band (51.8" aperture). For comparison the NGC 1068 SED (dots) as well as the mean QSO SED (line) from Elvis <i>et al.</i> (1994) are shown.	94
5.7	Plot of the average SEDs. The error bars are standard deviation of the average. Taken from Schmitt <i>et al.</i> 1997.	95

5.8	The power-law plus warm absorber unfolded spectrum for NGC 3147. The hard component is fitted with a power-law, whereas the soft component is represented by a warm absorbed power-law continuum. The solid line represents the integrated model.	101
5.9	The GIS2+GIS3 light curve for NGC 3147 in the 2-10 keV band.	101
5.10	The GIS2+GIS3 light curve for NGC 3147 in the 0.5-2 keV.	102
5.11	The NGC 3147 spectral energy distribution.	102
6.1	Optical spectrum through a 3"x 6" aperture of the southern nucleus of IRAS 19254-7245. This nucleus corresponds in position to the IRAS emission peak and shows a characteristic Seyfert 2 type spectrum.(Taken from Colina <i>et al.</i> 1991)	109
6.2	Optical spectrum of the northern nucleus using the same aperture as in Figure. 6.1. Only H_{α} and $[N_{II}]$ are detected in emission.(Taken from Colina <i>et al.</i> 1991)	110
6.3	H_{β} and $[OIII]4959,5007 \text{ \AA}$ emission line profiles showing four independent kinematical components. They are explained in terms of a biconical outflow model. (Taken from Colina <i>et al.</i> 1991)	110
6.4	The single power-law model with the spectral index as a free parameter. The top panel shows the data with the model and the bottom panel shows the data/model ratio. Data from the two GIS and two SIS have been combined for clarity. The stars represent the GIS data points and open squares the SIS points.	113
6.5	The single power-law model for $\Gamma=1.9$ and galactic absorption. The top panel shows the data with the model and the bottom panel shows the data/model ratio. Data from the two GIS and two SIS have been combined for clarity. The stars represent the GIS data points and open squares the SIS points.	114
6.6	The single power-law model for $\Gamma=1.9$ and $N_H = 0.54^{+0.46}_{-0.34} \times 10^{22} \text{ cm}^{-2}$. The top panel shows the data with the model and the bottom panel shows the data/model ratio. Data from the two GIS and two SIS have been combined for clarity. The stars represent the GIS data points and open squares the SIS points.	114

6.7	The “scatterer” model. The top panel shows the data with the model and the bottom panel shows the data/model ratio. Data from the two GIS and two SIS have been combined for clarity. The stars represent the GIS data points and open squares the SIS points.	118
6.8	The reflection model with the scattered power-law. The top panel shows the data with the model and the bottom panel shows the data/model ratio. Data from the two GIS and two SIS have been combined for clarity. The stars represent the GIS data points and open squares the SIS points. . . .	119
7.1	Image of Mrk609 obtained with WFPC2 on-board the HST. The arrowhead points north and the bar is east. The length of the eastern bar is 2”. Taken from Malkan <i>et al.</i> 1998.	128
7.2	Optical spectrum of Mrk609 observed through 8” aperture and shown in the rest frame. The prominent emission lines and stellar absorption features are also marked. Taken from Rudy <i>et al.</i> 1988.	129
7.3	Ultraviolet spectrum of Mrk609. The prominent emission lines are labeled. Taken from Rudy <i>et al.</i> 1988.	129
7.4	The 0.1-2 keV long-term light curve. The flux is decreasing.	131
7.5	The MECS 2-10 keV long-term light curve.	131
7.6	The MECS 2-5 keV long-term light curve.	132
7.7	The MECS 5-10 keV long-term light curve.	132
7.8	The 2-5 keV band light curve during the <i>first</i> observation.	134
7.9	The 2-5 keV band light curve during the <i>third</i> observation.	134
7.10	The 5-10 keV band light curve during the <i>first</i> observation.	135
7.11	The 5-10 keV band light curve during the <i>third</i> observation.	135
7.12	The 2-10 keV band light curve during the <i>first</i> observation.	135
7.13	The 2-10 keV band light curve during the <i>third</i> observation.	136
7.14	The <i>ROSAT</i> PSPC short-term light curve.	136

7.15	The <i>ROSAT</i> PSPC spectrum when the single power-law model discussed in the text is applied to the data. The top panel shows the data with the model and the bottom panel shows the data/model ratio.	139
7.16	The <i>ROSAT</i> PSPC spectrum when the power-law model plus the blackbody model discussed in the text is applied to the data. The top panel shows the data with the model and the bottom panel shows the data/model ratio. It is obvious that the inclusion of the Blackbody component does not improve the fit.	139
7.17	The <i>ROSAT</i> PSPC <i>unfolded</i> spectrum when the warm absorber model discussed in the text is applied to the data.	140
7.18	The <i>ROSAT</i> PSPC spectrum when the single Raymond-Smith model discussed in the text is applied to the data. It is clear that there is a significant soft excess that the model cannot explain. The top panel shows the data with the model and the bottom panel shows the data/model ratio.	140
7.19	The <i>BeppoSAX</i> time averaged spectrum, when the single power-law with $\Gamma = 1.57_{-0.10}^{+0.10}$, $\chi^2=98.89(\text{dof})$ is applied to the data. The filled squares represent the LECS data points and the stars the MECS data points. The top panel shows the data with the model and the bottom panel shows the data/model ratio	142
7.20	The <i>BeppoSAX</i> spectrum for the first observation for a power-law with $\Gamma = 1.63_{-0.16}^{+0.16}$, $\chi^2=55.75(38)$. The filled squares represent the LECS data points and the triangles the MECS data points. The top panel shows the data with the model and the bottom panel shows the data/model ratio.	145
7.21	The <i>BeppoSAX</i> spectrum for the third observation for a power-law with $\Gamma = 1.64_{-0.14}^{+0.14}$, $\chi^2=61.16(48)$. The filled squares represent the LECS data points and the triangles the MECS data points. The top panel shows the data with the model and the bottom panel shows the data/model ratio.	146
7.22	The <i>BeppoSAX</i> spectrum for the third observation for a power-law with $\Gamma = 1.64_{-0.14}^{+0.14}$, $\chi^2=61.16(48)$ and a gaussian line at $6.72_{-0.24}^{+0.22}$. The filled squares represent the LECS data points and the triangles the MECS data points. The top panel shows the data with the model and the bottom panel shows the data/model ratio.	147
7.23	The H_α line versus the 2-10 keV luminosity correlation from Ward <i>et al.</i> (1988). Mrk609 is marked as a filled circle.	150
7.24	The spectral energy distribution of Mrk609, from far infrared to hard X-rays.	151

List of Tables

1.1	Range of typical X-ray luminosities for each type of AGN.	8
2.1	Selection criteria	31
2.2	X-ray telescopes+detectors characteristics, from which the data I have used in this thesis.	33
3.1	List of ASCA fields	41
3.2	The list of the QSOs in the 6 fields. The columns contain the following information: (1) The source name; (2) ASCA position of the object; (3) The redshift of the optical counterpart; (4) ASCA GIS count rate in the 1-2 keV band, together with the photon errors in units of 10^{-3} count s^{-1} ; (5) same as (4) but in 2-10 keV band; (6) ASCA GIS flux in the 2-10 keV band for a power-law with $\Gamma=1.56$ and Galactic absorption, in units of $\times 10^{-14}$ erg cm^{-2} s^{-1} ; (7) hardness ratio; (8) flux at 1.4 GHz in mJy	42
3.3	Results of spectral fits, fixing the photoelectric absorption to the galactic values shown in Table 1.	50
4.1	The ASCA Seyfert 2 sample. The columns contain the following information: (1) The source name; (2) The sequence number of the observation; (3)&(4) Optical position of the object; (5) The exposure time for SIS-0 in ks; (6) The source redshift; (7) The line of sight Galactic hydrogen column density; (8) References to the previously published hard X-ray data.	58

4.2	The optical properties of the ASCA Seyfert 2 sample. The columns contain the following information: (1) The source name; (2) The host galaxy type; (3) internal reddening (mag); (4) Luminosity of the narrow component of H_{α} in units of erg s^{-1} , marked as lower limit (L) if the observing conditions were non-photometric; (5) Equivalent width of the narrow component of H_{α} in \AA ; (6) Magnitude in V band from de Vaucouleurs <i>et al.</i> 1991. . . .	59
4.3	Single power-law model	65
4.4	Power-law plus iron line	66
4.5	Scattering model	67
4.6	Composite Model	67
4.7	Compton thick model	69
4.8	Hard X-ray, [OIII] λ 5007 fluxes and classification	81
4.9	Summary of results. The columns contain the following information: (1) The source name; (2) the model which best describes the data; and (3) the column covering the power-law component.	86
6.1	Global properties of the Superantennae. Reproduced from Mirabel <i>et al.</i> (1991).	111
6.2	Measured emission-line flux. Reproduced from Colina <i>et al.</i> (1991).	112
6.3	Spectral fits to the ASCA data.	115
7.1	The properties of MKN609.	127
7.2	χ^2 for the long-term light curves.	130
7.3	χ^2 for the short-term light curves.	134
7.4	The spectral fits results on the <i>ROSAT</i> data.	137
7.5	The spectral fits results on the <i>BeppoSAX</i> data.	143

Chapter 1

Introduction

1.1 A brief History of X-ray astronomy

The only astronomical object known to emit X-rays 40 years ago was our Sun; It was the first celestial object detected emitting X-rays. Therefore most rocket observations of the 1950s were devoted to detailed studies of the Sun. However the true era of X-ray astronomy began in 1962 with an experiment aiming to search for X-rays from the Moon produced by the interaction of energetic solar wind particles with the lunar surface. The experiment failed to detect any X-rays from the Moon's surface, but it detected the first ever discovered extragalactic powerful X-ray source. The source is in the constellation Scorpius and thus it is was named Sco X-1.

After this exciting, at that time, discovery X-ray astronomy progressed rapidly. X-rays cannot penetrate the Earth's atmosphere, thus it is impossible to observe X-rays with ground-based instruments and in the late 1960s the technology did not allow the building of satellites to carry detectors. The means of observations were limited to rockets and balloons, which put constraints on the size and weight of the payload. The first sources detected at these early days were primarily X-ray binaries stars such as Cyg X-1 and Cen X-3. The first extragalactic source discovered was the active galaxy M87.

Yet the obvious questions such what these X-rays sources are and how the huge energy

output is generated were not answered until in 1970 with the launch of the first satellite devoted to X-ray observations, *UHURU*, which mapped the X-ray sky for the first time. Many sources were soon discovered, including extragalactic sources such as active galactic nuclei (AGN), quasi-stellar objects (QSOs) and clusters of galaxies, and galactic sources such as supernovae remnants, neutron stars and clusters of stars.

The development of mirror technology and new sophisticated types of detectors led to huge progress in X-ray astronomy. In the nineties the *Roentgen Observatory Satellite*, *ROSAT* with its high resolution imaging capability, conducted an all-sky survey in both the X-ray (0.1-2.4 keV) and EUV (extreme ultraviolet: 60-300Å). The *Advanced Satellite for Cosmology and Astrophysics*, *ASCA* sensitive in the range 0.5-10 keV, enabled spectroscopic observations of faint X-ray sources and medium resolution imaging in the hard X-ray regime, while *BeppoSAX* with its wide spectral coverage offered a window at even higher energy X-rays. The recent launch of *Chandra* which has an unprecedented X-ray imaging capability and the *XMM-Newton* with its good spectral resolution and large effective area over the 0.1-10 keV band promise to widen our knowledge of X-ray astrophysics.

1.2 The AGN phenomenon

Active Galactic Nuclei (AGN) are powerful sources of radiation in the central regions of galaxies. The galaxies which host an AGN are called active galaxies. Their bolometric luminosity span a wide range of values from $\sim 10^{41}$ to $\sim 10^{47}$ erg s⁻¹. From the variability observed in many AGNs, the luminosity is believed to emanate from a region much smaller than 1pc. The more extreme examples outshine their host galaxies by a factor of 100 or more, and thus have a starlike appearance. Because of this, when they were first discovered they were mistaken for stars and eventually they are given the name *quasi-stellar objects* (QSOs). In general a galaxy is classified as an AGN if any of the following is observed:

- Compact nuclear region, brighter than the corresponding region in galaxies of similar

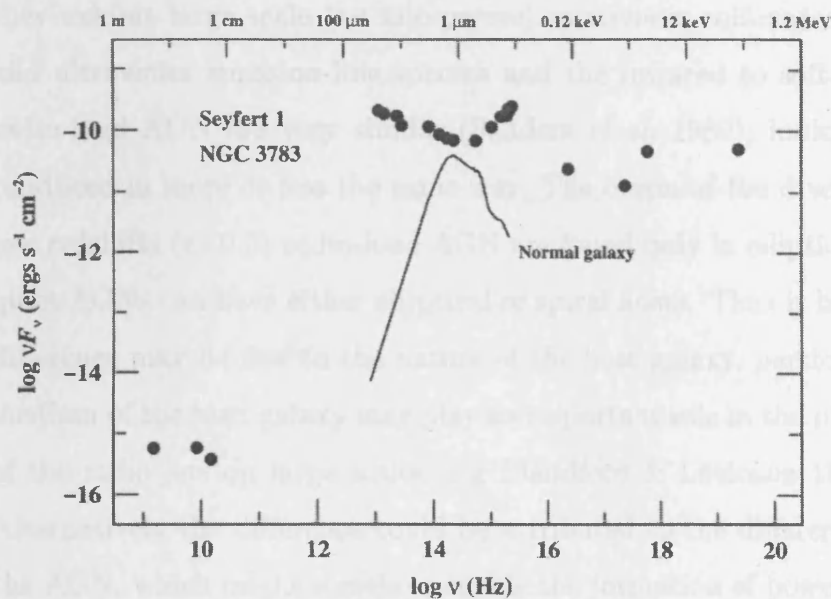


Figure 1.1: The spectral energy distribution of the Seyfert 1 galaxy NGC 3783 from radio to γ rays. For comparison the SED of a normal galaxy is shown (Peterson 1997).

Hubble type.

- Nonstellar nuclear continuum emission.
- Nuclear emission lines indicating excitation by a nonstellar continuum.
- Variable continuum and/or emission lines.

In addition the Spectral Energy Distribution (SED) of AGNs show that they are powerful emitters across the whole electromagnetic spectrum from radio to γ rays (Figure 1.1). Such amounts of energy cannot be attributed as being produced by stars within the galaxy, as is the case for normal galaxies. AGNs present a diversity of properties and hence an extensive observational classification scheme has developed. They are classified according to their luminosity and spectrum. The classification is based on their phenomenology and not on fundamental differences between the various types.

A fundamental division in the classification scheme is based on the radio properties of the AGNs. The majority of AGN fall into the *radio-loud* and *radio-quiet* class, with about 10 percent of them being radio-loud. The main characteristic of radio-loud AGNs is that

they exhibit large scale (i.e kilo-parsec) relativistic collimated jets. Usually the optical and ultraviolet emission-line spectra and the infrared to soft X-ray continuum of most radio-loud AGN are very similar (Sanders *et al.* 1989), indicating that the emission is produced in more or less the same way. The origin of the divergence is not yet clear. At low redshifts ($z < 0.5$) radio-loud AGN are found only in elliptical galaxies, whereas radio-quiet AGNs can have either elliptical or spiral hosts. Thus it has been suggested that the difference may be due to the nature of the host galaxy, particularly that the interstellar medium of the host galaxy may play an important role in the propagation and collimation of the radio jets on large scales (e.g Blandford & Levinson 1995; Fabian & Rees 1995). Alternatively the difference could be attributed to the difference in the central engine of the AGN, which might somehow enable the formation of powerful relativistic jet. Radio-quiet AGNs do not show large scale jets, but smaller-scale (parsec-scale) jets have been observed (Blundell *et al.* 1996). Larger scale radio structures have also been detected, but it is unclear whether these too are related to the AGN or are associated with starburst driven superwinds from the host galaxy (Baum *et al.* 1993). Below I briefly review the the various types of active galaxies. Table 1.1 shows their typical X-ray luminosities.

1.2.1 Seyferts

Seyfert galaxies owe their name to Carl Seyfert, who defined their properties in 1940. Since then Seyfert galaxies have been split into two main types. Seyfert 1 galaxies, whose optical spectrum has broad permitted emission lines (full width at half maximum (FWHM) up to $\sim 10^4$ km sec⁻¹) and relatively narrow forbidden lines (FWHM up to ~ 1000 km sec⁻¹), and Seyfert 2 galaxies, which differ from Seyfert 1 galaxies in that they have only narrow lines in their spectrum. In addition to the strong emission lines, both types exhibit weak absorption lines due to the late-type giant stars in the host galaxies. Figure 1.2 shows the optical spectrum of the Seyfert 1 galaxy NGC 5548, where the broad and narrow line are clearly seen. The full width half maximum (FWHM) of the broad components is about 5900 km sec⁻¹, and the width of the narrow components is about 400 km sec⁻¹. The spectrum shows major differences compared to the spectra of normal galaxies. The

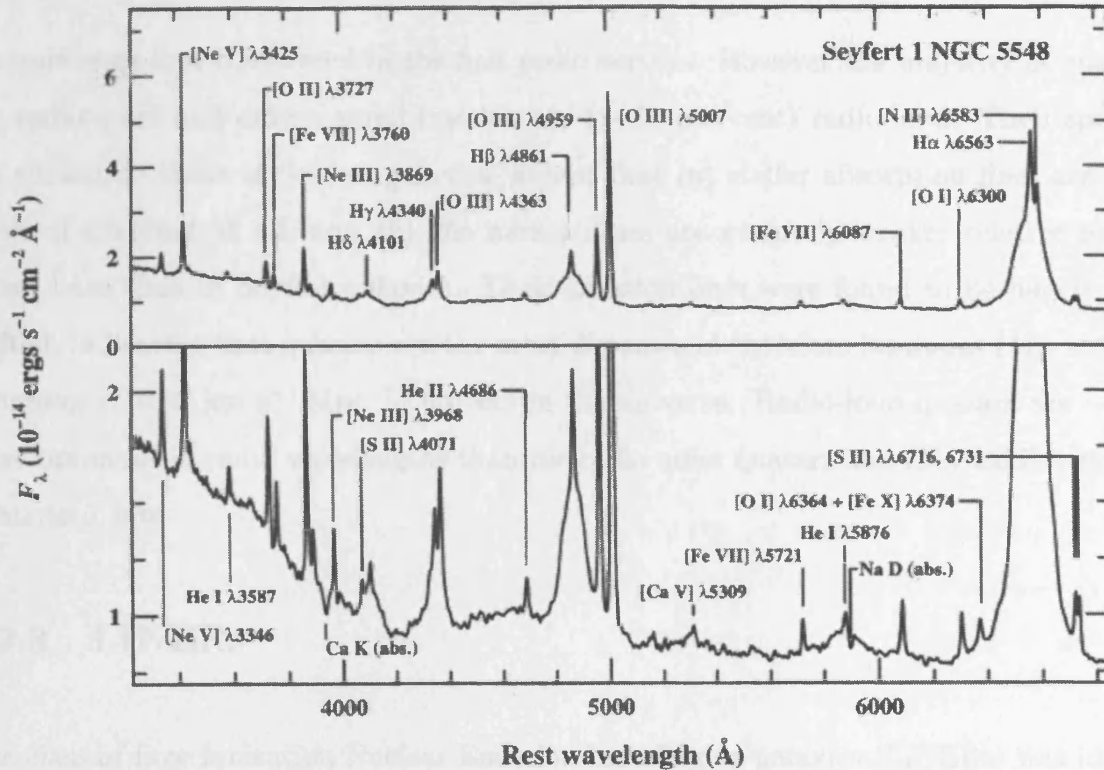


Figure 1.2: The optical spectrum of the Seyfert 1 galaxy NGC 5548. The prominent broad and narrow lines are labelled. The FWHM of the broad components is about 5900 km sec^{-1} , and the width of the narrow components is about 400 km sec^{-1} . The lower panel shows the same spectrum as in the upper panel, with the vertical scale expanded to show the weaker features (Peterson 1997).

latter contain stellar absorption lines and narrow emission lines whereas the emission lines in AGNs are strong and often broad. Osterbrock (1981) has introduced 3 further subclasses, namely Seyfert 1.5, 1.8 and 1.9 based on the relative strengths of the broad lines and narrow lines. However, caution must be taken in classifying the galaxies, since there are cases, where the broad-line emission variability is so strong that the classification changes with time. All Seyfert nuclei appear to reside in spiral galaxies.

1.2.2 Quasars

Quasars were first discovered in the first radio surveys. However the majority of quasars are radio-quiet and only a small fraction are (~ 10 per cent) radio-loud. Their spectra are similar to those of Seyfert galaxies, except that (a) stellar absorption lines are very weak, if detected at all, and (b) the narrow lines are generally weaker relative to the broad lines than in Seyfert galaxies. Their emission lines were found to be hugely redshifted, indicating that quasars are the most distant and therefore luminous ($M_B < -23.0$, assuming $H_0 = 50 \text{ km s}^{-1} \text{ Mpc}^{-1}$) objects in the universe. Radio-loud quasars are $\sim 10^4$ more luminous in radio wavelengths than the radio quiet quasars and they exhibit strong relativistic jets.

1.2.3 LINERs

The class of Low Ionisation Nuclear Emission Line Region galaxies (LINERs) was identified by Heckman (1980). Spectroscopically they resemble Seyfert 2 galaxies, except that they have relatively strong low ionisation lines (e.g $[OI]\lambda 6300$ and $[N_I I]\lambda\lambda 6548, 6583$) compared to the high ionisation lines (e.g $[OIII]\lambda\lambda 4959, 5007$), which are somewhat narrower ($200\text{-}400 \text{ km s}^{-1}$) than the narrow lines of Seyferts. In addition some of them show weak broad lines as well. They are the most common type of galaxy nuclear activity; one third of all the spiral galaxies with $B < 12.5$ show LINER spectra (Ho *et al.* 1996). It is an heterogeneous class of objects with ~ 24 per cent having a broad H_α line component. There is growing evidence that they represent the low luminosity end of the quasar phenomenon.

1.2.4 NELGs

Narrow Emission Line Galaxies (NELGs) were first identified in the early X-ray surveys and are also known as Narrow Line X-ray Galaxies (NLXGs). They possess narrow ($\text{FWHM} \leq 1000 \text{ km s}^{-1}$) emission lines, typically H_α , H_β , $[OIII]\lambda 5007$. Their X-ray lumi-

nosities ($L_x \sim 10^{42} \text{erg s}^{-1}$) are orders of magnitude higher than those of nearby normal galaxies with similar optical magnitudes (Fabbiano 1989). It is not clear whether the X-ray emission is thermal or whether it emanates from an active nucleus. It is possible that some of the activity may be associated with a starburst. About 10 per cent of the low redshift galaxies may be NELGs. In view of the fact that their X-ray spectrum is hard (Almaini *et al.* 1996; Romero-Colmenero *et al.* 1996) and that they are numerous, they are considered to be the best candidates for producing the bulk of the X-ray background.

1.2.5 Radio Galaxies

Radio galaxies are strong radio sources and they occur in elliptical galaxies. On the basis of their radio morphology and optical/UV properties the radio galaxies are divided into two sub-classes; Fanaroff-Riley type 1 (FR-I, Fanaroff & Riley 1974) radio galaxies ($L_{\text{radio}} \leq 10^{42} \text{erg s}^{-1}$), whose radio surface brightness profile fall continuously, as one proceeds from the nucleus to the edge of the radio lobe. Most FR-I did not show broad optical /UV emission lines (Urry & Padovani 1995). The Fanaroff-Riley type 2 (FR-II) radio galaxies ($L_{\text{radio}} \geq 10^{42} \text{erg s}^{-1}$) has a different morphology than the FR-I galaxies. Their radio surface brightness can be low in the central regions of the source (apart from the nucleus itself) and dramatically brighten towards the edge of the halo as the jets are seen to terminate at strong shocks. Two types of FR-II have been identified similar to the Seyfert1/Seyfert2 classification; broad line radio galaxies (BLRGs) and narrow line radio galaxies (NLRGs).

1.2.6 Blazars

All known blazars are radio sources, which are distinguished by the absence of strong emission or absorption lines in their optical/UV spectra and the very strong and variable emission at all wavelengths. It is believed that either these objects do not possess the emission line regions of other AGN-types or the line emission is present but swamped by the strong continuum.

Table 1.1: Range of typical X-ray luminosities for each type of AGN.

Type	Luminosity 2-10 keV in erg s ⁻¹
Quasars	10 ⁴⁴ – 10 ⁴⁵
Seyferts	10 ⁴¹ – 10 ⁴³
LINERs	10 ⁴⁰ – 10 ⁴¹
NELGs	10 ⁴⁰ – 10 ⁴²
BLAZARs	10 ⁴⁴ – 10 ⁴⁵

1.3 The Black Hole paradigm

Although the AGNs can be divided into various subclasses, they share common characteristics. One obvious link is that all forms of activity in these galaxies originate in the nucleus. The generic observational similarities can be grouped into four categories, as follows:

- AGNs emit energy at an enormous rate. The energy output of the AGN can exceed the total luminosity of all the stars in the galaxy by more than a factor of 100.
- AGNs are extremely compact. Variability studies have shown that the AGNs show rapid variability. They vary on timescales as short as a few hours in some cases.
- AGN radiation is nonthermal. This is established by the fact that AGNs emit comparable amounts of radiation over the whole electromagnetic spectrum and thus it is unlikely the radiation is produced by stars or gas.
- AGNs contain gas moving at extremely high speeds.

It is these similarities that established the class of AGNs as special objects and eventually led to a generally accepted physical interpretation of the AGN phenomenon. That is the black hole paradigm. Here I describe the basics of the model together with the supporting observational evidence. The common characteristics imply that there must a supermassive object in the central region of the AGN. The most plausible so far is a supermassive black

hole with a mass of $10^6 - 10^9 M_\odot$. While the processes, which lead to the formation of such a supermassive black hole are not clear (see Rees 1984 and references therein for various scenarios that can lead to the formation of such black holes), it is widely believed that the enormous luminosity of AGNs is produced by release of gravitational energy through the accretion of matter onto the black hole. The accreted material is thought to be surrounding gas and dust, and probably infalling stars, which are dragged in by the gravitational potential of the central black hole. The angular momentum of the infalling material is expected to cause an accretion disc to form around the black hole. In this process the matter gradually spirals inwards as it loses energy which is transformed into frictional heating and viscous dissipation. The accretion rate is thought to be up to \sim few M_\odot per year. In the context of this model the disk is self gravitating, geometrically thin and optically thick. Therefore it radiates locally as a blackbody.

Observational evidence for the presence of a black hole accreting via an accretion disk, in active galaxies has been accumulating over the past years. These include:

- The width of the broad optical/UV emission lines, implying Keplerian motions under the influence of a deep potential of a massive central object.
- X-ray variability studies, which suggest that the radiation must come from a region of the order of light days in size.
- The presence of fluorescent K_α iron emission line in the X-ray spectrum of AGNs. This line is thought to originate from the innermost regions of the accretion disk. Indeed the profile of the iron line obtained during a long *ASCA* observation of the Seyfert 1 galaxy MCG-6-30-15 is in exact agreement with that expected from material in a thin accretion disk near a black hole (Tanaka *et al.* 1995).
- The detection of masering clouds with VLBI in NGC 4258, which mapped out a nearly edge-on thin accretion disk about a light year across (Miyoshi *et al.* 1995). The material is found to be in almost Keplerian motion, suggesting a point-like mass with $M \sim 3.6 \times 10^7 M_\odot$.

- The existence of radio jets.
- The observation of a UV excess in spectra of several Seyfert 1 and quasars, known as 'big blue bump' (Malkan & Sargent 1982), which is interpreted as thermal emission from an accretion disk.

For the sake of completeness I should note here that the enormous activity of the active galaxies led researchers to the development of alternative models for the production of the AGNs' energy output. These models mainly postulate supermassive stars, cluster of stars or starbursts to be the long-lived 'central engine' of the AGN. However they either fail to predict many of the observed properties of the AGN or they are considered to be unstable and unlikely to represent more than a brief phase of the AGN life. Probably the only viable alternative model is the so-called 'starburst model for AGN' first proposed by Terlevich and collaborators (e.g Terlevich *et al.* 1992; Cid Fernandes 1997). In this model the energy is supplied by young stars in a nuclear star cluster and the UV/optical variability and broad emission lines are attributed to compact Supernova Remnants (cSNRs). However the model cannot account either for the broad K_{α} iron line or for the rapid X-ray variability. In addition radio loud objects have been excluded by the model, since it is unable to explain the radio loudness of some. High resolution imaging studies ($0''.05$) with the Hubble Space Telescope (HST) show that AGNs are unresolved. In the case of the nearest known AGN, NGC 4395 this translates to an upper limit for the size of the nucleus of 0.7pc (Filippenko *et al.* 1993). This means that the nuclear star cluster must be unusually compact. In conclusion the supermassive black hole model, which is also now considered the standard model for AGNs is the only model so far which fits the observations best, and as such is widely accepted.

1.4 Unification models for AGNs

It was soon realised that the properties of the narrow lines of type 1 and type 2 Seyferts are similar and it was therefore claimed that the differences between the two classes are due to

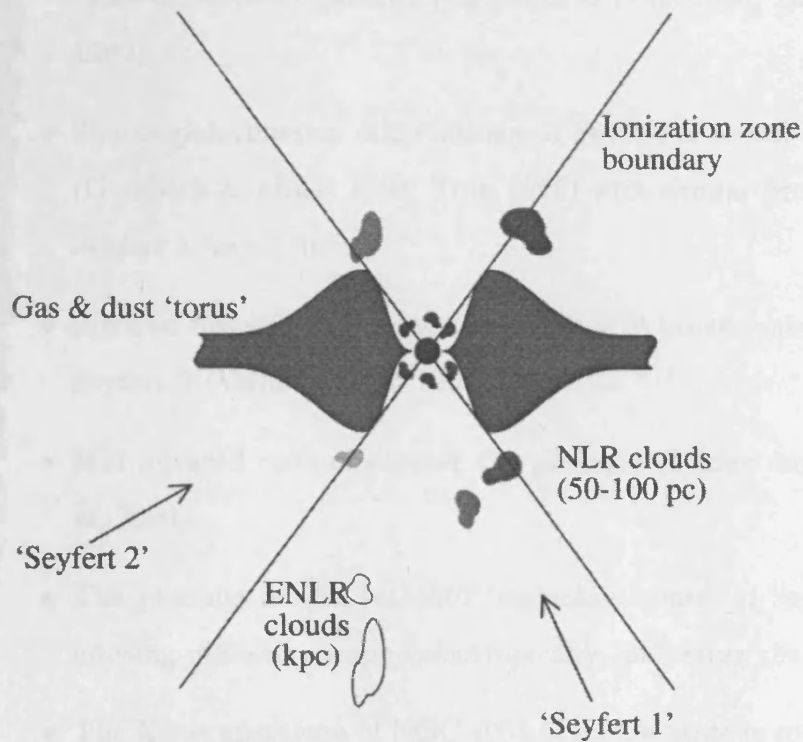


Figure 1.3: A schematic view of the central region of a Seyfert galaxy.

orientation effects. This led to the so-called 'Unified Model for AGN' (Antonucci 1993), which explains the differences between type 1 and type 2 Seyferts phenomenologically. According to the model both types are identical objects which possess a central black hole, accretion disk, a broad line region (BLR) and a thick molecular torus. Objects observed within the opening angle of the torus are classified as Seyfert 1 objects whereas those seen at angles intersecting the torus (and thus obscuring the BLR) appear as Seyfert 2 sources. The size of this central region is of the order of a few parsecs (pc), whereas the size of the region, where the narrow lines are produced is thought to be of the kpc scale and thus is visible in both classes. A schematic picture of the Unified Model of AGN is shown in Figure 1.3. Several observations support this classification scheme. Below follows a summary of the major observational evidence towards the Unification Model:

- X-ray observation of Seyfert 2 galaxies show column densities much higher than those of Seyfert 1 galaxies (e.g Smith & Done 1996, Turner *et al.* 1997, Risaliti *et al.* 1999).
- Spectropolarimetric observations of Seyfert 2 reveal broad optical emission lines (Goodrich & Miller 1994, Tran 1995) with similar properties (e.g. FWHM) to the Seyfert 1 broad lines.
- Infrared observations show the presence of broad emission lines in the spectrum of Seyfert 2 (Veilleux *et al.* 1997).
- Mid infrared colours suggest the presence of large amounts of dust (Murayama *et al.* 2000).
- The presence of $[OIII]\lambda 5007$ 'ionisation cones' in Seyfert 2 also suggest that the ionising photons escape anisotropically, indicating the presence of a torus.
- The X-ray spectrum of NGC 4051 in its low state is consistent with reflection of the primary continuum off distant (>150 light days) cold gas, which is interpreted as being the molecular torus.

A similar model exists for the Radio-Loud AGN. The only difference is the inclusion of relativistic jets. According to this scheme, blazars are objects in which our line of sight lies within the jet cone of the source. When the line of sight to the nucleus is within the opening angle of the torus but not of the jet we have a FR-II type 1 radio loud AGN (FR-II BLRG). For larger angles, where the nucleus is fully obscured by the torus the object is classified as a radio galaxy or FR-II NLRG. There is not clear yet how the FR-I radio galaxies fit into the scheme, but there is a lack of broad-line FR-I radio galaxies (see Urry & Padovani 1995), suggesting either a torus with a small opening angle or simply lack of a BLR in the FR-I galaxies.

I should add here that there are a few evolutionary models (e.g Sanders *et al.* 1988), which connect the different types of active galaxies. However any association of the different types of AGNs to evolutionary stages is premature at the moment.

1.4.1 The X-ray spectrum of Seyfert galaxies

The X-ray observations of AGNs are of great importance in understanding of the AGN phenomenon. Firstly because the X-ray emission accounts for about ~ 10 per cent of the bolometric luminosity of the AGNs and secondly because the X-ray emission is believed to be produced in the innermost regions of the AGNs, allowing us to probe the environment of the accreting black hole.

As has been already mentioned the black hole accretes matter via an accretion disk. The disk itself is expected to emit predominantly at optical/UV wavelengths, thus the most likely mechanism producing the X-rays is Compton up scattering of soft photons in a corona lying above and below the inner regions of the accretion disk. Multiple Compton scattering can indeed produce a power-law spectrum with $\Gamma \sim 2$, as observed. According to the standard model for accretion disk corona, energy is transferred from the accretion disk into an optically thin corona, although the exact mechanism is not yet known. In addition magnetic fields are likely to play an important role to the energy transfer process. The coronal heating produces either thermal or non-thermal electron distribution (Haardt & Maraschi 1991; Zdziarski *et al.* 1990, respectively). However, the non-detections by COMPTEL and the high energy cut-off indicating by OSSE (Jourdain *et al.* 1992; Maisack *et al.* 1993) and *BeppoSAX* (Matt *et al.* 1999) favours the thermal models for the generation of the X-ray spectrum.

A fraction of the primary emission irradiates the disk and is Compton 'reflected' (Lightman & White 1988; Guilbert & Rees 1988; George & Fabian 1991) in our light of sight. At low energies photoelectric absorption dominates so few photons are reflected. However the hard photons are rarely absorbed and are Compton scattered back out of the disk. The effect diminishes above ~ 100 keV due to Compton recoil. Additionally, fluorescent line photons will be emitted following the photoelectric absorption events. The most prominent of the lines is the K_{α} iron line at 6.4 keV. Figure 1.4 shows a Monte Carlo simulation of the reflected spectrum when a point source of a power-law with $\Gamma=1.9$ illuminates a semi-infinite slab of cold material.

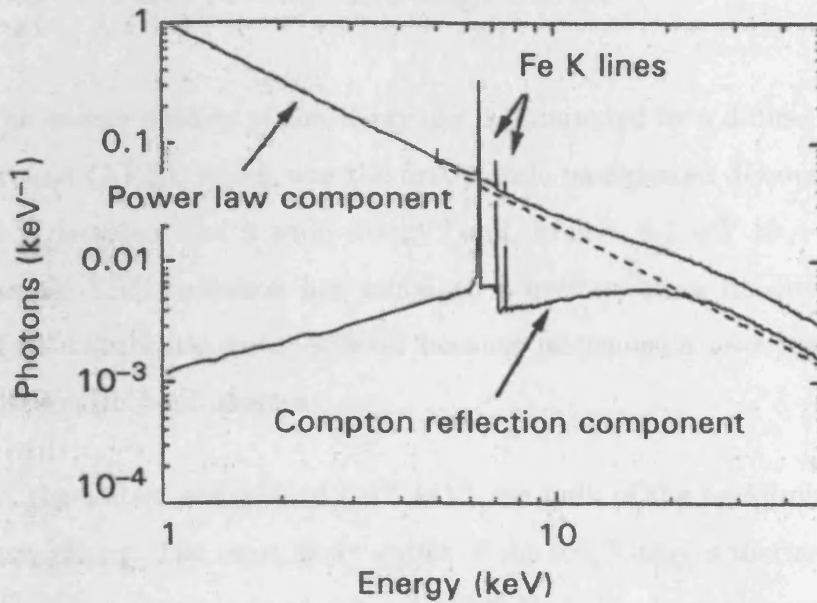


Figure 1.4: The X-ray reflection model.

At the soft energies K-shell absorption edges have been observed indicating the presence of partially-ionised, optically thin material in the vicinity of AGNs. This material is known as the warm absorber. A clear signature of its existence comes from the OVII and OVIII K-shell absorption edges detected with the *ROSAT* PSPC at 0.74 and 0.87 keV respectively (Nandra & Pounds 1994). However the location, density and distribution of this material are as yet unknown.

In the case of Seyfert 2 galaxies the underlying continuum is similar to that found for Seyfert 1s. However the X-ray spectrum exhibits a cut-off at low/medium energies due to the absorbing material ($N_H > 10^{22} \text{cm}^{-2}$) lying in our light of sight. The spectrum of Seyfert 2 galaxies shows also a soft excess (Turner *et al.* 1993; Turner *et al.* 1997). This feature is attributed either to the scattering of the primary emission by electrons in the central region or to starburst activity in the host galaxy.

1.5 The X-ray Background

The energy density of the X-ray sky is dominated by a diffuse radiation, the X-ray Background (XRB), which was the first cosmic background discovered (Giacconi *et al.* 1962). It is detected over a wide energy band, from ~ 0.1 keV to ~ 3 MeV. The origin of the cosmic XRB radiation has remained a mystery since its discovery. The determination of its nature has been difficult because instruments have had insufficient resolution to distinguish faint sources.

At the softest energies (0.1-0.5 keV) the bulk of the background comes from within our own galaxy. The most likely source of the soft X-rays is thermal emission from diffuse hot gas at a temperature of about 1×10^6 K. It has been observed that some galaxies have X-ray emitting halos which extend beyond the optical boundaries. If our Galaxy has one, the source of soft X-rays may be located in its hot galactic corona. However the lack of complete absorption in the plane rules out this as the only source of soft X-rays. The most likely explanation is an additional local source with emission coming from within 100 pc of the Sun; The local bubble, a region surrounding the Sun, which is full of hot ionised gas. A diameter of about 100 pc and a density of 10^{-2} electrons cm^{-3} would produce the observed emission.

At harder energies, where the relative contribution of the galactic component is low, the bulk of the emission is extragalactic. The origin of the extragalactic XRB could be explained by two main hypotheses: the point source hypothesis, where the XRB is assumed to originate by contribution of different classes of objects and the diffuse hypothesis. A substantial contribution from hot intergalactic gas is now ruled out since it would result in a Compton distortion of the microwave background spectrum, which is not observed by the *Cosmic Microwave Background Explorer* (COBE) (Mather *et al.* 1994). The observations set a stringent upper limit on the contribution of a diffuse hot intergalactic gas of 10^{-4} to the hard XRB (Wright *et al.* 1994). This implies that the bulk of the hard X-ray background arises in discrete sources. The number of contributed sources should

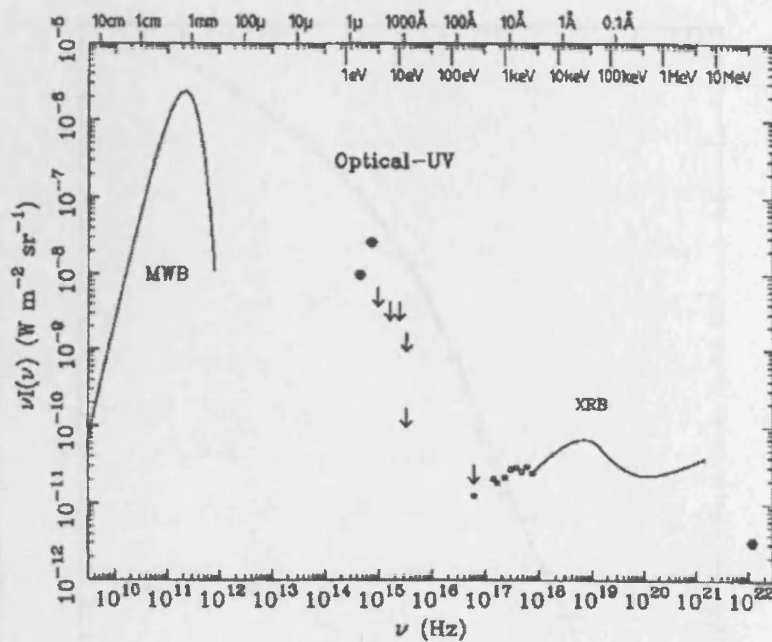


Figure 1.5: Spectrum of the extragalactic sky from the radio to γ rays. The bulk of the energy density at X-rays is emitted at around 30 keV (Fabian and Barcons, 1992).

be very large, since the background seems to be uniform.

1.5.1 The spectrum of the Cosmic X-ray background

At the energy range of 0.1-0.5 keV most of the background is galactic. A large fraction of the extragalactic component at these energies is absorbed by our galaxy. The bulk of the energy density is found at around 30 keV (Fabian and Barcons, 1992; see Figure 1.5).

The HEAO-1 A2 and A4 experiments provided a measurement of the XRB over the 3 to 6000 keV band. The observations showed that the spectrum is well-fitted by a ~ 40 keV thermal bremsstrahlung model (Marshall *et al.* 1980). Above 60 keV the sum of two power laws is further needed (Gruber *et al.* 1984): one is an extension of the bremsstrahlung spectrum and the other has an index of 0.7 which is the same as that of nearby AGNs. The spectrum of the XRB is shown in Figure 1.6, whereas the energy flux in units of $\text{keV}/(\text{cm}^2 \text{ s keV sr})$ is represented below:

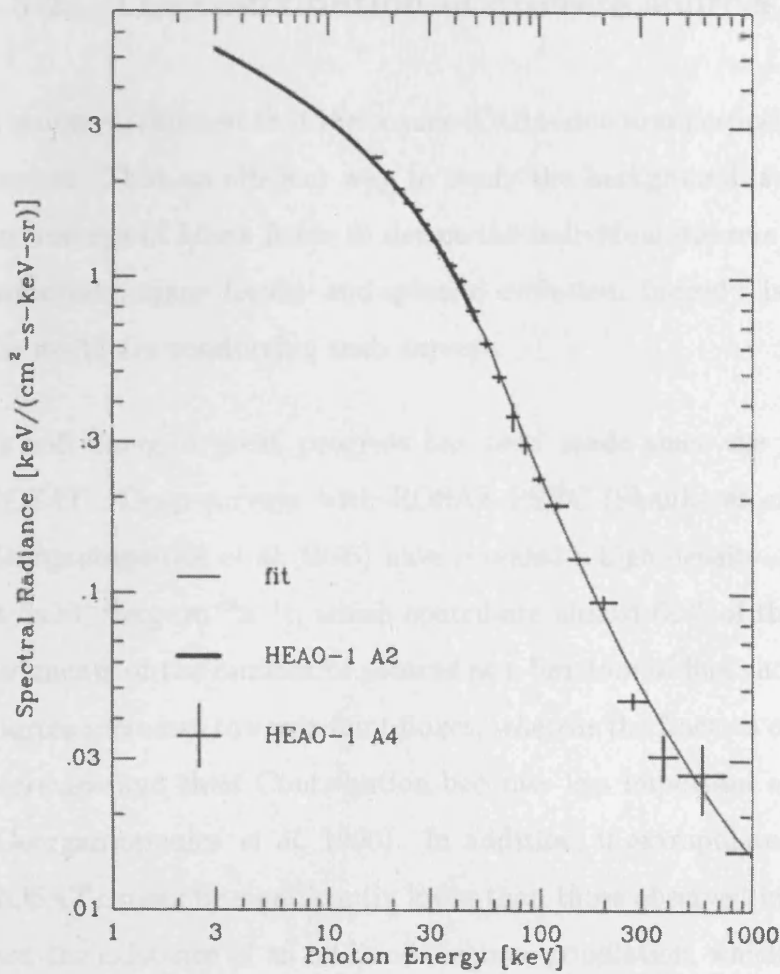


Figure 1.6: The spectrum of the X-ray background. The thin line is the empirical fit discussed in the text (taken from Charles And Seward 1995).

$$7.877E^{-0.29} \times \exp(-E/41.13), 3keV < E < 60keV \quad (1.1)$$

$$1652 \times E^{-2.0} + 1.754 \times E^{-7.0}, 60keV < E < 6000keV \quad (1.2)$$

The above description introduced the interesting possibility that hot plasma fills the universe. However, as already mentioned, this interpretation, although popular in the seventies and eighties, is now ruled out.

1.5.2 The contribution of discrete sources

It is now established that the cosmic XRB is due to superposition of discrete yet unresolved sources. Thus an efficient way to study the background is with high resolution deep X-ray surveys of blank fields to detect the individual discrete sources and then study their luminosity, space density and spectral evolution. Indeed a large number of groups all over the world are conducting such surveys.

At soft energies great progress has been made since the launch of the X-ray satellite *ROSAT*. Deep surveys with *ROSAT* PSPC (Shanks *et al.* 1991; Hasinger *et al.* 1993; Georgantopoulos *et al.* 1996) have revealed a high density of X-ray sources ($\geq 400\text{deg}^{-2}$, at $2 \times 10^{-15}\text{erg cm}^{-2}\text{s}^{-1}$), which contribute almost 60% of the soft (0.5-2keV) XRB. Measurements of the number of sources as a function of flux showed that the total number of sources increases towards faint fluxes, whereas the fraction of QSOs and Seyfert 1 galaxies decreases and their Contribution becomes less important at the very faintest flux limits (Georgantopoulos *et al.* 1996). In addition, if extrapolated to higher energies, the soft *ROSAT* counts lie significantly lower than those observed in hard X-rays. The above suggest the existence of an additional source population, which dominates at higher energies and fainter fluxes. Indeed a number of non-QSOs sources were identified with narrow emission line galaxies, but it is not clear whether their emission is due to AGN activity or some other mechanism. These sources are found to have much harder spectra than the QSOs', consistent with the XRB spectrum, and thus they are considered to produce the remaining soft XRB (Almaini *et al.* 1997).

On the other hand, the hard XRB, where the bulk of its energy density resides, remains less explored. The *HEAO-1* -1 experiment (Wood *et al.* 1984) detected several hundred sources over the whole sky, in the 2-10 keV band, with fluxes $\geq 5 \times 10^{-12}\text{erg cm}^{-2}\text{s}^{-1}$, contributing less than 5 per cent of the hard XRB density. The logN-logS from *HEAO-1* (Piccinotti *et al.* 1982) and *Ginga* (Kondo 1990) is represented by a Euclidean power-law with a normalization of a factor of 2 -3 above that of *ROSAT* counts distribution. *ASCA* resolved ~ 30 percent of the 2-10keV into discrete sources and the logN-logS is a factor

of 3 above the *ROSAT* counts in agreement with the previous results. The spectrum of the hard XRB is represented by a power law of ~ 1.4 (Marshall *et al.* 1980, Gendreau *et al.* 1995, Vecchi *et al.* 1999). However, nearby broad line AGNs have a power-law spectra with a photon index of $\Gamma = 1.7$ in the 2-10keV band (Turner & Pounds 1989) which again is significantly softer than that of the CXB. Thus the spectral paradox is extended to the hard energies as well. Both the spectrum of the XRB and the counts distribution suggest the presence of a hard spectrum population, other than the broad line AGN which contribute to the *ROSAT* counts.

ASCA surveys have detected another population with a flat hard X-ray spectra. Although there are hints that this could be associated with NELGS discovered in the *ROSAT* surveys, the limited statistics of the surveys and the spatial resolution of the ASCA detectors, a few identifications may be due chance coincidences (Georgantopoulos *et al.* 1997). A new population with harder indices ($a < 1.5$) is sought in order to explain the origin of the XRB.

The deep *Chandra* surveys deepened the riddle of the origin of the XRB even further. In the hard 2-10 keV band they probe fluxes at least an order of magnitude deeper than *ASCA* (Mushotzky *et al.* 2000) albeit with limited number statistics due to the small filed-of-view of the ACIS on-board *Chandra*. A large fraction of the detected sources is associated with QSOs which appear to have spectra steeper than the XRB. Surprisingly, no numerous, clearcut examples of the putative obscured AGN population at high redshift have yet been found. Instead, two 'new' populations emerged which are associated with either early-type galaxies or extremely faint optical counterparts.

1.5.3 Obscured AGN models for the X-ray background

Among the extragalactic sources, AGN are known to be the strongest X-ray emitters and have been considered to be the prime candidates to produce the XRB. The discrepancy of their spectral index to that of the XRB, as well as the flattening of the hard X-ray

spectrum of obscured sources has led to attempts to develop XRB spectrum with type 2 AGNs synthesis models using an appropriate mix of unabsorbed and absorbed AGNs (Madau *et al.* 1994; Comastri *et al.* 1995). The ratio of type 2 to type 1 objects as well as the distribution of the absorbing column density are the key parameters of the models and have to be assumed. A major problem of this model is that predicts the existence of a large number of obscured QSOs. However, apart from few exceptions, most notably RXJ 1343.4+0001 (Almaini *et al.* 1995, Georgantopoulos *et al.* 1999a) no such objects have been detected. The lack of a large amount of type 2 QSOs had been attributed to the possible ability of the luminous QSO nuclei to remove any obscuring dust from their vicinity. In addition Gunn & Shanks (1998) showed that moderately obscured objects although seen at X-ray energies, they are not detected in the optical due to the optical extinction taking the object below the spectroscopic identification limit. This suggest that the type 2 QSOs should be searched for in X-ray instead of optical surveys. Indeed results from the *BeppoSAX* High Energy LLarge Area Survey (HELLAS) and *ASCA* (see chapter 3), revealed that X-ray absorbed AGNs show a large variety of optical behaviour, and have been classified as intermediate type 1.5-1.9 objects or red quasars, or even typical broad line QSOs, indicating that the obscured QSOs are masked into other types in optical wavelengths.

Recently Gilli *et al.* (1999) using the most recent estimates of the AGN X-ray luminosity function and evolution, suggested that either a class of rapidly evolving obscured AGNs or intrinsically flat sources are needed in addition to the predictions of the standard scenario. The former sources could be the high redshift SCUBA sources. Indeed it is now believed that a significant fraction of the SCUBA sources (10-30%) will contain AGN (see Almaini 2000 for a review). The alternative hypothesis could instead be an accretion dominated accretion flow (ADAF) producing the X-ray emission (Di Matteo & Allen, 1999; Allen *et al.* 2000).

Criticisms of the obscured AGN model include the doubts on whether the observed smooth slope of the XRB can be produced by a superposition of many sources which contain emission lines in their spectra, in particular the strong iron line at 6.4 keV. Although

the sources span a wide range of redshifts and thus it would be expected the lines to be smeared out, this would have measurable effects on the shape of the XRB spectrum (Matt & Fabian 1994). However, Gilli *et al.* (1999) studied the effect of the iron features on the XRB and they found that the maximum contribution of the line to the XRB is less than 7 per cent, and thus the line contribution is undetectable within the dispersion of the current data, which is ~ 10 per cent for *ASCA* (Gendreau *et al.* 1995).

1.6 This thesis

In the previous sections I presented the phenomenological picture of the AGN phenomenon and outlined our current knowledge regarding the nature of the XRB. However, we should bear in mind that beyond the unified picture and the XRB synthesis models the real picture is not well understood. This thesis investigates the origin and nature of the Cosmic X-ray Background and the X-ray emission mechanisms of AGN, particularly of obscured AGN as these are believed to produce the largest fraction of the XRB especially at hard energies.

In particular in Chapter 2, I briefly present the capabilities of the satellites used to collect the data included in this thesis. Chapter 3 investigates the X-ray properties of the “typical” broad line quasars detected in six fields at faint fluxes. The aim is to examine whether this well known class of objects, which produces the bulk of the XRB at soft energies can produce the XRB at hard energies as well or whether another population with harder spectra is really needed.

In Chapter 4, a systematic analysis of a sample of Seyfert 2 galaxies- the nearby counterparts of high redshift type II objects, which is believed to produce the bulk of the XRB at the hard energies - with *ASCA* data is presented, intending to investigate the X-ray emission mechanism of obscured AGN locally. This analysis revealed two “odd” examples of Seyfert 2 galaxies, in the sense that no excess absorption above the Galactic is required by the X-ray data. The analysis of these two objects -NGC 3147 and NGC 4698- as well

as the investigation of possible scenarios explaining the X-ray and optical spectra are the subject of Chapter 5.

In Chapter 6, *ASCA* data of the ULIRG galaxy the 'Superantennae' are presented, aiming to investigate whether this galaxy harbours a buried AGN. ULIRGs are another candidate class of objects which may contribute significantly to the production of the hard X-ray background and as such their X-ray properties are interesting.

Chapter 7 presents an investigation into the X-ray nature of the composite object MKN609. This class of objects is particularly exciting as it bears remarkable similarities to the NLXGs in deep *ROSAT* fields. Thus the X-ray study of a nearby relatively bright object such MKN609 could shed light in the nature of NLXGs.

Finally a summary of this thesis with the conclusions and the complete picture emerging from the thesis as well as the questions raising from the study are given in Chapter 8.

Chapter 2

Instrumentation and Data Reduction

In this chapter I briefly describe the instrumentation from which the data have been used and review the data reduction and analysis procedures for each detector. Detailed description of the data reduction for each observation presented in this thesis will be given in subsequent chapters, where the quality of the data as well as the requirements of the analysis will be discussed.

2.1 *ROSAT*

ROSAT, the Röntgen Satellite (Trumper 1990), named after the German physicist Wilhelm Röntgen, was launched on the 1st of June 1990. The mission lasted almost nine years and ended on 12th of February 1999. The main aim of the *ROSAT* mission was a six-month, all-sky survey with the Position Sensitive Proportional Counters (PSPCs), after which the satellite began a series of pointed observations. *ROSAT* consists of the main X-ray telescope (XRT), which was sensitive over the 0.1-2.4 keV energy range, and the Wide Field Camera (WFC), which covers the extreme ultra-violet band (~ 0.05 -0.21 keV). The XRT has a 2.40 m focal-length mirror assembly (the X-ray Mirror Assembly, XMA), which consists of 4 nested grazing incidence Wolter-I mirrors with a maximum aperture of 83.5 cm. The X-rays are focused onto the focal plane detectors, namely two PSPCs and the High Resolution Imager (HRI).

The PSPCs which are multiwire proportional counters provide modest energy resolution ($\Delta E/E=0.43$), high spatial resolution that is dependent on both photon energy and off-axis angle (25 arcsec full width at half maximum -FWHM- at 1 keV) over a 2 degree diameter field-of-view, and relative time resolution down to 130 microseconds. The combined XMA+PSPC on-axis effective area is $\sim 200 \text{ cm}^2$ at 1 keV. During the first six months of operation, *ROSAT* performed the *ROSAT* All Sky PSPC Survey. Almost the whole sky was mapped and a catalogue of ~ 5000 X-ray sources down to a 0.1 2.4 keV flux of $5 \times 10^{-14} \text{ erg s}^{-1}$ was produced.

The HRI provides a 38 arcminutes square field-of-view, with 4 arcsec spatial resolution (FWHM). It has negligible energy resolution but provides relative time resolution down to 61 microseconds.

The background (excluding the XRB) is mainly produced by high energy charged particles and γ rays (cosmic rays), solar radiation scattered into the line of sight by the Earth's atmosphere and the instrumental background.

2.1.1 Data Screening-Calibration issues

For the PSPC at high energies (channel > 250) the spectral redistribution matrix is invalid. The effective area for $E > 2.0$ keV is underestimated. Thus the spectral analysis presented in this thesis were restricted to the 0.1 - 2.0 keV energy band. Due to vignetting uncertainties no data were used at off-axis angles $> 18'$ in the analysis. Furthermore, during times of high Master Veto Rate (MVR $> 170 \text{ counts s}^{-1}$), the spectral matrix is invalid, thus only data collecting with MVR lower than this value were used.

2.2 ASCA

The *Advanced Satellite for Cosmology and Astrophysics* (ASCA ; Tanaka *et al.* 1994) was launched on the 20th of February 1993. ASCA was Japan's fourth cosmic X-ray

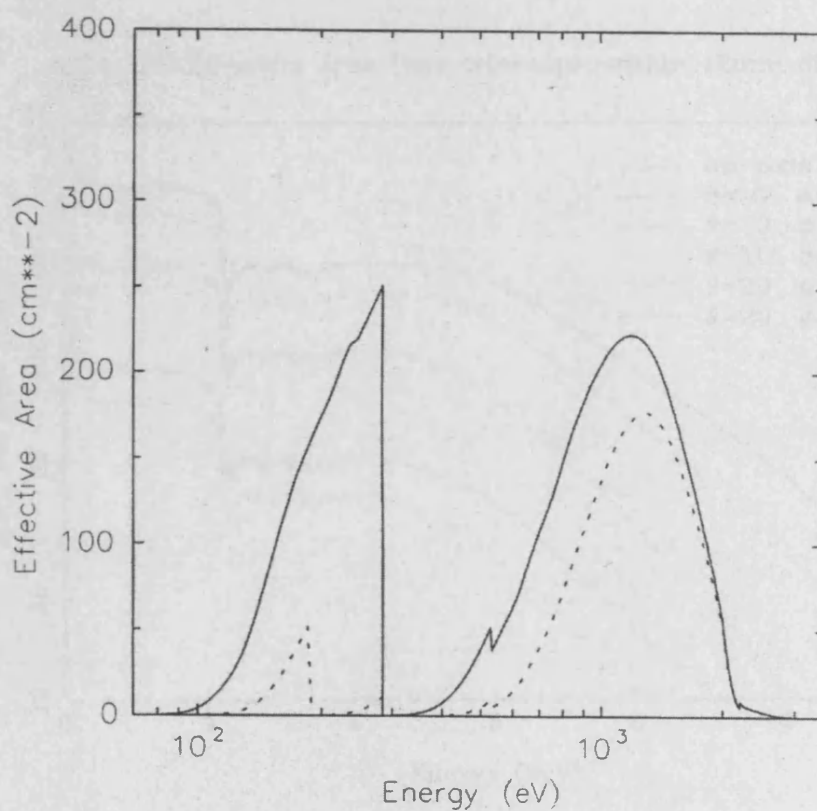


Figure 2.1: The effective on-axis area of the *ROSAT* XMA+PSPC combination with (dashed line) and without (solid line) the boron filter.

astronomy mission and carries four large-area X-ray telescopes (XRT). At the focus of two of the telescopes is a Gas Imaging Spectrometer (GIS), while a Solid-state Imaging Spectrometer (SIS) is at the focus of the other two. The GIS is a gas imaging scintillation proportional counter, whereas the two SIS are identical Charge Coupled Device (CCD). *ASCA* is the first X-ray astronomy mission to combine imaging capability with a broad pass band, good spectral resolution, and a large effective area. The mission also was the first satellite to use CCDs for X-ray astronomy.

The combined four XRT provide:

- Effective area: 1,300 cm² at 1 keV, 600 cm² at 7 keV
- Pass band: 0.5-12 keV

ASCA XRT Effective Area (one telescope, within 12mm diameter)

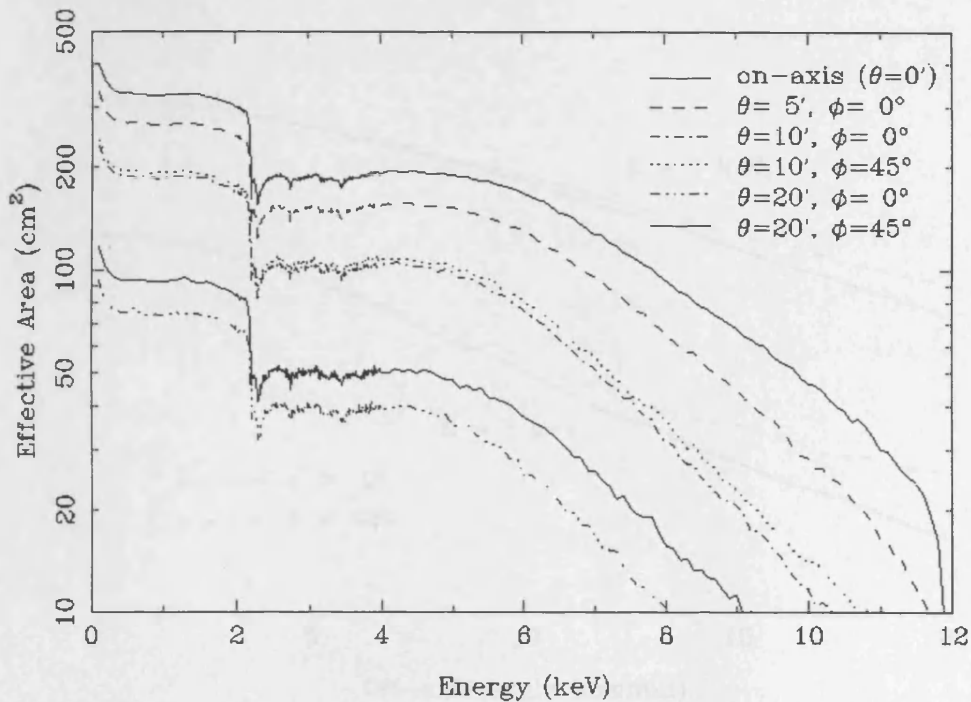


Figure 2.2: The effective area of one XRT, as derived from in-flight calibration. The absorption features between 2-4 keV are the M edges of gold, the reflecting surface of the mirrors. Also shown is the dependence of the effective area on off-axis angle and on azimuthal angle.

- Field of view: 24 arcmin radius
- Resolution: 2.9 arcmin HPD (Half Power Diameter).

The fields of view of the GIS is circular (50 arcmin in diameter) and of the SIS is square (22 arcmin). The effective area of one XRT is shown in Figure 2.2. Figure 2.3 shows the effective area as a function of off-axis angle. Thirty arcminutes off center the flux is 10-20 per cent (depending on energy) of the on-axis value. Figures 2.4 and 2.5 show the combined GIS+XRT and SIS+XRT (respectively) effective area for five off-axis angles. The FWHM at 1 keV is 24 arcmin.

The GIS has limited spatial resolution compared to the SIS. The GIS Point Spread Func-

Angular Response of ASCA XRT

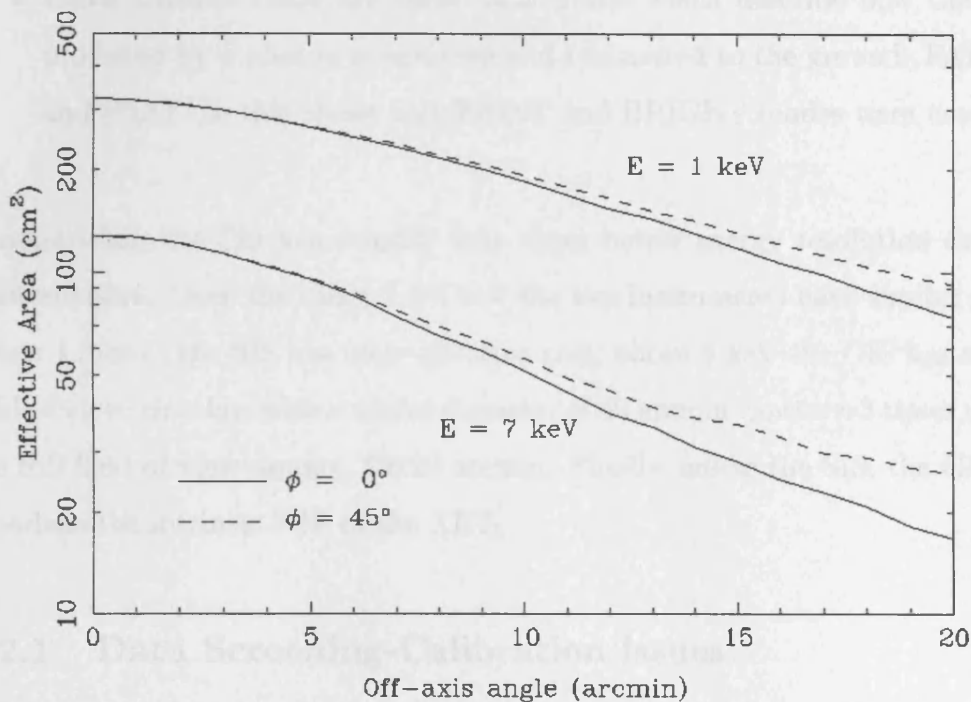


Figure 2.3: The decrease of XRT effective area as a function of off-axis angle for two energies, 1 keV and 7 keV.

tion (PSF) is $\text{FWHM} \sim 0.5\sqrt{5.9/E(\text{keV})}$ much broader than that of the XRT alone. The energy resolution of the GIS is about $7.8\sqrt{(5.9/E(\text{keV}))}$ per cent (FWHM).

The SIS has superb energy resolution with resolving power $E/\Delta E$ of 50 at 6 keV and ~ 20 at 1.5 keV. During an observation the SIS operate in two concurrent modes: clocking mode (or CCD mode) and data mode.

- CCD Modes:** There are four CCD modes, which determine the timing resolution of the field of view available to each observation: 4-CCD, 2-CCD, 1-CCD and the parallel sum mode. In 4-CCD mode all four chips are exposed, giving the maximum field of view but the worst timing resolution (16s). Two CCDs are exposed in 2-CCD mode giving 8s timing resolution. The 1-CCD mode gives time resolution of 4s but only a quarter of the maximum field of view. The parallel sum mode is used

in conjunction with the FAST data mode.

- **Data Modes:** There are three data modes which describe how the charge cloud, produced by a photon is analysed and telemetred to the ground: FAINT, BRIGHT and FAST. In this thesis only FAINT and BRIGHT modes were used.

Summarising, the SIS has roughly four times better energy resolution than the GIS at most energies. Over the range 1.5-5 keV the two instruments have similar effective areas. Below 1.5 keV, the SIS has more effective area; above 5 keV the GIS has more. The GIS field of view—circular, with a useful diameter of 40 arcmin—covers ~ 3 times more area than the SIS field of view—square, 22x22 arcmin. Finally, unlike the SIS, the GIS significantly broadens the intrinsic PSF of the XRT.

2.2.1 Data Screening-Calibration issues

The GIS performance does not vary within ~ 15 arcmin of the FOV. Data taken in the range 15-20 arcmin can still be used for most purposes, but beyond 20 arcmin the calibrations are unreliable and beyond 22 arcmin the particle background completely dominates the signal. Note that it is estimated that the GIS gain is uncertain by ~ 1 per cent within a radius of 15 arcmin; by ~ 2 per cent between 15 and 20 arcmin; and up to ~ 10 per cent outside 20 arcmin. Also note that only events inside the 22 arcmin radius (as a default) are tagged with the corresponding sky coordinates derived from the attitude solution. Thus in this thesis only data within the central 15 arcmin were used.

In this thesis combined true and converted SIS BRIGHT mode data are used and the GIS data are taken in PH mode.

The data analysed here were selected following the screening criteria given below:

- The angle between the Earth's limb and the pointing direction of the satellite (elevation angle: ELV) greater than 5 degrees, in order to avoid absorption and/or

Effective Area of one XRT + GIS (within 12mm diameter)

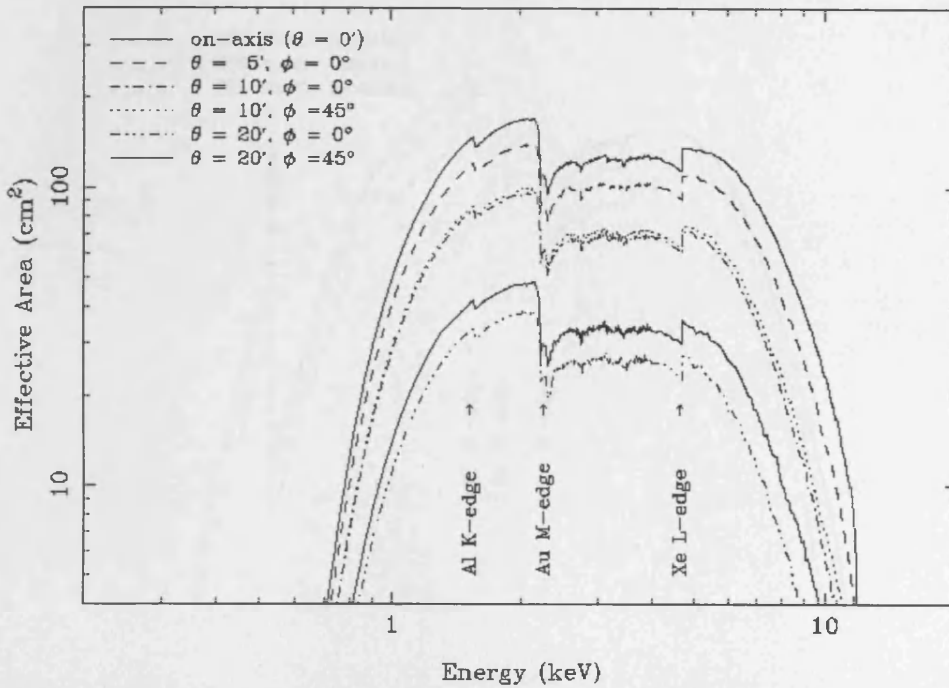


Figure 2.4: The effective area of a single GIS combined with a single XRT for five off-axis angles (0, 5, 10, 15, 20 arcmin).

scattering of X-ray photons due to the outer atmosphere and hence avoid spectral distortion. Negative ELV identifies Earth occultation.

- Rejection of events for which the satellite attitude fluctuates too much. In such a case the photons of the same part of the sky are not incident on the same part of the detector leading to inaccurate results. Thus the root mean square deviation of the instantaneous pointing from the mean pointing (mkf column ANG_DIST) was selected to be less than 0.01 degrees.
- The magnetic Cut-off Rigidity (COR) which is linked to the threshold momentum a cosmic ray requires to penetrate as far as the satellite's orbit. In order to exclude the events with high background, only data taken when COR is greater than 6 GeV/s are selected.

Effective Area of one XRT + SIS (within 12mm diameter)

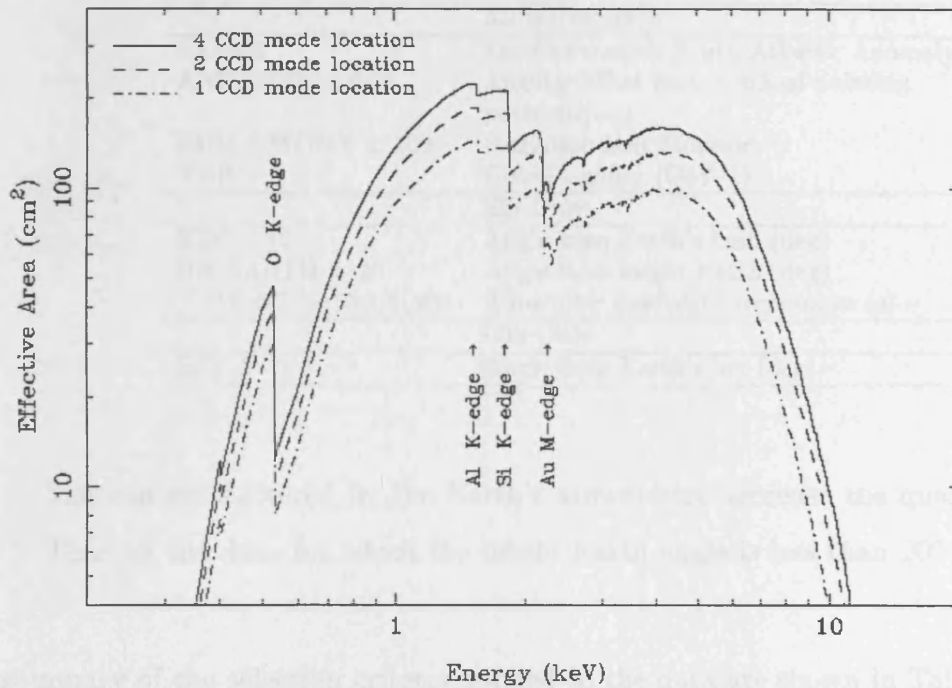


Figure 2.5: The effective area of a single SIS and XRT combined for three off-axis angles (0, 5, 10 arcmin).

- The South Atlantic Anomaly (SAA) is related to a weakness of the Earth's magnetic field allowing cosmic rays to penetrate further into the Earth's atmosphere. Therefore the particle background is extremely high. In the analysis all the data taken during the SAA passages are excluded by requiring the mkf column SAA to be zero.
- Grade gives information of the shape of the charge cloud, created by an event in a CCD. Only events with grade 0,2,3,4 are likely to be X-ray events and the combination of the four provides good resolution and signal-to-noise.
- The angle between the Earth's limb and the pointing direction of the satellite when the earth is bright is given by the mkf column BR_EARTH. In the case of the SIS, which is sensitive to optical and UV radiation, optical UV and soft X-rays from the

Table 2.1: Selection criteria

Criterion	Description
	All Instruments
SAA=0	Satellite outside South Atlantic Anomaly
ANG_DIST < 0.01	Angular offset from nominal pointing position(peg)
RUM_CWONT < 100	Radiation Belt Monitor
XOR > 6	Cutoff rigidity (GeV/c)
	SIS Only
ELV > 10	Angle from Earth's limb (deg)
BR_EARTH > 20	Angle from bright Earth (deg)
T_DY_NT > 50,100,200	Time after day/night terminator (s)
	GIS Only
ELV > 5	Angle from Earth's lim (deg)

Sun can be scattered by the Earth's atmosphere decrease the quality of the data. Thus all the data for which the bright Earth angle is less than 20° are excluded.

A summary of the selection criteria applied to the data are shown in Table 2.1.

2.3 *BeppoSAX*

The X-ray astronomy satellite *BeppoSAX* is a project by the Italian Space Agency (ASI) with participation of the Netherlands Agency for Aerospace Programs (NIVR) and ESA (SSD). It was launched April 30 1996. The main scientific characteristic of the mission is the wide spectral coverage, ranging from 0.1 to over 200 keV. It is the first satellite to have the capability of observing sources over more than three decades of energy - from 0.1 to 200 keV - with a relatively large area, a good energy resolution, associated with imaging capabilities (resolution of about $1'$) in the range of 0.1-10 keV. The instrument complement dedicated to such purpose is composed by a medium energy (1-10 keV) concentrator optics/spectrometer, MECS, consisting of three units, a low energy (0.1-10 keV) concentrator optics/spectrometer, LECS, a high pressure gas scintillation proportional counter (3-120 keV), HPGSPC, and a phoswich detector system (15-300 keV), PDS, all of which have narrow fields and point in the same direction (Narrow Field Instruments,

NFI). In addition there are two coded mask proportional counters (Wide Field Cameras, WFC) pointing in diametrically opposed directions perpendicular to the NFI, monitoring large regions of the sky with a resolution of 5' in the range 2-30 keV to study long term variability of sources down to 1 mCrab and to detect X-ray transient phenomena. The MECS have energy resolution of 8 per cent at 6 keV. At the same energy, the angular resolution is about 1.2 arcmin (Half Power Radius). In the overlapping energy range the MECS effective area is 150 cm², ~ 3 times that of LECS. The exposure time for the LECS is limited by stronger operational constraints to avoid UV light contamination, thus it is operated during Earth dark time only. Finally the LECS PSF is a strong function of energy and it is wider than that of MECS below 1 keV while it is similar to that of MECS above 2 keV.

2.3.1 Data screening-Calibration issues

The *BeppoSAX* mirrors suffers from significant vignetting. Figure 2.6 shows the the effective area of one MECS at different off axis-angles, whereas Figure 2.7 illustrates how the vignetting is more important at higher energies as the off-axis angle increases. Because of this the LECS and MECS background strongly varies with the position in the detector. Thus the standard background subtraction method for both instruments involves the extraction of a background spectrum from a “blank fields” event file from a region similar to the source extraction region in detector coordinates.

The PDS light curves exhibit “spikes” on time scales between a fraction of second to a few seconds. These spikes are due to single particles hits, which illuminate one crystal and produce fluorescence cascades. The spectrum of the spikes is soft and should be removed before any spectral analysis.

In addition all the data taken when the Earth elevation angle was greater the 3°, as well as data taken inside the SAA should be excluded. Also all the data events for which there is no attitude solution are also excluded.

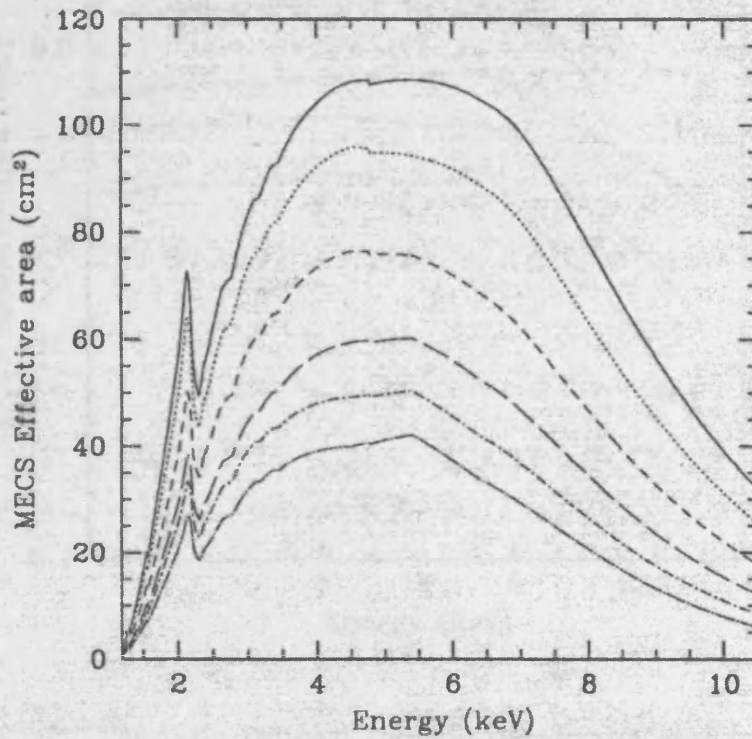


Figure 2.6: The effective area of the MECS at different off-axis angles.

Table 2.2: X-ray telescopes+detectors characteristics, from which the data I have used in this thesis.

Mission	Detector	Energy band (keV)	Field of view	Effective area (cm ⁻²)	Spatial resolution	Spectral resolving power $E/\Delta E$
ROSAT	PSPC	0.1-2.4	2°	250@1 keV	30"	2.3@1 keV
	HRI	0.1-2	0.6°	160@1 keV	4"	-
ASCA	GIS	0.4-12	0.8°	400@1 keV	3'	12@6 keV
	SIS	0.25-12	0.4°	400@1 keV	3'	50@6 keV
BeppoSAX	LECS	0.1-10	0.5	22@0.25 keV	1'	19@1 keV
	MECS	1.3-10	0.5	150@6 keV	1'	8@6 keV
	PDS	15-300	1°5	6800@20 keV	-	6@60 keV

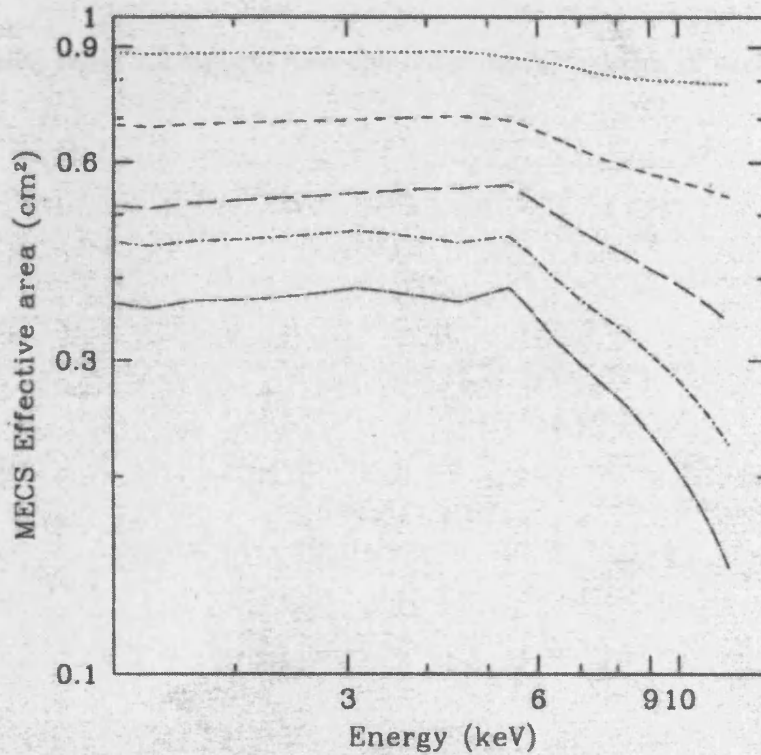


Figure 2.7: The ratio between the off-axis effective area to the on-axis. The curves correspond to the effective area at off-axis angles (0, 4, 6, 8, 12, 16 and 20 arcmin).

2.4 Software-Analysis

The *ROSAT*, *ASCA*, and *BeppoSAX* files are in FITS format, the required format for the standard data screening/analysis software package FTOOLS. The data selection and image, spectrum and light curve extraction was performed in XSELECT. Image procession was performed with ASTERIX software collection and XIMAGE. The spectral analysis was carried out using XSPEC. Throughout the thesis the values of $H_0 = 75 \text{ kms}^{-1}\text{Mpc}^{-1}$ and $q=0.5$ are adopted, except where otherwise stated.

The terminology used in describing the energy range is artificial and is imposed by the technology used in the observation. So, three energy bands constitute the X-ray energy range, that is, the soft band (photo energies $E \leq 2 \text{ keV}$), the hard band $2 \text{ keV} \leq E \leq$

100 keV and the soft gamma-ray band $100 \text{ keV} \leq E \leq 3 \text{ MeV}$.

Finally, table 2.2 summarises the basic characteristics of each detector.

Chapter 3

The X-ray spectrum of hard X-ray selected QSOs

3.1 Introduction

As has been already described in Chapter 1, the nature of the sources making up the XRB at hard energies is not known. In this chapter, the broad-band (0.5-8 keV) spectral properties of the 'typical' (ie high redshift, faint) hard X-ray selected QSOs in our deep *ASCA* survey (Georgantopoulos *et al.* 1997) are derived. These contribute a large fraction of the soft XRB and therefore comparison of their spectrum with that of the XRB is expected to shed more light on the spectral paradox. It should be noted that the objects in this sample span a wide range of redshifts, and hence no physical significance should be attributed to the models applied and no straightforward constraints on the AGN accretion physics can be derived. In contrast the aim of this analysis is to parameterise the "average" QSO spectrum over a large redshift range and compare it with that of the cosmic XRB.

Due to the faint nature of the sources observed in the *ASCA* GIS (typically ≤ 100 counts over the 1-10 keV band), spectral fitting is not possible for individual objects. Firstly, therefore, a hardness ratio analysis (which is a two-point spectral fit) was undertaken, for the individual sources and then spectral analysis was performed on the stacked spectra

for the QSOs.

3.2 The sample

An *ASCA* follow-up (Georgantopoulos et al. 1997) of the deep *ROSAT* survey (Georgantopoulos et al. 1996) has been performed. 6 fields (SGP2, QSF1, QSF3, GSGP4, BJS855, BJS864) have been observed and in the first, quick-look analysis, 39 sources down to a flux limit of $S_{(2-10\text{keV})} \sim 5 \times 10^{-14} \text{erg cm}^{-2} \text{s}^{-1}$ in the 2-10 keV band were detected.

The 2-10 keV number-count distribution, logN-logS was calculated (R.E Griffiths, private communication). In Figure 3.1 the *ASCA* logN-logS is compared to the 0.5-2 keV extragalactic *ROSAT* logN-logS Georgantopoulos *et al.* 1996 converted to the 0.5-2 keV band using a spectral index of $\Gamma = 2.0$. The distribution is a factor of two above the *ROSAT* counts. This suggests the presence of a population with flat or absorbed spectra. In Figure 3.1 *Ginga* results are also shown, as are results from *ASCA* (Cagnoni *et al.* 1998, dotted lines) (Ogasaka *et al.* 1998, triangles) and from *BeppoSAX* (Giommi *et al.* 2000, crosses). All are in good agreement.

Optical identifications for the vast majority of the sources were obtained using the 3.9m AAT telescope. Most (21 objects) are QSOs. All but one (AXJ1343.5-0004) have been detected in the soft X-rays by *ROSAT*. AXJ1343.5-0004 is identified as a UV excess quasar from Boyle *et al.* 1990. Their redshifts range from $z=0.145$ to $z=1.952$ with a mean of $z \sim 1$ (see Georgantopoulos *et al.* 1997 and Boyle et al. 1998b) There is also evidence for the presence of QSOs obscured in X-rays with some modest amount of reddening. These objects have narrow lines in the optical range but they clearly present broad lines in their infrared spectra (eg Georgantopoulos et al. 1999).

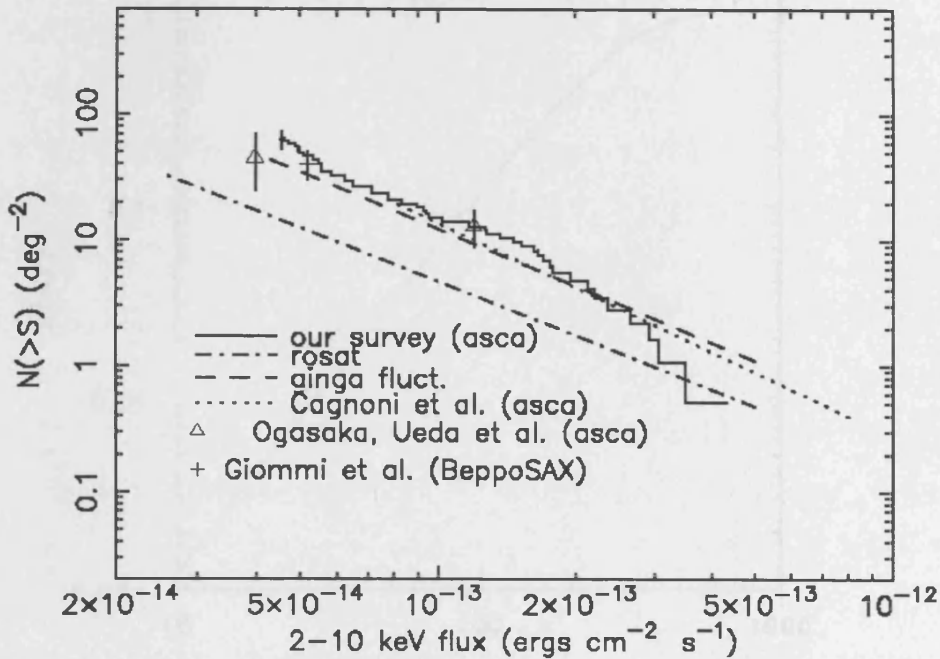


Figure 3.1: The derived integral logN-logS in the 2-10 keV band from our survey; see text for details

3.2.1 Radio cross-correlation

Before proceeding to the analysis, it was investigated whether or not the QSOs detected in the fields are radio-loud. This is important as the radio-loud QSOs have in general X-ray spectra flatter than their radio-quiet counterparts (e.g. Reeves *et al.* 1999). Since in this work, the X-ray spectra of the stacked QSOs is going to be studied, the inclusion of a relatively large number of radio-loud objects may introduce a bias towards flatter spectra.

The list of the QSOs was cross correlated with the NRAO VLA Sky Survey (NVSS) list of radio sources (Condon *et al.* 1998). The NVSS covers the sky north of J2000 $\delta = -40^\circ$ at 1.4 GHz down to a flux limit of $S=2.5$ mJy. Therefore it does not cover our QSF1 and QSF3 fields. Of 12 QSOs in the other three fields, one has a possible NVSS counterpart

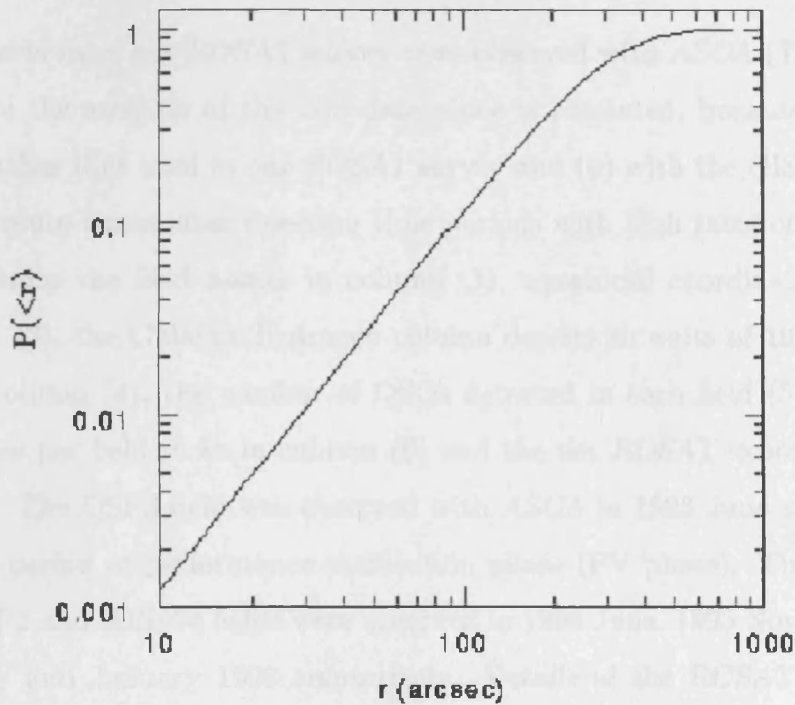


Figure 3.2: Probability of finding an NVSS source within a given radius of an arbitrary position

within 1 arcmin. Figure 3.2 shows the probability of finding an NVSS source within a given radius of an arbitrary position. It turns out that the probability of finding a source within 1 arcmin of an arbitrary position is 0.0145. Boyle *et al.* (1993, 1995) made a deep observation at 1.472 GHz with the Australia Telescope Compact Array of the QSF3 field. They found 6 coincidences with *ROSAT* sources within 15 arcsec. Out of our 6 QSOs in the field only one (AX J0342.0-4403) is associated with a radio source. Hereafter, the two (possible) radio-loud QSOs are included in the analysis. I note in advance that neither has spectral properties different from the population as whole.

3.3 Data reduction and analysis

6 fields from our *ROSAT* survey were observed with *ASCA* (Tanaka, Inoue & Holt 1994). Here the analysis of the GIS data alone is presented, because (a) the GIS field of view matches that used in our *ROSAT* survey and (b) with the GIS we maximize the effective exposure times after rejecting time periods with high rates of particle events. Table 3.1 contains the field names in column (1), equatorial coordinates (J2000) in columns (2) and (3), the Galactic hydrogen column density in units of 10^{20}cm^{-2} (Stark *et al.* 1992) in column (4), the number of QSOs detected in each field (5), the net *ASCA* exposure times per field in ks in column (6) and the net *ROSAT* exposure times in ks in column (7). The QSF3 field was observed with *ASCA* in 1993 June and 1993 September during the period of performance verification phase (PV phase). The GSGP4, BJS855, QSF1, SGP2 and BJS864 fields were observed in 1994 June, 1995 November, 1997 January, 1997 July and January 1998 respectively. Details of the *ROSAT* observations are given in Blair *et al.* (2000). In Table 3.2 the list of QSOs is presented. The names are given in column (1), their *ASCA* position in column (2), the redshift of their optical counterpart (3), the count rate in the 1-2 keV and 2-10 keV bands in (4) and (5) respectively and their 2-10 keV flux in column (6); in column (7) the hardness ratio; in column (8) the radio flux (mJy) is given. The X-ray fluxes are estimated for a single power-law model with $\Gamma=1.56$ and Galactic absorption. This model was chosen because it describes the *ASCA* data adequately (see §3.4.2). If, on the other hand, the standard AGN spectrum is used, namely a single power-law with $\Gamma=1.7$, the obtained fluxes are $\sim 5\%$ lower.

As the sources are quite faint, a circular source region centered on the source of only 1 arcmin radius was used, which includes 33 per cent of the total energy. In addition, by using such a small region overlapping of extraction regions is avoided, since some of our sources lie close to each other. Background counts were estimated from a source-free circular region centered in the field of view of the GIS detector. Because the sources lie at different off-axis angles, the vignetting was taken into account, by correcting the source counts for this effect. The counts were also corrected taking into account the light

Table 3.1: List of ASCA fields

Field	R.A. J2000	Dec. J2000	N_H ($\times 10^{20} \text{cm}^{-2}$)	number of QSOS	ASCA exposure (ksec)	ROSAT exposure (ksec)
(1)	(2)	(3)	(4)	(5)	(6)	(7)
QSF3	03 41 44.4	-44 07 04.8	1.7	6	78	52
QSF1	03 42 10.4	-44 54 38.5	1.7	3	44	49
SGP2	00 52 08.7	-29 05 00.6	1.8	3	50	24
GSGP4	00 57 29.78	-27 37 21.0	1.8	4	41	47
BJS855	10 46 21.36	-00 20 17.8	1.8	2	46	27
BJS864	10 46 21.36	-00 20 17.8	1.9	3	45	23

falling out of the 1 arcmin extraction radius. Due to considerable contamination from the Galactic background as well as some uncertainties in the low energy calibration of ASCA (George *et al.* 1998) restricted this spectral analysis is restricted to the 0.8-8.0 keV energy band. Above 8 keV the signal-to-noise drops rapidly and thus I choose to ignore these data.

ch

3.4 X-ray spectrum

3.4.1 Individual source spectra

Since the photons from the individual QSOs are too few to give reliable spectra, clues for the properties of each QSO come from their hardness ratios (HR). The hardness ratio analysis provides an insight into the spectral nature of faint sources. Here the hardness ratio is defined as $h-s/h+s$, where h and s are the total number of counts, (background subtracted and corrected) in a 1 arcmin radius cell for each object, in the 2-10 keV and 1-2 keV bands respectively. In the case where there was no detection in the 1-2 keV band, the 3σ upper limit following Kraft *et al.* (1991) was estimated. I tested for possible systematic biases that may arise due to the combined energy and radial dependence of the PSF, by splitting the entire sample into sources lying within the 12-arcmin radius from the center of the GIS and those lying beyond. Additionally, I created simulated spectra

Table 3.2: The list of the QSOs in the 6 fields. The columns contain the following information: (1) The source name; (2) *ASCA* position of the object; (3) The redshift of the optical counterpart; (4) *ASCA* GIS count rate in the 1-2 keV band, together with the photon errors in units of 10^{-3} count s^{-1} ; (5) same as (4) but in 2-10 keV band; (6) *ASCA* GIS flux in the 2-10 keV band for a power-law with $\Gamma=1.56$ and Galactic absorption, in units of $\times 10^{-14}$ erg cm^{-2} s^{-1} ; (7) hardness ratio; (8) flux at 1.4 GHz in *mJy*.

Name	<i>ASCA</i> position	<i>z</i>	count rate 1-2 keV	count rate 2-10 keV	<i>ASCA</i> flux 2-10 keV	HR	$S_{1.4GHz}$
(1)	(2)	(3)	(4)	(5)	(6)	(7)	(8)
AX J0050.8-2902	00 50 53.8 -29 02 16	0.428	2.1 ± 0.2	2.7 ± 0.3	16.5 ± 1.7	$+0.1 \pm 0.1$	< 2.5
AX J0051.9-2913	00 51 56.7 -29 13 56	2.056	0.6 ± 1.3	1.4 ± 0.2	8.2 ± 1.1	$+0.3 \pm 0.3$	< 2.5
AX J0053.0-2927	00 53 05.1 -29 11 39	0.830	1.3 ± 0.2	2.1 ± 0.3	13.0 ± 1.6	$+0.3 \pm 0.1$	< 2.5
AX J0056.4-2748	00 56 25.6 -27 48 48	0.145	9.1 ± 0.7	6.1 ± 0.5	30.7 ± 2.8	-0.2 ± 0.1	< 2.5
AX J0056.5-2729	00 56 31.1 -27 29 47	1.010	3.0 ± 0.5	2.5 ± 0.3	15.2 ± 1.8	-0.1 ± 0.1	0.086
AX J0057.3-2731	00 57 20.8 -27 31 53	1.209	2.8 ± 0.5	1.9 ± 0.3	11.7 ± 1.6	-0.2 ± 0.1	< 2.5
AX J0057.8-2735	00 57 48.4 -27 35 56	0.57	<0.2	0.8 ± 0.3	3.70 ± 1.7	> 0.5	< 2.5
AX J0342.4-4511	03 42 27.0 -45 11 58	0.443	1.7 ± 0.3	3.0 ± 0.3	18.1 ± 1.8	$+0.3 \pm 0.2$	-
AX J0343.2-4451	03 43 16.3 -44 51 44	1.410	1.3 ± 0.3	2.2 ± 0.2	13.3 ± 1.5	$+0.3 \pm 0.1$	-
AX J0342.5-4502	03 42 35.0 -45 02 19	0.185	1.1 ± 0.3	1.6 ± 0.2	9.5 ± 1.2	$+0.2 \pm 0.1$	-
AX J0341.1-4412	03 41 04.5 -44 12 04	1.808	0.8 ± 0.1	1.2 ± 0.4	7.2 ± 2.2	$+0.2 \pm 0.2$	< 0.125*
AX J0341.4-4410	03 41 23.0 -44 10 47	0.505	<0.2	1.0 ± 0.3	6.1 ± 1.7	>0.6	< 0.125*
AX J0342.0-4410	03 42 01.1 -44 10 53	1.840	<0.1	1.3 ± 0.3	7.6 ± 1.7	>0.8	< 0.125*
AX J0342.0-4403	03 42 02.4 -44 03 51	0.635	<0.1	1.0 ± 0.3	6.0 ± 1.8	>0.7	0.142*
AX J0342.3-4412	03 42 19.1 -44 12 38	1.091	<0.3	0.8 ± 0.3	4.9 ± 1.9	>0.5	< 0.125*
AX J0342.6-4404	03 42 35.4 -44 04 41	0.377	0.2 ± 0.3	1.4 ± 0.4	8.4 ± 2.5	$+0.7 \pm 0.3$	< 0.125*
AX J1046.1-0020	10 46 05.1 -00 20 48	1.070	0.5 ± 0.1	0.9 ± 0.1	5.4 ± 0.6	$+0.3 \pm 0.1$	< 2.5
AX J1046.2-0022	10 46 13.4 -00 22 16	1.952	<0.4	1.9 ± 0.1	5.3 ± 0.6	>0.6	< 2.5
AX J1344.6-0015	13 44 57.8 -00 15 09	0.244	6.4 ± 0.5	5.9 ± 0.5	35.6 ± 2.8	-0.1 ± 0.1	< 2.5
AX J1343.5-0004*	13 43 26.0 -00 16 14	1.511	<0.2	1.2 ± 0.2	7.0 ± 1.1	>0.6	< 2.5
AX J1343.3-0016	13 43 51.8 -00 04 41	1.14	<0.3	2.4 ± 0.3	14.4 ± 1.7	>0.7	< 2.5

* From Boyle *et al.* 1995.

* object not detected with *ROSAT*.

of sources lying at various distances from the center and estimated their hardness ratio. No trend in HR with off-axis angle is apparent at any flux and spectral shape. In fig. 3.3 the hardness ratio of each object versus the observed flux in the 2-10 keV band is shown. The hardness ratios for four different power-law models assuming Galactic absorption are shown (left hand scale). The right hand scale indicates the expected spectrum in the case of $\Gamma = 1.9$ for different absorbing column densities. One interesting result is that although our objects are optically classified as QSOs, the data require a moderate absorption ($\sim 10^{22}\text{cm}^{-2}$) in order to reproduce the flat spectra observed. However, as it will be discussed in the next section this is probably a phenomenological requirement and it is highly likely that the QSOs are not obscured by significant column density above the Galactic. It is clear that the spectrum flattens towards faint fluxes, suggesting the emergence of a hard X-ray QSO population. This is in agreement with previous results by Ueda *et al.* (1999) and Della Ceca *et al.* (1999). The flattening could be attributed to intrinsic absorption. Indeed, a relatively small amount of absorption ($< 10^{22}\text{cm}^{-2}$) could easily yield an effective index of $\Gamma \sim 1.5$. Some high redshift QSOs with high column densities have been found in the HELLAS 5-10 keV *BeppoSAX* survey (Fiore *et al.* 2000) and elsewhere (Georgantopoulos *et al.* 1999, Boyle *et al.* 1998, Halpern *et al.* 1998, Akiyama *et al.* 2000, Reeves & Turner 2000).

Investigating the origin of the flattening

To investigate the origin of the flattening, the hardness ratio versus the redshift was plotted in Fig. 3.4. For example, Vikhlinin *et al.* (1995) suggested that absorbed QSO spectra may originate due to damped *Ly α* clouds associated with protogalaxies. In such a case the *Ly α* clouds produce the X-ray obscuration and hence the flattening. Under this scenario, it should be expected that the X-ray spectrum of the QSOs will flatten towards higher redshifts. However, there is no clear trend for spectral evolution with redshift. I then examined whether the flattening of the spectrum is due to spectral evolution with luminosity. The hardness ratio versus the 2-10 keV luminosity was plotted in Fig. 3.5. Again no trend for spectral evolution with luminosity is apparent.

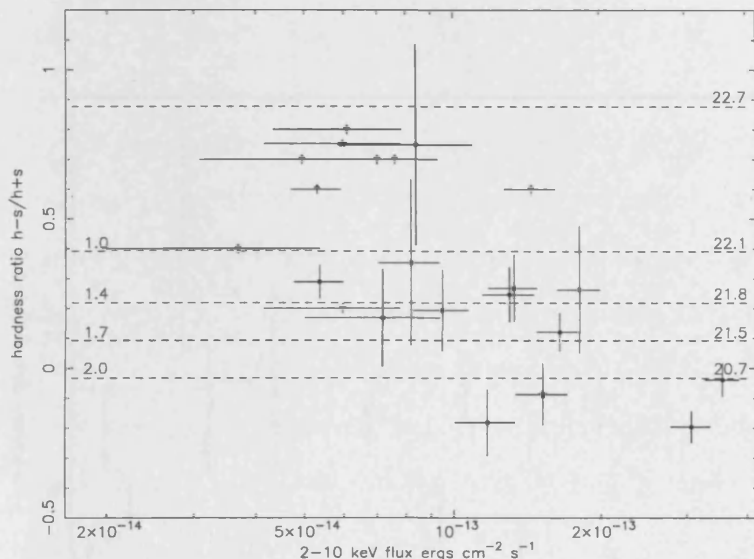


Figure 3.3: The hardness ratio (HR) versus flux for our QSOs with predicted HRs for various power-law indices (left hand scale) and for a power-law with $\Gamma = 1.9$ and a range of absorption (right hand scale). The two with possible radio counterparts are shown (stars). Arrows indicate lower limits.

Finally, it was investigated whether the observed hardening of the spectrum can be attributed to any systematic effects. A possible source of systematics may have to do with the background subtraction. Since the spectrum of the X-ray background is flat ($\Gamma \sim 1.4$, see chapter 1), any over-subtraction of the background will produce a flat spectrum. This effect will be apparent at faint sources close to the limit of the survey, since at this faint limit, the sources have fluxes comparable to that of the background. At higher fluxes this effect will be negligible.

Another source of systematic effects as suggested by Della Ceca *et al.* (1999), may be due to spectral bias in the source selection. They showed that for sources with same flux but different spectra, different number of counts will be detected. As we approach the flux limit of the survey, sources with a favourable spectrum will be detected, whereas sources with the same flux but with an unfavourable spectrum will be missed. However they showed that in the case of the *ASCA* GIS, this selection effect favours the detection of steep spectrum sources. In addition to this, it is clear from Figure 3.3 that the hardening of the spectra is observed in the brighter data as well. The last two arguments give support to the reality of the observed trend.

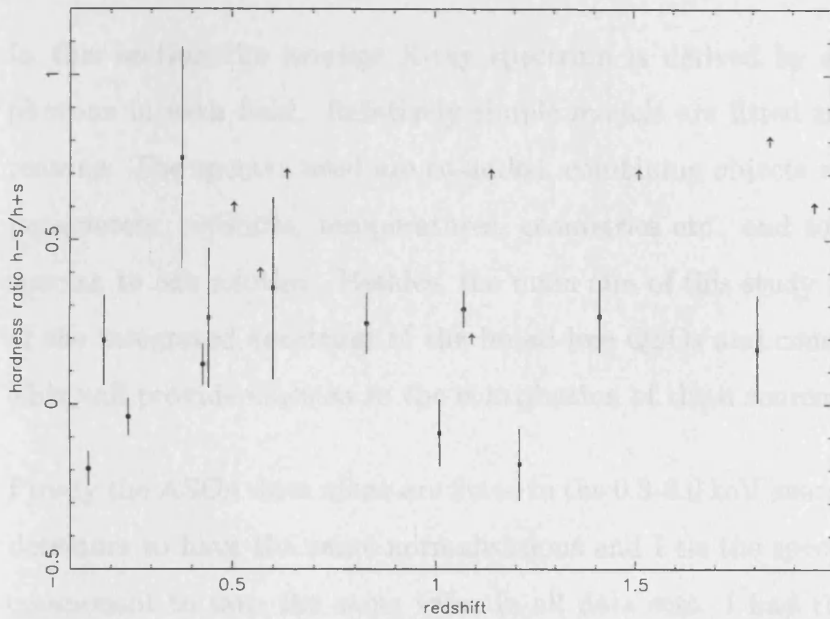


Figure 3.4: The HR versus the redshift of the sources.

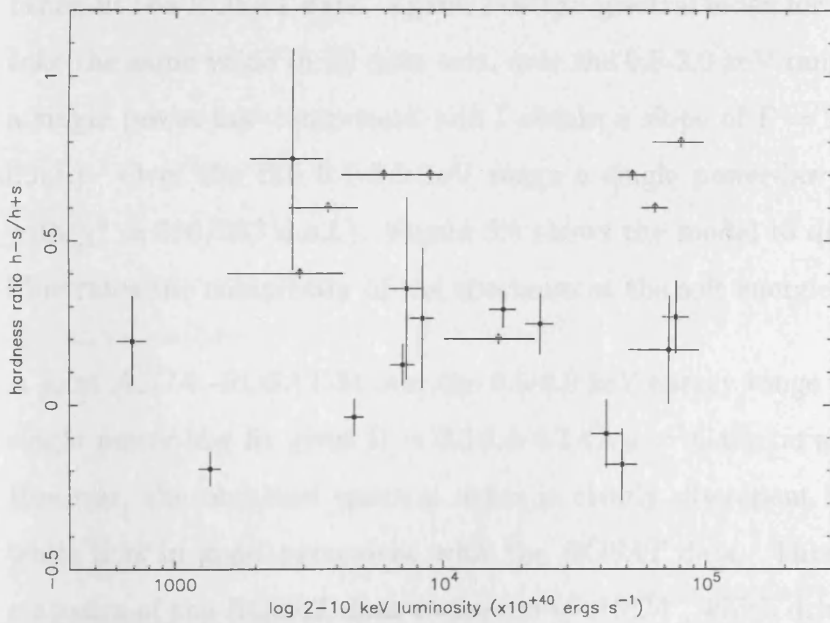


Figure 3.5: The HR versus the 2-10 keV luminosity.

3.4.2 The integrated QSO spectrum

In this section the average X-ray spectrum is derived by stacking together the QSOs photons in each field. Relatively simple models are fitted to the data, for a number of reasons: The spectra used are co-added, combining objects which have different physical parameters, redshifts, temperatures, geometries etc., and so might have different X-ray spectra to one another. Besides, the main aim of this study is to parameterise the shape of the integrated spectrum of the broad-line QSOs and compare it to that of the XRB. This will provide clues as to the contribution of these sources to the XRB.

Firstly the *ASCA* data alone are fitted in the 0.8-8.0 keV energy band, forcing the two GIS detectors to have the same normalisations and I tie the spectral index for the power-law component to take the same value in all data sets. I find that a single power law (PL) with $\Gamma = 1.56 \pm 0.18$ for $\chi^2 = 104.89/99$ degrees of freedom (d.o.f.) with the hydrogen column density fixed to the Galactic value (in the range of $1.7 \times 10^{20} \text{cm}^{-2} - 1.9 \times 10^{20} \text{cm}^{-2}$) is a reasonable fit, in agreement with the hardness ratio analysis.

I then fit the *ROSAT* data. Again, I tie the spectral index for the power-law component to take the same value in all data sets, over the 0.5-2.0 keV range. The data are fitted with a single power-law component and I obtain a slope of $\Gamma = 2.32 \pm 0.2$ ($\chi^2 = 170.23/173$ d.o.f.). Over the full 0.1-2.0 keV range a single power-law gives a poor fit ($\Gamma = 2.44$ with $\chi^2 = 690/333$ d.o.f.). Figure 3.6 shows the model to data ratio. The figure clearly illustrates the complexity of the spectrum at the soft energies.

A joint *ASCA -ROSAT* fit over the 0.5-8.0 keV energy range was carried out as well. The single power-law fit gives $\Gamma = 2.16 \pm 0.1$ ($N_H = \text{Galactic}$ and $\chi^2 = 309.21/273$ d.o.f.). However, the obtained spectral index is clearly discrepant with the *ASCA* data alone, while it is in good agreement with the *ROSAT* data. This is attributed to the better statistics of the *ROSAT* data compared to *ASCA*, which drive the spectral fitting. However, it has been suggested that the spectral index discrepancy may be due to calibration uncertainties in the PSPC and GIS response matrices causing a fake soft excess (Iwasawa,

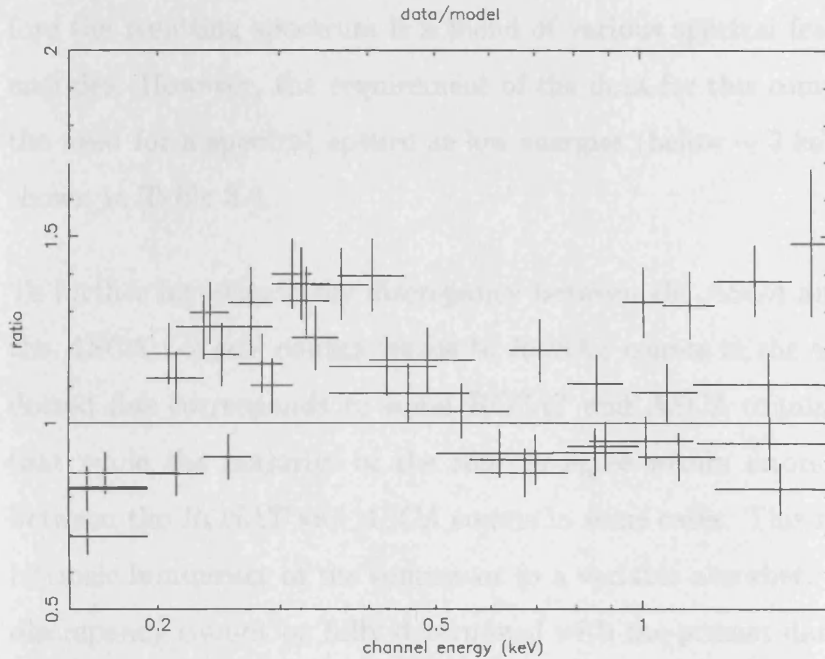


Figure 3.6: The *ROSAT* model to data ratio for the single power-law model over the 0.1-2 keV band, as discussed in the text.

Nandra, Fabian 1999). The observed spectral upturn has been parameterised with a broken power-law model (BKN PL model). In this case the soft and hard components of the spectrum are represented by two power-law with spectral indices Γ_1 and Γ_2 , respectively. I obtained a good fit with $\Gamma_1 = 2.35^{+0.11}_{-0.11}$ and $\Gamma_2 = 1.47^{+0.22}_{-0.20}$ and an energy for the break point of $1.48^{+0.32}_{-0.19}$ keV. It is clear that these are in agreement with the indices obtained by fitting the data of each detector alone. I then added a soft-excess black-body component with $kT=0.1$ keV to the joint *ROSAT* -*ASCA* fit (PL+BB model). In this case I obtain a good fit as well ($\chi^2 = 271.46/261$ d.o.f.), with $\Gamma = 1.71^{+0.19}_{-0.17}$. The value of the slope is consistent within the 90 percent errors bars, with the slope obtained by fitting the *ASCA* data alone. The parameters derived when including the blackbody component are in excellent agreement with the findings of Blair *et al.* (2000). The above authors derived the average *ROSAT* spectrum of soft X-ray selected QSOs using 150 objects. They split the sample into five redshift bins and they obtained a power-law slope of $\Gamma = 1.8 - 1.9$ (and a soft excess with $kT=0.1$ keV), in all bins. It should be emphasized that although the above models parameterise successfully the data, no real physical significance should be attributed. This is due to the fact that our data span a wide range of redshifts and there-

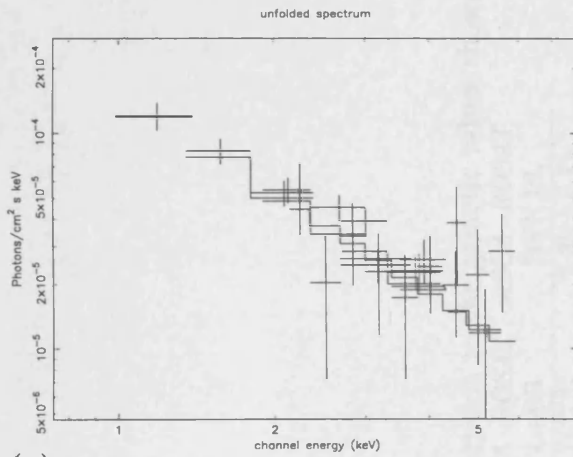
fore the resulting spectrum is a blend of various spectral features at different rest-frame energies. However, the requirement of the data for this component clearly demonstrates the need for a spectral upturn at low energies (below ~ 2 keV). A summary of the fits is shown in Table 3.4.

To further investigate the discrepancy between the *ASCA* and *ROSAT* spectra, I plotted the *ASCA* 1-2 keV counts versus to *ROSAT* counts in the same band (Figure 3.8). The dotted line corresponds to equal *ROSAT* and *ASCA* counts. It is clear from the figure that while the majority of the sources agree within errors there is indeed a variation between the *ROSAT* and *ASCA* counts in some cases. This may be due to changes in the intrinsic luminosity of the sources or to a variable absorber. In any case the origin of the discrepancy cannot be fully determined with the present data.

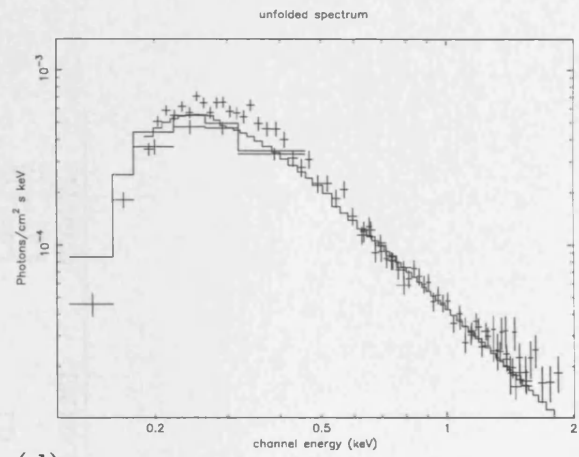
3.5 Summary and Conclusions

In this chapter the properties of the typical, high redshift, hard X-ray selected QSOs were investigated using a sample of 21 objects detected in six deep *ASCA* fields. The hardness ratio analysis showed that the source spectra harden towards fainter fluxes. The majority of them have spectral indices $\Gamma \leq 1.7$. This flattening has been previously reported by Ueda *et al.* (1999) and Della Ceca *et al.* (1999). However, unlike the above our sample consists exclusively of QSOs. Therefore it appears that over the hard band the QSOs show evidence for spectral hardening towards fainter fluxes. The spectral analysis of the stacked spectrum shows that the *ASCA* yields an effective spectral index of $\Gamma = 1.56 \pm 0.18$, for type-1 QSOs. This is significantly lower than the canonical spectral index of bright, radio-quiet, nearby QSOs (eg Reeves *et al.* 1999, Lawson *et al.* 1998). In contrast, the above spectral index is more consistent with both the XRB spectrum and the spectrum of Seyfert-1 type galaxies (Nandra & Pounds 1994). Page (1997) studied the stacked spectrum of 34 *soft X-ray selected* QSOs from the RIXOS *ROSAT* survey using *ASCA*. He finds a spectral index of $\Gamma = 1.8 \pm 0.1$ consistent with that of QSOs in the 2-10 keV band.

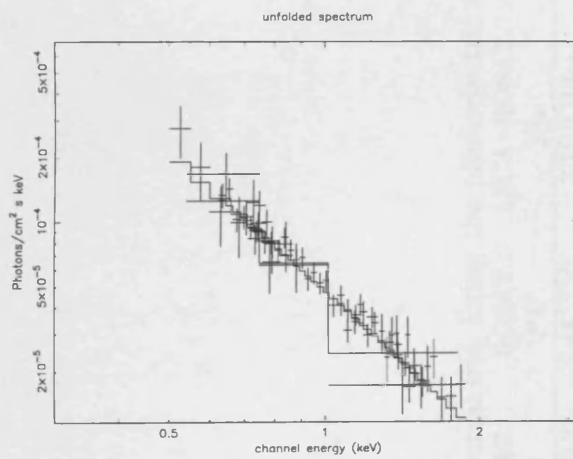
(a)



(b)



(c)



(d)

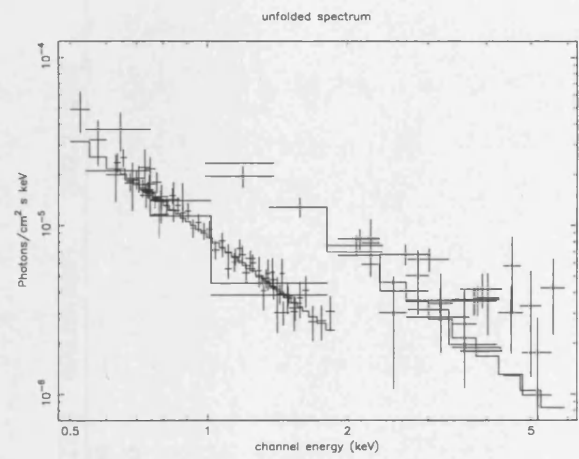


Figure 3.7: The unfolded spectrum for the power-law model for (a) the *ASCA* data over the 0.8-8.0 keV; (b) the *ROSAT* data over the 0.1-2.0 keV; (c) *ROSAT* data over the 0.5-2.0 keV and (d) the joint data over the 0.5-8.0 keV. The model fits are shown by solid histogram.

Table 3.3: Results of spectral fits, fixing the photoelectric absorption to the galactic values shown in Table 1.

	ASCA PL	ROSAT PL^a	ROSAT PL^b	ASCA -ROSAT PL	ASCA -ROSAT PL+BB	ASCA -ROSAT BKN PL
Γ	1.56 ± 0.18	2.32 ± 0.22	$2.44^{+0.01}_{-0.02}$	2.16 ± 0.1	$1.71^{+0.19}_{-0.17}$	2.35 ± 0.11
kT or E(keV)	-	-	-	-	0.1	$1.48^{+0.32}_{-0.19}$
Γ_2	-	-	-	-	-	$1.47^{+0.22}_{-0.20}$
$\chi^2(dof)$	104.89(99)	170.23(173)	690.69(333)	309.21(273)	271.46(261)	276(271)

^aspectral fitting in the 0.5-2.0 keV band^bspectral fitting in the 0.1-2.0 keV band

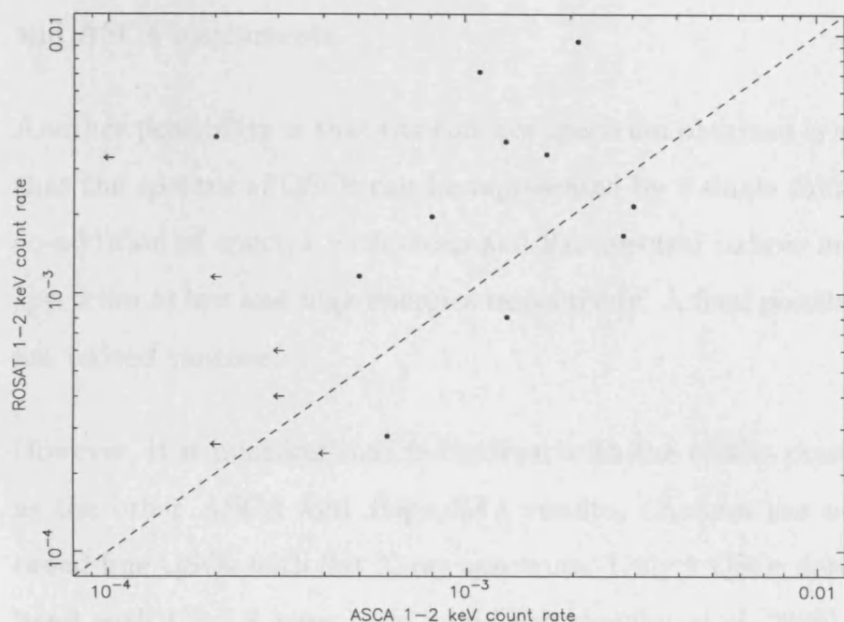


Figure 3.8: The *ROSAT* 1-2 keV count rate versus the *ASCA* count rate in the same band. The dotted line corresponds to equal *ROSAT* and *ASCA* counts.

At first glance, the spectral flattening of the hard X-ray selected QSOs witnessed here could be due to an increasing percentage of absorbed sources at faint fluxes. Indeed, a few high redshift QSOs with large amounts of absorption have been found so far in hard X-ray surveys (eg Fiore et al. 1999). Then the *ROSAT* counts could be due to scattered emission or contribution from thermal emission (see Chapter 4 for details on the X-ray spectrum of absorbed AGNs). The stacked *ROSAT* spectrum alone has a spectral index $\Gamma \approx 2.3$ consistent with the spectral index of individual soft X-ray selected QSOs in the soft 0.1-2 keV band (eg Laor et al., 1997, Fiore et al. 1998). Consequently, when we fit simultaneously the *ROSAT* and *ASCA* spectra, the data suggest the presence of a spectral upturn at soft energies. This upturn can be naively modeled with a black body component with $kT \sim 0.1$ keV, although this obviously has no physical interpretation. Then the power-law index becomes $\Gamma = 1.7 \pm 0.2$, in good agreement with the spectrum of nearby QSOs. Here, it should be noted that Iwasawa, Nandra & Fabian (1999) raised some questions about the consistency of the *ROSAT* and *ASCA* spectral fits. In particular they fitted simultaneous *ROSAT* and *ASCA* spectra of NGC5548 finding that the *ROSAT* spectrum can be steeper by as much as $\Delta\Gamma \sim 0.4$ in the common 0.5-2 keV band. This discrepancy could be possibly attributed to uncertainties in the calibration of both *ROSAT*

and *ASCA* instruments.

Another possibility is that the concave spectrum obtained is an artifact of our assumption that the spectra of QSOs can be represented by a single value of Γ . More specifically the co-addition of spectra with steep and flat spectral indices may result in a steep and flat spectrum at low and high energies respectively. A final possibility is that the QSO spectra are indeed concave.

However, it is puzzling that in contrast with the results presented in this chapter as well as the other *ASCA* and *BeppoSAX* results, *Chandra* has not found a large number of broad line QSOs with flat X-ray spectrum. Only 2 QSOs detected in the 2-10 keV energy band with $\Gamma \sim 1.8$ have been found (Mushotzky *et al.* 2000). Possibly this is due to the sensitivity of *Chandra* which peaks below 2 keV and is lower than the *ASCA* sensitivity above ~ 7 keV and, therefore, probably biases the results in favour of steep spectrum X-ray sources.

XMM with its high effective area as well as its broad bandpass (0.1-12 keV) is expected to shed more light on the spectrum of individual, faint, high redshift QSOs which produce the largest fraction of the XRB.

Chapter 4

The X-ray spectrum of optically selected Sy2 galaxies.

In this chapter a uniform analysis of 8 Seyfert 2s chosen from the sample of Ho *et al.* 1997 is presented. The objects were selected for their high $[OIII]\lambda 5007$ flux. Such a sample is believed to be representative of the Seyfert 2 population in the sense that it does not introduce a bias towards X-ray bright Seyfert 2s, which tend to be the least absorbed. In §4.1 the current status and problems of Seyfert 2 research is described; §4.2 introduces the sample; in §4.3 the analysis method is described; in §4.4 the results of the spectral analysis is presented; in §4.5 the results on the individual objects are discussed and the nature of the X-ray is investigated; in §4.6 the results are discussed in the context of the current phenomenological picture and the current X-ray background synthesis models; finally in §4.7 the conclusions of this work are summarised.

4.1 Introduction

The discovery of hidden Seyfert 1 nuclei in many Seyfert 2 galaxies has given much support to the unified theories of Seyferts (e.g Antonucci *et al.* 1994 for NGC 1068). According to the current unification models both are identical objects which possess a core-central black hole, accretion disk, broad-line region- and a thick molecular torus.

Objects observed within the opening angle of the torus are classified as Seyfert 1 objects whereas those seen at angles intersecting the torus appear as Seyfert 2 sources. Around the core is ionised gas (warm scatterer) which scatters the primary emission. In some cases nuclear starburst regions have been observed. It should be pointed out that the unified theories explain the differences between type 1 and type 2 Seyferts (and in general active galaxies) phenomenologically, attributing any difference to orientation effects only. The X-ray data support the above picture. The X-ray spectra of X-ray selected Seyfert 2 galaxies (eg Turner & Pounds 1989, Smith & Done 1996, Turner *et al.* 1997) show column densities much higher than those of Seyfert 1 objects. These columns completely block the soft X-ray flux but become transparent to energies ≥ 2 keV. Thus X-rays prove to be a powerful tool for the study of the type 2 -obscured- objects, since X-ray photons can penetrate the obscuring medium and reveal the core to the observer.

Some objects although classified as Seyfert 2 galaxies (e.g. NGC 1068 and Circinus, Matt *et al.* 1997, 1999 respectively) appear to have no excess absorption. It has been shown that in such cases the direct component in the 2-10 keV range is suppressed and we only observe scattered (warm and/or cold) emission, usually little absorbed. The deficit in the hard X-ray flux is due to the fact that the torus is optically thick to Compton scattering, thus the hard X-ray photons in the 2-10 keV range are shifted to lower energies, and finally they are absorbed after a few scatterings. Therefore Compton thick objects can show low obscuration below 10 keV. *BeppoSAX* observations with PDS have revealed that a power-law emerges through a high column density ($> 10^{24}\text{cm}^{-2}$) above 10 keV in such cases. The obscuration is large enough to completely block the direct emission leaving a low “pseudocolumn” below 10 keV but small enough to allow transmission above this energy. In addition the observed equivalent width of the K_{α} iron line increases as it is measured against a suppressed continuum.

Until recently, Seyfert 2 studies were restricted to relatively X-ray bright Seyfert 2 mainly taken from all-sky X-ray surveys leading to bias in favour of galaxies with low N_H . Maiolino *et al.* (1998) studied a sample of X-ray weak Seyfert 2 galaxies selected by their $[OIII]\lambda 5007$ flux and found that the average obscuration of type 2 AGNs is much higher

than that derived by the former X-ray studies. This is because the $[OIII]\lambda 5007$ flux can be considered to represent the central engine and thus provide us with an unbiased sample of Seyfert 2 galaxies. Recently Risaliti *et al.* (1999) studied a large sample of $[OIII]\lambda 5007$ selected late-type Seyfert galaxies (Seyfert 1.8, 1.9, 2.0, $[OIII]\lambda 5007 > 40 \times 10^{-14} \text{erg cm}^{-2} \text{ s}^{-1}$). The galaxies came from Maiolino & Rieke (1995), completed with NGC 1808. Using X-ray data from the literature (with the exception of 5 objects, where the authors analysed the data), they showed that the average column density for these objects is $N_H = 10^{23.5}$, with all the Seyfert 2s being obscured by columns with $N_H > 10^{22} \text{cm}^{-2}$, giving strength to the simple model, proposed by the unified theories. Furthermore they showed that about half are Compton thick ($N_H > 10^{24} \text{cm}^{-2}$) and they confirmed that intermediate type 1.8-1.9 Seyferts are characterised by an average N_H distribution lower than that of the genuine Seyfert 2 galaxies.

Although the above standard model describes very well the spectrum of most Seyferts, recently examples of Seyfert 2 galaxies were found which challenge the unification scenarios. These show no intrinsic absorption (for example NGC 3147, Ptak *et al.* 1997, NGC 7590, Bassani *et al.* 1999) while their high $f_{HX}/f_{[OIII]}$ ratios are inconsistent with the idea of being Compton thick objects (see Bassani *et al.* 1999). The peculiar spectra of these Seyfert 2 could be explained, for instance, either by the absence of a broad line region or by a high dust to (\sim neutral) gas ratio. In the former case, their appearance as Seyfert 2 is intrinsic and not due to absorption. The lack of absorbing columns in these galaxies raises important questions about the validity and universality of the standard AGN unification schemes. The distribution of the absorbing columns in AGN is also vital for models for the synthesis of the XRB (eg Comastri *et al.* 1995). It is evident that the range of column densities of the absorbing material, its structure and geometry remain as yet unconstrained and need to be determined with larger samples of galaxies selected in different wavebands.

In this chapter, a comprehensive and uniform X-ray spectral analysis with *ASCA* of 8 optically selected Seyfert 2 galaxies from the spectroscopic sample of Ho *et al.* (1997) is presented. While a few of the objects analysed here have been retrieved from the public

ASCA database, some are presented here for the first time (NGC 1167, NGC 2273, NGC 3486, NGC 4698). The goal is to explore the validity of the standard model and study the distribution of absorbing columns in a sample of bona-fide Seyfert 2 galaxies with very accurately defined optical properties.

Motivation

A $[OIII]\lambda 5007$ bright sample is considered to be relatively free from selection effects such as intrinsic absorption (Ueno *et al.* 1998) and differences in viewing angle (Mulchaey *et al.* 1994). Such a sample should be representative of the whole class of Seyfert 2 galaxies. Ho *et al.* (1997) provided the most accurate spectroscopic classification as yet (see next section) and thus this sample is an excellent database for Seyfert 2 population studies.

The study of the sample presented in this chapter was initiated by some questions; what is the real distribution of column densities in the local universe?; What are the universal properties of the Seyfert 2 galaxies?; Although the limited number of objects studied here, constrain us from deriving firm conclusions, this work nevertheless provides an insight into the complexity of the X-ray spectra of Seyfert 2 galaxies and its implications.

4.2 The data

Here an analysis of 8 optically selected Seyfert 2 galaxies observed with the ASCA satellite is presented. The list of the data is presented in Table 4.1, whereas the optical properties of the galaxies are given in Table 4.2. Data come from both proprietary observations and from the ASCA archive. The galaxies are taken from the Ho *et al.* (1997) spectroscopic sample of nearby galaxies. This sample contains objects selected from the Revised Shapley-Ames Catalogue of Bright Galaxies (RSA; Sandage & Tammann 1981) with magnitude limit $B_r = 12.5$ mag in the northern ($\delta > 0^\circ$) sky. The authors obtained high signal-to-noise and moderate to high resolution optical spectra for this sample. In addition the stellar contribution has been subtracted using the “template subtraction”

method, that is by subtracting suitably scaled template spectrum that best represents the continuum and absorption line strength of the stellar component for each galaxy. A long slit of width 2 arcsec was used in most of the cases. Therefore accurate spectroscopic classifications exist for all galaxies. As a consequence all these objects included in the sample are indeed bona-fide Seyfert 2 galaxies. The eight objects are selected on the basis of their high $[OIII]\lambda 5007$ flux. Some of the galaxies (see Table 4.1) have been previously analysed by other authors in the hard X-ray band. However, here I re-analyse the data in order to present a uniform, comprehensive analysis of the brightest $[OIII]\lambda 5007$ selected Seyfert 2, for which X-ray data were/became available, in the Ho *et al.* sample. The $[OIII]\lambda 5007$ line originates in regions above or below the torus, as a result it is not affected by obscuration (but see § 4.6.1 for possible caveats), and thus an $[OIII]\lambda 5007$ selected sample should be relatively free from the selection effects and biases that might appear through X-ray or other optical selection, such as intrinsic absorption or differences in viewing angle (Ueno *et al.* 1998). For only 5 of the sources spectral analysis was performed. For the other 3 (NGC 1167, NGC 1667 and NGC 3486), insufficient X-rays were detected for a full spectral analysis and consequently only hardness ratio analysis was performed.

4.3 Data reduction

Both *ASCA GIS* and *SIS* data were utilised. The standard “Revision 2” processed data from the Goddard Space Flight Center (GSFC) have been used. These data have been screened using the criteria presented in Chapter 2.

For *GIS* data a circular source region centered on the source is used. Background counts were estimated from source-free annuli centered on the source cell. Due to calibration differences between the four *SIS* chips, this analysis is limited to the on-source chip for each *SIS*. A circular extraction cell of 3 to 4 arcminutes in radius is used.

In the case of NGC 2273 where an additional serendipitous source close to the galaxy is

Table 4.1: The ASCA Seyfert 2 sample. The columns contain the following information: (1) The source name; (2) The sequence number of the observation; (3)&(4) Optical position of the object; (5) The exposure time for SIS-0 in ks; (6) The source redshift; (7) The line of sight Galactic hydrogen column density; (8) References to the previously published hard X-ray data.

Name	ASCA Sequence	R.A J2000	Dec. J2000	SIS-0 exp	z	$N_H(\text{Gal})$ ($\times 10^{21} \text{cm}^{-2}$)	References
(1)	(2)	(3)	(4)	(5)	(6)	(7)	(8)
NGC1167	77072000	03 01 42.4	+35 12 21	38	0.016	1.14	-
NGC1667	71032000	04 48 37.1	-06 19 12	14.5	0.015	0.55	1,2
NGC2273	74039000	06 50 08.7	+60 50 45	34	0.006	0.68	3
NGC3079	60000000	10 01 57.8	+55 40 47	29	0.004	0.08	4
NGC3147	60040000	10 16 53.6	+73 24 03	23	0.009	0.36	5
NGC3486	77074000	11 00 23.9	+28 58 30	41.3	0.002	0.19	-
NGC4698	77073000	12 48 23.0	+08 29 14	40.5	0.003	0.19	-
NGC5194(M51)	60017000	13 29 52.35	+47 11 53.8	30.5	0.001	0.16	6

REFERENCES.(1)Ueno *et al.* 1997; (2)Turner *et al.* 1997; (3)Maiolino *et al.* 1998; (4)Ptak *et al.* 1999; (5)Ptak *et al.* 1996; (6)Terashima *et al.* 1998.

Table 4.2: The optical properties of the ASCA Seyfert 2 sample. The columns contain the following information: (1) The source name; (2) The host galaxy type; (3) internal reddening (mag); (4) Luminosity of the narrow component of H_α in units of erg s^{-1} , marked as lower limit (L) if the observing conditions were non-photometric; (5) Equivalent width of the narrow component of H_α in \AA ; (6) Magnitude in V band from de Vaucouleurs *et al.* 1991.

Name (1)	Galaxy type (2)	E(B-V) (3)	$\log L(H_\alpha)$ (4)	EW(H_α) (5)	m_V (6)
NGC1167	SA0	0.59	40.21	9.47	-
NGC1667	SAB(r)c	0.26	40.54L	10.38	12.07
NGC2273	SB(r)a	0.50	40.41	40.07	11.66
NGC3079	SB(s)c	2.24	38.76	11.66	10.86
NGC3147	SA(rs)bc	0.53	39.47	2.00	10.61
NGC3486	SAB(r)c	0.06	37.79	2.77	10.53
NGC4698	SA(s)ab	0.05	38.69	2.36	10.55
NGC5194(M51)	SA(s)	1.01	38.88L	9.93	8.36

detected, Thus a circular source region of 1.5 arcmin in radius is used in both *GIS* and *SIS* in order to minimise any contamination by the nearby source. In cases of NGC 3147 and M51 where the source was centered close to the gap between the chips in the *SIS*, the process described in the ASCA ABC guide (Yaqoob 1997) was followed. Briefly due to the fact that the chips have different responses, a source region containing the entire source counts were created, excluding the inter chip gap. Then the spectrum of the entire source is extracted as well as the spectra for each sub-region is each separate chip. The response file for each of the sub-regions are produced and combined, weighting each file by the total number of counts in the corresponding spectrum. The combined response file was used to generate the ancillary file. In the spectral fitting the whole source region spectrum (gaps excluded), the combined response file and the ancillary file derived as described above are used. Background was estimated using rectangular regions at the source chip, excluding the source.

4.4 Spectral analysis

To perform the spectral analysis, the data are binned so that there are at least 20 counts in each bin (source plus background). Quoted errors to the best-fitting spectral parameters

are 90 per cent confidence regions for one parameter of interest ($\Delta\chi^2=2.71$). Spectral fitting was performed, allowing the normalisation for the *SIS* and *GIS* detectors to vary. The fluxes and luminosities given in the tables are referred to the *GIS* data. Throughout this paper values of $H_o = 75 \text{ km s}^{-1} \text{ Mpc}^{-1}$ and $q_o=0.5$ are assumed. From the analysis, all data below 0.8 keV are excluded due to uncertainties in the calibration matrices (see George *et al.* 1998 for a discussion on this). I applied relatively simple spectral models, so as to describe the properties of the whole sample in the context of the unified model. All the models are applied to all the data sets even though the most complex models may not be required in some cases. Where fits gave absorption values consistent with the galactic column density or lower I have fixed the column to the galactic value. The latter was determined using the *nh ftool*, which utilises a map based on 21-cm measurements and has resolution of about 0.7 degrees (see Dickey and Lockman, 1990).

4.4.1 Building the standard model

I have used the four major components of the “standard model” in steps: a) firstly a single power-law - with absorption if required - was applied to all of the objects, b) then a Gaussian line representing the iron K_α emission was added, c) a second power-law component representing scattered emission was added; d) finally a Raymond-Smith component at low energies representing a star-forming component is added to the data.

Single power-law model.

According to the current theories the primary UV and soft X-ray photons produced by the disk are Compton scattered by a medium of hot electrons ($\sim 50 \text{ keV}$) and reradiated at hard energies. Such a process can produce a power-law with an index of $\Gamma \sim 1.9$, in agreement with observational results, which suggest that the intrinsic X-ray spectrum of Seyfert 1 galaxies is well represented by a power-law with a “canonical” spectral index with $\Gamma \sim 1.9$. In the case of Seyfert 2 galaxies, where our line of sight intersects the torus, we expect the spectrum to show a low energy cutoff as well. Thus the data were fitted with

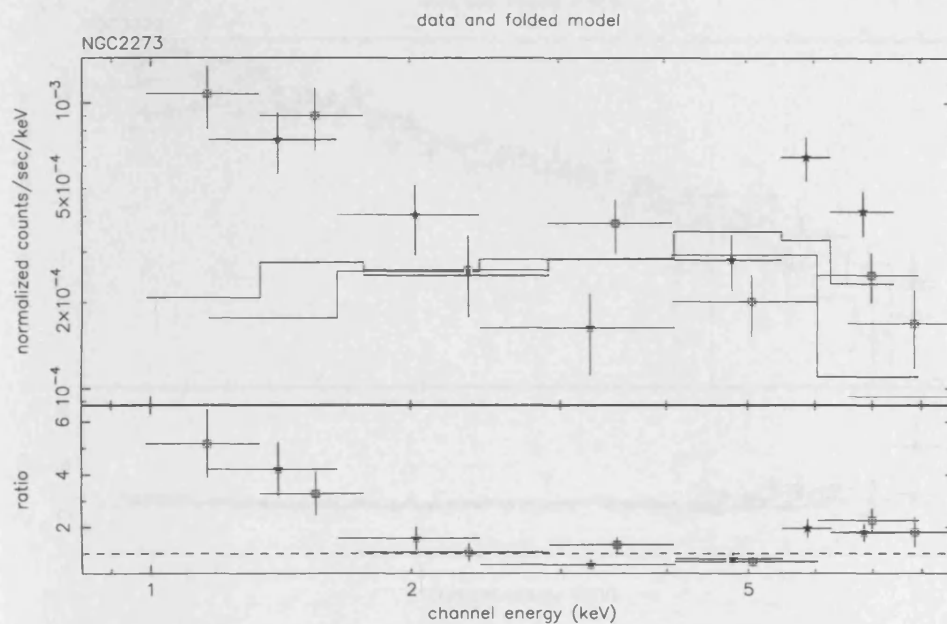


Figure 4.1: The single power-law model for NGC 2273 with $\Gamma = -0.55^{+0.11}_{-0.11}$, $\chi^2(\text{dof})=82.92(22)$. The top panel shows the data with the model and the bottom panel shows the data/model ratio. Data from the two GIS and two SIS have been combined for clarity. The stars represents the GIS data points and open squares the SIS points.

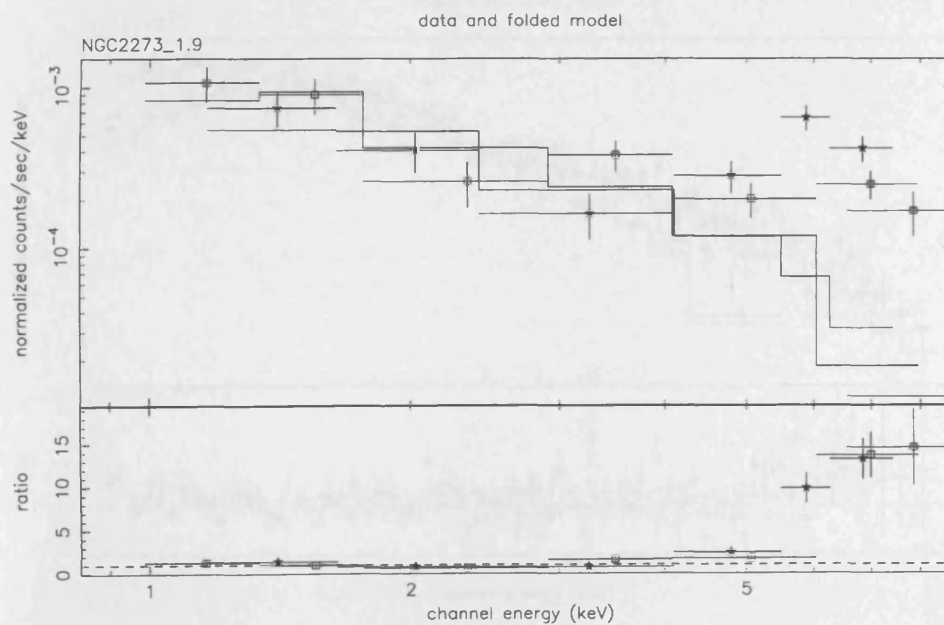


Figure 4.2: The single power-law model with $\Gamma=1.9$ for NGC 2273, $\chi^2(\text{dof})=117.47(22)$. The top panel shows the data with the model and the bottom panel shows the data/model ratio. Data from the two GIS and two SIS have been combined for clarity. The stars represents the GIS data points and open squares the SIS points.

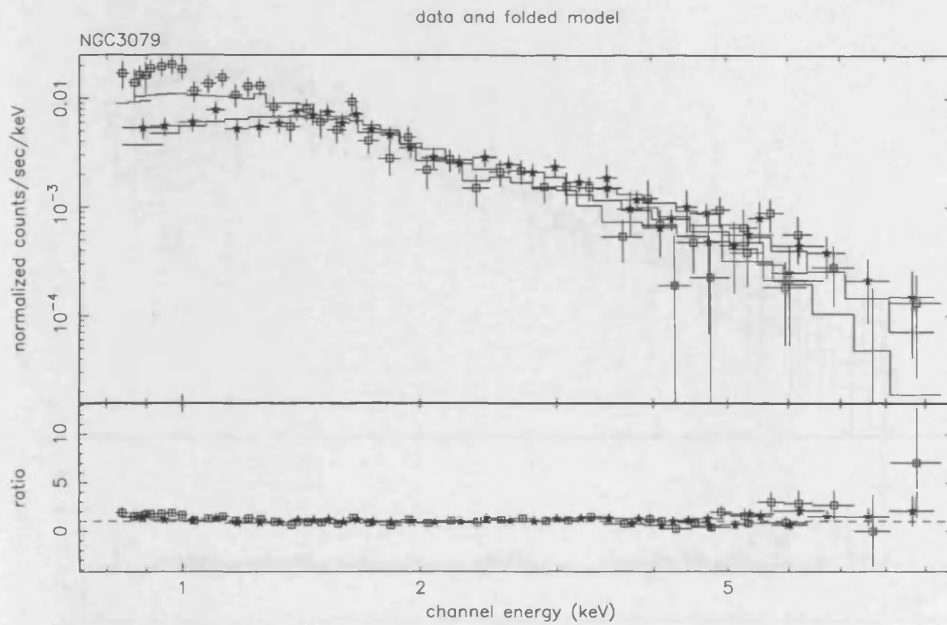


Figure 4.3: The single power-law model for NGC 3079 with $\Gamma = 1.93^{+0.12}_{-0.12}$, $\chi^2(\text{dof})=228.06(143)$. The top panel shows the data with the model and the bottom panel shows the data/model ratio. Data from the two GIS and two SIS have been combined for clarity. The stars represents the GIS data points and open squares the SIS points.

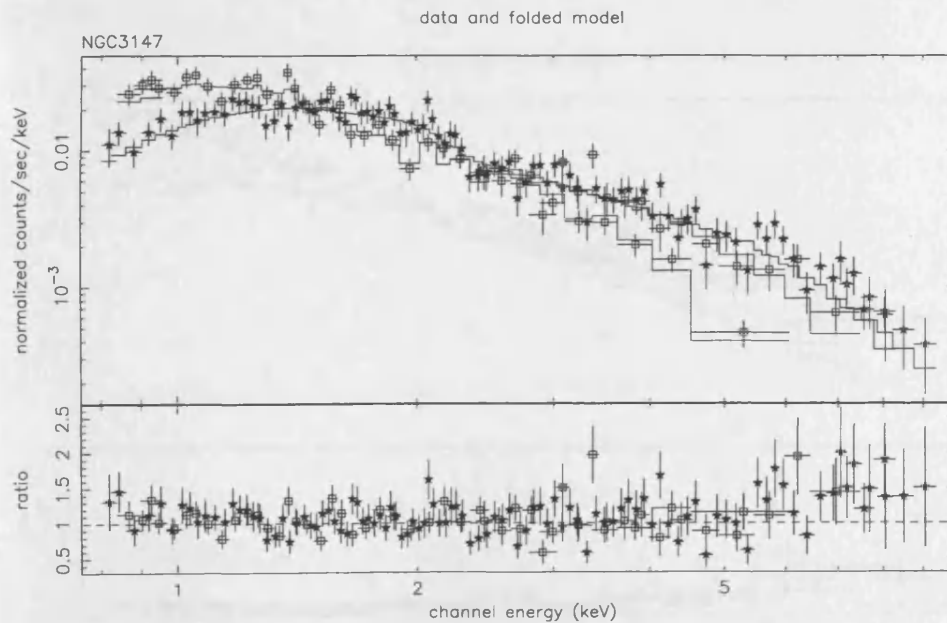


Figure 4.4: The single power-law model for NGC 3147 with $\Gamma = 1.82^{+0.05}_{-0.06}$, $\chi^2(\text{dof})=289.22(285)$. The top panel shows the data with the model and the bottom panel shows the data/model ratio. Data from the two GIS and two SIS have been combined for clarity. The stars represents the GIS data points and open squares the SIS points.

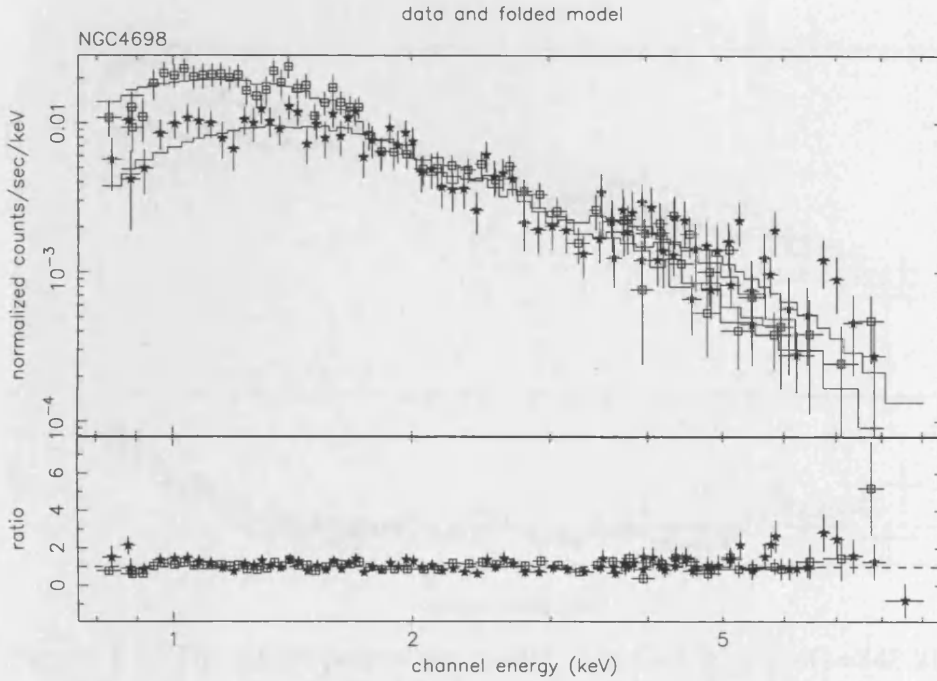


Figure 4.5: The single power-law model for NGC 4698 with $\Gamma = 1.91^{+0.14}_{-0.14}$, $\chi^2(\text{dof})=243.90(250)$. The top panel shows the data with the model and the bottom panel shows the data/model ratio. Data from the two GIS and two SIS have been combined for clarity. The stars represents the GIS data points and open squares the SIS points.

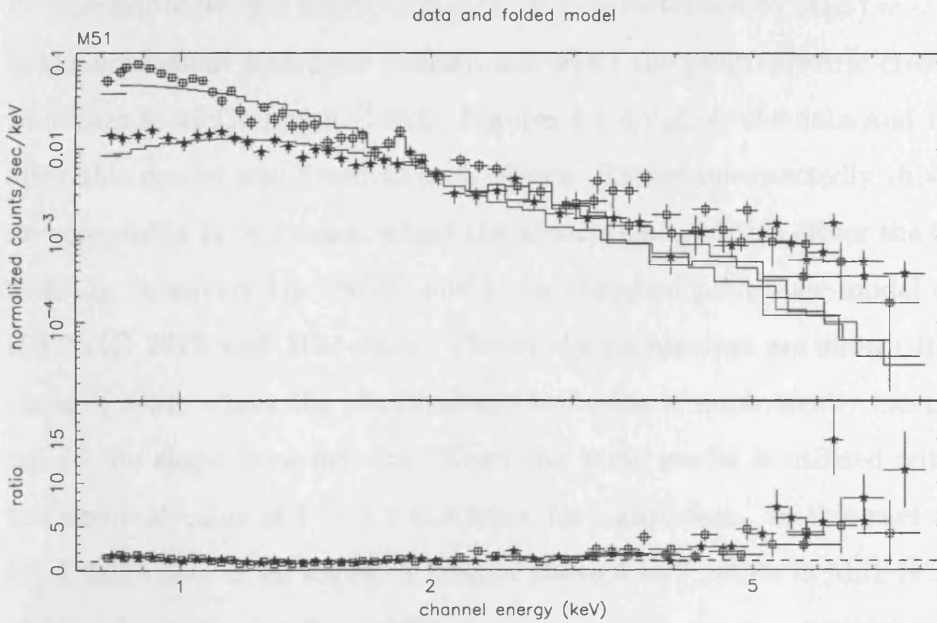


Figure 4.6: The single power-law mode for M51 with $\Gamma = 3.07^{+0.06}_{-0.06}$, $\chi^2(\text{dof})=568.88(178)$. The top panel shows the data with the model and the bottom panel shows the data/model ratio. Data from the two GIS and two SIS have been combined for clarity. The stars represents the GIS data points and open squares the SIS points.

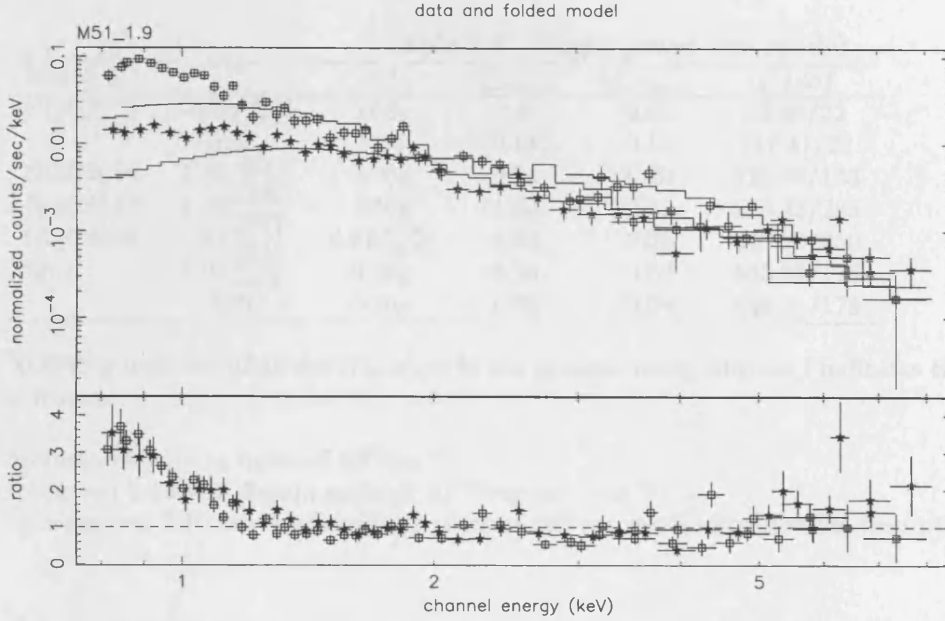


Figure 4.7: The single power-law model with $\Gamma=1.9$, $\chi^2(\text{dof})=848.21(179)$ for M51. The top panel shows the data with the model and the bottom panel shows the data/model ratio. Data from the two GIS and two SIS have been combined for clarity. The stars represents the GIS data points and open squares the SIS points.

a power-law model $N(E)dE \propto E^{-\Gamma}dE$, where $N(E)$ is the photon number density at energy E . The photoelectric absorption $A(E)$ is parameterised by $A(E) = e^{(-N_H \times \sigma(E))}$ where N_H is the equivalent hydrogen column and $\sigma(E)$ the photo-electric cross-section taken from Morrison & McCammon (1983). Figures 4.1-4.7 show the data and the data/model ratio after this model was fitted to each object. Rather unexpectedly this model does provide an acceptable fit in 2 cases, where the absorption needed is either the Galactic value (NGC 3147) or relatively low (NGC 4698). An absorbed power-law model is clearly rejected by the NGC 2273 and M51 data. The model parameters are shown in Table 4.3. For the cases of M51, where the obtained spectral slope is unphysically steep and for NGC 2273, where the slope is rather flat. Then the same model is utilised with the slope fixed at the nominal value of $\Gamma = 1.9$ this time, for comparison. In this case as Figure 4.2 that in NGC 2273 here is an excess of counts above 4 keV, while in M51 (Figure 4.7) there is an excess of counts at soft energies.

Table 4.3: Single power-law model

Name	Γ	N_H^a	$f_{2-10\text{keV}}^b$	$L_{2-10\text{keV}}^c$	χ^2/dof
NGC2273	$-0.55^{+0.11}_{-0.11}$	0.68g	0.9	0.65	82.92/22
	1.9f	5.86	0.18	0.14	117.47/22
NGC3079	$1.93^{+0.12}_{-0.12}$	0.08g	0.74	0.20	228.06/143
NGC3147	$1.82^{+0.05}_{-0.06}$	0.36g	1.63	2.76	289.22/285
NGC4698	$1.91^{+0.14}_{-0.14}$	$0.81^{+0.82}_{-0.78}$	1.04	0.22	243.90/250
M51	$3.07^{+0.06}_{-0.06}$	0.16g	0.35	0.02	568.88/178
	1.9f	0.16g	0.90	0.04	848.21/179

NOTE: g indicates that the N_H is set to the galactic value, whereas f indicates that the parameter value is frozen.

^acolumn density in units of 10^{21}cm^{-2}

^bobserved 2-10 keV flux in units of $10^{-12}\text{erg sec}^{-1}\text{cm}^{-2}$.

^cunobscured 2-10 keV luminosity in units of $10^{41}\text{erg sec}^{-1}$, corrected for absorption quoted in column 3.

Iron K_α line

Strong evidence supporting the presence of an accretion disk in the vicinity of a black hole has been given by the detection of an asymmetric broad emission line at a rest energy of ~ 6.4 keV in the Seyfert 1 galaxy MCG-6-30-15. This is interpreted as K_α iron emission originating by fluorescence in the very inner parts of an accretion disk, $3R_S \leq R \leq 10R_S$, about a massive black hole of Schwarzschild radius R_S (Tanaka *et al.* 1995). The profiles and intensities of the iron lines are expected to be complex (asymmetric, double peaked) but the sensitivity of the current detectors cannot provide us with such detailed profiles for the majority of the observed objects. In the Seyfert 2s, reprocessing of the nuclear radiation by the obscuring torus may also contribute to the line flux. The mean equivalent width for a sample of Seyfert 2 galaxies studied with ASCA is 363 ± 254 eV (Gilli *et al.* 1999).

Some of the objects show line like residuals in the 6-7 keV energy range, providing evidence for an iron line, which can be parameterised by a Gaussian line. For the purposes of the study the width of the line is fixed to $\sigma=0.01$ keV. This is smaller than the instrumental response and thus is effectively narrow. The addition of an iron line provides a significantly better fit (at $\geq 99\%$ confidence) for three of the objects (NGC 2273, NGC 3147 and M51) although it should be noted here that the line strengths determined may be strongly

Table 4.4: Power-law plus iron line

Name	Γ	N_H^a	EW (eV)	$f_{2-10\text{keV}}^b$	$L_{2-10\text{keV}}^c$	χ^2/dof
NGC2273	$1.09^{+0.43}_{-0.32}$	0.68g	9080^{+7000}_{-4500}	0.54	0.41	33.32/20
NGC3079	$2.02^{+0.13}_{-0.11}$	0.08g	< 2600	0.84	0.22	217.71/141
NGC3147	$1.80^{+0.10}_{-0.05}$	0.36g	593^{+288}_{-223}	1.67	2.82	267.02/283
NGC4698	$1.91^{+0.12}_{-0.10}$	$0.95^{+0.36}_{-0.42}$	< 425	1.04	0.21	243.89/248
M51	$2.90^{+0.05}_{-0.05}$	0.16g	5520^{+1515}_{-1516}	0.53	0.02	532.33/176

NOTE: g indicates that the N_H is set to the galactic value.

^acolumn density in units of 10^{21}cm^{-2}

^bobserved 2-10 keV flux in units of $10^{-12}\text{erg sec}^{-1}\text{cm}^{-2}$.

^cunobscured 2-10 keV luminosity in units of $10^{41}\text{erg sec}^{-1}$, corrected for absorption quoted in column 3.

influenced by the continuum shape. The energy of the iron line is consistent with the line expected by cold iron for all of the objects, for which the line is detected. No line was detected in the spectrum of NGC 3079 or NGC 4698, for which only the 90 per cent upper limits for an iron line at 6.4 keV are given. The model parameters are given in Table 4.4.

A scattering model

According to the unified model it is expected that a fraction f of the primary emission should be Thomson scattered into our line of sight by a photoionised medium. The scattered spectrum has the same shape as the incident spectrum. Optical polarimetric observations (Tran 1995) have shown that up to ~ 10 per cent of the primary emission can be scattered. The above scenario can be modeled using two power-laws with the same photon index but different normalisations and absorptions. The results are shown in Table 4.5. Again the energy of the line is consistent with the expected 6.4 keV. For M51 the obtained slope is unphysically steep and although the fit has been improved, the model does not describe the data adequately. For NGC 4698 although the model yields an acceptable fit, the normalisations of the two power-law components are comparable, and neither component requires any absorption below 10 keV. In the case of NGC 3147 the column density is too high to be properly constrained in the *ASCA* energy range, thus the spectral parameters are not quoted in Table 4.5. Finally, in the case of NGC 2273, the normalisations of the scattered power-law component is almost two orders of magnitude

Table 4.5: Scattering model

Name	Γ	N_H^a	EW (eV)	f	$f_{2-10\text{keV}}^b$	$L_{2-10\text{keV}}^c$	χ^2/dof
NGC2273	$1.78^{+0.61}_{-0.27}$	982^{+196}_{-433}	555^{+4000}_{-520}	0.04	1.11	7.80	14.28/18
NGC3079	$2.20^{+0.30}_{-0.20}$	950^{+525}_{-117}	< 3000	0.23	1.13	0.21	192.18/140
M51	$4.40^{+0.36}_{-0.21}$	$64.7^{+8.8}_{-8.0}$	4100^{+2300}_{-2110}	0.01	0.60	0.06	298.81/174

^acolumn density in units of 10^{21}cm^{-2}

^bobserved 2-10 keV flux in units of $10^{-12}\text{erg sec}^{-1}\text{cm}^{-2}$.

^cunobscured 2-10 keV luminosity in units of $10^{41}\text{erg sec}^{-1}$, corrected for absorption quoted in column 3.

Table 4.6: Composite Model

Name	Γ	N_H^a	KT	EW(eV)	$f_{2-10\text{keV}}^b$	$L_{2-10\text{keV}}^c$	χ^2/dof
NGC3079	$0.79^{+0.31}_{-0.26}$	17^{+93}_{-17}	-	-	0.11	0.3	156.42/139
	-	66^{+12*}_{-14}	$0.69^{+0.11}_{-0.09}$	-	-	-	-
M51	$1.70^{+0.15}_{-0.19}$	$0^{+1.6}_{-0}$	$0.71^{+0.05}_{-0.02}$	947^{+812}_{-528}	0.9	0.07	235.18/173

NOTE:*this value is referred to the column obscuring the thermal component.

^acolumn density in units of 10^{21}cm^{-2}

^bobserved 2-10 keV flux in units of $10^{-12}\text{erg sec}^{-1}\text{cm}^{-2}$.

^cunobscured 2-10 keV luminosity in units of $10^{41}\text{erg sec}^{-1}$, corrected for absorption quoted in column 3.

lower than that of the primary power-law component, suggesting ~ 2 per cent scattered flux, in agreement with what it is typically found for the obscured Seyfert galaxies (Sy 1.9-2.0).

Composite model

Infrared (Maiolino *et al.* 1995) and X-ray studies of Seyfert 2 galaxies (Turner *et al.* 1997) show that their host galaxies tend to have energetic starburst regions. Indeed some of the objects show line like residuals at soft energies, suggesting thermal emission arising from hot gas. Thus, an emission spectrum from hot, diffuse gas (Raymond model in XSPEC) is utilised to model any starburst component, along with a single power-law to account for the hard photons. The temperature is set to be $\leq 1.0\text{keV}$, in order to constrain the starburst contribution to the soft band. This model is applied to NGC3079 and M51 data because these galaxies show evidence for thermal emission. In the case of M51 the thermal component is absorbed by the Galactic column, whereas in NGC3079 excess absorption is required. This model gives a good fit for both galaxies (see Table 4.6).

4.4.2 The Compton thick models

If the column density exceeds $\sim 10^{24}\text{cm}^{-2}$, the obscuring medium is optically thick to Compton scattering and thus the primary emission is suppressed and we only observe the scattered emission from either the warm matter or the inner surface of the torus itself. Here I will consider the case where the Compton reflection from the inner surface of the torus dominates the observed emission in the 2-10 keV energy band. Therefore I utilise the pexrav model in XSPEC, which describes reflection occurring from a slab of neutral material subtending a solid angle of 2π sr to an X-ray point source located above the slab, to account for the total hard X-ray emission and a power-law to represent the soft emission. For the purpose of this study the slope of the underlying power-law spectrum is fixed at 1.9 and Galactic absorption.

The normalisation of the reflection is given by $R=\Omega/2\pi$, where Ω is the solid angle subtending by the reflector. However, the intensity of the intrinsic power-law, which is being reflected, cannot be measured directly, and thus the value of R is not physical. This is because the normalisation of the power-law and the value of R are highly correlated in the spectral fits in order to produce the observed counts. Thus the value of R is not always representative of the real strength of the reflection component. Therefore the ratio $A=R \times f_{(2-10\text{keV})} / f_{(2-10\text{keV})_{sc}}$ is defined as an indicator of the fractional contribution that would have been made to the observed spectrum after correction for absorption in the pexrav reflector. $f_{(2-10\text{keV})}$ is the flux that would have been produced by the underlying spectrum in the 2-10 keV band assuming that the emission is not absorbed by the torus whereas $f_{(2-10\text{keV})_{sc}}$ is the observed flux of the fitted scattered component in the same band. Given that typically the scattering accounts for ~ 1 per cent of the total X-ray emission, any value of A that is less than 1 suggests we see only a small portion of the reflector, and small values mean the reflected contribution to the observed flux is almost insignificant. We apply this model to NGC 2273, NGC 3147 and NGC 4698 which show low absorption. That model provides a good representation of the data for NGC 4698 ($\chi^2=245.04$ for 250 degrees of freedom), NGC 2273 ($\chi^2=24.88$ for 18 d.o.f.) and NGC

Table 4.7: Compton thick model

Name	Γ	EW(eV)	A^a	$f_{2-10\text{keV}}^b$	χ^2/dof
NGC2273	1.9f	4460^{+900}_{-3610}	$3^{+\infty}_{-1.7}$	0.62	24.88/19
NGC3147	1.9f	548^{+508}_{-387}	$0.11^{+0.08}_{-0.09}$	0.02	267.11/282
NGC4698	1.9f	-	$0.15^{+0.02}_{-0.01}$	0.01	245.04/250

^athe meaning of parameter A is explained in section 4.2.

^bobserved 2-10 keV flux in units of $10^{-12}\text{ergsec}^{-1}\text{cm}^{-2}$.

3147 ($\chi^2=267.11$ for 282 d.o.f.) (see also Table 4.7).

4.5 Results on single objects

In this section the results of the spectral fitting for each individual object in these sample are discussed and compared to the results from previous X-ray studies.

NGC 1167, NGC 1667 and NGC 3486 did not give sufficient counts for a full spectral analysis to be performed. However, a $> 3\sigma$ detection in the 2-10 keV band for both objects was obtained. Clues for the spectral shape of the sources come from their hardness ratio. Here the hardness ratio is defined as $(h-s)/(h+s)$, where h and s are the total number counts in the detection cells, in the 2-10 and 1-2 keV bands respectively. For this analysis GIS data only were used, because the SIS efficiency especially at soft energies is steadily decreasing with time, which could lead to an artificial hardening of the spectrum.

4.5.1 NGC 1167

The hardness ratio of the source is -0.22 ± 0.12 , which corresponds to a power-law of $\Gamma = 2.5 \pm 0.3$ assuming galactic absorption. This corresponds to an observed flux in the 2-10keV band of $4.0 \times 10^{-14}\text{erg cm}^{-2} \text{ s}^{-1}$ and a luminosity of $2.0 \times 10^{40}\text{erg s}^{-1}$. The derived spectral index is rather steeper than is typical for Seyfert galaxies, suggesting the possible presence of an additional soft component, possibly coming from a starburst region in the vicinity of the AGN.

The low $f_{HX}/f_{[OIII]}=0.23$ ratio (see section 4.6.1 for a detailed discussion on the implications of this ratio) for this source would suggest it as a Compton thick Seyfert 2 galaxy. On the other hand the HR analysis showed that NGC 1167 has a steep spectrum, while in the context of a Compton thick interpretation it would be expected NGC 1167 to show a flat spectrum. Unfortunately the HR analysis provides only an indication for the spectral shape and no information for any components contributing to the spectrum. It is quite likely that the X-ray spectrum of NGC 1167 is quite complex with different components contributing to different energies. For example a very strong soft excess, possibly originating from intense starforming activity, could produce a steep spectrum even if the emission from the central source is completely blocked by a Compton thick absorption screen. However, since NGC 1167 is too faint for any further spectral analysis to be performed, the nature of its X-ray emission cannot be determined.

4.5.2 NGC 1667

NGC 1667 is a remarkable object. It has shown a decrease of a factor of ~ 150 in the 2-10 keV flux between its discovery (e.g. Polleta *et al.* 1996, Turner *et al.* 1997). The object was too faint to perform any spectral analysis. The hardness ratio of the source is -0.52 ± 0.14 , which corresponds to a power-law of $\Gamma = 3.2 \pm 0.4$. Assuming Galactic absorption the observed 2-10 keV flux is then $\sim 8 \times 10^{-14} \text{erg cm}^{-2} \text{s}^{-1}$, which corresponds to a luminosity of $1.3 \times 10^{41} \text{erg s}^{-1}$. The slope is steeper than the canonical for Seyfert galaxies and, again, could be attributed to starburst emission. Indeed, Radovich & Rafanelli (1996) find evidence for star formation within 10 kpc of this source, and thus favouring the latter interpretation. To examine this possibility I estimated the expected starburst contribution in the 0.5-4.5 keV band. The starburst activity produce infrared emission probably due to dust reprocessing of the radiation produced by the stars. This is given by the following equation (David *et al.* 1992):

$$F_{fir} = 1.26 \times 10^{-23} [2.58 \times 10^{12} f_{\nu}(60\mu m) + 10^{12} f_{\nu}(100\mu m)] \text{erg cm}^{-2} \text{s}^{-1} \quad (4.1)$$

where $f_\nu(60\mu m)$ and $f_\nu(100\mu m)$ are the colour corrected flux densities in Jy. The coefficients before the fluxes are the IRAS band passes in Hz. However the infrared flux could arise from nuclear reprocessed emission from the obscuring medium, and thus any the starburst contribution to the X-ray flux may be overestimated by simply assuming that the bulk of the infrared emission is originated by the starburst. Thus the derived flux could only be an upper limit to the expected contribution to the X-ray flux.

The expected X-ray contribution from stars was calculated using the empirical relationship between infrared and X-ray luminosity (David *et al.* 1992):

$$\log L_x = (0.95_{-0.05}^{+0.06}) \log L_{fir} - (1.1_{-2.6}^{+3.0}) \quad (4.2)$$

This gives $L_x = 8.67_{-4.77}^{+12.44} \times 10^{40} \text{ erg s}^{-1}$ in the 0.5-4.5 keV. On the other hand the luminosity derived assuming a spectrum with slope 3.2 and Galactic absorption is $\sim 6 \times 10^{41} \text{ erg s}^{-1}$. Thus the maximum contribution from starburst activity in this energy band is about 4 per cent.

The low $f_{HX}/f_{[OIII]}$ ratio for this source would suggest it as a Compton thick candidate.

The substantial reduction in the hard X-ray flux over a ~ 20 yr timescale which has, presumably, not yet been reflected in the narrow-line region would provide an alternative hypothesis to explain the anomalous ratio. Indeed, assuming that the reduction in the hard X-ray flux over a ~ 20 yr timescale, has not yet been reflected in the narrow-line region, we find that the Narrow Line Region in NGC 1667 should be located at >6 pc. Given that the NLR lies 10-100 pc from the central source it appears that indeed the substantial change in the hard X-ray flux has not reached the NLR yet. This explanation is the most likely explanation of the low $f_{HX}/f_{[OIII]}$ ratio and NGC 1667 is probably Compton thin.

4.5.3 NGC 2273

This galaxy has been studied by Maiolino *et al.* (1998) using *BeppoSAX* data. They found that the data could be represented by both a Compton thin transmission model with $\Gamma = 0.7$ and $N_H < 10^{23} \text{cm}^{-2}$ and a Compton thick model with $N_H > 10^{25} \text{cm}^{-2}$. However, they classified this object as Compton thick, taking into account its flat spectral index and the large equivalent width of the iron line. In addition they did not detect any emission with the PDS on board *BeppoSAX* and thus they suggested that if the Compton thick model is valid the absorbing column in our light of sight must be larger than 10^{25}cm^{-2} . The “scattering” model provides a better fit to the *ASCA* data (with a column close to 10^{24}cm^{-2} and an equivalent width of $\sim 500 \text{eV}$) and thus it is preferred. The fit is shown in Figure 4.8. The excess in the hard counts has now diminished.

It is apparent from Figure 4.1 that the flat spectrum originally obtained from a simple power-law fit is caused by a turn-up in the spectrum at energies above $\sim 5 \text{keV}$. Indeed a spectral fit over the restricted 0.2-5 keV range give a good fit to power-law with a slope of 1.5 ± 0.6 consistent with the canonical AGN and the scattering interpretation.

The ratio of the unobscured hard X-ray emission to the $[\text{OIII}]\lambda 5007$ emission is low, indicating that we do not observe the primary emission. However the Compton thick model described in the text, yields a poor fit. It is likely that the spectrum of NGC 2273 is more complex. Probably a warm absorber medium and/or starburst emission contribute to the soft X-ray spectrum of this Seyfert 2, whereas the emission line around 6.4 keV could be a blend of iron lines. Unfortunately the low quality of these data do not allow the determination of the components, which contribute to the NGC2273 X-ray spectrum.

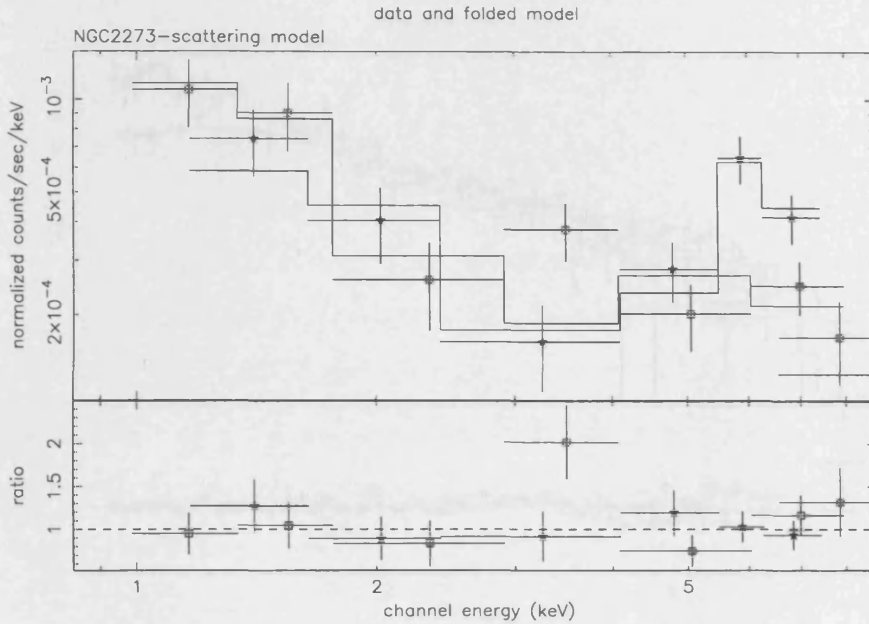


Figure 4.8: The scattering model for NGC 2273. The top panel shows the data with the model and the bottom panel shows the data/model ratio. Data from the two GIS and two SIS have been combined for clarity. The stars represents the GIS data points and open squares the SIS points.

4.5.4 NGC 3079

The *Einstein* IPC detected NGC 3079 at the 3.2σ level (Fabbiano *et al.* 1982), with a flux of $3.7 \times 10^{-13} \text{erg cm}^{-2} \text{s}^{-1}$. The *ROSAT* PSPC data are dominated by a nuclear point source but emission is detected up to $2'.5$ from the nucleus (Reichert *et al.* 1994). Pietsch *et al.* (1998) resolved the X-ray emission with *ROSAT* PSPC and HRI into three components. a) extended emission in the innermost region, with $L_x = 3 \times 10^{40} \text{erg s}^{-1}$, coincides with the super-bubble seen in optical images, b) emission from the disk of the galaxy that can partly resolved in 3 point-like sources and c) very soft X-shaped emission from the halo extending to a diameter of 27 kpc. Ptak *et al.* (1999) first presented the *ASCA* data for this galaxy. Their best-fit spectral parameters have large uncertainties: the power-law $\Gamma \sim 2.20^{+2.0}_{-1.0}$ and $N_H \approx 6^{+4}_{-5} \times 10^{21} \text{cm}^{-2}$. The starforming component, was described by a Raymond-Smith model with $kT=0.14(<0.54) \text{keV}$. The results for NGC 3147 are in broad agreement with Ptak *et al.* (1999), although the spectral index is somewhat flatter. The best-fit model is the “composite” one (see Table 4.6) while

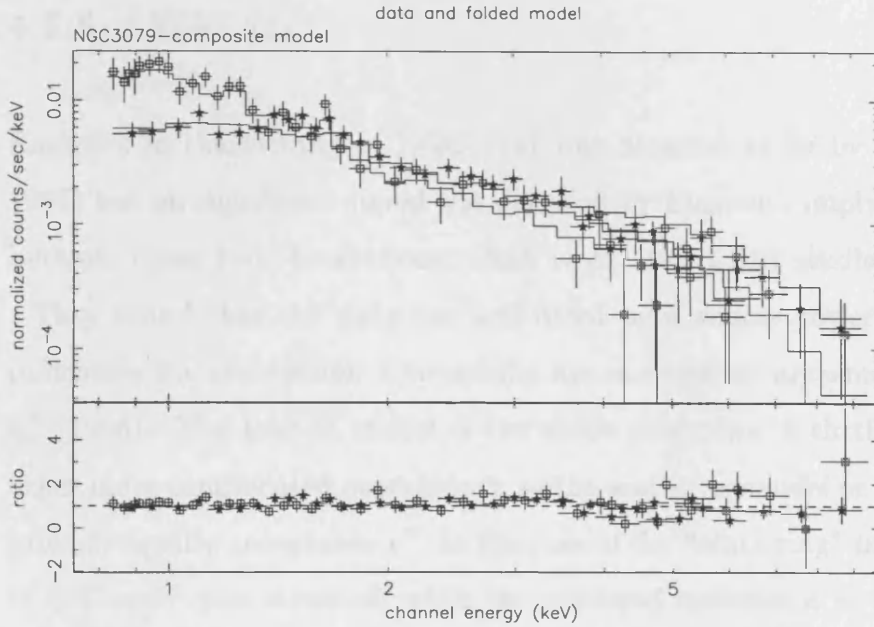


Figure 4.9: The composite model for NGC 3079. The top panel shows the data with the model and the bottom panel shows the data/model ratio. Data from the two GIS and two SIS have been combined for clarity. The stars represents the GIS data points and open squares the SIS points.

no significant iron K_{α} emission is detected (see also Figure 4.9). No variability was detected by Ptak *et al.* (1998) consistent with a Compton thick scenario and a substantial starburst contribution. However, both the lack of an iron line as well as the X-ray to infrared ratio argue against the Compton thick interpretation. Given that the *ROSAT* data show extended emission, it is important to make an estimate of the contribution of the starburst activity to the X-ray flux. Using equations 4.1 and 4.2 the predicted 0.4-4.5 keV luminosity for the starburst contribution in NGC 3079 is $2.29_{-1.12}^{+3.68} \times 10^{40} \text{erg s}^{-1}$. The *ASCA* luminosity in the same energy band is 2.5×10^{40} . Thus the starburst emission contributes a significant fraction of the X-ray *ASCA* spectrum. The above strengthens the applicability of the composite model. Summarising, NGC 3079 seems to have a complex spectrum and the nature of the X-ray emission cannot be determined with the current data.

4.5.5 NGC 3147

Emission in the vicinity of NGC 3147 was detected at 3σ by *HEAO-1* (Rephaeli *et al.* 1995) but no significant signal was detected by *Einstein*, implying a decrease in the flux between these two observations. Ptak *et al.* (1996) first studied this object with *ASCA*. They found that the data are well fitted by a simple power-law with $\Gamma=1.9$ with no indication for absorption. Our results are in excellent agreement with those of Ptak *et al.* (1996). The best-fit model is the single power-law with the iron line. In principle, other more complicated models such as the scattering model or the Compton thick model provide equally acceptable χ^2 . In the case of the “scattering” model, a very large column of 10^{24} cm^{-2} was obtained, while the scattered emission is ~ 5 per cent of the primary component. In addition the Compton thick model provides an equally good representation of the data statistically; here it is the scattering component which dominates the fit. The absence of significant short-term variability (see next chapter, also Ptak *et al.* 1998) could in principle favour such models. However, although the above models provide good fits to the data they are rather contrived as the *ASCA* bandpass does not allow us to constrain any models with an obscuring column higher than $\sim 10^{24} \text{ cm}^{-2}$. Indeed, a single power-law model is identical to a scattering model with $N_H > 10^{24} \text{ cm}^{-2}$ in the *ASCA* band as these columns absorb most photons below 10 keV. It is therefore interesting that the [OIII] λ 5007 emission does not favour the above two models (composite and scattering). A detailed discussion on this object is presented in next chapter.

4.5.6 NGC 3486

The hardness ratio is 0.29 ± 0.12 . This corresponds to a quite flat power law of $\Gamma = 1.2 \pm 0.3$ over the 1-10 keV energy band, assuming Galactic absorption, suggestive of high amounts of obscuration. For example the well-known nearby Compton thick AGN (eg Circinus, NGC 1068) exhibit flat spectra below 20 keV due to the combination of the reflection and the scattering components. The observed flux assuming Galactic absorption is $\sim 5 \times 10^{-14} \text{ erg cm}^{-2} \text{ s}^{-1}$. Then simulations were carried out, in order to determine the

amount of obscuring medium needed to obtain a change of Γ from 1.9, which is the nominal value for AGNs to 1.2. It is derived that the source should be obscured by a column density of $N_H = 3.2 \times 10^{21} \text{cm}^{-2}$. Using $\Gamma = 1.9$ and $N_H = 3.2 \times 10^{21} \text{cm}^{-2}$, observed flux is $\sim 5 \times 10^{-14} \text{erg cm}^{-2} \text{s}^{-1}$, which corresponds to a luminosity of $\sim 5 \times 10^{38} \text{erg s}^{-1}$. This is too low for a Seyfert galaxy, again indicating high absorption in our line of sight (but see Roberts & Warwick 2000). On the other hand the derived luminosity of NGC3486 is typical for Galactic black hole binaries. The $[\text{OIII}]\lambda 5007$ ratio is relatively low (2.9). In order for the ratio to be comparable to the ratios observed in Seyfert galaxies (see section 4.6.1) the source should be obscured by a column density of $\sim 1 \times 10^{24}$ assuming a power-law of $\Gamma=1.9$. This is much higher than the column derived from the HR analysis assuming $\Gamma=1.9$. This indicates that the spectrum cannot be represented by a single power-law model, and that other components contribute to the X-ray spectrum as well.

4.5.7 NGC 4698

NGC 4698 was observed with *Einstein* and its 0.2-4.0 keV flux is $2.8 \times 10^{-13} \text{erg cm}^{-2} \text{s}^{-1}$. The *ASCA* flux at the same band is 1.13×10^{-12} . However the *Einstein* flux is subject to ~ 25 per cent uncertainty and this could easily account for the difference. The data are well fitted with a single power-law model with $\Gamma \sim 1.9$ and $N_H \sim 8 \times 10^{20} \text{cm}^{-2}$. The Compton thick model provide a good representation of the data as well. However the $f_{\text{HX}}/f_{[\text{OIII}]}$ and the low value of A do not favour this interpretation.

A detailed discussion on this object is presented in next chapter.

4.5.8 M51

M51 is known as the 'Whirlpool galaxy'. The *Einstein* HRI detected X-ray emission from M51 with a luminosity $L_x = 3.0 \times 10^{40} \text{erg s}^{-1}$ in the 0.2-4.0 keV band. The emission is extended and the luminosity of a point source at the nucleus is $L_{0.2-4.0\text{keV}} < 1.5 \times 10^{39} \text{erg s}^{-1}$ (Palumbo *et al.* 1985). The *ROSAT* PSPC spectrum of the M51 nucleus is fitted

with a thermal plasma of $kT \sim 0.4$ keV (Marston *et al.* 1995; Read *et al.* 1997) indicating that the AGN does not dominate the nuclear soft X-ray emission. The *ROSAT* PSPC observations revealed extended emission (Ehle *et al.* 1995). At the hard energies the *Ginga* data are fitted with a photon index of $\Gamma = 1.4$ and an X-ray luminosity of $L_{2-20\text{keV}} = (1.2 \pm 0.6) \times 10^{41}$ erg s⁻¹ from a ~ 1 deg² field containing M51 (Makishima *et al.* 1990). The data are also fitted with a $kT=7$ keV thermal bremsstrahlung model plus a power-law with $\Gamma = 1.6$ absorbed by a column of 4×10^{23} cm⁻². Terashima *et al.* (1998) analysed *ASCA* data and found extended emission from M51 in the 2-5 keV energy range. They detected a soft thermal emission represented by either $kT \sim 0.4$ keV with low iron abundance or two kT plasmas (~ 0.3 keV and ~ 0.8 keV). The hard emission is represented by a power-law with $\Gamma \sim 1.4$ and ~ 1 respectively. The fact that extended emission is observed in the 2-5 keV band, clearly suggests that the AGN emission contributes only to the hardest end of the *ASCA* spectrum and is either suppressed at the softer energies or is not the dominant contributor of the energy output at these energies.

The best fit model for M51 is the composite model with $kT \sim 0.7$ keV and a spectral slope of ~ 1.7 . However we obtained an upper limit for the column density of 1.6×10^{21} cm⁻². This is not sufficient to obscure the AGN X-ray emission up to ~ 5 keV, as it is indicated by the analysis of the brightness profile of M51. The emission could be interpreted as the superposition of thermal emission at soft energies (below 2 keV), emission from low-mass X-ray binaries (LMXBs), which contribution dominates at the 2-5 keV band and a power-law component from the AGN, which is revealed above 5 keV. In this case the active nuclei should be obscured by a column of $> 5 \times 10^{23}$ cm⁻². However, because the AGN and the LMXBs, both show a power-law spectrum of $\Gamma \sim 1.7 - 1.8$, it is possible both components to be fitted by the power-law model with no need of excess absorption. On the basis of its $[OIII]\lambda 5007$ flux, M51 is a Compton thick candidate. It should be noted here that a Compton thick model was also applied to the data, with either 2 Raymond-Smith models and a reflected continuum (pexrav model), or a Raymond-Smith model, a power-law model to account for the possible LMXBs contribution and the reflection component. However, although we obtained good fits the reflection component did not

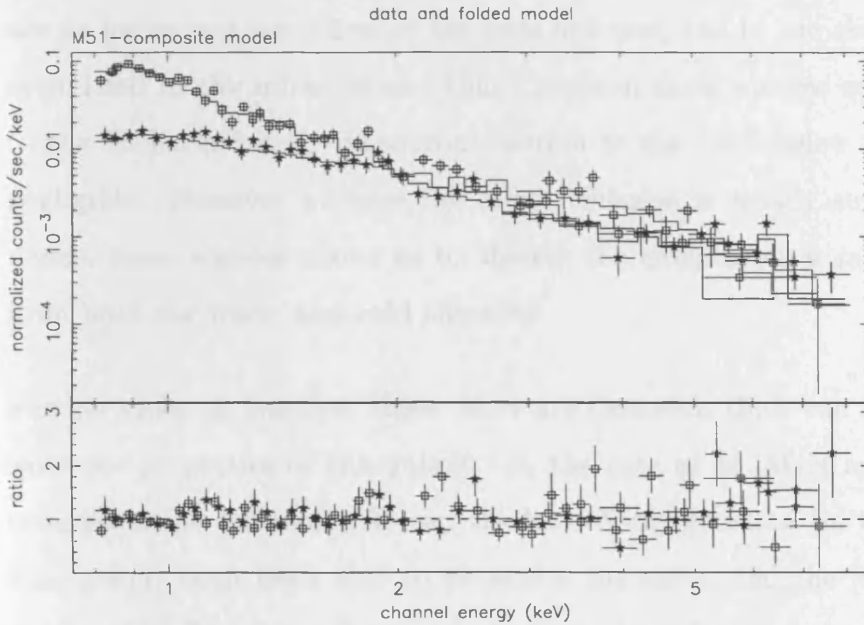


Figure 4.10: The composite model for M51. The top panel shows the data with the model and the bottom panel shows the data/model ratio. Data from the two GIS and two SIS have been combined for clarity. The stars represents the GIS data points and open squares the SIS points.

contribute in the ASCA band leaving the possibility where the hard X-ray emission is dominated by a scattered component more plausible in this band.

4.6 Discussion

4.6.1 Are most of our objects Compton thick ?

A couple of the objects in this sample show no evidence for intrinsic absorption. It should be pointed out here that in the case of poor photon statistics, a Compton thick object could be misidentified for a low- N_H , steep spectrum, type-1 AGN, especially if the steep scattered emission dominates over the reflected component; It is thus possible that ASCA only 'sees' the scattered component. Therefore, the lack of intrinsic absorption in some of the galaxies may indicate that these objects are Compton thick. Compton thick sources are an important "class" of Seyfert 2 galaxies mainly because a) as shown by Risaliti *et al.* (1999) half of the Sy2 population is believed to be Compton thick sources and thus they

are an important ingredient of the local universe, and b) the absorbed X-ray photons are re-emitted in the infra-red and thus Compton thick sources are important contributors to the IR background. Their contribution to the XRB below 10 keV is expected to be negligible. However because the X-ray emission is totally suppressed in the observed bands, these sources allows us to observe the circumnuclear matter as well as reflection from both the warm and cold absorber.

Further clues on whether these AGN are Compton thick can be given by studying the isotropic properties of the galaxy. In the case of an AGN as isotropic emission, it is considered the infrared (IR) and the hard X-ray emission (in the case of Compton thin absorption) both been able to penetrate the torus, and the $[OIII]\lambda 5007$ line emission produced in the narrow line region, and thus free of viewing angle effects. Indeed, Alonso-Herrero *et al.* (1997) showed that the ratio of the 2-10 keV flux to the $[OIII]\lambda 5007$ and to the IR flux are comparable for obscured and unobscured AGNs. The advantage of studying isotropic properties, is that they act as an indicator of the strength of the nuclear source. Maiolino *et al.* (1998) have proposed that the measurement of the unabsorbed hard X-ray flux (2-10 keV) against the $[OIII]\lambda 5007$ flux, is indeed a powerful diagnostic. Moreover, although the line is emitted on the Narrow Line Region (NLR) scales, the host galaxy disk might obscure part of the NLR and should be corrected for the extinction deduced from the Balmer decrement (Maiolino & Rieke 1995). The corrected $[OIII]\lambda 5007$ flux is given by the following relation (Bassani *et al.* 1999):

$$F_{[OIII]cor} = F_{[OIII]obs} \times [(H_\alpha/H_\beta)/(H_\alpha/H_\beta)_0]^{2.94} \quad (4.3)$$

Assuming an intrinsic Balmer decrement $(H_\alpha/H_\beta)_0 = 3$.

All well studied Seyfert 1 galaxies have $f_{HX}/f_{[OIII]} \geq 1$ (Maiolino 1998). To illustrate the effect of obscuration in the 2-10 keV X-ray flux to the $[OIII]\lambda 5007$ ratio, the ratio is plotted against the column density obscuring the primary X-ray emission (Figure 4.11). Again, it has been assumed that the underlying power-law has a spectral index of $\Gamma=1.9$ and that the unobscured $f_{HX}/f_{[OIII]}$ is 70. The actual value of the ratio is not important at this stage as we are only interested in the changes of the ratio due to obscuration. An

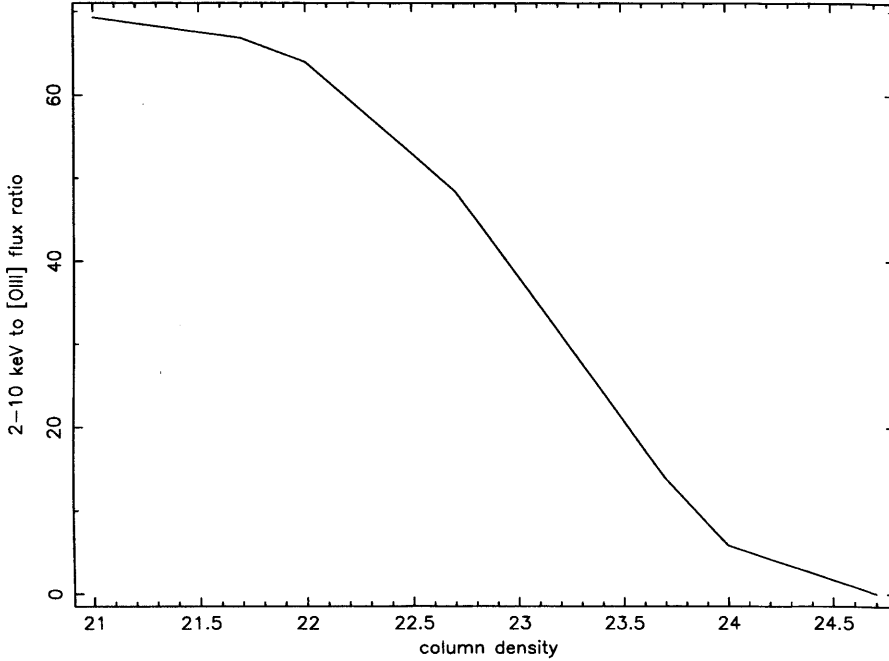


Figure 4.11: The $f_{HX}/f_{[OIII]}$ versus the column density obscuring the primary X-ray emission.

absorption of less than a few times 10^{23} cm^{-2} will lower this ratio by a factor of ~ 5 with respect to Seyfert 1s. When $N_H > 10^{24} \text{ cm}^{-2}$ then the reduction is about two orders of magnitude.

In Table 4.8 the flux ratios using the absorption corrected as well as the observed 2-10 keV flux are quoted. For the former ratio, the flux has been derived using the most plausible model for each object. Of course one has to be cautious as there may be some limitations on the use of the $[OIII]\lambda 5007$ flux ratio as an indicator of the unobscured X-ray emission. Indeed, in cases where the ionisation cone axis lies perpendicular or close to the minor axis of the galaxy there might be lack of ionised gas. Then the $[OIII]\lambda 5007$ flux may not be a good indicator of the nuclear strength. However the disk height for a typical spiral galaxy is of the order of ~ 100 pc whereas the size of the region where the bulk of the $[OIII]\lambda 5007$ flux is produced is of a similar size. Thus it is most likely that the relative orientation of the nuclear accretion to the host galaxy disk will not significantly affect the $[OIII]\lambda 5007$ flux. Another consideration that it should be taken into account is whether the torus hides the innermost regions of the NLR from our view and thus the observed $[OIII]\lambda 5007$ is lower than the actual flux produced. Again the small size

Table 4.8: Hard X-ray, [OIII] λ 5007 fluxes and classification

Name	f_{HX}^a	f_{HX}^b	$f_{[OIII]}^c$	$f_{HX}/f_{[OIII]}^d$	$f_{HX}/f_{[OIII]}^e$	$type^f$	$type^g$
NGC1167	0.04	0.04	17	0.23	0.23	?	CT
NGC1667	0.08	0.08	197	0.04	0.04	?	CTn
NGC2273	1.11	3.65	277	0.40	1.32	CTn	CT
NGC3079	0.11	1.10	90	0.11	1.20	CTn	CT
NGC3147	1.63	1.64	9.0	18.11	18.22	CTn	CTn
NGC3486	0.05	0.05	1.7	2.94	2.94	?	CT/CTn
NGC4698	1.04	1.10	2.0	52	55	CTn	CTn
M51	0.11	0.55	150	0.07	0.37	CTn	CT

^a 2-10 keV observed flux in units of $10^{-12}\text{erg cm}^{-2} \text{s}^{-1}$.

^b 2-10 keV unobscured flux in units of $10^{-12}\text{erg cm}^{-2} \text{s}^{-1}$, using the most plausible model for each object.

^c corrected [OIII] λ 5007 flux in units of $10^{-14}\text{erg cm}^{-2} \text{s}^{-1}$, taken from Risaliti *et al.* 1999.

^d using the observed 2-10 keV flux.

^e using the absorption corrected 2-10 keV flux for the most plausible model for each object.

^f whether the object is Compton thin (CTn) or Compton thick (CT) after taking into consideration the spectral fitting.

^g whether the object is Compton thin (CTn) or Compton thick (CT) after taking into consideration the $f_{HX}/f_{[OIII]}$ ratio.

of the torus (a few pc) relative to the size of the NLR (kpc scale) implies that such an effect does not affect significantly the above ratio. In addition Mulchaey *et al.* (1994) compared the properties of samples of Seyfert 1 and Seyfert 2 galaxies and showed that the ratio of the [OIII] λ 5007 emission to the unobscured hard X-ray emission, is the same for both types of galaxies, indicating that the [OIII] λ 5007 flux cannot be obscured by the torus. In the case of the IR emission caution must be taken since the IR emission may be contaminated by starburst emission particularly in the case of low luminosity AGN where the star formation in the host galaxy dominates the emission. Indeed multiwavelength observations of objects presented in this chapter have shown that indeed some of them contain starburst activity (see §4.5). Therefore, this criterion is not applied to the data.

In Table 4.8 it is also noted whether the object is Compton thin or thick on the basis of the X-ray spectral analysis and the $f_{HX}/f_{[OIII]}$ ratio. It is clear that in some cases there is a discrepancy on the classifications inferred from the spectrum and the $f_{HX}/f_{[OIII]}$ ratio. This is probably due to the limited diagnostic capabilities of the X-ray data. It is likely that the X-ray spectrum of Seyfert 2 galaxies and especially those with high column densities, where the medium and hard X-ray photons are suppressed, and emission

from the host galaxy, circumnuclear starburst and warm absorbers contributes to the spectrum significantly. However the present *ASCA* data does not allow us to determine the contribution of these components.

Summarizing, NGC 1167, NGC 2273, NGC 3079 and M51 are Compton thick candidates according to their $f_{HX}/f_{[OIII]}$ ratio. However the spectral analysis for three of them, namely NGC 2273, NGC 3079 and M51 does not favour this interpretation, but instead the data are better fitted by an obscured power-law (Compton thin model). The discrepancy is probably due to complexity of the X-ray spectrum as has been already explained for example for M51. However the current data do not allow us to determine the spectral components, especially in the case of NGC 2273, but are only sufficient to support analysis with simplistic models. NGC 3486 is probably a heavily obscured Sy2. NGC 1667 is probably Compton thin. A decrease in the 2-10 keV flux is probably the cause for the low $f_{HX}/f_{[OIII]}$ ratio in NGC 1667. NGC 3147 and NGC 4698 have high $f_{HX}/f_{[OIII]}$ ratios and comparable to the value obtained by Alonso-Herrero *et al.* (1997) if we take into account the extinction in the NLR, clearly showing that the 2-10 keV X-ray emission is not affected by absorption.

4.6.2 The distribution of absorbing columns and its implications for the X-ray background

The work presented here showed that some of the objects included in this sample show no absorption above the Galactic. On the other hand studies of Seyfert 1 galaxies (George *et al.* 1998, Reynolds 1997), show that some Seyfert 1s have column densities well above the Galactic, some of them with columns $\sim 10^{21}\text{cm}^{-2}$. For that reason it seems that it is not straightforward to identify the N_H value which best separates the two classes of Seyfert galaxies. On the other hand it seems that Seyfert 1 galaxies although unobscured in the optical, are subject of absorption in X-rays.

However, it should be noticed that the column density distribution is model dependent and that there is not an independent way of deriving N_H values. Given the limited energy

band covered by the current detectors in conjunction with their sensitivity at low energies, it is becoming apparent that it is difficult to obtain accurate values for the N_H .

Furthermore, latest results from *ASCA* and *BeppoSAX* (see Chapter 3, Comastri *et al.* 2000, respectively) show that there is a population of objects at high redshifts, with broad lines in optical, which have high amounts of X-ray absorption. All the above suggest that the distribution of column densities is complex, and one cannot use a simple recipe for the N_H distribution.

Figure 4.12 shows the N_H distribution by compiling all the Seyfert 2 galaxies from the Risaliti *et al.* (1999) sample. In the same histogram the Seyfert 2 studied in this chapter are shown as well. It is clear that the majority of the Seyfert 2 galaxies presented here have $N_H < 10^{22}\text{cm}^{-2}$, whereas *all* the Seyfert 2 galaxies in the Risaliti sample have $N_H > 10^{22}\text{cm}^{-2}$, and thus this work extends the N_H distribution towards lower columns. However as has been already noted the spectra of the Seyfert 2s presented in this chapter is probably complex, but due to the relatively low signal-to-noise ratio, complex models cannot be applied to the data. To this add the *ASCA* energy band as well. Therefore it is possible that the column densities derived are not the real values. The same may be the case for several other Seyfert 2 galaxies studied with *ASCA*.

The uncertainties in the distribution of column densities has important implications for the X-ray Background synthesis models. The X-ray background is believed to be produced by the superposition of discrete sources. In the soft band at a flux limit of $1 \times 10^{-15}\text{ergcm}^{-2}\text{s}^{-1}$ the dominant population are broad line AGNs (Hasinger *et al.* 1998). On the other hand only $\sim 30\%$ of the 2-10 keV CXB has been resolved into discrete sources (Georgantopoulos *et al.* 1997) the majority of which are again broad line AGNs. However broad line AGNs have power-law spectra with a photon index of $\Gamma \sim 1.9$ (Nandra & Pounds, 1994), which is significantly softer than that of the CXB in that band (~ 1.4 , Gendreau *et al.* 1995). Thus there must be a large number of undetected objects which have harder X-ray spectra than the local broad-line AGNs. This population should be obscured because it does not come up in the softer energies. Therefore all the current models which try to reconstruct

the X-ray background spectra utilise a population of objects with an underlying spectral index equivalent of those of unobscured AGNs ($\Gamma=1.9$) and a range of obscuring columns. Observational support for such a model comes from the detection in deep *ROSAT* surveys (Boyle *et al.* 1995) of a large number of faint X-ray sources. The optical counterparts of these sources are galaxies with narrow lines only and thus they are considered to be that 'obscured' AGN population. In addition, the lack of a population with spectral index similar to the X-ray background which again indicate that a large population of heavily obscured AGN should emerge at hard energies.

Many Seyfert 2 galaxies, as has been already reported earlier in this chapter have a scattered component, which does not suffer absorption. It is assumed to be \sim a few per cent. However, in reality there is a large range in the scattering fraction. As pointed out by Yaqoob (2000), the fraction can be from \sim 0.2 per cent for NGC 7172 to \sim 40 per cent for NGC 2992. Furthermore, X-ray studies of Seyfert 2 galaxies (e.g this chapter, Turner *et al.* 1997) show that their host galaxies have energetic starbursts contributing to the X-ray spectrum. Neither the starburst nor the scattered component are taken into account in the majority of the X-ray background synthesis models and at the moment their contribution is difficult to be constrained (but see Fabian *et al.* (1998) for a model where nuclear starburst obscuration is taken into account.)

This analysis showed that simple models probably cannot describe the spectrum of the Seyfert 2 galaxies adequately. Especially in the case of heavily obscured or Compton thick objects, where the medium and/or hard X-ray emission is suppressed and emission from the host galaxy, circumnuclear starbursts and/or warm absorbers contributes significantly and imprints features on the spectrum. Surprisingly also two of the Seyfert 2s (NGC 3147 and NGC 4698) do not show evidence for absorption above the Galactic. It becomes evident that the complexity of the Seyfert 2 spectrum should be taken into account when constructing models for the synthesis of the X-ray Background.

The compilation of large Seyfert 2 samples as well as the study of obscured AGN at high redshift will shed new light on the X-ray background synthesis models.

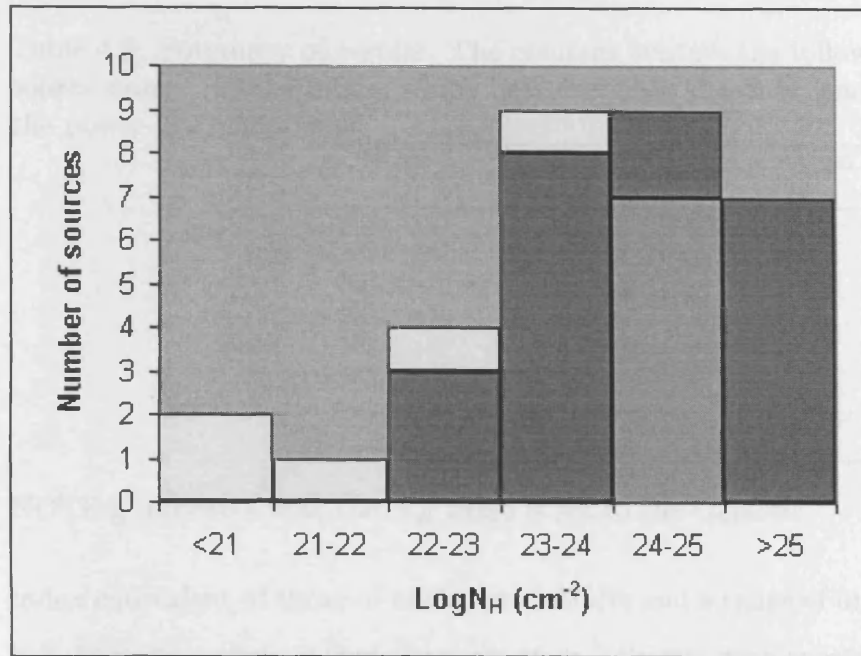


Figure 4.12: The column density distribution of all the Seyfert 2 galaxies from the Risaliti sample. The light grey part in the fifth column includes all the sources for which only a lower limit of 10^{24}cm^{-2} is available. The white part represents the objects presented in this Chapter.

4.6.3 Conclusions

Here a systematic analysis of 8 bona-fide Seyfert 2 galaxies was presented. The uniform analysis showed that in general the Seyfert 2 galaxies included in this sample do not show the nominal Seyfert 2 spectrum presenting a low amount of intrinsic absorption. On the basis of the $[OIII]\lambda 5007$ the Compton thick possibility was ruled out for two of the low absorption objects, namely NGC 3147 and NGC 4698, leaving open questions for the nature of these objects. For NGC 2273, the spectral analysis favours the scattering model, while its $[OIII]\lambda 5007$ flux is too low, and favours the Compton thick interpretation. In the case of M51, where the reflection dominated Compton thick model is not favoured by the data but its $f_{HX}/f_{[OIII]}$ is low, it is suggested that the discrepancy may be explained either with a warm scatter model for the hard X-ray emission or optical or X-ray variability. In Table 4.9 the best-fit model as well as the inferred column density are quoted. Finally, the above results may be important in the study of the X-ray background, since all the current XRB synthesis models utilise a population of objects with an underlying spectral

Table 4.9: Summary of results. The columns contain the following information: (1) The source name; (2) the model which best describes the data; and (3) the column covering the power-law component.

Name (1)	best-fit (2)	$N_H \times 10^{21} \text{cm}^{-2}$ (3)
NGC1167	-	?
NGC1667	-	?
NGC2273	scattering	982^{+196}_{-433}
NGC3079	composite	17^{+93}_{-17}
NGC3147	single power-law	0.36g
NGC3486	-	?
NGC4698	single power-law	$0.81^{+0.82}_{-0.72}$
M51	composite	$0^{+1.6}$

NOTE:g indicates that the N_H value is set to the Galactic.

index equivalent of those of unobscured AGNs and a range of obscuring columns, whereas it is becoming obvious that there are type 2 objects with spectrum quite untypical of the one expected and that the X-ray spectrum is composed by several components, which should be taken into account when constructing such models. Discovery of more Seyfert 2 galaxies with spectra distinct from the 'nominal' Seyfert 2 spectra will show whether these objects contribute significantly to the X-ray background or not, while *XMM-Newton* observations of Seyfert 2 galaxies will allow us to determine the spectral components contributing to the total X-ray spectrum, whereas *Chandra* observations will de-convolve any starburst/extended emission from the Seyfert nucleus.

Chapter 5

What are NGC 4698 and NGC 3147?

The most striking objects of the sample studied in chapter 4 are NGC3147 and NGC4698. They are bona-fide Seyfert 2 galaxies from their optical spectra and yet have negligible X-ray absorption. In this chapter a further analysis of these two objects is presented and the X-ray data are analysed in more detail, aiming to determine the real nature of these objects. Firstly, the X-ray spectrum and the variability of each source is studied and then the results and possible scenarios are discussed.

5.1 NGC 4698

NGC 4698 is classified a Sa galaxy by Sandage & Tammann (1981) and Sab(s) galaxy by de Vaucouleurs et al. (1991) and Ho *et al.* (1997). Sandage & Bedke 1994 presented NGC 4698 as an example of the early-to-intermediate Sa type. They describe the galaxy as characterized by a large central E-like bulge in which there is no evidence of recent star formation or spiral structure. NGC 4698 belongs to the Virgo Cluster. Its total B-band magnitude is $B=11.46$ mag (de Vaucouleurs et al. 1991), which corresponds to $M=-19.69$ mag assuming a distance of 16.8 Mpc (Freedman *et al.* 1994). The nuclear emission lines are quite narrow ($\text{FWHM}\sim 170 \text{ km s}^{-1}$). No trace of broad H_α is visible in the relatively high S/N spectrum presented by Ho *et al.* (1997). (see Figure 5.1). The narrow line H_α luminosity is $4.9\times 10^{38} \text{ erg s}^{-1}$. The $[\text{OIII}]/\text{H}_\beta$ vs $[\text{NII}]/\text{H}_\alpha$ and $[\text{OIII}]/\text{H}_\beta$ vs

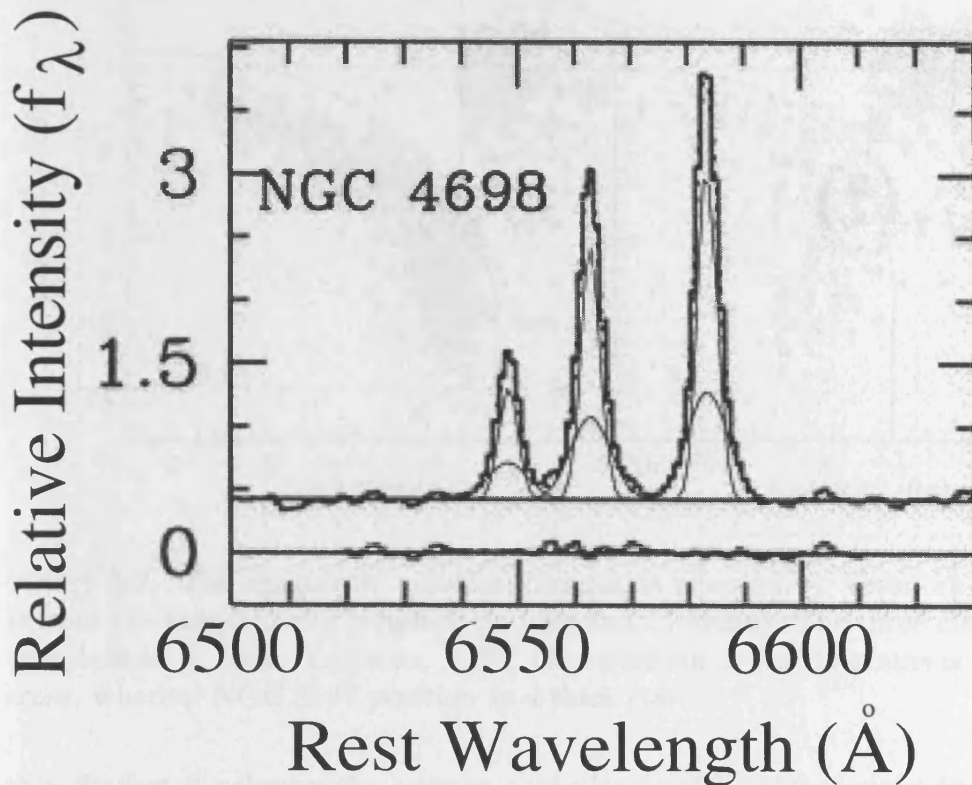


Figure 5.1: Optical spectrum from the nucleus of NGC 4698. No trace of broad H_{α} is visible.

$[O I]/H_{\alpha}$ diagnostic diagrams place NGC 4698 on the borderlines between Liners/Seyferts and HII/Liners respectively (see Figure 5.2).

Details about the X-ray observations and the data reduction method are given in the previous chapter.

5.1.1 The ASCA spectrum

The most striking example from our low absorption Seyfert 2 in Chapter 4, is NGC 4698. The X-ray data do not require absorption and the alternative hypothesis of Compton thickness was ruled out on the basis of the $[O III]\lambda 5007$ flux. Further evidence for the amount of obscuring material can be obtained from the iron line emission. For Compton

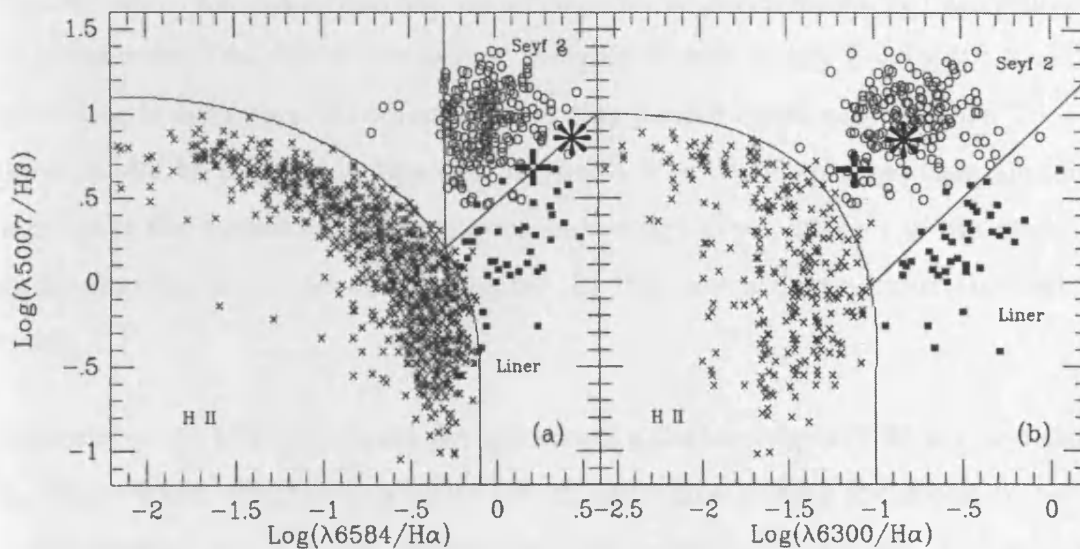


Figure 5.2: The diagnostic emission line ratios adopted by Veron *et al.* (1997) for HII regions (crosses), Liners (squares) and Seyfert 2 (circles). The three classes of objects are well defined in these diagrams. NGC 4698 position in the diagrams is marked as a thick cross, whereas NGC 3147 position as a thick star.

thin Seyfert 2 galaxies the average equivalent width value derived from *ASCA* data, is 360 ± 250 (Gilli *et al.* 1999), whereas for Compton thick objects the equivalent width can be well above 1 keV (e.g for NGC 6240 the iron K_{α} line has an $EW \sim 1.58$ keV). However, we do not obtain a significant detection of line emission but can only set a 90 per cent upper limit to the equivalent width of such a feature of 425 eV. This value is too low for a Compton thick object and in that sense rules out the Compton thick interpretation for this object.

The lack of column density could also be explained by the presence of a dusty warm absorber. The presence of dust accounts for the optical obscuration of the broad line region, whereas the lack of X-ray absorption is due to the ionisation state of the absorber. In such a case cold absorption is no longer required. We note here that when we discuss dusty warm absorber models we should consider that there are two grain destruction mechanisms that must be taken into account. Firstly the sublimation of the grains when they become too hot (~ 2000 K) and secondly, thermal sputtering, which destroys the dust once the gas electron temperature reaches 10^6 K (Draine & Salpeter 1979; Laor &

Draine 1993). Assuming that the warm absorber is photoionised, the gas temperature in a typical warm absorber where oxygen is highly ionised is only $T \sim 5 \times 10^4$ K and thermal sputtering is negligible. If collisional ionisation plays a significant role then $T \sim 10^6$ K and the dust will be destroyed. However, Reynolds *et al.* (1997) showed that photoionisation dominates the ionisation of the plasma unless $r \geq 100$ pc, where r is the distance of the warm absorber from the central engine. In this case a dusty warm absorber model is viable.

Komossa *et al.* (1998) predicted the presence of a Carbon edge at 0.28 keV and showed that the dusty warm absorber smoothes the oxygen edges making it difficult to be detected. Unfortunately *ASCA* is not sensitive enough at these soft energies, and we cannot test an actual dusty warm absorber model to our data. Since in the energies above 0.3 keV both the dusty warm absorber and the warm absorber are expected to imprint similar spectral features in the spectrum and because the X-ray photons above ~ 0.5 keV are not affected by the dust, we fit our data in the energy range 0.5-10 keV with a warm absorber model in order to examine the possibility of the presence of ionised material in the very central region of NGC 4698. Although we obtain a good fit to the data ($\chi^2 = 244.8$ for 265 d.o.f) the ionisation parameter ($\xi = L/n_e R^2$) of the warm material cannot be constrained and we obtain a lower limit of 5000. This clearly demonstrates that the data do not require any absorption. The value of ξ is much higher than the values obtained for the warm absorber in Seyfert 1 galaxies ($\xi \sim 30$ ergs cm sec⁻¹ Reynolds 1997). Figure 5.3 shows the unfolded spectrum for the warm absorber model discussed above. The solid line represents the integrated model. In addition such highly ionised gas should produce the 6.96 keV iron line. However, there is no evidence for such a line in the *ASCA* X-ray spectrum. Thus it is most likely that the warm absorber model is not viable for NGC 4698 and thus it will not be discussed further.

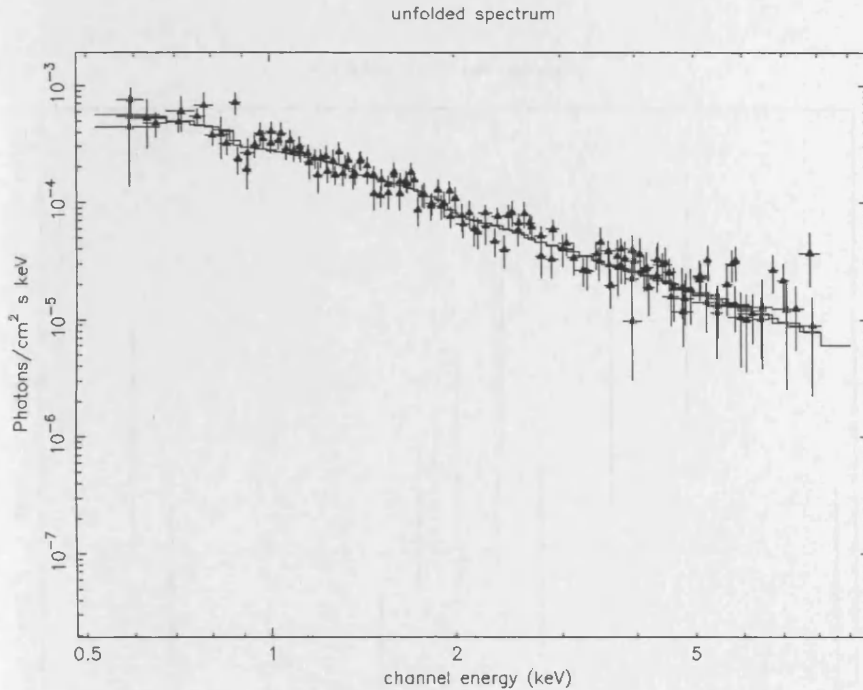


Figure 5.3: The power-law plus warm absorber unfolded spectrum for NGC 4698. The hard component is fitted with a power-law, whereas the soft component is represented by a warm absorbed power-law continuum. The solid line represents the integrated model.

5.1.2 Variability

Further clues on the nature of this galaxy come from looking for short time variability, thus background subtracted light curves in the 2-10 keV and 0.5-2 keV energy bands were constructed. The light-curves were created by accumulating photons in 1000 second bins in order to increase the signal to noise ratio. For the same reason, the GIS2 and GIS3 light curves were merged. The curves are shown in Figure 5.4 and 5.5. Using a χ^2 test to check the non-variability hypothesis, I find reduced χ^2 of 7.56/11 and 17.22/11 in the soft and hard band energy band respectively. The null hypothesis probability is then 0.75 and 0.1. Thus the probabilities are less than 25 and 90 per cent that a fit of a constant is unacceptable. Therefore it seems that because of limited statistics no firm conclusion regarding variability can be derived.

5.1.3 What lies in the heart of NGC 4698?

NGC4698 2-10 keV lightcurve

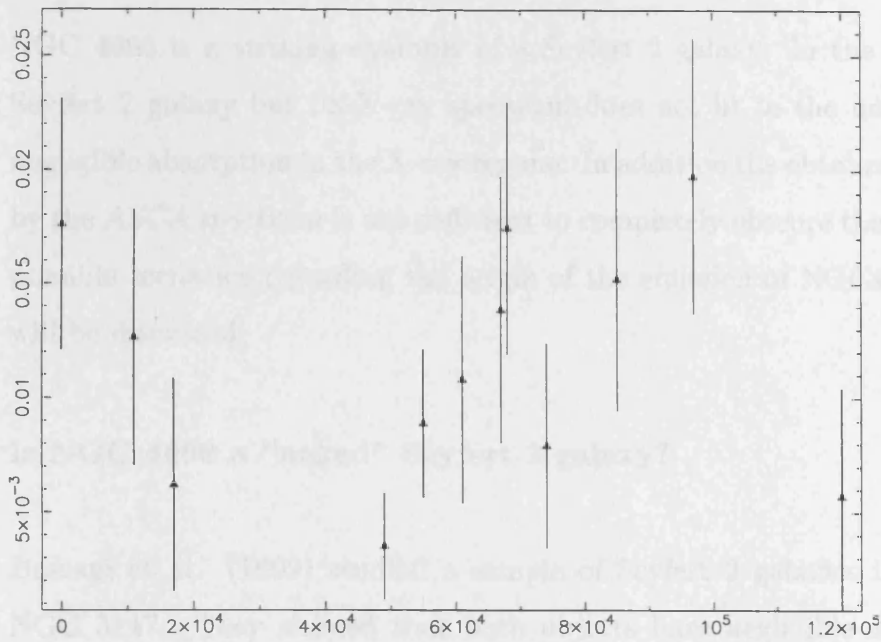


Figure 5.4: The GIS2+GIS3 light curve for NGC 4698 in the 2-10 keV band.

NGC4698 0.5-2 keV lightcurve

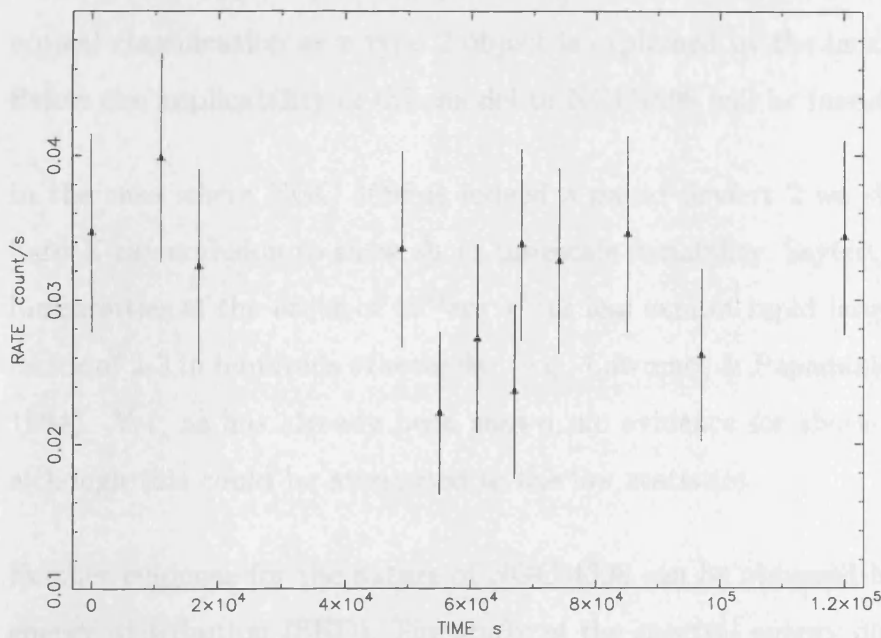


Figure 5.5: The GIS2+GIS3 light curve for NGC 4698 in the 0.5-2 keV.

5.1.3 What lies in the heart of NGC 4698?

NGC 4698 is a striking example of a Seyfert 2 galaxy. In the optical it is classified as Seyfert 2 galaxy but its X-ray spectrum does not fit to the unification model, showing negligible absorption in the X-ray regime. In addition the obtained column density derived by the ASCA spectrum is not sufficient to completely obscure the broad line region. Below possible scenarios regarding the origin of the emission of NGC4698 as well as its nature will be discussed.

Is NGC 4698 a “naked” Seyfert 2 galaxy?

Bassani et al. (1999) studied a sample of Seyfert 2 galaxies including NGC 7590 and NGC 3147. They showed that both objects have negligible absorption in X-rays (see previous/this chapter for NGC 3147), although classified as a Seyfert 2 galaxies. Using the [OIII] $\lambda 5007$ criterion (see chapter 4) the latter authors ruled out the Compton thick possibility for NGC 3147 and NGC 7590 and suggested that these lack a broad line region so that their appearance as Seyfert 2 is intrinsic and not due to absorption. Then the optical classification as a type 2 object is explained by the lack of the broad line region. Below the applicability of this model to NGC4698 will be investigated.

In the case where NGC 4698 is indeed a naked Seyfert 2 we should expect at least the hard X-ray emission to show short timescale variability. Seyfert 1 galaxies with 2-10 keV luminosities of the order of 10^{42} erg s⁻¹ or less exhibit rapid large amplitude variability, a factor of 2-3 in hundreds of seconds. (e.g., Lawrence & Papadakis 1993; Nandra & Pounds 1994). Yet, as has already been shown, no evidence for short-time variability is found, although this could be attributed to the low statistics.

Further evidence for the nature of NGC 4698 can be obtained by studying their spectral energy distribution (SED). The study of the spectral energy distribution of the galaxies is useful in studying the energy output at different wavebands. For Seyfert 2 galaxies the torus suppresses the UV and optical emission from our line of sight and reradiates

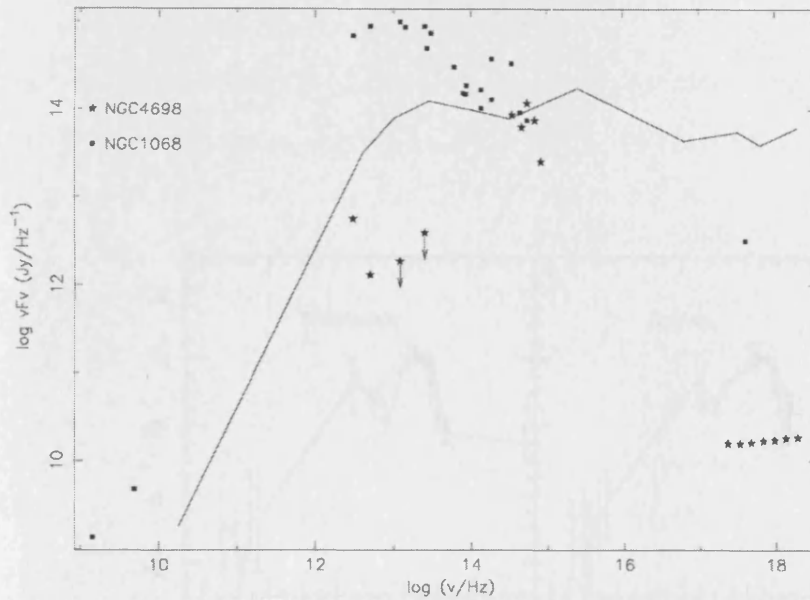


Figure 5.6: The NGC 4698 spectral energy distribution (stars). The fluxes are taken from NED. Where there are multiple observations, data obtained using the smallest aperture were used. Specifically, V band magnitude 11.39(64.9" aperture), I band magnitude 10.54 (36" aperture) and H band (51.8" aperture). For comparison the NGC 1068 SED (dots) as well as the mean QSO SED (line) from Elvis *et al.* (1994) are shown.

it in the far infrared. Thus the far infrared emission dominates the SED. On the other hand in the case of broad line AGNs (quasars and Seyfert 1s) the far infrared flux is comparable to the optical and X-ray fluxes. The NGC 4698 SED (Figure 5.6) reveals an unexpected continuum emission distribution by showing a deficit in flux in the far infrared band such that the optical emission dominates the total output. This implies that there is not dusty material to produce thermalised photons and consequently no production of far infrared radiation. This intriguing result gives support to the the scenario where neither an obscuring medium nor a broad line region are required. For comparison Figure 5.6 shows the SED for the Compton thick galaxy NGC 1068, as well as the mean radio-quiet QSO SED from Elvis *et al.* (1994). Figure 5.7 shows the average SEDs of different classes of galaxies. The difference in the shape of the Seyfert 2 SED compared to NGC 4698 is clear with the emission showing a peak at the far-infrared wavelengths due to the presence of cold dust in the obscuring medium.

Although the naked Seyfert 2 scenario explains the properties of NGC 4698 very well, it

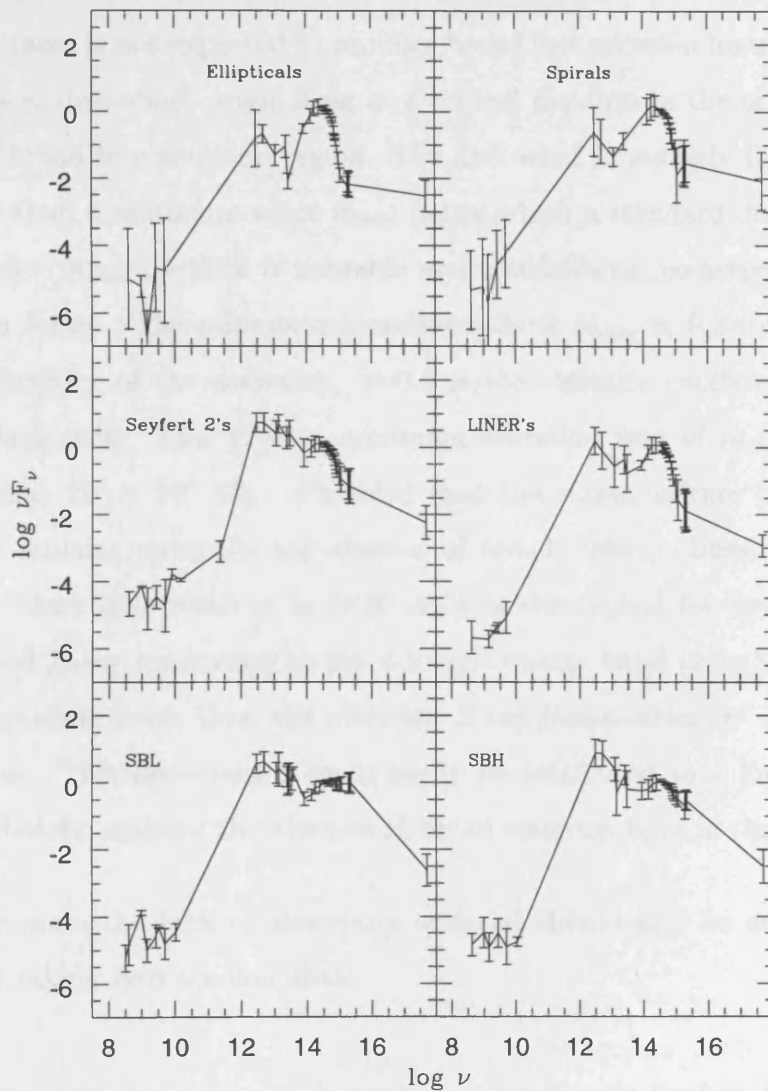


Figure 5.7: Plot of the average SEDs. The error bars are standard deviation of the average. Taken from Schmitt *et al.* 1997.

provides just a phenomenological description. But why does NGC 4698 lack the broad line region and the torus? And in addition can the properties of such objects be explained in the context of the unified models? Below these three points will be discussed.

Recently, Nicastro (2000) presented a model in which a standard accretion disk accreting at low rates is not expected to produce broad line emission lines. According to this model a vertical disk wind, originating at a critical distance in the accretion disk, is the origin of the broad line emission region. The disk wind forms only for external accretion rates higher than a minimum value \dot{m}_{min} below which a standard disk is stable. For accretion rates $\dot{m} > \dot{m}_{min}$ the disk is unstable and a stabilising, co-accreting “disk/corona+wind” system forms. The minimum accretion rate is $\dot{m}_{min} \simeq 0.3n(am)^{-1.8}$, where $n=0.06$ is the efficiency of the accretion, $a=0.1$ is the viscosity coefficient and m is the mass of the black hole. This gives a minimum accretion rate of $\dot{m}_{min} \sim (1-4) \times 10^{-3}$ for m in the range $10^6 - 10^9 M_{\odot}$. Provided that the accretion rate in NGC 4698 is low, this model explains naturally the absence of broad emission lines. Assuming that the mass of the black hole residing in NGC 4698 is the typical for Seyfert galaxies $10^7 M_{\odot}$, the observed X-ray luminosity in the 2-10 keV energy band (2.2×10^{40} erg s⁻¹) is ~ 3 orders of magnitude lower than the observed X-ray luminosities ($\sim 10^{43}$ erg s⁻¹) in Seyfert 1 galaxies. This discrepancy could easily be attributed to a lower accretion rate, which immediately explains the absence of broad emission lines in the spectrum of NGC 4698.

Furthermore the lack of absorbing material should also be explained. Recently, Matt (2000) taking into account that:

- there is, on average enhanced starformation in Seyfert 2 galaxies with respect to Seyfert 1s (Maiolino *et al.* 1997)
- The average morphologies between galaxies hosting type 1 and 2 nuclei are different, those hosting type 2 being on average more irregular (Maiolino *et al.* 1997, Malkan *et al.* 1998)
- there is a greater overall dust content in Seyfert 2s (Malkan *et al.* 1998)

pointed out that there must be a greater chance of producing a torus in Seyfert 2s than it is in Seyfert 1s. Thus he suggested that not all Seyfert 1 galaxies have a torus. The above explains the absence of a torus in the context of the unified models and NGC 4698 would fit very well in the above hypothesis provided that the BLR is absent as well. No examples of Seyfert 1 galaxies with no torus have been discovered so far, probably because it is impossible to discriminate between the two types of Seyfert 1s by the spectrum alone. Multiwavelength observations are required in order to check whether the model by Matt (1999) is viable.

The naked Seyfert 2 model explains well the discrepancy between the optical and X-ray spectrum and it does not violate the unification models.

Re-awakening of an AGN

Recently a few examples of dying AGNs have been presented in the literature (Weaver *et al.* 1996 for NGC 2992; Bassani *et al.* 1999 for NGC 1808; chapter 4 for NGC 1667). For these sources a systematic decrease in the 2-10 keV luminosity has been reported over the last 20 years. Particularly in the case of NGC 2992, Weaver *et al.* (1996) has observed a decrease of a factor of ~ 16 in the 2-10 keV luminosity, whereas the iron line flux decreased only by a factor of 2-3 and the reflection component became 5 times stronger. The authors explained the differences in the flux changes as a lag between reprocessed and intrinsic fluxes and located the reprocessor at the torus. In addition, a *BeppoSAX* observation of NGC 4051 in 1998 showed that its luminosity in the 2-10 keV band was about 20 times fainter than in past observations (Guainazzi *et al.* 1998). The authors explained the flat spectrum ($\Gamma=0.8$) and strong iron line ($EW=600$ eV) as the residual reflection component from an AGN, which has switched off. Since then, the source has become active once more (Uttley *et al.* 1999).

NGC 4698 could be a further example of an AGN which has switched off and then on again. The NGC 4698 optical spectrum was obtained on the 25/2/1985, whereas the X-ray spectrum was obtained on the 16-17/6/1999. According to this interpretation, the

AGN was switched off during the optical observation, however this had not been reflected in the narrow line region at the time. Thus the spectra do not show broad but only narrow emission lines. By the time of the X-ray observation the nucleus was switched on again, and thus the X-ray spectrum resembles the unabsorbed Seyfert 1 spectra. Although there are only a few examples of AGNs which have switched off and only one of an AGN which switched on again and although it is not known what makes a “fossil” AGN to become active again, this scenario is attractive and explains adequately the optical and X-ray spectra of NGC 4698. However it does not account for the “odd” NGC 4698 SED. To check this scenario new optical observations are required.

The super-luminous source scenario

A careful look at Figure 5.7 reveals that the NGC4698 SED resembles the SED of normal galaxies. Could NGC 4698 be a normal galaxy instead of an AGN? But then what produces the X-ray emission? The existence of super-luminous X-ray sources could provide a reasonable explanation for the X-ray emission.

Einstein imaging observations first revealed that the X-ray emission from several spiral galaxies is dominated by a small number of luminous ($L_x \sim 10^{38} - 10^{40} \text{ erg s}^{-1}$) X-ray sources outside the central region of the galaxy (Fabbiano 1989). These sources appear to have luminosities factors of 10 to 100 times the Eddington luminosity for a neutron star. Recently *ROSAT* and *ASCA* observations (Lira *et al.* 2000, Roberts *et al.* 2000) have confirmed this for many nearby galaxies. The nature of these sources is still unknown but candidates for explaining this phenomenon include supernova remnants, accretion onto a compact object, unresolved complexes of X-ray sources or even a new “exotic” class of objects. Recently Kaaret *et al.* (2000) presented *Chandra* HRC observations of the starburst galaxy M82. For the most luminous X-ray source detected, dynamical arguments place an upper limit of the mass of this object of $1.3 \times 10^6 M_\odot$, whereas the X-ray luminosity places a lower limit to the mass of $500 M_\odot$. The low X-ray luminosity of NGC 4698 could easily be produced by such an X-ray luminous source. In this case,

NGC 4698 is not required to contain the typical $10^6 M_{\odot}$ super massive black hole thought to power an AGN, but may instead be a normal galaxy which contains a super-luminous X-ray source. Under this scenario NGC 4698 is expected to be highly variable.

This model accounts for the normal galaxy like SED, with the super luminous X-ray source justifying the X-ray emission.

The starburst scenario

Given that the $[\text{OIII}]/\text{H}_{\beta}$ vs $[\text{OI}]/\text{H}_{\alpha}$ diagnostic diagram places NGC 4698 on the borderlines between HII/Liners, and its low X-ray luminosity, it was also examined whether the bulk of the X-ray emission is produced by starburst activity.

To examine the applicability of the starburst model to NGC 4698, the expected starburst contribution in the 0.5-4.5 keV energy band was estimated using equations 4.1 and 4.2. The maximum expected contribution from stars is then $L_x \sim 1.4 \times 10^{39} \text{ erg s}^{-1}$, whereas the absorption corrected luminosity in the same band is $\sim 3 \times 10^{40} \text{ erg s}^{-1}$. This clearly shows that stars do not contribute more than 5 per cent to the 0.5-4.5 keV luminosity and that another component, probably an AGN, contributes significantly to the NGC 4698 luminosity.

5.2 NGC 3147

NGC 3147 is at a distance of 56 Mpc (assuming $H_0=50 \text{ km sec}^{-1} \text{ Mpc}^{-1}$) and is almost face-on. The H_{α} luminosity is $2.9 \times 10^{39} \text{ erg s}^{-1}$. The $[\text{OIII}]/\text{H}_{\alpha}$ vs $[\text{NII}]/\text{H}_{\beta}$ diagnostic diagram places NGC3147 on the borderline between Liners/Seyferts, while the $[\text{OIII}]/\text{H}_{\beta}$ vs $[\text{OI}]/\text{H}_{\alpha}$ diagram places it on the Seyfert 2 region (see Figure 5.2).

5.2.1 The ASCA spectrum

This is another example of a Seyfert 2 galaxy, which shows no evidence for absorption above the Galactic. As in the case of NGC 4698, the Compton thickness for NGC 3147 was ruled out on the basis of the $[OIII]\lambda 5007$ flux. To investigate the spectrum of NGC3147 further, a warm absorber model to represent the soft emission is utilised, as in NGC 4698. Again the ionisation parameter ξ cannot be constrained and I obtain a lower limit of 5000 ($\chi^2=316.1$ for 295 dof). In figure 5.8, the unfolded spectrum of NGC 3147 is shown. The solid line represents the integrated model. It becomes clear from the figure that the warm absorber plus power-law model is equivalent to the single power-law model, indicating that the data do not require extra absorption.

5.2.2 Variability

Then light curves in the 0.5-2 keV and 2-10 keV energy bands were constructed. The light curves were created by accumulating photons in 800 seconds bins in order to increase the signal to noise ratio. Since the source counts fall across chip boundaries and gaps in SIS, no SIS data are used. In Figures 5.9 and 5.10 the GIS2+GIS3 light-curves in the 2-10 keV and 0.5-2 keV energy bands respectively are shown. Using a χ^2 test to check the non-variability hypothesis, I find reduced χ^2 of 10.3/14 and 35.6/14 for the hard and soft bands respectively. The null hypothesis probability is then 0.61 and 1.19×10^{-3} . Thus, in the soft band short X-ray variability is clearly detected, whereas there is no evidence for variability in the hard energy band.

5.2.3 What is NGC 3147?

NGC3147 is another example of an optically classified Seyfert 2 galaxy with no X-ray absorption. In Figure 5.11 the NGC 3147 SED was compiled using the published multi-wavelength data on NGC 3147. This SED resembles the SED of Seyfert 2 galaxies (see Figure 5.7).

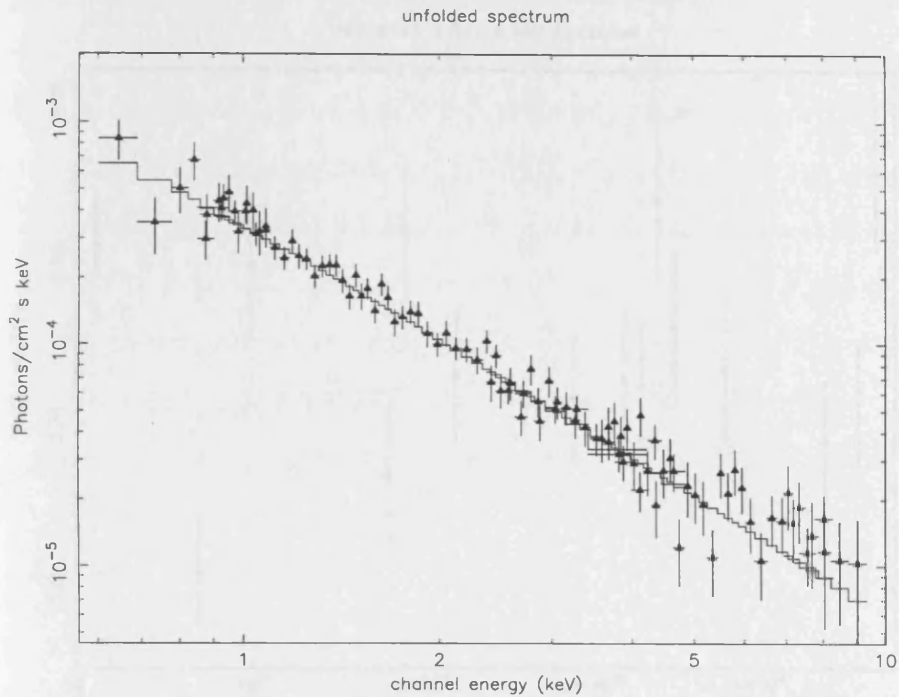


Figure 5.8: The power-law plus warm absorber unfolded spectrum for NGC 3147. The hard component is fitted with a power-law, whereas the soft component is represented by a warm absorbed power-law continuum. The solid line represents the integrated model.

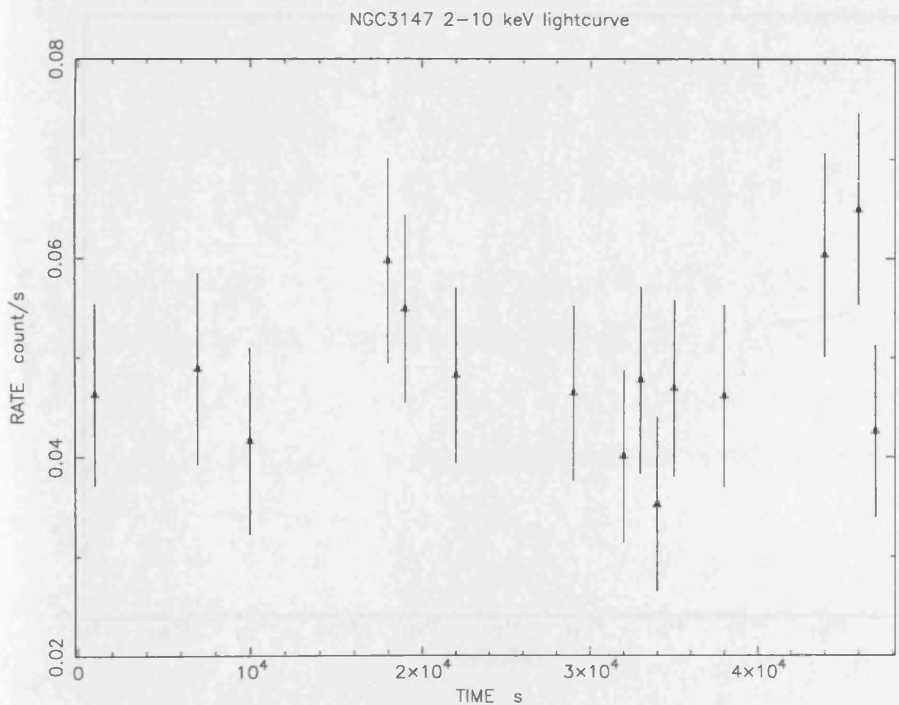


Figure 5.9: The GIS2+GIS3 light curve for NGC 3147 in the 2-10 keV band.

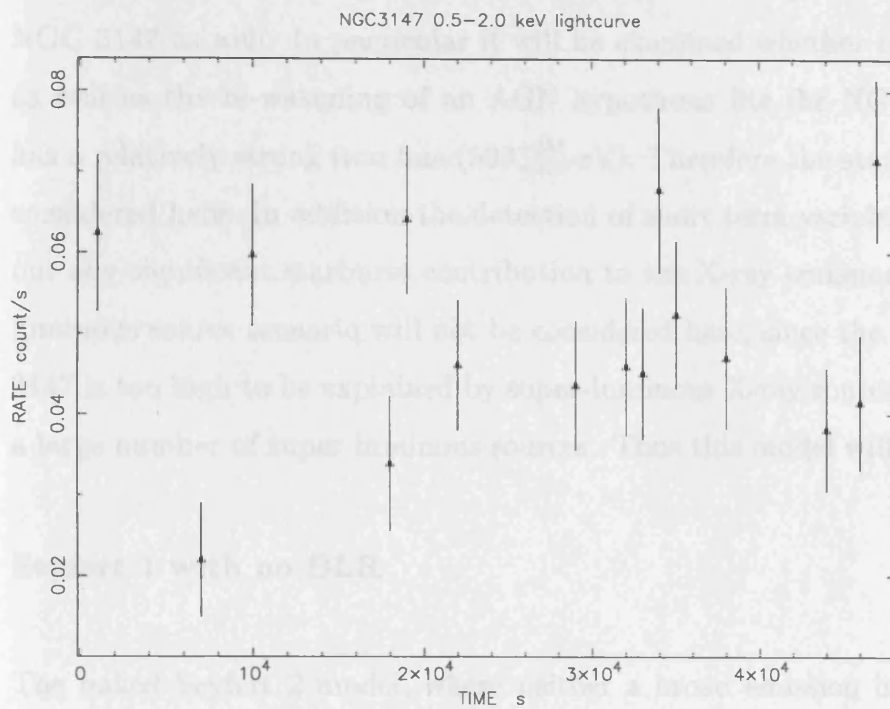


Figure 5.10: The GIS2+GIS3 light curve for NGC 3147 in the 0.5-2 keV.

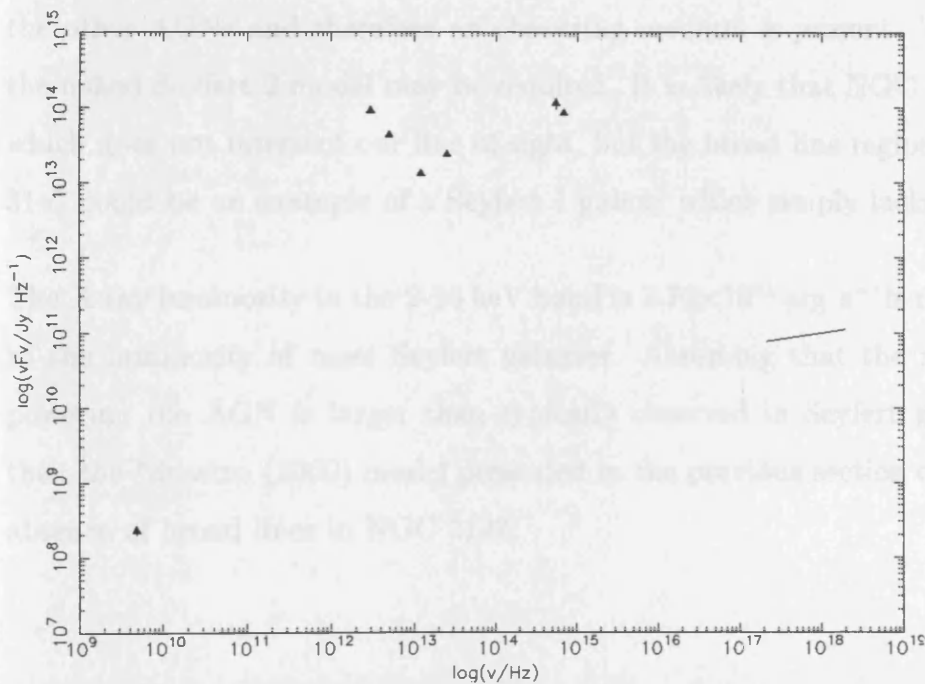


Figure 5.11: The NGC 3147 spectral energy distribution.

Below I will examine whether the models proposed to explain the NGC 4698 can apply to NGC 3147 as well. In particular it will be examined whether the naked Seyfert 2 model as well as the re-wakening of an AGN hypothesis fits the NGC 3147 data. NGC 3147 has a relatively strong iron line (593_{-223}^{+288} eV). Therefore the starburst scenario will not be considered here. In addition the detection of short term variability in the soft band rules out any significant starburst contribution to the X-ray emission in this band. The super luminous source scenario will not be considered here, since the X-ray luminosity of NGC 3147 is too high to be explained by super-luminous X-ray sources, unless the galaxy hosts a large number of super luminous sources. Thus this model will not be discussed further.

Seyfert 1 with no BLR

The naked Seyfert 2 model, where neither a broad emission line region nor a torus are required, could explain the discrepancy between the optical and the X-ray spectra, as in the case of NGC 4698. However the SED (see Figure 5.12) does not show evidence for dust deficiency. This may indicate that the dust content of NGC 3147 is comparable to the other AGNs and therefore an obscuring medium is present. Thus a modification of the naked Seyfert 2 model may be required. It is likely that NGC 3147 possesses a torus, which does not intersect our line of sight, but the broad line region is absent. Thus NGC 3147 could be an example of a Seyfert 1 galaxy which simply lacks a broad line region.

The X-ray luminosity in the 2-10 keV band is 2.76×10^{41} erg s^{-1} ; is relatively low compared to the luminosity of most Seyfert galaxies. Assuming that the mass of the black hole powering the AGN is larger than typically observed in Seyfert galaxies (i.e. $> 10^6 M_{\odot}$) then the Nicastro (2000) model presented in the previous section could again explain the absence of broad lines in NGC 3147.

Re-awakening of an AGN

The scenario where NGC 3147 switched off before the optical observation but the change has not been reflected to the narrow line region during the observation and thus the spectrum exhibits narrow lines only and later switched on again, could explain the discrepancy between the optical and X-ray spectra. The NGC3147 optical spectrum was obtained on the 23/2/1986, whereas the *ASCA* X-ray spectrum was obtained on 29-30/9/1993. It is therefore possible that between the two observations NGC 3147 became active again for some reason. Again new optical observations are required to check the validity of this hypothesis.

5.3 Conclusions

In this chapter the nature of NGC 4698 and NGC 3147 was investigated. Both galaxies although classified as Seyfert 2s have no absorption above the Galactic in X-rays. The lack of column density could be explained by the presence of a dusty warm absorber. The presence of dust accounts for the optical obscuration of the broad line region, whereas the lack of X-ray absorption is due to the ionisation state of the absorber. However it was shown that the dusty warm absorber model is not a viable model to explain the NGC 4698 and NGC 3147 data.

The NGC 4698 SED differs from the typical Seyfert 2 SED, in that it shows a deficit in the far-infrared emission relative to the optical and resembles more the SED of normal elliptical and spiral galaxies. The multiwavelength properties of NGC 4698 fit well to the 'naked' Seyfert 2 model, where the galaxy lacks a broad line region so that its appearance as a Seyfert 2 is intrinsic and not due to absorption. Then the presence of narrow emission lines only in the optical spectrum of NGC 4698, can be attributed to the lack of the broad line region. Alternatively, NGC 4698 may not contain the typical $10^6 M_{\odot}$ supermassive black hole thought to power an AGN but may instead be a normal galaxy, which contains a super luminous X-ray source as recently seen in several galaxies. This scenario is

supported by the low luminosity emission lines, low X-ray luminosity, and the SED which resembles the SED of normal galaxies. Finally an AGN which was turned off during the optical observation but turned on again before the X-ray observation could account for the observed discrepancy between the optical and X-ray spectra.

Likewise, NGC 3147 could be explained with the 'naked' Seyfert 2 model although the SED argues against it by demonstrating that the NGC 3147 dust content is similar to the other Seyfert 2 galaxies. Thus the hypothesis where NGC 3147 is a Seyfert 1 galaxy which simply lacks the broad line region is more plausible. Alternatively, the optical and X-ray spectra could be explained by the 're-awakening of an AGN' hypothesis.

Unfortunately the current data do not allow us to derive firm conclusions regarding the nature of these two objects. Further observations with *Chandra* may resolve the X-ray emitting region in NGC 4698 and we will be able to confirm whether the emission is due to a super luminous X-ray source and *XMM-Newton* will provide high quality spectra and we will be able to detect the iron line if present. In addition observations with *XMM-Newton* will determine whether there is any short term variability.

Chapter 6

X-ray observations of the Ultraluminous Infrared Galaxy IRAS19254-7245 (The Superantennae)

This chapter describes in detail the data analysis and interpretation of the X-ray properties of the remarkable Ultraluminous Infrared Galaxy (ULIRG) IRAS19254-7245.

6.1 IRAS19254-7245

6.1.1 An overview of ULIRGs

The IRAS Ultraluminous Infrared Galaxies (ULIRGs), $L_{IR} \geq 10^{12}L_{\odot}$, are among the most luminous objects in the Universe. ULIRGs emit most of their energy in the far-infrared (see Sanders & Mirabel 1996 for a recent review). The nature of this powerful emission has been hotly debated. The far-IR emission is clearly produced by thermal reradiation by dust. However, it remains unclear whether the heating of the dust is due to a hidden AGN and/or massive star-forming regions. Optical and near imaging surveys (eg Duc, Mirabel & Maza 1997) show that most ULIRGs are close interacting or merging systems. Optical spectroscopic surveys show that a large fraction (about 30 per cent) of ULIRGs

are associated with Seyfert nuclei (Kim 1995, Duc et al. 1997 Sanders et al. 1998). The rest appear to host either starforming or LINER nuclei. Lutz *et al.* (1999) have reached similar conclusions using far-IR spectroscopy from the ISO mission.

ULIRGs in X-rays

ULIRGs have been observed with both the *ROSAT* HRI and PSPC at soft X-ray energies. Some have not been detected, indicating that the sources are obscured by column densities $N_H > 10^{23} \text{cm}^{-2}$ (ie Wilman *et al.* 1998). The rest show a composite spectrum with a thermal component attributed to superwind outflow from a starburst and a power-law thought to originate from a Seyfert nucleus (ie Schultz *et al.* 1998 for NGC6240).

In addition a handful of ULIRGs have been observed with *ASCA* and *BeppoSAX* at hard energies: IRAS09104+4109 (Fabian *et al.* 1994), IRAS15307+3252, IRAS 20460+1925 (Ogasaka et al. 1997), IRAS 23060+0505 (Brandt et al. 1997), NGC6240, Arp220, Mrk 273, and Mrk231 (Iwasawa & Comastri 1998), NGC4945 (Guainazzi *et al.* 2000). All have been detected apart from IRAS15307+3252. Most of the above ULIRGs present high 2-10 keV luminosities $L_x > 10^{42} \text{erg s}^{-1}$ clearly suggesting the presence of a buried AGN. These high X-ray luminosity objects have power-law spectra absorbed by large neutral hydrogen columns, typically $N_H > 10^{22} \text{cm}^{-2}$; their spectra also show evidence for an Fe-K line at 6.4 keV which again suggests the presence of large amounts of neutral matter near the nucleus. However, the origin of the X-ray emission in Arp 220 and Mrk231 appears to be thermal (Iwasawa & Comastri 1998).

Motivation

Although the ULIRGs are a rare phenomenon in the local universe ($z < 0.1$) they are excellent laboratories in which the physics and the phenomenon of the galaxy formation as well as the AGN phenomenon can be studied. Moreover, in conjunction with the fact that in the high redshift universe the ULIRG phenomenon seems to be frequent, it is a fair

question to ask whether the ULIRG phase is a stage of the formation of galaxies and/or AGNs.

The X-ray observations of the ULIRGs by remaining largely unaffected by absorption, are vital in checking for the presence of an AGN in the nuclei of the ULIRG. This is important in order to comprehend the nature of these objects and trace their “formation” as well as understand why there are ULIRGs with an AGN and ULIRGs without one. In addition because ULIRGs are associated with the XRB. ULIRGs which have an AGN like spectrum may be associated with the long sought population of type 2 QSOs -QSOs with a Seyfert 2 type spectrum but bolometric luminosities comparable with those of QSOs- which are believed to produce the bulk of the cosmic XRB (see chapter 1). Furthermore, Gilli *et al.* (1999) showed that a rapidly evolving population of hard X-ray sources is required up to $z \sim 1.5$ to explain the XRB. So in this context the local ULIRGs and SCUBA sources are candidates to host a population of highly obscured AGNs.

6.1.2 IRAS19254-7245 (The Superantennae)

The Superantennae ($L_{IR} = 1.1 \times 10^{12} L_{\odot}$) is a remarkable ULIRG with a redshift of $z = 0.0617$ (Mirabel, Lutz & Maza 1991). The global properties of the Superantennae are given in Table 6.1. It presents giant tails extending to an unprecedented size of 350 kpc. These emanate from a merger of two giant gas-rich galaxies whose nuclei are now separated by 10 kpc. The southern nucleus is heavily obscured ($A_V \sim 4 - 5$) and the optical observations give a Seyfert 2 classification (Mirabel et al. 1991). The fluxes of some prominent optical emission lines are given in Table 6.2. Mid-infrared spectroscopy (Lutz, Veilleux & Genzel 1999) of the Superantennae again suggest an AGN classification.

Figures 6.1 and 6.2 show the optical spectrum of the southern and northern nucleus respectively. The spectrum of the southern optical nucleus shows that all emission lines are formed by several different components. This phenomenon is particularly clear in the strong $[OIII]\lambda 5007$ line as well as in the H_{β} and $[OI]\lambda 6300$ (Figure 6.3). This has been

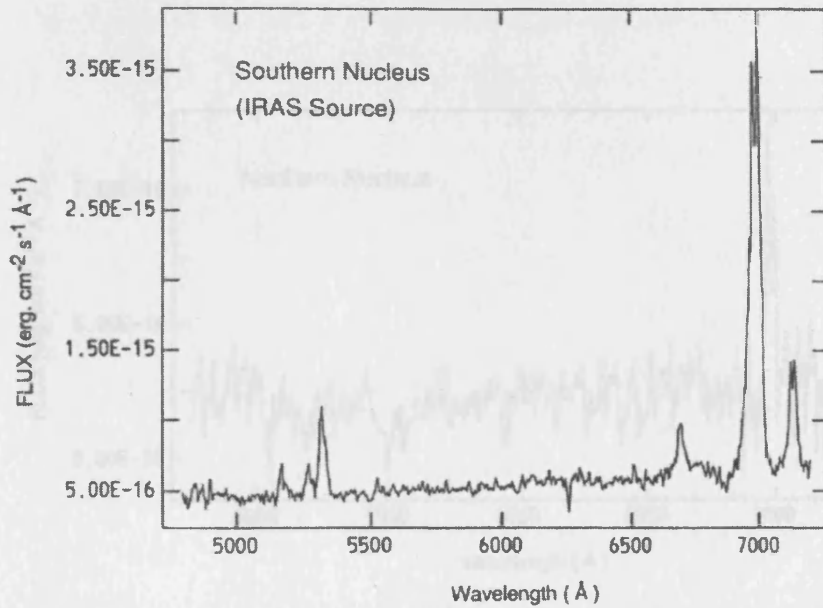


Figure 6.1: Optical spectrum through a 3" x 6" aperture of the southern nucleus of IRAS 19254-7245. This nucleus corresponds in position to the IRAS emission peak and shows a characteristic Seyfert 2 type spectrum. (Taken from Colina *et al.* 1991)

interpreted by Colina *et al.* (1991) as a biconical outflow generated in a massive burst of star formation.

Melnick and Mirabel (1990) reported the presence of a huge amount of molecular gas $M_{CO} = 3 \times 10^{10} M_{\odot}$, 10 times larger than in our galaxy. The mass of the ionised gas in the emission-line regions is $M_g = 1.1 \times 10^8 M_{\odot}$ (Colina *et al.* 1991). The latter authors find that the starburst produces too few high energy photons to explain the observed line intensities and thus infer that the Superantennae must contain a luminous $> 10^{45} \text{erg s}^{-1}$ AGN.

Despite the classification of the southern galaxy as a Seyfert-2 on the basis of optical and far-IR spectra, spectropolarimetric observations of the Superantennae (Heisler *et al.* 1997), revealed no scattered broad line component. The authors attributed this to geometric effects. According to their model the scattering particles, which produce the observed polarised lines, must lie very close to or within the plane of the torus (see also Miller & Goodrich 1990) so that if we see the galaxy edge-on, we can't see the polarised

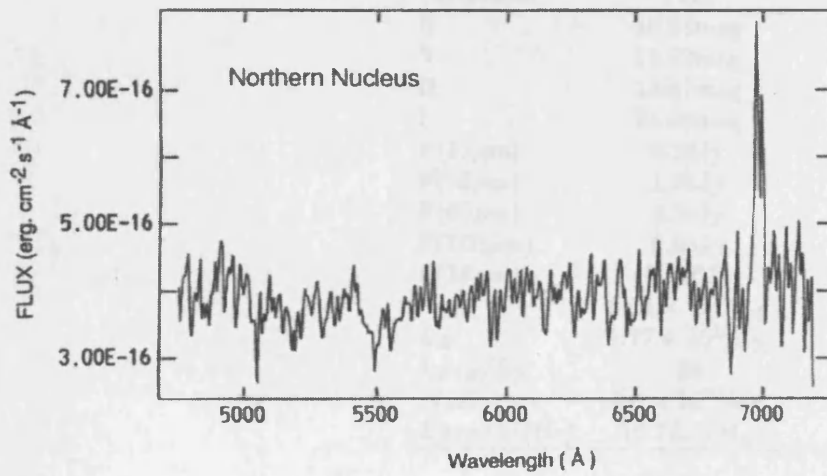


Figure 6.2: Optical spectrum of the northern nucleus using the same aperture as in Figure 6.1. Only H_{α} and $[N_{II}]$ are detected in emission. (Taken from Colina *et al.* 1991)

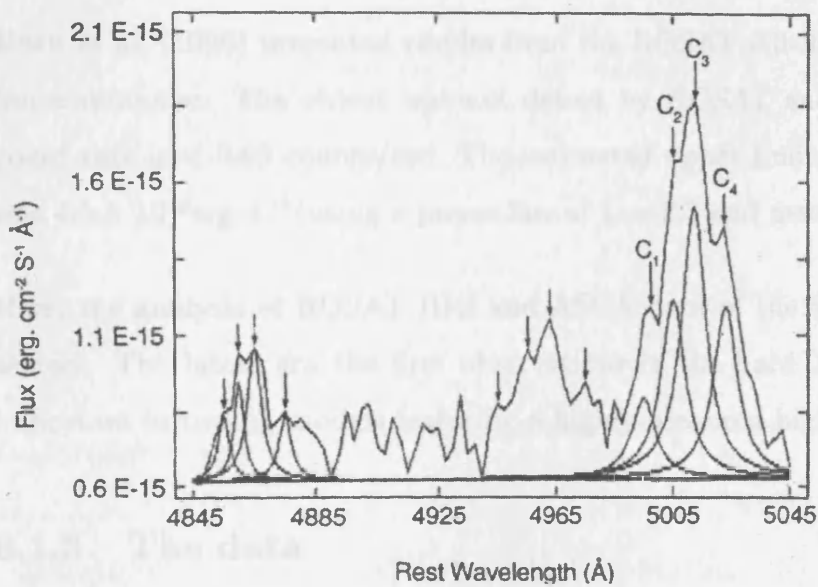


Figure 6.3: H_{β} and $[OIII]4959,5007 \text{ \AA}$ emission line profiles showing four independent kinematical components. They are explained in terms of a biconical outflow model. (Taken from Colina *et al.* 1991)

Table 6.1: Global properties of the Superantennae. Reproduced from Mirabel *et al.* (1991).

Parameter	Flux
B	16.21mag
V	15.22mag
R	14.57mag
I	13.90mag
F(12 μ m)	0.22Jy
F(25 μ m)	1.33Jy
F(60 μ m)	5.39Jy
F(100 μ m)	6.95Jy
F(18 μ m)	0.016Jy
L_{FIR}	$5.02 \times 10^{11} L_{\odot}$
L_B	$1.77 \times 10^{10} L_{\odot}$
L_{FIR}/L_B	28
$M(H_2)$	$3.0 \times 10^{10} M_{\odot}$
$L_{FIR}/M(H_2)$	$16.7 L_{\odot}/M_{\odot}$

flux. At near-IR wavelengths the Seyfert nucleus dominates the emission; at 10 μ m it is more than 5 times brighter than the northern component (Sanders & Mirabel 1996) and it is likely to be the source of the far-infrared emission detected by IRAS (Mirabel *et al.* 1991).

Rush *et al.* (1996) presented results from the ROSAT All-Sky Survey observation of the Superantennae. The object was not detected by ROSAT and the 2σ upper limit on the count rate is < 0.03 counts/sec. The estimated upper limit on the 0.1-2 keV luminosity was 4.5×10^{42} erg s $^{-1}$ (using a power-law of $\Gamma = 2.3$ and assuming Galactic absorption).

Here, the analysis of ROSAT HRI and ASCA data of the Superantennae galaxy is presented. The latter are the first observations in the hard X-ray band and as such are important in testing models featuring a highly-obscured high luminosity nucleus.

6.1.3 The data

The Superantennae were observed with ASCA (Tanaka *et al.* 1994) on 16/10/96. The net exposure time for each GIS is $\sim 30 \times 10^3$ sec, while the SIS0 net exposure time is $\sim 22 \times 10^3$ sec and the SIS1 is $\sim 10 \times 10^3$ sec. We have used the ‘‘Revision 2’’

Table 6.2: Measured emission-line flux. Reproduced from Colina *et al.* (1991).

Line	Flux ^a
H_{β}	7.1
[OIII]5007	33.8
[OI]6300	25.4
[NII]6548	40.1
H_{α}	92.1
[NII]6584	122.0
[SII]6717	20.1
[SII]6731	22.3

^aFlux is given in units of 10^{-15} erg cm⁻² s⁻¹ without internal reddening correction.

processed data from the Goddard Space Flight Center (GSFC). A circular extraction cell for the source of 3 arcminute radius has been used. Background counts were estimated from source-free annuli centred on the source cell. The observed flux in the 2-10keV band is $f_{2-10keV} \simeq 2.4 \times 10^{-13}$ erg cm⁻² s⁻¹ while the flux in the 0.5-2 keV band is $f_{0.5-2keV} = 5.6 \times 10^{-14}$ erg cm⁻² s⁻¹.

ROSAT (Trumper 1984) observed the Superantennae with the High Resolution Imager (HRI) for $\sim 8 \times 10^3$ sec between 17/04 and 20/04/93. There were no X-rays detected and the 3σ upper limit to emission from a point source obtained in the 0.5-2keV band is 3.2×10^{-3} counts/sec, which corresponds to a flux of $f_{1-2keV} = 9.4 \times 10^{-14}$ erg cm⁻² s⁻¹ assuming the spectral model adopted in section 1.1.4. This does not conflict with the ASCA observation as it is above the flux obtained with ASCA.

6.1.4 Spectral analysis

I first performed spectral fitting, allowing the normalisation for each ASCA detector to vary and I obtained reasonably consistent results. I have therefore jointly fitted the spectra from all four detectors, tying their normalisations together. The results of the spectral fits are given in Table 6.3. Entries with no associated uncertainties were fixed at this value during the spectral fit.

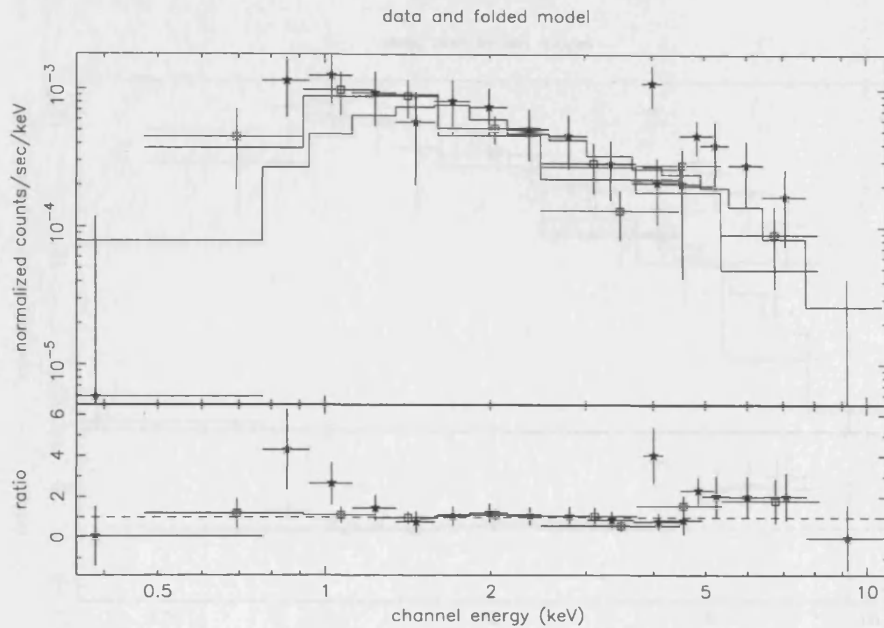


Figure 6.4: The single power-law model with the spectral index as a free parameter. The top panel shows the data with the model and the bottom panel shows the data/model ratio. Data from the two GIS and two SIS have been combined for clarity. The stars represent the GIS data points and open squares the SIS points.

Obscured AGN Models

Given that the optical and mid-infrared observations of the Superantennae suggest an AGN classification I fit the GIS and SIS data with a single power law model with absorption. I obtain a flat slope of 1.0 ± 0.35 with no requirement for absorption above the Galactic. This model together with the data points and the data to model ratio are plotted in Figure 6.4. Data from the two GIS and two SIS have been combined for clarity.

This slope is normally much flatter than is seen in radio quiet AGN and the low absorption is not consistent with the A_V estimates from the narrow lines or the absence of broad line emission. A hard continuum is, however, often seen in Seyfert 2 galaxies (e.g. Georgantopoulos *et al.* 1999 for Markarian 3). When I fix the slope at the 1.9 value, which is typical of the underlying continuum of Seyfert galaxies, I obtain an unacceptable fit with $\chi^2 = 54.31$ for 36 degrees of freedom (dof) and I find that there is a significant “hard tail” towards higher energies (Figure 6.5). In addition there is evidence for an upturn at the soft X-ray energies. By letting the absorption vary the fit is improved ($\chi^2 = 48.5$, for 35

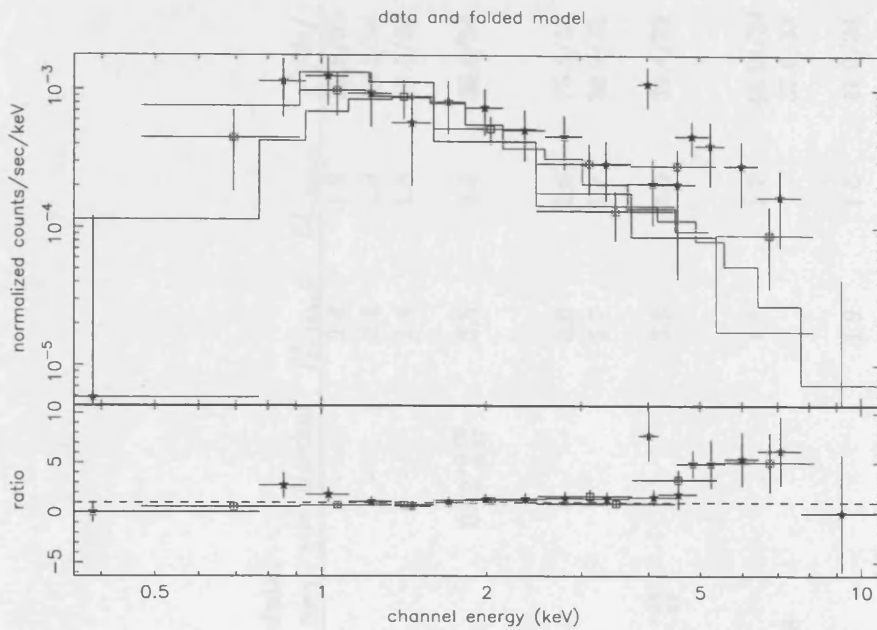


Figure 6.5: The single power-law model for $\Gamma=1.9$ and galactic absorption. The top panel shows the data with the model and the bottom panel shows the data/model ratio. Data from the two GIS and two SIS have been combined for clarity. The stars represent the GIS data points and open squares the SIS points.

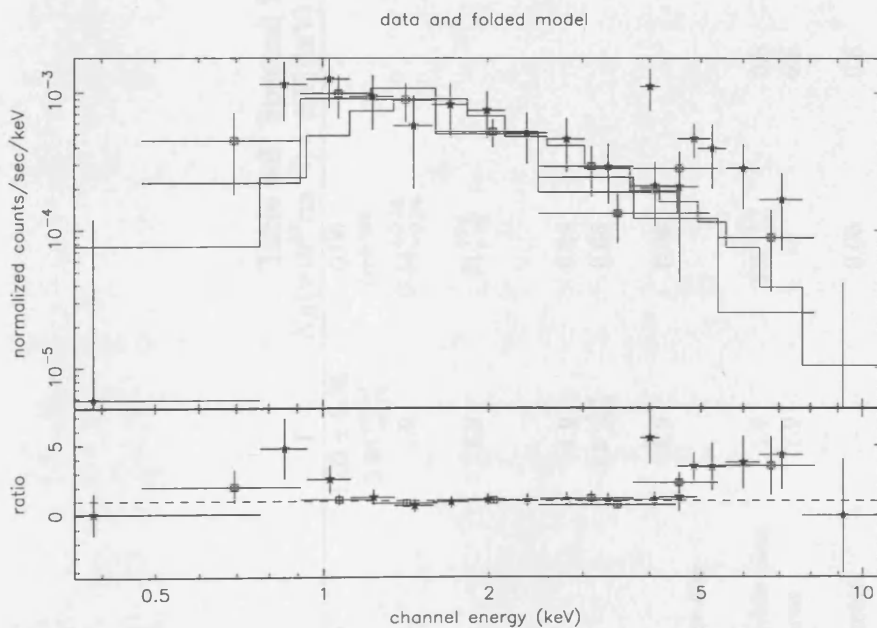


Figure 6.6: The single power-law model for $\Gamma=1.9$ and $N_H = 0.54^{+0.46}_{-0.34} \times 10^{22} \text{cm}^{-2}$. The top panel shows the data with the model and the bottom panel shows the data/model ratio. Data from the two GIS and two SIS have been combined for clarity. The stars represent the GIS data points and open squares the SIS points.

Table 6.3: Spectral fits to the ASCA data.

model	Γ	$N_H(\times 10^{22}\text{cm}^{-2})$	$KT_1(\text{keV})$	$KT_2(\text{keV})$	R or n_{H_2}	cov. fraction	$f_{2-10\text{keV}}^a$	$L_{2-10\text{keV}}^b$	χ^2/dof
single power-law	1.03 ± 0.35	0.06	-	-	-	-	2.4	1.9	39.8/35
	$0.98^{+0.37}_{-0.34}$	$0^{+0.285}$	-	-	-	-	2.4	2.0	39.3/34
	1.9	$0.54^{+0.46}_{-0.34}$	-	-	-	-	1.4	1.3	48.5/35
“scatterer”	1.9	21^{+79}_{-18}	-	-	-	$0.82^{+0.08}_{-0.17}$	2.5	4.3	36.8/34
Reflection	1.9	0.06	-	-	-	-	3.6	2.6	75.3/35
	$3.5^{+0.4}_{-0.3}$	0.06	-	-	-	-	2.7	1.7	39.9/33
Reflection plus a scattered power-law	1.9	0.06	-	-	34.8^{+23}_{-19}	-	3.8	3.0	36.4/35
Absorbed power-law plus thermal component	1.9	$1.8^{+2.0}_{-0.9}$	0.8	-	-	-	1.7	1.7	43.16/34
	1.9	15	0.8	5.	0.8	-	-	-	37.6/33
Two thermal plasma model	-	0.06	0.8	>12	-	-	1.9	1.6	41.0/34

^aobserved 2-10 keV flux in units of $10^{-13}\text{erg sec}^{-1}\text{cm}^{-2}$.

^bunobscured 2-10 keV luminosity in units of $10^{42}\text{erg sec}^{-1}$

dof). However in this case the data require excess absorption ($N_H = 0.54_{-0.34}^{+0.46} \times 10^{22} \text{cm}^{-2}$; see Figure 6.6).

While the single power-law model is formally acceptable, it is clear that it is inadequate and the data require more complex models. I have therefore also tried a “scatterer” model in which a fraction of the X-ray emission, f , is covered by an absorption screen and a fraction of the X-ray emission is scattered into our line of sight. Fixing the slope at the 1.9 value, I obtain an absorbing column of $2 \times 10^{23} \text{cm}^{-2}$ and $\chi^2 = 36.8$ for 34 degrees of freedom, a marginal improvement on the simple power-law model. Using this model and correcting for absorption, an intrinsic 2-10 keV luminosity of $4.3 \times 10^{42} \text{erg s}^{-1}$ is derived. The “scatterer” model together with the data points and the data to model ratio are plotted in Figure 6.7

Most Seyfert galaxies show strong narrow iron K emission lines and these features are usually enhanced in Seyfert 2s. When I add a Gaussian emission line to the partial covering model, constraining its energy and width at 6.4 (rest-frame) and 0.01 keV, we do not obtain a significant detection of line emission but can only set a 90% upper limit to the equivalent width of such a feature of ~ 3 keV.

Alternatively, the flat power-law slope might suggest that Compton reflection dominates in the ASCA energy range (eg Matt et al. 1996). For that reason I have also tried a pure reflection model. This assumes that the reflection occurs from a slab of neutral material subtending a solid angle of 2π sr to an X-ray source located above the slab. Again fixing the intrinsic power-law slope at 1.9 we obtain a completely unacceptable fit with $\chi^2 = 75.3$ for 34 dof. Relaxing the constraint on the power-law slope does improve the statistical acceptability of this model ($\chi^2 = 39.9$ for 33 dof) but results in power-law slope of $\Gamma = 3.45_{-0.27}^{+0.42}$, which is much steeper than is seen in AGN except some narrow-line Seyfert 1s.

Furthermore introducing a reflection model with a scattered power law when the absorption is fixed at the Galactic value and Γ at 1.9 gives a similar quality fit to the partial

covering model with $\chi^2 = 36.4$ for 35 dof. I tie the spectral index of the two power-law components to have the same value, since this is what is expected by the elastic scattering of the primary emission by warm plasma. This model is plotted in Figure 6.8. The further addition of a Gaussian line at 6.4 keV, (rest-frame), does not improve the fit ($\chi^2 = 35.5$ for 34 dof).

Thermal Models

While the optical emission line strengths are highly suggestive of a luminous AGN at the core of the Superantennae, some fraction of the X-ray emission must come from the numerous star-forming regions. Recent studies of starburst galaxies such as NGC 3690 (Zezas, Georgantopoulos & Ward 1998) provide evidence for a hard thermal component in the spectrum of luminous star-forming galaxies. In addition, as already noted in the introduction the ULIRGs Arp220 and Mrk231 show no evidence for the presence of a supermassive black hole and their X-ray emission appears to be thermal. For completeness therefore I have investigated a model in which the emission consists of two thermal (Raymond-Smith) components. I have fixed the temperature of the soft component to 0.8 keV following Zezas et al. (1998) while I assumed a Galactic absorption and a solar metallicity. This again provides a reasonable statistical description of the data ($\chi^2 = 41.0/34$ dof), albeit with a poorly constrained temperature for the hard component (> 12 keV). Fixing the temperatures of the two components to the values determined by Zezas et al but allowing the thermal components to be absorbed improves the fit of this model ($\chi^2 = 37.9/33$ dof) and gives column densities of $\sim 7 \times 10^{21} \text{cm}^{-2}$, similar to that inferred from the value of A_V , and $\sim 10^{23} \text{cm}^{-2}$ for the hard .

Mixed Models

Given the evidence of a strong starburst in the object and the case for an AGN nucleus, it is not unnatural to investigate a model in which X-ray emission from both contribute to the ASCA spectrum. I adopt as a baseline for this model a power-law (with $\Gamma = 1.9$)

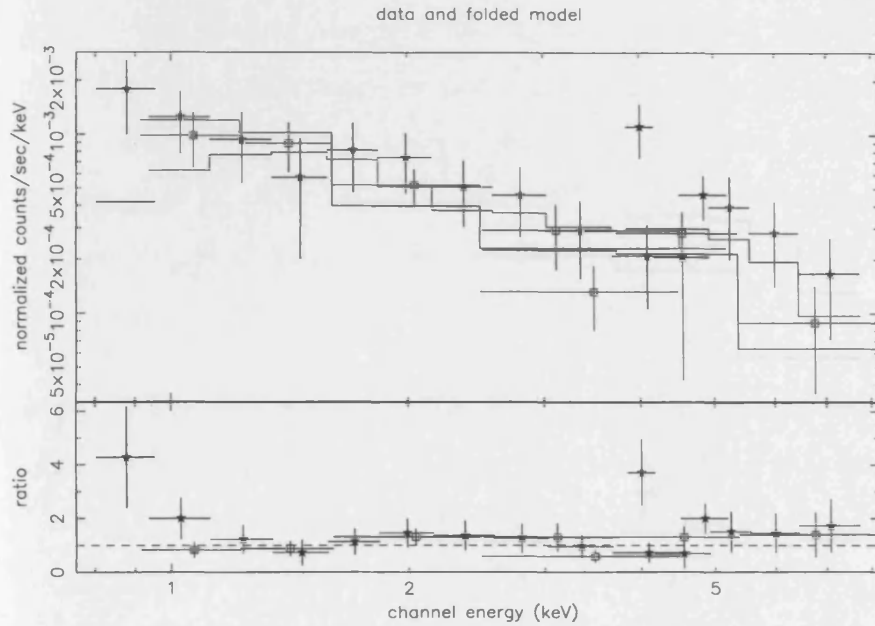


Figure 6.7: The “scatterer” model. The top panel shows the data with the model and the bottom panel shows the data/model ratio. Data from the two GIS and two SIS have been combined for clarity. The stars represent the GIS data points and open squares the SIS points.

to represent the nuclear emission and a Raymond-Smith thermal component to represent the starburst. The power-law component is allowed to have additional absorption over and above that of the thermal component. Again I fix the temperature of the thermal component at 0.8 keV. This results in an acceptable fit with $\chi^2 = 43.2$ for 34 dof with a column of $N_H = 1.80 \times 10^{22} \text{ cm}^{-2}$ for the power-law. Again allowing the thermal component to be absorbed improves the fit ($\chi^2 = 36.7$ for 33 dof) with a column of $\sim 8 \times 10^{21} \text{ cm}^{-2}$.

6.1.5 Discussion

It becomes evident that the X-ray data alone are not sufficient to define the nature of this enigmatic object. The X-ray data are well fit by both power-law models and thermal models. The temperatures in the latter are not inconsistent with those found by Zezas et al. (1998) in the case of the luminous IRAS galaxy NGC3690 which clearly shows no sign of AGN activity. The derived luminosity ($L_x \sim 10^{42} \text{ erg s}^{-1}$) for the Superantennae

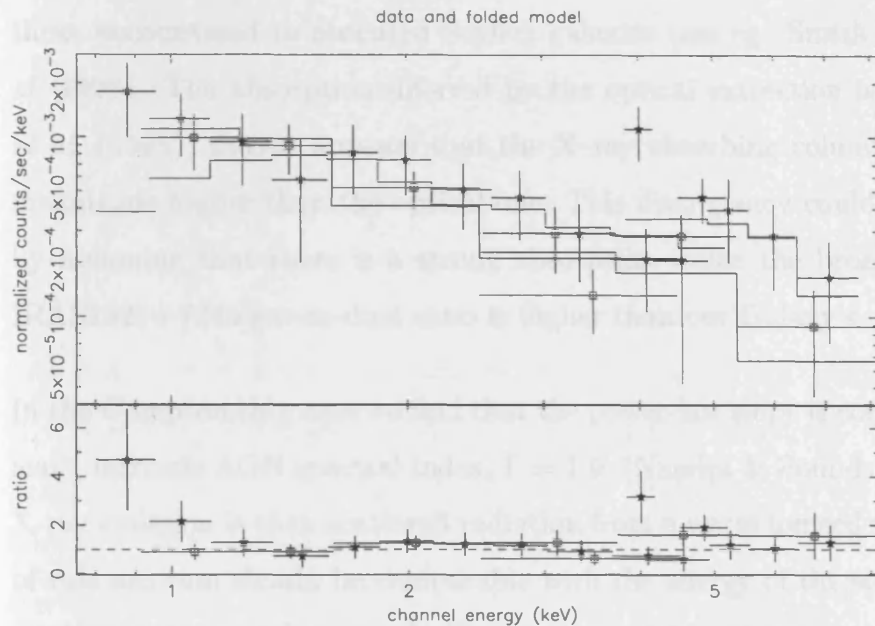


Figure 6.8: The reflection model with the scattered power-law. The top panel shows the data with the model and the bottom panel shows the data/model ratio. Data from the two GIS and two SIS have been combined for clarity. The stars represent the GIS data points and open squares the SIS points.

is again comparable with that of NGC3690.

However, as the optical spectrum reveals a Seyfert-2 nucleus in the southernmost of the two merging nuclei, (Colina et al. 1991), it is most probable that a large fraction of the X-ray emission comes from the active nucleus. Indeed, the hard X-ray spectrum observed ($\Gamma = 1.0 \pm 0.35$) is reminiscent of highly absorbed Seyfert 2 galaxies ($N_H \sim 10^{23-24} \text{ cm}^{-2}$) such as Markarian 3 (Georgantopoulos et al. 1999). Alternatively, the possibility remains that even in the *ASCA* band we are not sensitive to the intrinsic nuclear emission of the Superantennae. This would require the source to be totally obscured by a Compton thick absorber ($N_H > 10^{24} \text{ cm}^{-2}$) in a similar fashion to NGC1068 (Ueno et al. 1994) or the Circinus (Matt et al. 1996). Indeed, both the Compton thin (power-law and scatterer model) and Compton thick models (reflection plus a scattered power-law component) give comparable χ^2 values making it difficult to distinguish between the two possibilities.

In the Compton-thin case, the hard X-ray emission should emerge from an optically thin screen (possibly in the form of the torus); the derived $N_H \sim 10^{23} \text{ cm}^{-2}$ is comparable to

those encountered in obscured Seyfert galaxies (see eg. Smith & Done 1996, Risaliti *et al.* 1999). The absorption inferred by the optical extinction is $9.3 \times 10^{21} \text{cm}^{-2}$, Colina *et al.* (1991); thus it appears that the X-ray absorbing column is at least one order of magnitude higher than the optical one. This discrepancy could then be explained either by assuming that there is a strong absorption inside the broad line region or that the IRAS19254-7245 gas-to-dust ratio is higher than our Galaxy's.

In the Compton thin case we find that the power-law slope is compatible with the “canonical”, intrinsic AGN spectral index, $\Gamma = 1.9$, (Nandra & Pounds 1994). The observed soft X-ray emission is then scattered radiation from a warm ionised medium (the temperature of this medium should be comparable with the energy of the soft X-ray photons, so that elastic scattering takes place). The above model has become the standard model for the X-ray emission in obscured Seyfert nuclei (Mushotzky, Done & Pounds 1993). Then the scattered component and the intrinsic hard X-ray emission together with high amounts of obscuration or reflection can easily mimic a flat spectrum (eg as in the case of IRAS 23060+0505, Brandt *et al.* 1997).

In the case of IRAS 19254-7245, we find that the amount of the scattered emission towards our line of sight is about 20 per cent. This is higher than typically found for the obscured Seyfert (Seyfert 1.9-2.0) nuclei, where the scattered component is usually of the order of a few percent. Colina *et al.* (1991) suggested that massive star formation should take place in order to explain the properties of the Superantennae (see also Mirabel *et al.* 1991). Under this scenario the excess in the soft X-ray emission could be explained by a star forming component. The inferred soft X-ray luminosity, in the 1-2 keV band $L_x \sim 10^{41} \text{erg s}^{-1}$ is quite typical of that expected in massive star-forming galaxies (eg Zezas *et al.* 1998). If instead we assume that all the soft X-ray emission is mainly due to scattering, we can derive interesting constraints on the location of the scattering medium. If we require the ionisation parameter of the scattering medium to be $\log \xi = 3$ and the electron density $n_e = 10^5 \text{cm}^{-3}$, comparable to the values encountered in Mrk 3 (Griffiths *et al.* 1998), we can derive the distance R of the scattering medium from the continuum source. We obtain $R \sim 0.1 \text{ pc}$ suggesting that the scattering medium lies close to the nucleus.

In contrast with the “scatterer” model, spectropolarimetric observations (Heisler *et al.* 1997) of the Superantennae revealed no scattered emission. The authors attributed the absence of optical scattering to geometrical effects. In such a case we should not expect to observe any X-ray scattered emission as well. This suggest that either the scattering model is invalid for this galaxy or that in Superantennae the X-ray and optical photons do not scatter off electrons as it is widely believed in the case for more other Seyfert galaxies. The alternative hypothesis of scattering off dust particles is ruled out because of the strong wavelength dependence expected in this case. The alternative hypothesis would be if the scattering medium is atoms. In such a case the optical photons would be absorbed, so no optical scattering is expected. However, the optical depth for photoelectric absorption at 1 keV is ~ 6000 for hydrogen atoms and thus effectively all the soft X-ray flux is absorbed. Therefore atomic scattering cannot produce the observed soft emission. The above indicates that the scattering model does not provide a physical representation of the data.

In the Compton thick case, the X-ray emission comes from both a reflection and a scattered power-law component. The geometry is similar to the one described above in the case of the Compton thin model, with the exception that now the torus is optically thick ($N_H > 10^{24} \text{ cm}^{-2}$). We note that in both the Compton thick and thin case we should detect a strong Fe line at 6.4 keV. Especially, in the Compton thick case, the equivalent width of the line could reach few keV as in eg the case of NGC6240 (Iwasawa & Comastri 1999). Our data do not show strong evidence for an Fe K emission line. However, the obtained upper limit to the equivalent width ($\sim 3 \text{ keV}$) does not in this case rule out the Compton thick possibility. Vignati *et al.* (1999) recently showed, using *BeppoSAX* data that the ULIRG NGC6240 hosts a Compton thick ($N_H \sim 2 \times 10^{24} \text{ cm}^{-2}$) Seyfert-2 type nucleus. NGC6240 has a LINER classification in the optical while it is classified as an HII galaxy on the basis of IR spectroscopy (Lutz *et al.* 1999). The LINER classification most probably comes from low ionisation gas in a superwind. It is interesting that although the Superantennae has similar X-ray properties to NGC6240, they present strong AGN characteristics in the optical. This difference may be related to the distribution of obscuring material in the

galaxy.

Further clues on the nature of the hidden AGN can be given by studying the isotropic properties of the galaxy. Here, we will consider as isotropic emission the infrared (IR), the hard X-ray emission (in the case of Compton thin absorption) and the $[OIII]\lambda 5007$ line emission produced in the narrow line region, and thus free of viewing angle effects. The advantage of studying isotropic properties, is that they act as an indicator of the strength of the nuclear source. Maiolino et al. (1998) have proposed that the measurement of the unabsorbed hard X-ray flux (2-10 keV) against the $[OIII]\lambda 5007$ flux, is indeed a powerful diagnostic. Of course, this tool may be less efficient in the case of ULIRGs which have large amounts of dust. Moreover, although the line is emitted on Narrow Line Region (NLR) scales, the host galaxy disk might obscure part of the NLR and should be corrected for the extinction deduced from the Balmer decrement (Maiolino & Rieke 1995). To estimate the corrected flux we used the observed $[OIII]\lambda 5007$ flux from Colina et al. (1991) corrected for the optical reddening using the following relation (Bassani et al. 1998):

$$F_{[OIII]cor} = F_{[OIII]obs} \times [(H_\alpha/H_\beta)/(H_\alpha/H_\beta)_0]^{2.94} \quad (6.1)$$

Assuming an intrinsic Balmer decrement $(H_\alpha/H_\beta)_0 = 3$, the $L_{x(2-10keV)}/L_{[OIII]}$ ratio of Superantennae is ~ 0.01 favouring the Compton-thick interpretation for IRAS 19254-7245. Then on the basis of the mean $L_{x(2-10keV)}/L_{[OIII]}$ ratio, the *intrinsic* luminosity of the Superantennae should exceed 10^{44} erg s⁻¹ suggesting that obscuration in our line of sight prevents us from seeing any of the nuclear X-ray emission directly. Furthermore following Mulchaey et al. (1994) we use the IR to hard X-ray flux ratio as an indicator. The infrared flux is given by (Mulchaey et al. 1994):

$$F(IR) = S_{25\mu m} \times (\nu_{25\mu m}) + S_{60\mu m} \times (\nu_{60\mu m}) \quad (6.2)$$

where S_λ is the flux density at wavelength λ . They showed that the expected $\log(f_{IR}/f_x)$ (the IR to *unabsorbed* hard X-ray flux ratio) is ~ 0.9 . We find that for the Superantennae this ratio is ~ 3 , clearly indicating a deficit in the hard X-ray emission compared to that expected from a Compton thin Seyfert 2 galaxy. This again suggests a high column density in our light of sight, which absorbs the photons in the ASCA band. We should

note here, that the f_{IR}/f_x ratio in the ULIRGs may be high due to excess IR emission from a starburst component. However, ISO observations suggest an AGN classification for the Superantennae (Lutz *et al.* 1999), indicating that the AGN contribution to the infrared flux dominates over the star-forming one.

6.2 Conclusions

In this chapter *ROSAT* HRI and *ASCA* X-ray observations of the ULIRG IRAS 19254-7245 (the Superantennae) have been presented. This object is not detected by the *ROSAT* HRI. However, hard X-ray emission with *ASCA* is detected. The emission shows a very flat spectrum in the 1-10 keV band, reminiscent of the spectra of highly obscured AGN locally. Therefore, the X-ray data indirectly argue in favor of the existence of a super-massive black hole in IRAS 19254-7245. In particular, the X-ray data can be modeled with a power-law spectrum with a photon index slope of $\Gamma = 1.9$ emerging through a Compton thin torus ($N_H \sim 10^{23} \text{cm}^{-2}$). A scattered component (of the order of 20 per cent of the nuclear component at 1 keV) or alternatively a large star-forming component ($L_x \sim 10^{41} \text{erg s}^{-1}$) is also present. No Fe line at 6.4 keV is detected, with the 90 per cent upper limit on the equal width being 3 keV. The X-ray data are also well modeled by a Compton thick, reflection dominated model with some fraction of the nuclear emission scattered into the line of sight. Although the limited quality of the present data does not allow one to distinguish between the above two models, indirect evidence (absence of optical scattered emission and isotropic properties of the galaxy) strongly points towards the Compton thick interpretation for the Superantennae. If this is the case, the Superantennae along with NGC6240 are the only Compton thick ULIRGs found so far.

Chapter 7

Mrk609 – A composite galaxy with flat X-ray spectrum

7.1 Introduction

Moran & Helfand (1996), after careful spectroscopy of a sample based on the cross-correlation of the IRAS PSC and *ROSAT* All Sky Survey, reported the discovery of an “anomalous” class of objects. The optical spectra of these sources are dominated by the features of starburst galaxies, yet their X-ray luminosities are typical of Seyfert 2 galaxies. Close examination of their optical spectra reveals some weak Seyfert-like features: [OIII] broader than found in HII type galaxies and in some cases a weak broad H_α component. The authors designated these objects starburst/Seyfert composite galaxies and presented them as a new class of X-ray luminous source.

The Baldwin *et al.* (1981) or Veilleux & Osterbrock (1987) emission line diagnostic diagrams allows secure classification of the nuclear emission line region of most galaxies into one of three categories: nuclear HII regions/starbursts, Seyfert 2 galaxies and LINERS. Composite galaxies fall either on the starburst region or on the borderlines between the different classes, so that they cannot be identified unambiguously. In the literature these galaxies have been termed “transition” objects as well.

Veron *et al.* (1997) presented spectral observations of 15 objects with “transition” spectra at high-dispersion (66\AA mm^{-1}) around the H_α , $[\text{NII}]\lambda\lambda 6548, 6584$ and/or H_β , $[\text{OIII}]\lambda\lambda 4959, 5007$ emission lines. They showed that most of them (10) have composite spectra, resulting from the simultaneous presence of a Seyfert nucleus and a HII region.

The composite galaxies bear close resemblance to the narrow-line X-ray galaxies (NLXGs) detected in large numbers in deep *ROSAT* surveys (eg Boyle *et al.* 1995, Griffiths *et al.* 1996). These NLXGs again have spectra composite of Seyfert and starburst galaxies (Boyle *et al.* 1995) with luminosities $L_{2-10\text{keV}} \sim 10^{42-43}\text{erg s}^{-1}$. Unfortunately the faint fluxes of these NLXGs do not allow their detailed study in either optical or X-ray wavelengths.

Although it is unclear whether these nearby “composites” are the same class of objects as those found in *ROSAT* deep field NLXGs, their high luminosities need to be explained. It is unclear how their intense X-ray emission can be reconciled with weak or absent Seyfert characteristics.

7.1.1 Other composite galaxies observed in X-rays

Only two composite galaxies have been studied so far in X-rays. IRAS00317-2142 (Georgantopoulos 2000) has been observed with *ASCA* and is the most luminous object ($L_x \approx 10^{43}\text{erg s}^{-1}$ in the 0.1-2 keV band) in the Moran *et al.* (1996) sample. The spectrum is represented by a power-law with $\Gamma \sim 1.76$ and there is no evidence for absorption above the Galactic value. Strong variability in the 1-2 keV band (by a factor of three) is detected between the *ROSAT* and *ASCA* observations. These characteristics indicate an AGN origin for the X-ray emission. However no iron line is detected and the 90 per cent upper limit on the equivalent width is 0.9 keV. The ratio $f_{\text{HX}}/f_{[\text{OIII}]}$ ~ 2.5 (see chapter 4) rule out the Compton thick interpretation for IRAS00317-2142. However, the precise nature of this object and the relative contribution of the starburst and AGN components could not be determined.

The other composite object studied in X-rays with *ROSAT* and *ASCA* is AXJ1749+684 (Iwasawa *et al.* 1997). AXJ1749+684 was serendipitously detected with the *ASCA* GIS. Its X-ray spectrum is flat ($\Gamma = 1.23_{-0.27}^{+0.21}$). The flatness is attributed by the authors to absorption mainly because of the: (a) large Balmer decrement in the narrow line region, $H_\alpha/H_\beta=7.32$ and (b) lack of significant X-ray detection at <0.4 keV. On the other hand, the optical counterpart of AXJ1749+684 is detected in the Kiso Schmidt Survey of UV-excess galaxies. Iwasawa *et al.* (1997) claimed that the UV emission is due to large-scale starburst activity, however in this case strong far infrared emission should be expected, which is inconsistent with the non-detection of this source by IRAS. They concluded that the X-ray spectrum of AXJ1749+684 is well fitted by an obscured ($N_H = 2.1_{-2.1}^{+6.2} \times 10^{21}$ cm $^{-2}$) Seyfert nucleus embedded within a star-forming galaxy.

Recently Levenson *et al.* 2001, examined NGC6221 as a further example of a composite galaxy. They proposed that the X-ray spectrum of this object is characterised by a Seyfert 1 like spectrum. They detect an iron line and continuum variability on short- and long-term time-scales. The source has a column density of $N_H=10^{22}$ cm $^{-2}$. They proposed that the central region is obscured by a surrounding starburst. Thus the optical spectrum has the characteristics of the starburst component alone.

7.1.2 Mrk609

In this chapter an X-ray analysis of the “composite” galaxy Mrk609 is presented. An optical image of the galaxy is shown in Figure 7.1. Mrk609 is at a redshift of 0.034. The optical position of the object is 03 25 25.3, -06 08 39 (J2000) and the Galactic absorption is $N_H=4.41 \times 10^{20}$ cm $^{-2}$. It is taken from the Veron *et al.* (1997) sample. This sample has very good optical spectra which make their classification secure. The broad H_α/H_β value is 7.8 (Osterbrock 1981) and was then classified as a Seyfert 1.8 galaxy. In a later observation, Rudy *et al.* (1988) obtained a value for the broad $H_\alpha/H_\beta=5$. The discrepancy was attributed to continuum variability. The high broad H_α/H_β value was attributed by Osterbrock 1981 to reddening of the broad line region. However the broad Ly_α/H_β value

Table 7.1: The properties of MKN609.

Parameter	Flux
F(25 μ m)	0.48 Jy
F(60 μ m)	2.55 Jy
F(100 μ m)	4.76 Jy
L_{FIR}	5.6×10^{44} erg s $^{-1}$
Ly_{α}/H_{β}	16
H_{α}/H_{β}	5
$L(H_{\alpha})_b$	8.43×10^{39} erg s $^{-1}$
$L(H_{\alpha})_n$	3.33×10^{39} erg s $^{-1}$
J	0.37 mag
H	0.47 mag
K	0.63 mag

is 16, which is large for Seyfert 1 galaxies, ruling out obscuration.

In Table 7.1 the properties of Mrk609 are summarised, whereas in Figures 7.2 and 7.3 the optical and ultraviolet spectra obtained by Rudy *et al.* (1988) are shown.

Motivation

Mrk609 provides an excellent opportunity to study the X-ray spectral properties of the composite galaxies and in particular to investigate the nature of the hard X-ray emission of these objects, which is still unknown. Furthermore, since the local composite galaxies resemble the NLXGs detected in deep *ROSAT* surveys, their studies in X-rays is expected to have an impact in our understanding of the NLXGs and X-ray background.

7.2 Observations and Data Reduction

Mrk609 was observed by *BeppoSAX* three times. The first observation was carried out on 20/01/2000 for ~ 18 ksec (LECS exposure 7.13 ksec), the second one on 14/02/2000 for ~ 2.5 ksec (LECS exposure 1.4 ksec) and the third one on 4/03/2000 for ~ 28 ksec (LECS exposure 6668 ksec). It should be reminded here, that the exposure time for the LECS is lower than the MECS because it is limited by stronger operational constraints



MRK 609 (929 pc/'')

Figure 7.1: Image of Mrk609 obtained with WFPC2 on-board the HST. The arrowhead points north and the bar is east. The length of the eastern bar is 2''. Taken from Malkan *et al.* 1998.

to avoid UV light contamination, thus it is operated during Earth dark time only.

Spectra and light curves of Mrk609 have been extracted from circular regions centred on the source. I used a circular extraction cell of 4 and 6 arcminutes in radius for MECS and LECS data respectively. The background spectra were extracted from blank deep field exposures, using the same region of the detector in each case.

In order to check whether there is any flux or spectral variability in the soft band, an unpublished *ROSAT* PSPC observation of Mrk609 was analysed. Mrk609 was observed by *ROSAT* on the 29th of January 1997 for 5801 seconds. A source spectrum has been extracted from a circular region of ~ 1.5 arcmin radius around the centroid of the source, while the background spectrum was extracted from an annulus of internal and external

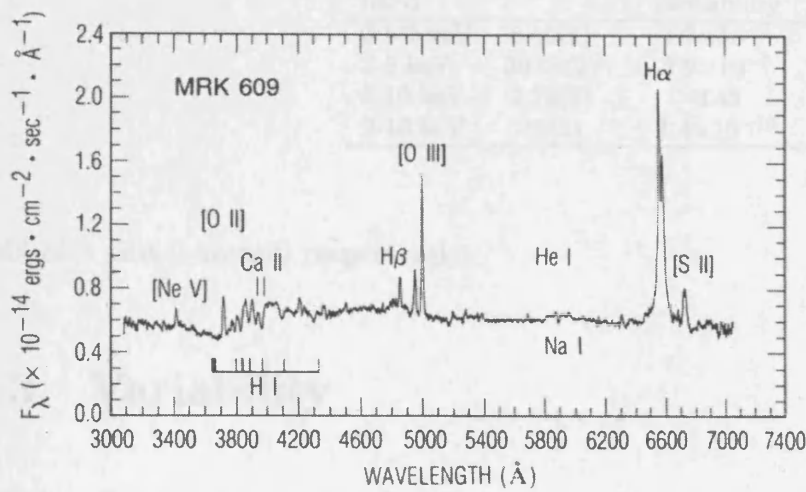


Figure 7.2: Optical spectrum of Mrk609 observed through 8" aperture and shown in the rest frame. The prominent emission lines and stellar absorption features are also marked. Taken from Rudy *et al.* 1988.

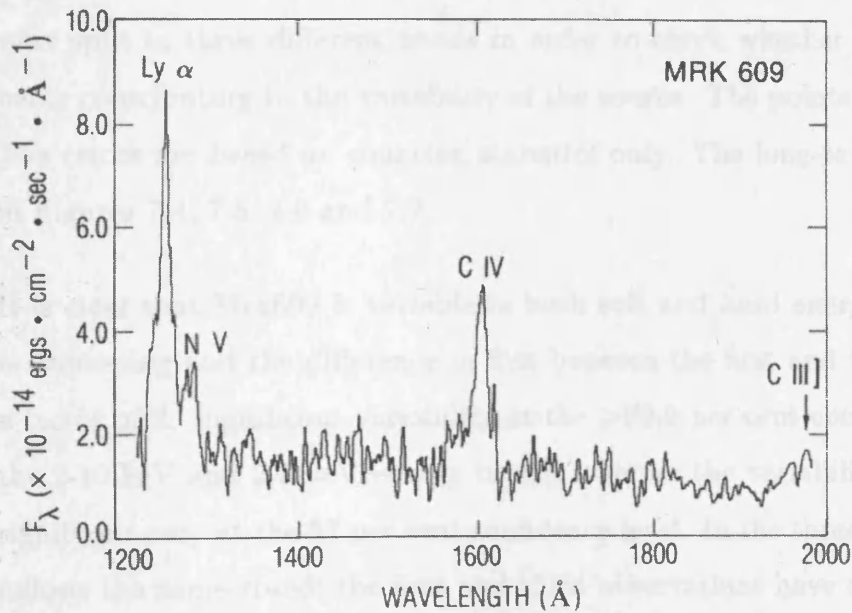


Figure 7.3: Ultraviolet spectrum of Mrk609. The prominent emission lines are labeled. Taken from Rudy *et al.* 1988.

Table 7.2: χ^2 for the long-term light curves.

Energy band	χ^2 (dof)	null hypothesis probability
0.1-2 keV	8.16(2)	1.7×10^{-2}
2-5 keV	30.08(2)	2.9×10^{-7}
5-10 keV	2.76(2)	0.43
2-10 keV	45(2)	1.4×10^{-10}

radii of 3 and 9 arcmin respectively.

7.3 Variability

7.3.1 Long-term variability

In order to investigate the nature of the X-ray source, long term light curves were constructed. Then the variability was tested by means of a χ^2 test against the hypothesis that the flux was constant. The χ^2 values are quoted in Table 7.2 for four light curves: LECS 0.1-2 keV, MECS 2-10 keV, MECS 2-5 keV, MECS 5-10 keV. The MECS data were split in three different bands in order to check whether there are different components contributing to the variability of the source. The points are in chronological order; The errors are based on counting statistics only. The long-term light curves are plotted in Figures 7.4, 7.5, 7.6 and 7.7.

It is clear that Mrk609 is variable in both soft and hard energies. In the LECS the flux is decreasing and the difference in flux between the first and third observations is about a factor of 2. Significant variability at the >99.9 per cent confidence level is detected in the 2-10 keV and 2-5 keV energy bands, whereas the variability in the 5-10 keV band is significant only at the 57 per cent confidence level. In the three hard bands the variability follows the same trend; the first and third observations have comparable fluxes, whereas during the second observation the flux drops by up to a factor of 3. The similarity of the variability shape in the three hard bands suggests that the whole hard X-ray emission is produced by the same mechanism and in the same region.

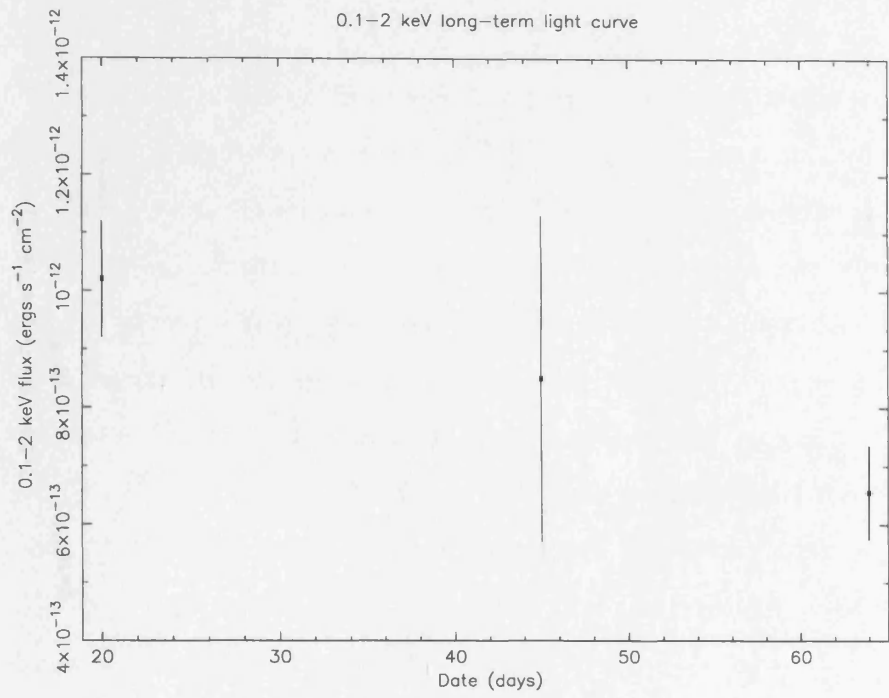


Figure 7.4: The 0.1-2 keV long-term light curve. The flux is decreasing.

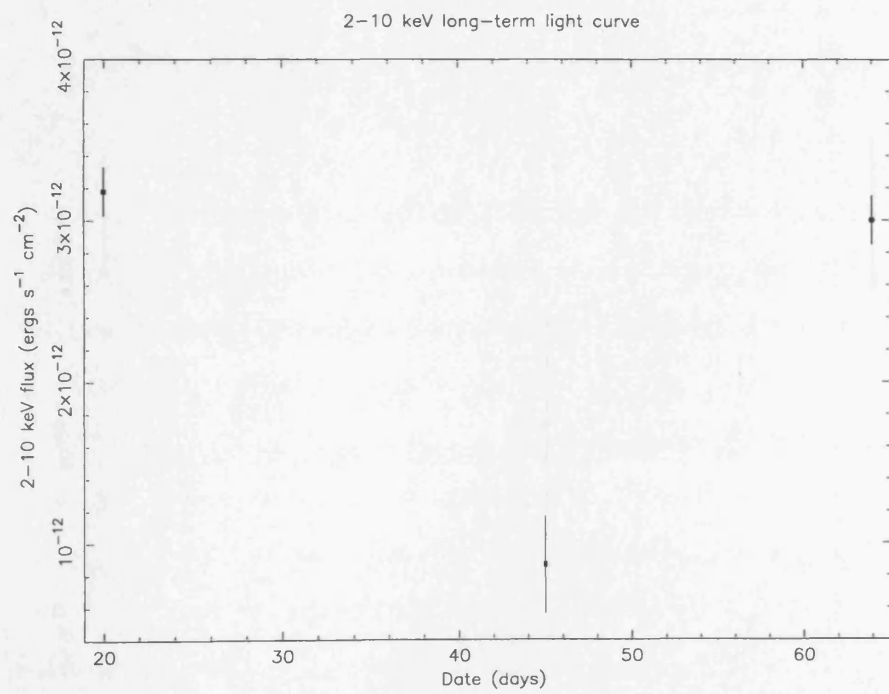


Figure 7.5: The MECS 2-10 keV long-term light curve.

7.3.2 Short-term variability

2-5 keV long-term light curve

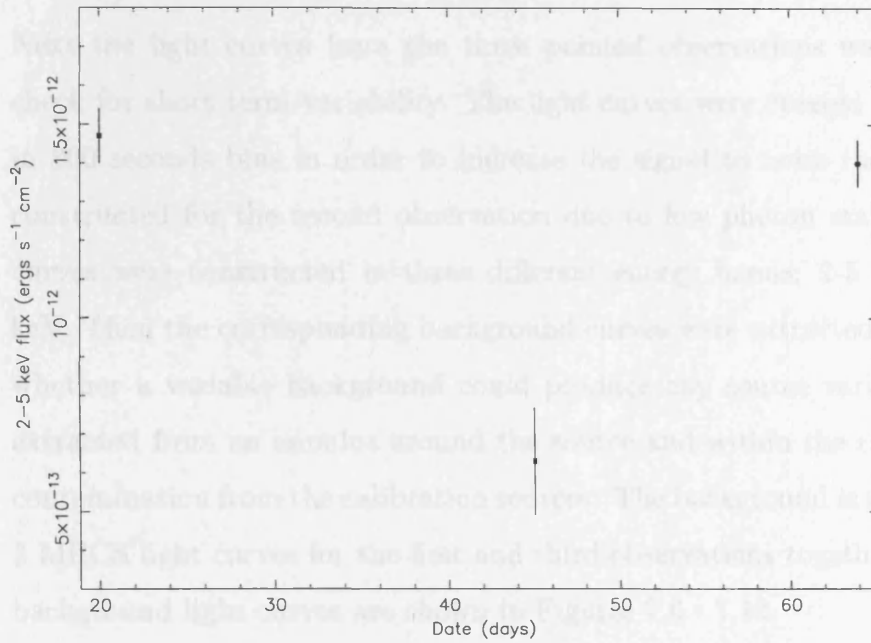


Figure 7.6: The MECS 2-5 keV long-term light curve.

5-10 keV long-term light curve

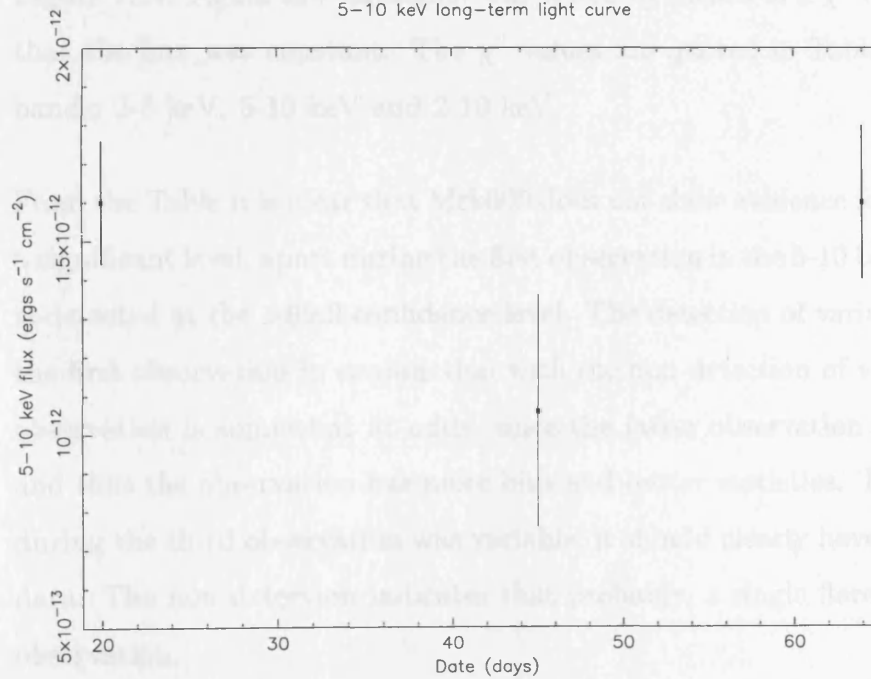


Figure 7.7: The MECS 5-10 keV long-term light curve.

7.3.2 Short-term variability

Next the light curves from the three pointed observations were extracted, in order to check for short term variability. The light curves were created by accumulating photons in 800 seconds bins in order to increase the signal to noise ratio. No light curves were constructed for the second observation due to low photon statistics. Again the MECS curves were constructed in three different energy bands; 2-5 keV, 5-10 keV, and 2-10 keV. Then the corresponding background curves were extracted as well, in order to check whether a variable background could produce any source variability. The counts were extracted from an annulus around the source and within the central 10 arcmin to avoid contamination from the calibration sources. The background is more or less stable and the 3 MECS light curves for the first and third observations together with the corresponding background light curves are shown in Figures 7.8 - 7.13.

In the soft band, variability was examined in the *ROSAT* observation, since LECS observations give few photons for temporal analysis. The *ROSAT* light curve is shown in Figure 7.14. Again the variability was tested by means of a χ^2 test against the hypothesis that the flux was constant. The χ^2 values are quoted in Table 7.3 for the three MECS bands; 2-5 keV, 5-10 keV and 2-10 keV.

From the Table it is clear that Mrk609 does not show evidence for short-time variability at a significant level, apart during the first observation in the 5-10 keV band, where variability is detected at the >99.9 confidence level. The detection of variability in this band during the first observation in conjunction with the non detection of variability during the third observation is somewhat at odds, since the latter observation is longer than the former and thus the observation has more bins and better statistics. This means that if the flux during the third observation was variable, it should clearly have been detected with these data. The non detection indicates that probably, a single flare occurred during the first observation.

Table 7.3: χ^2 for the short-term light curves.

	Energy band	χ^2 (dof)	null hypothesis probability	χ^2 (dof)	null hypothesis probability
		source		background	
observation 1	2-5 keV	14.22(13)	0.36	15.30(13)	0.62
	5-10 keV	21.23(13)	6.6×10^{-2}	11.76(13)	0.55
	2-10 keV	12.20(13)	0.36	30.64(13)	0.48
observation 3	2-5 keV	30.91(31)	0.47	34.27(31)	0.31
	5-10 keV	28(31)	0.62	29.30(31)	0.55
	2-10 keV	30.64(31)	0.48	23.70(31)	0.86
PSPC	0.1-2 keV	4.04(3)	0.4	-	-

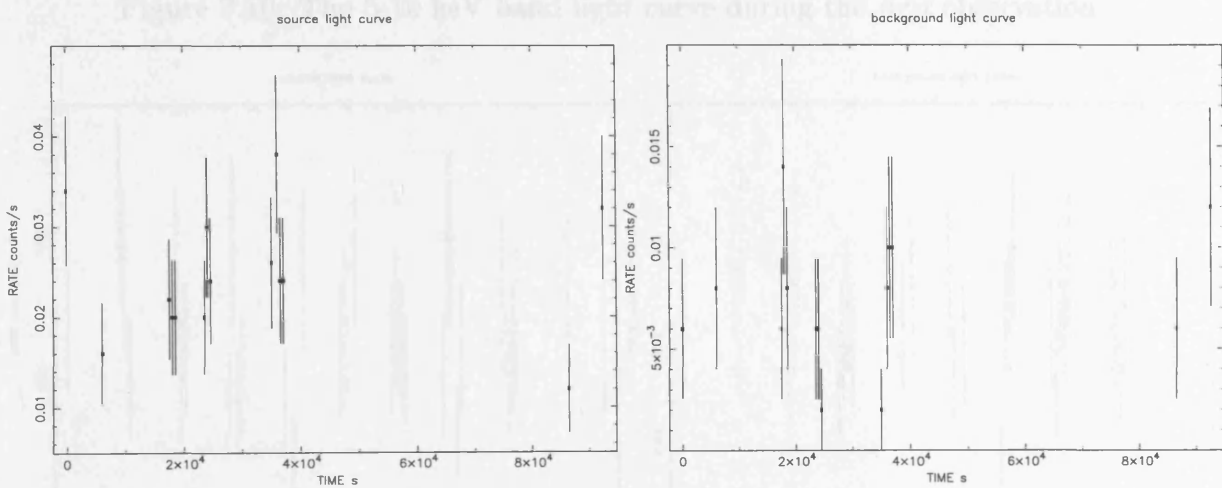


Figure 7.8: The 2-5 keV band light curve during the *first* observation.

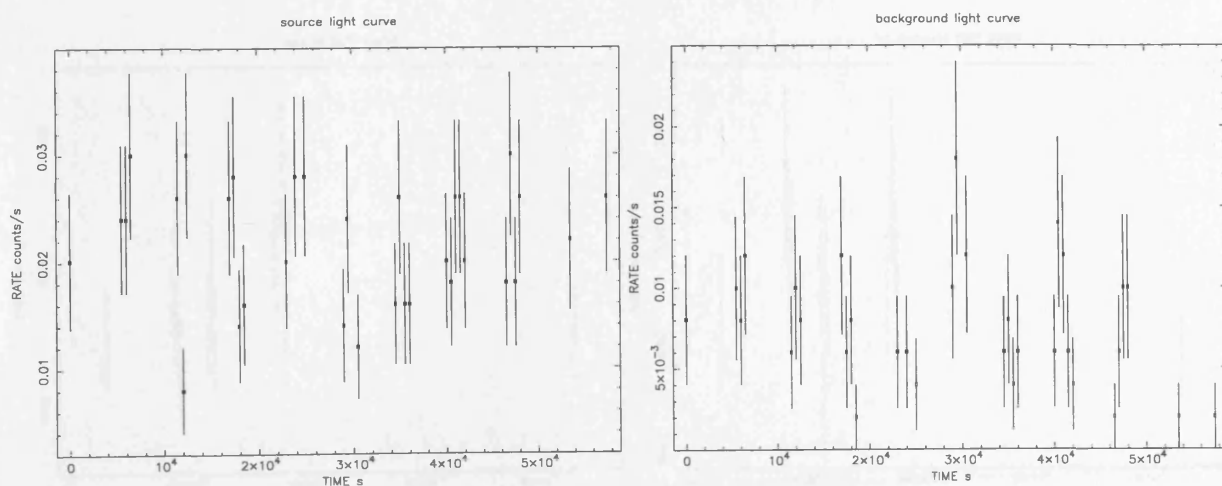


Figure 7.9: The 2-5 keV band light curve during the *third* observation.

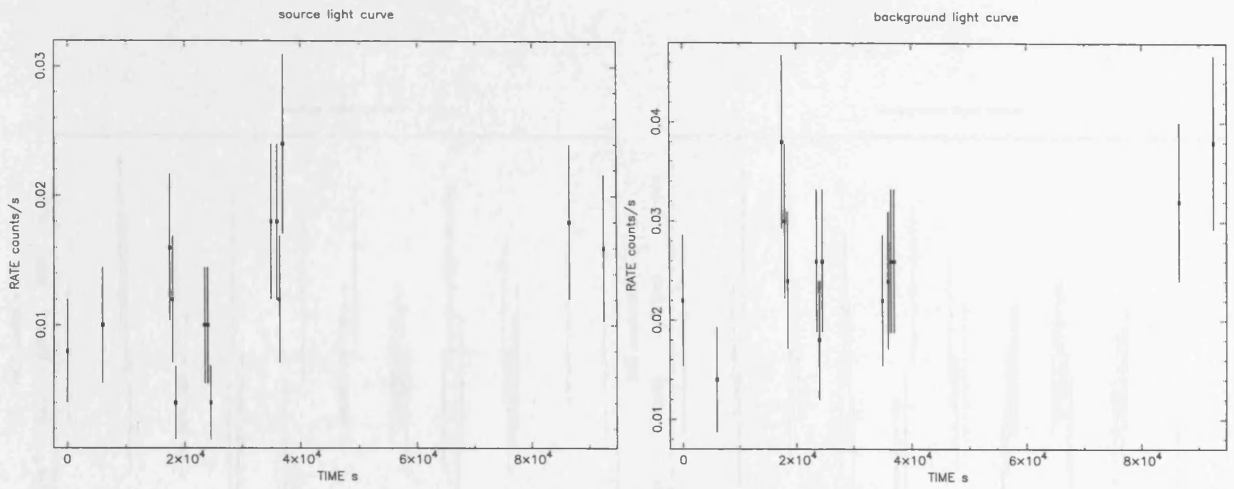


Figure 7.10: The 5-10 keV band light curve during the *first* observation.

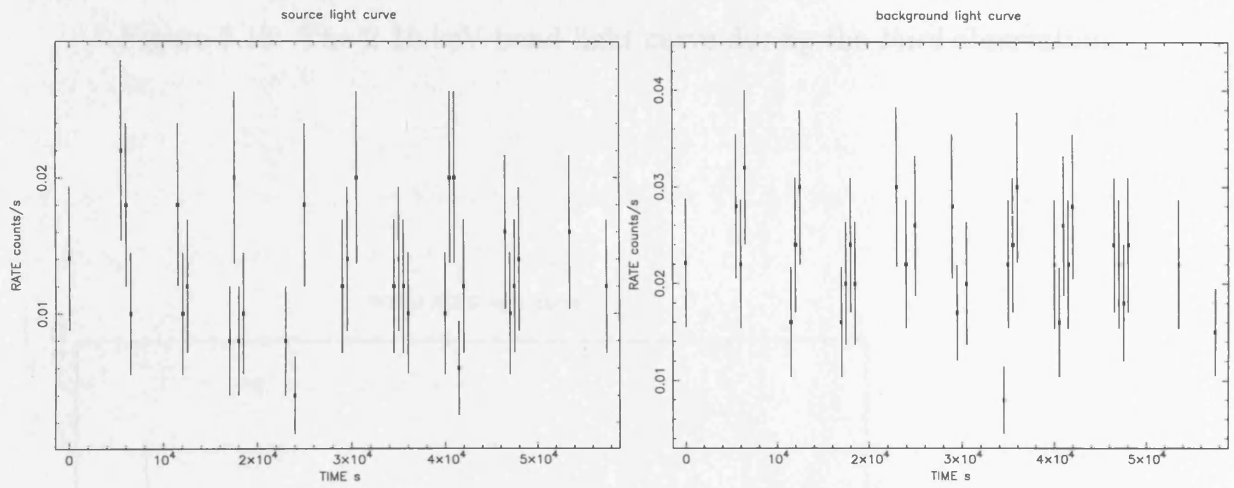


Figure 7.11: The 5-10 keV band light curve during the *third* observation.

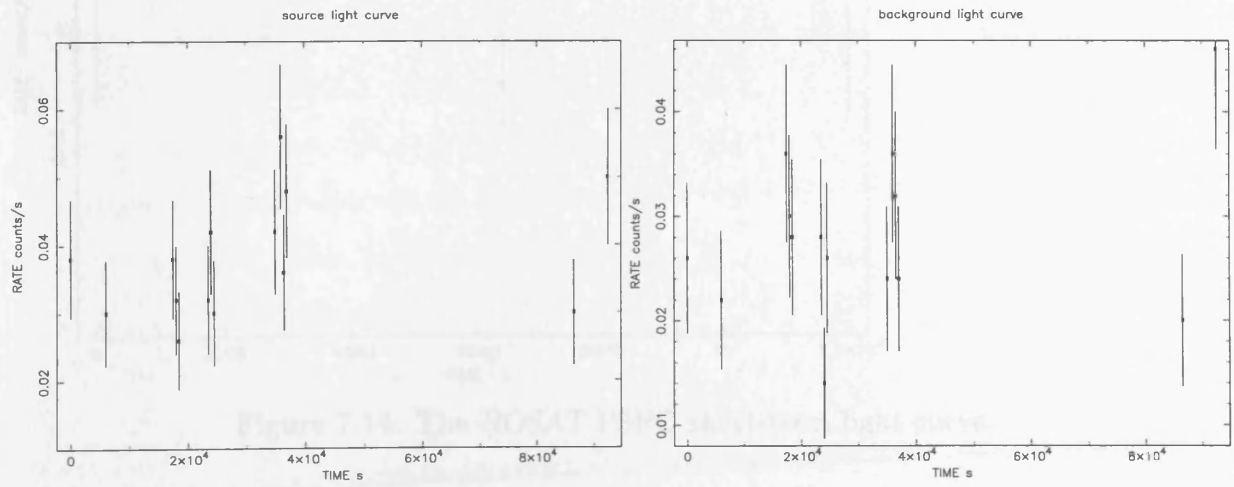


Figure 7.12: The 2-10 keV band light curve during the *first* observation.

Table 7.4: The spectral fit results for the ROSAT data.

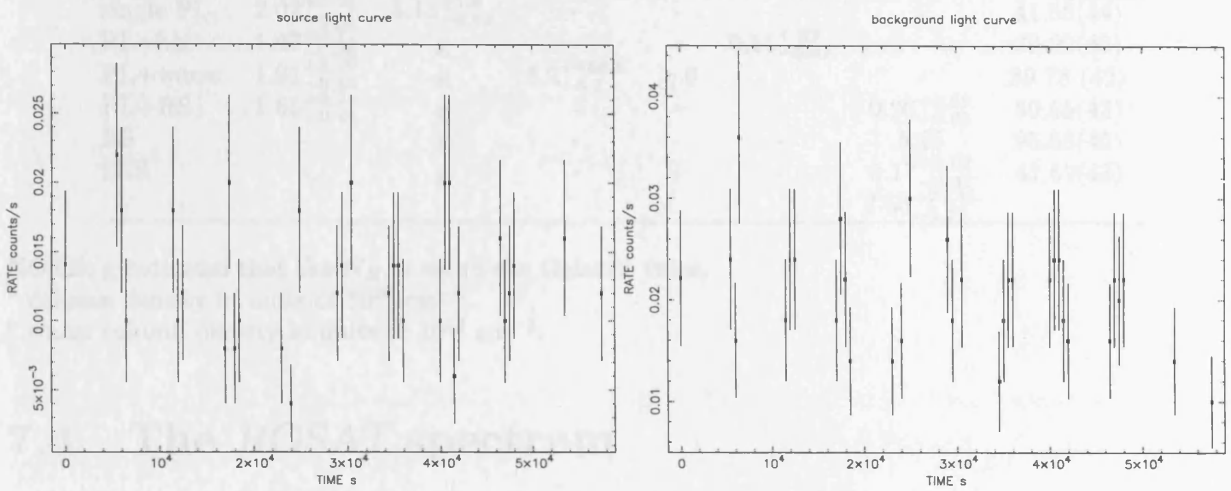


Figure 7.13: The 2-10 keV band light curve during the *third* observation.

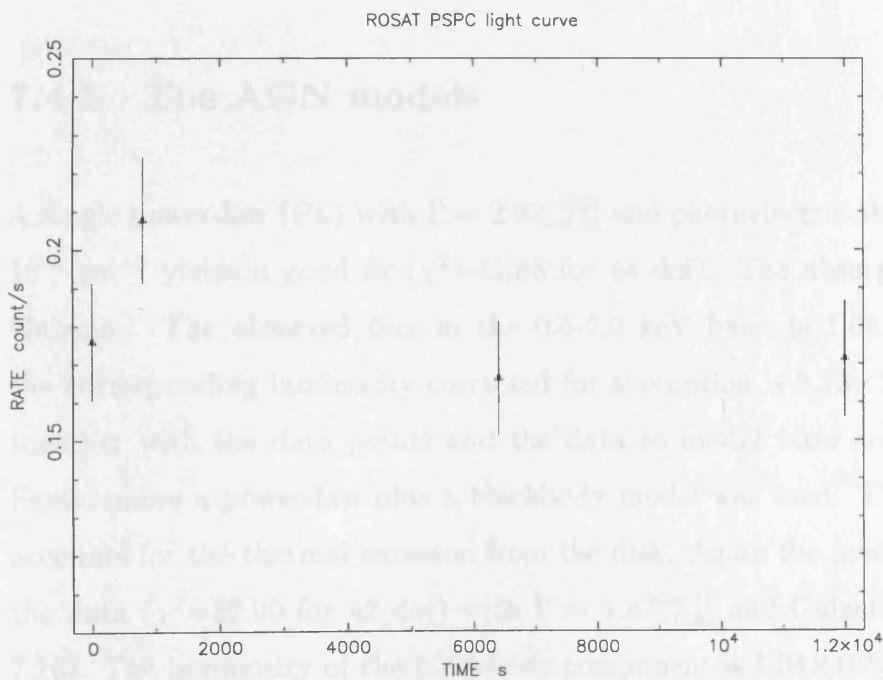


Figure 7.14: The ROSAT PSPC short-term light curve.

Table 7.4: The spectral fits results on the *ROSAT* data.

Model	Γ	N_H^a	N_{Hw}^b	ξ	kT _{bb}	kT _{RS}	χ^2 (dof)
single PL	$2.02^{+0.24}_{-0.25}$	$5.13^{+1.0}_{-0.92}$	-	-	-	-	41.88(44)
PL+bb	$1.47^{+0.71}_{-0.66}$	g	-	-	$0.11^{+0.02}_{-0.02}$	-	39.90(42)
PL+warm	$1.91^{+0.49}_{-0.55}$	g	$8.2^{+486.8}_{-8.2}$	≥ 0	-	-	39.78 (42)
PL+RS	$1.65^{+0.24}_{-0.41}$	g	-	-	-	$0.20^{+0.18}_{-0.05}$	39.55(43)
RS	-	g	-	-	-	5.95	95.88(45)
2RS	-	g	-	-	-	$0.17^{+0.03}_{-0.02}$	41.52(43)
						$7.55^{+23.45}_{-3.77}$	

NOTE: g indicates that the N_H is set to the Galactic value.

^a column density in units of 10^{20} cm^{-2} .

^b warm column density in units of 10^{22} cm^{-2} .

7.4 The *ROSAT* spectrum

To perform spectral fitting, the appropriate PSPC-B redistribution matrix for the observation date (pspcb_gain2.rmf) has been used and the effective area was calculated using the tool pcarf. The analysis was performed in the 0.1-2.0 keV energy band. A summary of the spectral fitting results is given in Table 7.4.

7.4.1 The AGN models

A single power-law (PL) with $\Gamma = 2.02^{+0.24}_{-0.25}$ and photoelectric absorption $N_H = 5.13^{+1.0}_{-0.92} \times 10^{20} \text{ cm}^{-2}$ yields a good fit ($\chi^2 = 41.88$ for 44 dof). The absorption is comparable with Galactic. The observed flux in the 0.5-2.0 keV band is $1.68 \times 10^{-12} \text{ erg cm}^{-2} \text{ s}^{-1}$ and the corresponding luminosity corrected for absorption is $3.73 \times 10^{42} \text{ erg s}^{-1}$. This model together with the data points and the data to model ratio are plotted in Figure 7.15. Furthermore a power-law plus a blackbody model was used. The blackbody component accounts for the thermal emission from the disk. Again the model provides a good fit for the data ($\chi^2 = 39.90$ for 42 dof) with $\Gamma = 1.47^{+0.71}_{-0.66}$ and Galactic absorption (see Figure 7.16). The luminosity of the blackbody component is $1.04 \times 10^{42} \text{ erg s}^{-1}$.

Finally, since ~ 50 per cent of the Seyfert 1 galaxies have a warm absorber (Reynolds 1997 and George *et al.* 1998), this model (PL+warm) was applied to Mrk609 as well with

the temperature fixed at $T=10^5$ K (Brandt *et al.* 1999). The fit yields an acceptable fit ($\chi^2=39.78$ for 42 dof) with $\Gamma = 1.91_{-0.55}^{+0.49}$ and $N_H = 8.2_{-8.2}^{+486.8} \times 10^{21} \text{ cm}^{-2}$, however the ionisation parameter value ξ is unconstrained ($\xi \geq 0$). The unfolded spectrum for the warm absorber model is shown in Figure 7.17. The solid line is the integrated model. An edge, possibly the [OVIII] at 0.87 eV, is apparent.

7.4.2 The composite model

Given the composite nature of Mrk609 in the optical, I fit the data with a power-law model plus a Raymond-Smith model (PL+RS). This model gives $\Gamma = 1.65_{-0.41}^{+0.24}$ and $kT=0.20_{-0.05}^{+0.18}$ keV, while no excess absorption above the Galactic is required. The model again yields an acceptable fit ($\chi^2=39.55$ for 43 dof).

7.4.3 The starburst models

Although the optical spectrum is suggestive of the presence of an AGN in Mrk609, for completeness pure starburst models were examined as well. Firstly a single Raymond-Smith model (RS) was utilised. However it does not describe the data adequately, failing to fit the counts below 0.5 keV (see fig 7.18) and an unacceptable fit is obtained ($\chi^2=95.88$ for 45 dof). On the other hand, a two Raymond-Smith model (2RS) yields an acceptable fit with $kT_1 = 7.55_{-3.77}^{+23.45}$ keV and $kT_2 = 0.17_{-0.02}^{+0.03}$ ($\chi^2=41.52$ for 43 dof).

It is apparent that the data do not allow us to discriminate between the different models and the single power-law model (AGN representation), the composite power-law plus Raymond-Smith model as well as the two Raymond-Smith model (starburst representation), all provide equally acceptable fits. In addition it is evident that the data do not require any absorption above the Galactic.

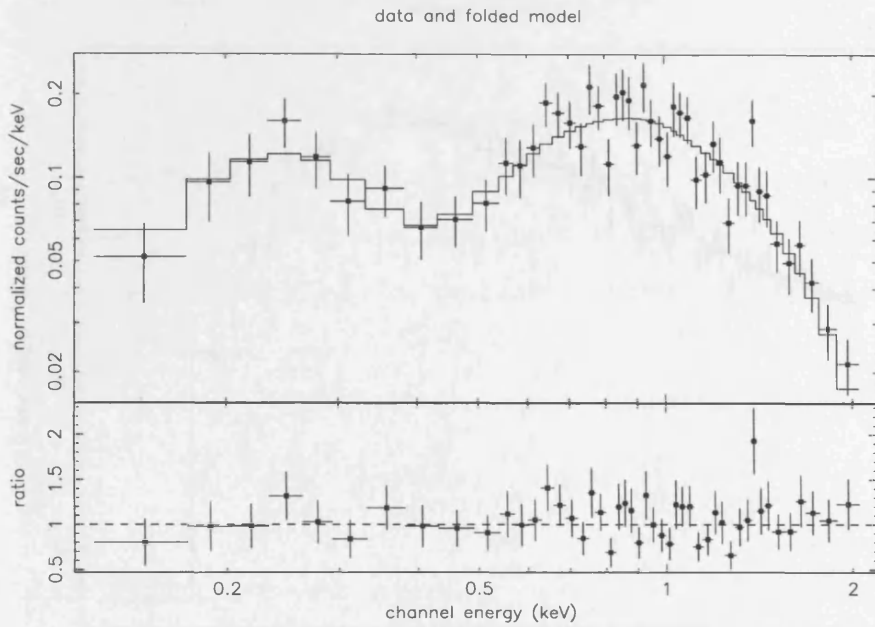


Figure 7.15: The *ROSAT* PSPC spectrum when the single power-law model discussed in the text is applied to the data. The top panel shows the data with the model and the bottom panel shows the data/model ratio.

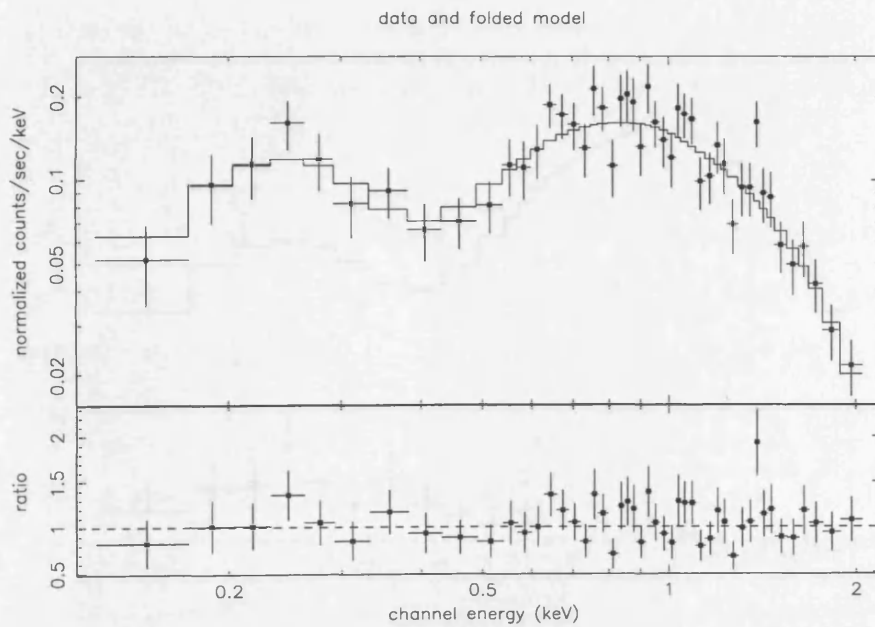


Figure 7.16: The *ROSAT* PSPC spectrum when the power-law model plus the blackbody model discussed in the text is applied to the data. The top panel shows the data with the model and the bottom panel shows the data/model ratio. It is obvious that the inclusion of the Blackbody component does not improve the fit.

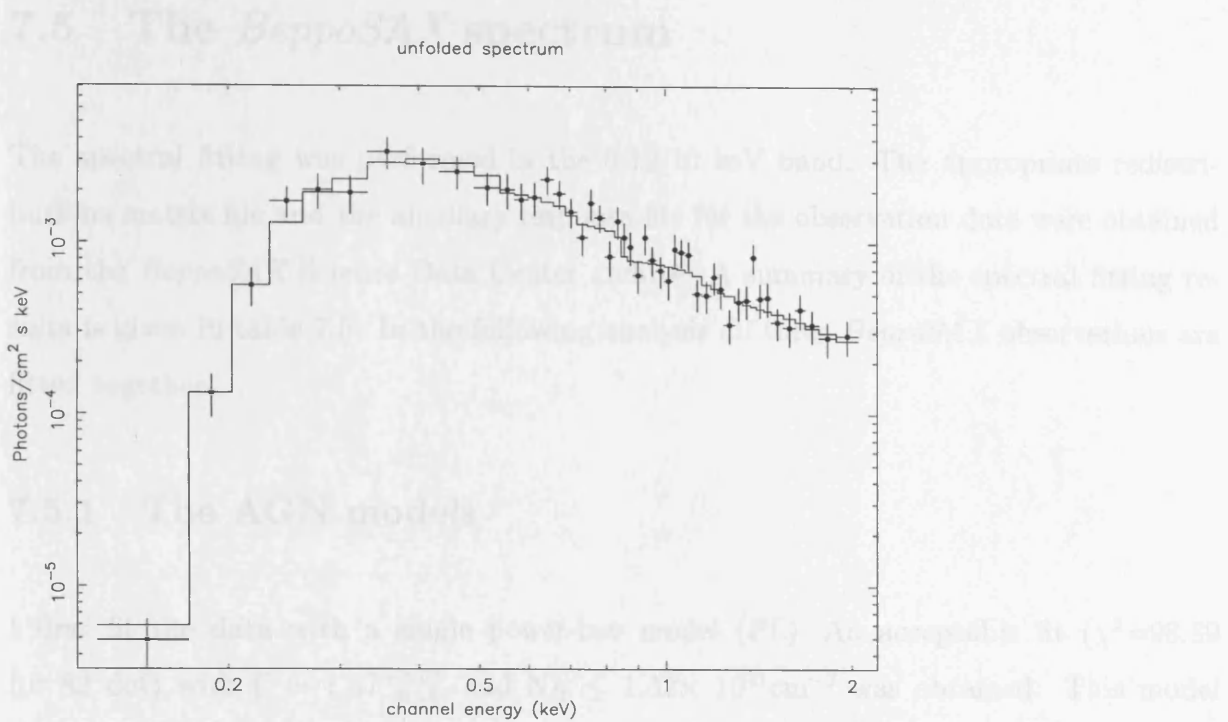


Figure 7.17: The *ROSAT* PSPC *unfolded* spectrum when the warm absorber model discussed in the text is applied to the data.

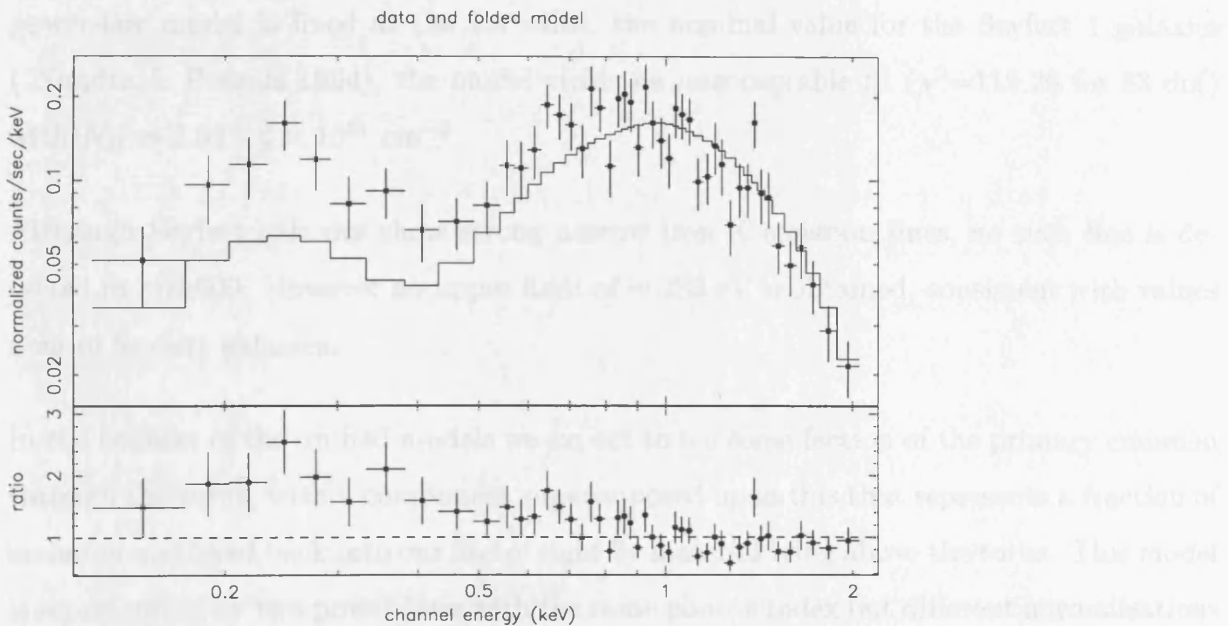


Figure 7.18: The *ROSAT* PSPC spectrum when the single Raymond-Smith model discussed in the text is applied to the data. It is clear that there is a significant soft excess that the model cannot explain. The top panel shows the data with the model and the bottom panel shows the data/model ratio.

7.5 The *BeppoSAX* spectrum

The spectral fitting was performed in the 0.12-10 keV band. The appropriate redistribution matrix file and the ancillary response file for the observation date were obtained from the *BeppoSAX* Science Data Center archive. A summary of the spectral fitting results is given in table 7.5. In the following analysis all three *BeppoSAX* observations are fitted together.

7.5.1 The AGN models

I first fit the data with a single power-law model (PL). An acceptable fit ($\chi^2=98.89$ for 82 dof) with $\Gamma = 1.57_{-0.10}^{+0.10}$, and $N_H \leq 1.32 \times 10^{21} \text{cm}^{-2}$ was obtained. This model together with the data points and the data to model ratio are plotted in Figure 7.19. The observed flux in the 2-10 keV band for this model is $2.86 \times 10^{-12} \text{ erg cm}^{-2} \text{ s}^{-1}$, which corresponds to a luminosity of $6.3 \times 10^{42} \text{ erg s}^{-1}$ in the same band. If the slope of the power-law model is fixed at the 1.9 value, the nominal value for the Seyfert 1 galaxies (Nandra & Pounds 1994), the model yields an unacceptable fit ($\chi^2=119.26$ for 83 dof) with $N_H = 2.03_{-1.8}^{+1.5} \times 10^{21} \text{ cm}^{-2}$.

Although Seyfert galaxies show strong narrow iron K emission lines, no such line is detected in Mrk609. However an upper limit of $\sim 283 \text{ eV}$ is obtained, consistent with values seen in Seyfert galaxies.

In the context of the unified models we expect to see some fraction of the primary emission through the torus, with a component superimposed upon this that represents a fraction of emission scattered back into our line of sight by material lying above the torus. This model is represented by two power-laws with the same photon index but different normalisations and absorptions - the scattering model. When this model is applied to the data, the normalisations of the two power-laws are comparable, whereas no excess absorption above the Galactic is required and thus this model effectively is the same as the single power-

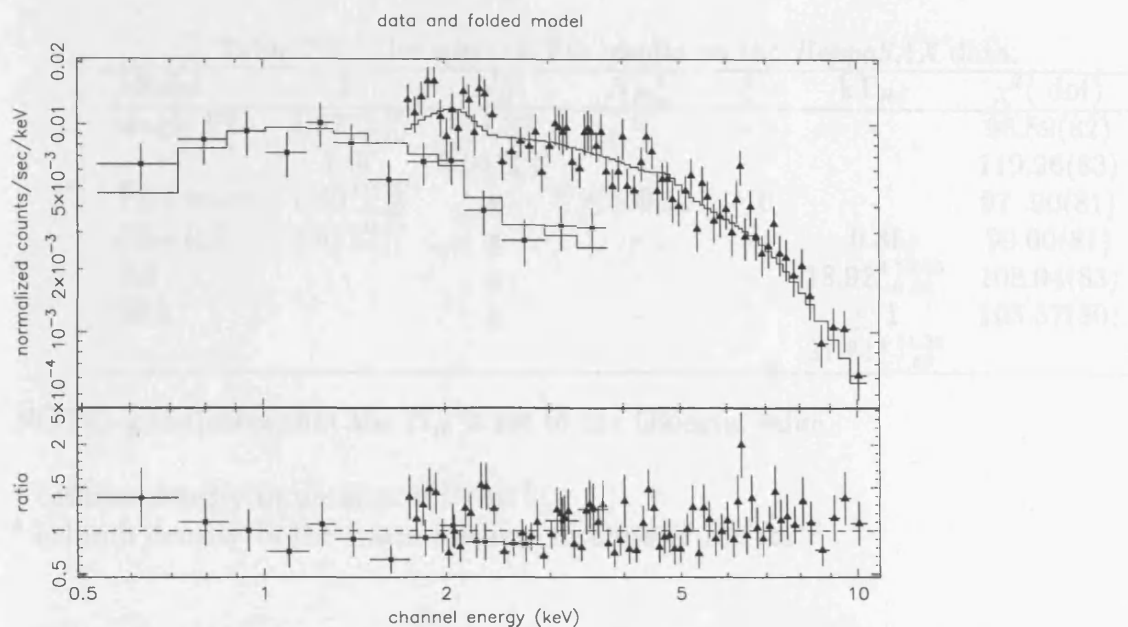


Figure 7.19: The *BeppoSAX* time averaged spectrum, when the single power-law with $\Gamma = 1.57_{-0.10}^{+0.10}$, $\chi^2=98.89(\text{dof})$ is applied to the data. The filled squares represent the LECS data points and the stars the MECS data points. The top panel shows the data with the model and the bottom panel shows the data/model ratio

law model. Therefore it is evident that the scattering model does not provide a good representation of the data.

Finally, an ionised warm absorber model in addition to the Galactic column density was fitted to the data (PL+warm). The temperature of the absorber is fixed at $T=10^5$ K (Brandt *et al.* 1999). The model provides an acceptable fit ($\chi^2=98.84$ for 81 dof) but does not represent a statistically significant improvement to the single power-law model. The best fit parameters are $\Gamma = 1.60_{-0.12}^{+0.16}$ and warm column density $N_{Hw} = 6.73_{-6.73}^{+25.47} \times 10^{21} \text{ cm}^{-2}$, while the ionisation parameter is practically unconstrained, possibly because of the poor statistics of the data.

7.5.2 The composite model

Given the composite classification of this object, it is natural to investigate a model in which X-ray emission originates from both a starburst and an AGN. A power-law plus

Table 7.5: The spectral fits results on the *BeppoSAX* data.

Model	Γ	N_H^a	$N_{H_w}^b$	ξ	kT _{RS}	χ^2 (dof)
single PL	$1.57^{+0.10}_{-0.10}$	≤ 1.32	-	-	-	98.89(82)
	1.9f	$2.03^{+1.53}_{-0.98}$				119.26(83)
PL+warm	$1.60^{+0.16}_{-0.12}$	g	≤ 369.11	≥ 0	-	97.90(81)
PL+RS	$1.57^{+0.09}_{-0.11}$	g	-	-	0.8f	99.00(81)
RS	-	g	-	-	$18.92^{+10.05}_{-6.02}$	108.94(83)
2RS	-	g	-	-	≤ 1	105.57(80)
					$21.81^{+14.33}_{-7.69}$	

NOTE: g indicates that the N_H is set to the Galactic value.

^a column density in units of 10^{21}cm^{-2} .

^b column density in the warm medium in units of 10^{21}cm^{-2} .

a Raymond-Smith model (PL+RS) with the temperature fixed at 0.8 keV is adopted. The power-law component is allowed to have additional absorption over and above that of the thermal component. This model yields an acceptable fit ($\chi^2=99.81$ for 81 dof) with $\Gamma = 1.57^{+0.09}_{-0.11}$, whereas no excess absorption above the Galactic is required. When the temperature of the thermal component is a free parameter, I find kT >18 keV and $\Gamma = 2.81^{+2.59}_{-0.96}$ ($\chi^2=95.00$ for 80 dof). However, the temperature of the thermal component is far too high for a starburst and thus this model cannot provide a physical description of the data.

7.5.3 The pure starburst model

For completeness pure starburst models have also been investigated. Firstly a single Raymond-Smith model (RS) was fitted to the data. An acceptable fit was obtained ($\chi^2=108.94$ for 83 dof) with $kT_1=18.92^{+10.15}_{-6.02}$ keV. No starbursts with such a high temperature have been found as yet.

Then a two Raymond-Smith model representing thermal emission from a pure starburst galaxy following Zezas *et al.* 1998 was utilised. The soft emission is parameterised by a thermal component with $kT_1 \leq 1$ keV and the emission in the hard band by $kT_2=21.8^{+14.33}_{-7.69}$

keV, again too high for a starburst. Therefore it is obvious that this model cannot provide a physical description of the data.

From the above it is evident that the pure starburst model is ruled out, whereas the composite model does not provide a physically accepted model, apart from the case where the temperature is set to $kT=0.8$ keV. In addition the the single power-law model yields an acceptable fit.

7.6 Spectral variability

Mrk609 was observed three times with *BeppoSAX*, allowing us to examine whether there is spectral variability. In particular it is interesting to see whether the drop in the flux during the second observation is related to a change in the spectrum of Mrk609 and examine whether the X-ray behaviour is similar to that of black hole candidates (BHC) in our galaxy during their high and low states. For this analysis only the single power-law is applied to the MECS data.

In addition any spectral variability at soft energies will be examined by comparing the *ROSAT* PSPC and LECS data.

7.6.1 Observation 1

The power-law model yields a fit ($\chi^2=55.75$ for 38 dof) with $\Gamma = 1.63_{-0.16}^{+0.16}$ and Galactic absorption. The observed flux in the 2-10 keV band for this model is 2.85×10^{-12} erg $\text{cm}^{-2} \text{ s}^{-1}$, which corresponds to a luminosity of 6.32×10^{42} erg s^{-1} in the same band. No iron line at 6.4 keV is detected but an upper limit of 540 eV is obtained. The model with the data and the data to model ratio is plotted in Figure 7.20.

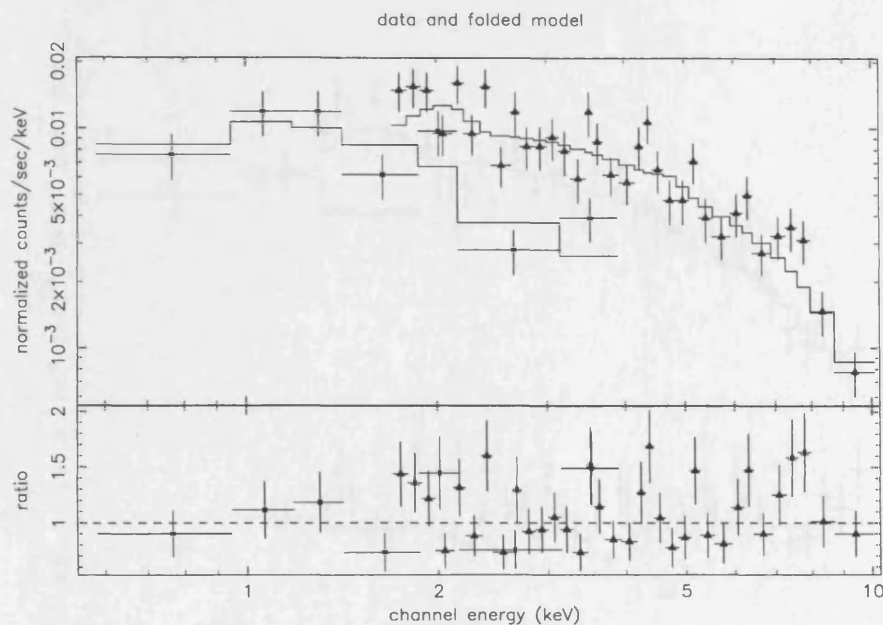


Figure 7.20: The *BeppoSAX* spectrum for the first observation for a power-law with $\Gamma = 1.63_{-0.16}^{+0.16}$, $\chi^2=55.75(38)$. The filled squares represent the LECS data points and the triangles the MECS data points. The top panel shows the data with the model and the bottom panel shows the data/model ratio.

7.6.2 Observation 2

During the second observation Mrk609 was observed for ~ 2.5 ksec only, and no reliable spectrum was extracted. However clues for the spectral shape of the spectrum of Mrk609 during this short observation come from the hardness ratio (HR) of the source. As in Chapter 3 the HR is defined as $h-s/h+s$, where h and s are the total number of counts, in the 2-10 keV and 1-2 keV respectively. Only MECS data were used since Mrk609 is not detected in the LECS. The HR is 0.31 ± 0.18 , which corresponds to a power-law of $\Gamma = 1.2 \pm 0.70$ assuming Galactic absorption. Unfortunately the uncertainty in the value of Γ is too high for any firm conclusion about spectral changes to be derived.

7.6.3 Observation 3

The power-law model yields a $\Gamma = 1.64_{-0.14}^{+0.14}$ and Galactic absorption ($\chi^2=61.16$ for 48 dof). The observed flux in the 2-10 keV band for this model is 2.72×10^{-12} erg cm $^{-2}$ s $^{-1}$,

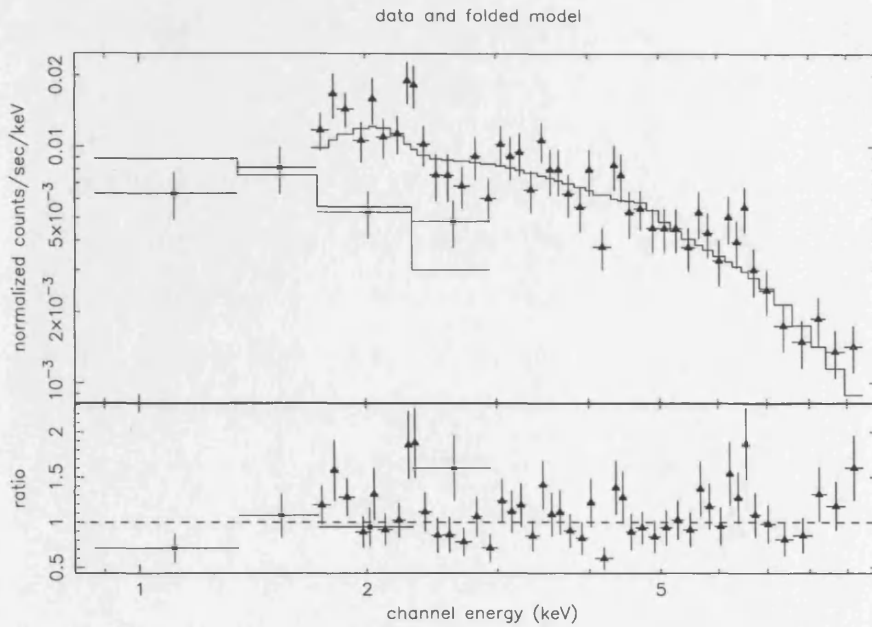


Figure 7.21: The *BeppoSAX* spectrum for the third observation for a power-law with $\Gamma = 1.64_{-0.14}^{+0.14}$, $\chi^2=61.16(48)$. The filled squares represent the LECS data points and the triangles the MECS data points. The top panel shows the data with the model and the bottom panel shows the data/model ratio.

which corresponds to a luminosity of 6.02×10^{42} erg s^{-1} in the same band. In the energy range 6-7 keV there is some evidence for residuals (see Figure 7.21). So a Gaussian line was added to the model. The best fit energy for the line is $6.72_{-0.24}^{+0.22}$ keV, clearly inconsistent with the line originating from cold iron. The model is acceptable ($\chi^2=56.31$ for 46 dof) with $\Gamma = 1.70_{-0.15}^{+0.16}$ and an equivalent width for the iron line 394_{-286}^{+391} eV (see Figure 7.22).

7.6.4 LECS/PSPC spectra comparison

The *ROSAT* spectrum is well represented by a single power-law with $\Gamma = 2.02_{-0.25}^{+0.24}$, much steeper than the *BeppoSAX* spectrum ($\Gamma \sim 1.6$). However due to the poor statistics of the LECS data compared to the MECS, the spectral slope of the former is probably driven by the latter and thus the discrepancy might not be real. Therefore, in order to check whether the PSPC and LECS slopes are inconsistent the LECS data will be fitted alone with a single power-law model in the 0.12-2.0 keV energy range. The best fit parameters are $\Gamma = 1.97_{-0.53}^{+0.51}$ and Galactic absorption ($\chi^2=3.22$ for 6 dof). The slope is consistent

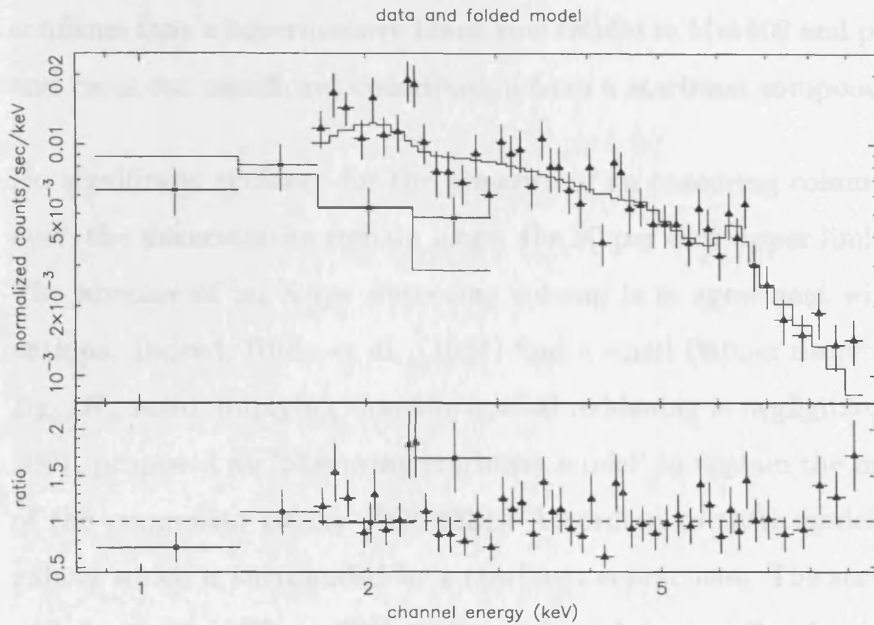


Figure 7.22: The *BeppoSAX* spectrum for the third observation for a power-law with $\Gamma = 1.64_{-0.14}^{+0.14}$, $\chi^2=61.16(48)$ and a gaussian line at $6.72_{-0.24}^{+0.22}$ keV. The filled squares represent the LECS data points and the triangles the MECS data points. The top panel shows the data with the model and the bottom panel shows the data/model ratio.

with both the PSPC and MECS slopes, and thus any variability between the *ROSAT* and *BeppoSAX* observations as well as any spectral upturn within the *BeppoSAX* observations cannot be examined.

7.7 Discussion

Mrk609 displays an X-ray continuum, which is somewhat at odds with its optically composite nature. A simple power-law is a good description of the data over the whole 0.1-10 keV energy range, with a rather flat index ($\Gamma = 1.57_{-0.10}^{+0.10}$). Still, this value is not inconsistent with those encountered in Seyfert-1 spectra (Nandra & Pounds 1994). Moreover no iron emission line was detected when all three observations are fitted together and the upper limit of the equivalent width of the line is ~ 283 eV. For the third observation, where the data-to-model ratio shows line like residuals in the 6-7 keV band, the inclusion of the iron line improves the fit significantly. The best fit line is $6.72_{-0.24}^{+0.22}$ keV with an equivalent width of 394_{-286}^{+391} eV. Nevertheless the detection of significant X-ray variability

confirms that a supermassive black hole resides in Mrk609 and powers the X-ray emission, and rules out significant contribution from a starburst component to the X-ray emission.

No significant evidence for the presence of an obscuring column have been found. However, the uncertainties remain large: the 90 per cent upper limit is rather high 1.3×10^{22} . The absence of an X-ray obscuring column is in agreement with optical and UV observations. Indeed, Rudy et al. (1988) find a small Balmer decrement together with a high Ly_{α}/H_{α} ratio, implying that the optical reddening is negligible. Recently Levenson *et al.* 2001, proposed an 'obscuring starburst model' to explain the multiwavelength properties of the composite galaxy NGC6221. According to their model NGC6221 is a Seyfert 1 galaxy which is surrounded by a starburst component. The starburst accounts for the X-ray obscuration ($N_H \sim 10^{22} \text{ cm}^{-2}$) and its characteristics dominate the optical spectrum. Although in principal this model can explain qualitatively the optical appearance of the composite galaxies it doesn't seem to fit the X-ray observations of Mrk609. Our object does not show concrete evidence for significant X-ray absorption and thus a dusty obscuring circumnuclear starburst is probably ruled out. It is note here that the spectral X-ray properties of Mrk609 are similar to the composite IRAS00317-2142 (Georgantopoulos *et al.* 2000). Again this galaxy has a low column density, consistent with the Galactic, and thus the obscuring starburst model cannot explain the properties of IRAS00317-2142.

Although the single power-law model yields a good representation of the Mrk609 spectrum the X-ray long term variability indicates that the spectrum of Mrk609 consists of more than one components. An AGN covered by a warm absorbing screen could provide an explanation for the observed long term variability. In this case changes in the X-ray continuum flux, will be followed by changes in the ionisation state of the warm absorber resulting in changes in the emission in the soft band. However, the quality of the data does not allow to examine the viability of the model to Mrk609.

Given the composite nature of Mrk609 it is natural to investigate whether emission from starburst regions contribute to the X-ray wavelengths. In principle, in a composite starburst-AGN model, the power-law component is heavily absorbed, and thus the

star-forming component, which is located outside the obscuring screen, dominates the soft emission. However, when this model is applied to Mrk609 data, no excess absorption above the Galactic is required by the data for the power-law component. In addition the poor quality of the data at energies below ~ 2 keV do not allow us to constrain the temperature of the thermal emission and make an unambiguous estimate of the starburst contribution to the X-ray emission. The strength of the star-forming component can be indirectly estimated from the observed IR flux. The expected X-ray contribution from stars was calculated using the empirical relationship between infrared and X-ray luminosity (equation [2] David *et al.* 1992) found in a sample of IRAS galaxies. However, note that some of the infrared (IR) flux could arise from nuclear reprocessed emission from the obscuring medium. Thus any starburst contribution to the X-ray flux derived using the above relation may be overestimated and the derived flux should only be treated as an upper limit. First the IR luminosities were calculated using the fluxes IRAS fluxes at $60\mu m$ and $100\mu m$ and equation [1] from David, Jones & Forman 1992. It is found that the upper limit of the expected contribution of a starburst in the 0.5-4 keV band is $2.75 \times 10^{42} \text{ erg s}^{-1}$. The luminosity in the same band derived by the spectral fitting is $\sim 4.7 \times 10^{42} \text{ erg s}^{-1}$, indicating that indeed the whole soft emission may be due to an intense starburst component. However, the variable soft X-ray emission clearly argues that any starburst contribution in soft energy band should be low.

To further test the AGN interpretation of Mrk609 the broad H_α line and the 2-10 keV flux were compared. Ward *et al.* (1988) found a strong correlation between the two quantities in a sample of IRAS selected Seyfert 1 galaxies. The observed luminosity of the broad H_α is $L(H_\alpha) = 8.4 \times 10^{39} \text{ erg s}^{-1}$, whereas the 2-10 keV luminosity is $\sim 7.5 \times 10^{42} \text{ erg s}^{-1}$. According to the above relation the predicted broad H_α luminosity should be ~ 40 times higher (see Figure 7.23). The above discrepancy between the optical and X-ray spectrum could be explained by variability. Possibly the AGN was weaker during the optical observation (1984), but brightened over the ~ 15 years timescale between the optical and X-ray observations. Alternatively the source may have unusually low UV emission. Then the photoionised emission lines would have lower fluxes than those typical

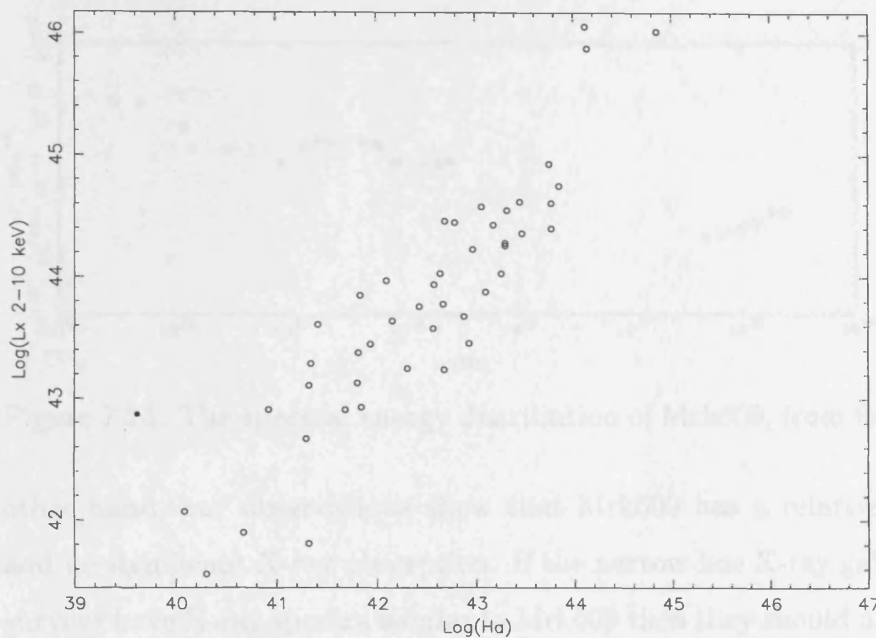


Figure 7.23: The H_{α} line versus the 2-10 keV luminosity correlation from Ward *et al.* (1988). Mrk609 is marked as a filled circle.

for AGNs. To examine this possibility the Mrk609 spectral energy distribution (SED) was computed. This is shown in Figure 7.24. It is indeed clear that Mrk609 lacks a big blue bump (BBB). This feature is characteristic of high luminosity unobscured AGNs and is thought to be a signature of the presence of a cold accretion disk around the black hole (see Koratkar & Blaes 1999). We note here that lack of ultraviolet excess has also been observed in a sample of low-luminosity AGN (Ho 1999). Low accretion rate models have been employed to account for the absence of the BBB feature. Note that Mrk609 presents a very strong Ly_{α} line (Rydy *et al.* 1988). The only known objects with stronger Ly_{α}/H_{β} ratios are the Seyfert-1 galaxies Mrk359 and Mrk1018. According to Rudy *et al.* (1988) the abnormally strong Ly_{α} line is readily explained if the Lyman continuum optical depth in the region where the lines form is significantly less than believed typical for Seyfert-1 galaxies.

As mentioned in the introduction the optical spectrum of the composite objects like Mrk609 bear close resemblance to the narrow line X-ray galaxies detected in *ROSAT* surveys. The X-ray spectrum of these sources is flat (Almaini *et al.* 1998) but it is unclear whether the flatness of the spectrum is intrinsic or due to obscuration. On the

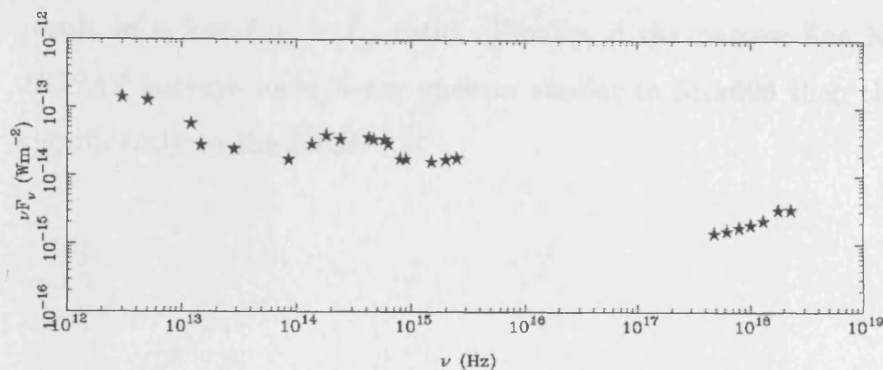


Figure 7.24: The spectral energy distribution of Mrk609, from far infrared to hard X-rays.

other hand, our observations show that Mrk609 has a relatively steep X-ray spectrum and no significant X-ray absorption. If the narrow line X-ray galaxies detected in *ROSAT* surveys have X-ray spectra similar to Mrk609 then they should not contribute significantly to the XRB.

7.8 Conclusions

In this chapter *BeppoSAX* data of the composite galaxy Mrk609 have been analysed. The spectrum is described by a power-law $\Gamma = 1.6$ with negligible absorption. The absence of absorption is consistent with the small Balmer decrement and the large Ly_{α} flux observed (Rudy et al. 1988). The absence of significant obscuring column clearly does not fit the absorbed starburst model proposed by Levenson *et al.* 2001 to explain the multiwavelength properties of the composite galaxies. In addition, the detection of significant soft and hard X-ray variability, clearly suggests that the AGN emission dominates the X-ray spectrum. Any starburst contribution to the X-ray emission should be small. Furthermore Mrk609 does not follow the $L_{H_{\alpha}} - L_x$ correlation of bright AGN (Ward *et al.* 1988), showing a weak broad H_{α} component (~ 40 times less than predicted by the X-ray flux). The discrepancy between the optical and X-ray spectrum can be explained as a deficit of UV ionising photons. This is supported by the SED, which shows no upturn of the spectrum below 3000\AA , implying the absence of a UV bump. Alternatively, as the optical and the X-ray observations were taken 15 years apart, dramatic variability in the X-ray flux could

result in a low $L_{H\alpha} - L_x$ ratio. Finally, if the narrow line X-ray galaxies detected in *ROSAT* surveys have X-ray spectra similar to Mrk609 then they should not contribute significantly to the XRB.

Chapter 8

Conclusions

The origin of the XRB is of great interest. The XRB is the sum of all the X-ray emission produced in the universe over a wide range of redshifts. Inevitably the study of the XRB has cosmological implications in the sense that it can trace the accretion history of AGNs. The aim of this thesis is to investigate the nature of the sources producing the bulk of the XRB at the hard energies (2-10 keV). Therefore the thesis is concerned with the spectroscopic properties of some classes of sources that are candidates to produce the bulk of the hard XRB. This chapter summarises the main conclusions of the work presented here, and discuss the exciting future prospects in this area of research.

8.1 Broad line QSOs

In chapter 3, it has been investigated whether broad line QSOs, which produce the bulk of the X-ray background in the soft energies, can produce the hard X-ray background as well. The aim was to parameterise the average X-ray spectrum of these QSOs over a wide range of redshifts and compare it with the spectrum of the XRB. The integrated spectrum of the broad line QSOs over the 0.8-8.0 keV can be parameterised by a single power-law model with $\Gamma=1.56\pm 0.18$. This is flatter than that of the bright radio-quiet QSOs, and is more consistent with that of the XRB. To examine the origin of this flat spectrum the individual QSOs spectra has been investigated. The sources are too faint for a proper

spectral analysis, however a '2-colour' estimate of the spectrum can be made, allowing crude determinations of both absorbing column density and spectral index to be made for each individual object. Therefore the hardness ratio HR for each QSO has been derived. It is found that the spectra of the QSOs flattens as we go towards fainter fluxes. Most of the sources have spectra flatter than $\Gamma \sim 1.7$. Although these sources have been classified in the optical as broad line QSOs a moderate obscuration (10^{22} cm^{-2}) is required by the data in order to reproduce the flat spectra observed. However the present data do not allow determination of the origin of the flattening. In other words it is not clear whether the sources are intrinsically flat or they have flat spectra due to absorption. Nevertheless, this analysis suggests the emergence of a hard X-ray QSO population. *XMM-Newton* will shed light in the X-ray spectrum of the high redshift faint QSOs and the origin of the flattening will be determined.

8.2 Seyfert 2 galaxies

In chapter 4 a comprehensive and uniform analysis X-ray analysis of 8 Seyfert 2 galaxies was presented. It has been shown that the Seyfert 2 galaxies are in general heavily obscured. In addition the X-ray spectrum of the Seyfert 2 galaxies appears to be complex. Starburst emission, thermal emission from the host galaxy, scattered emission and reflection contribute to the X-ray spectrum significantly. The latter suggests that the X-ray background synthesis models should take into account the complexity of the X-ray spectrum. It is believed that *XMM-Newton* observations will determine the spectrum of the Seyfert 2 galaxies as well as their contribution to the X-ray spectrum.

NGC 3147 and NGC 4698 (chapter 5) although classified as Seyfert 2 galaxies in the optical do not show evidence for absorption above the Galactic. It has been shown that both galaxies are not Compton thick objects. In chapter 5 the possible scenarios for the 'odd' behaviour of these two objects were investigated. NGC 3147 may be a Seyfert 1 galaxy, which lacks its broad line region. Therefore the optical spectrum shows only narrow lines. Alternatively variability as discussed in chapter 5 may play an important

role in the discrepancy between the optical and X-ray spectra. NGC 4698 is an extremely interesting object. The naked Seyfert 2 scenario can explain well the optical and X-ray spectra. In addition the hypothesis, in which NGC 4698 may not contain a SMBH thought to power an AGN but instead a super luminous X-ray source, is in agreement with the optical and X-ray spectra as well as its SED. *Chandra* observations of NGC 4698 will reveal whether an off axis X-ray sources produces the X-ray emission of the galaxy, whereas *XMM-Newton* observations will detect any variability or iron line that may exist.

8.3 ULIRGs – The Superantennae

The ULIRGs are a rare phenomenon in the local universe. However they appear to dominate the cosmic energy budget in the high redshift universe. Therefore it is believed that the high redshift ULIRGs may harbor the long sought population of type 2 QSOs predicted by the X-ray background synthesis models. Only a handful of ULIRGs have been observed above 2 keV. The majority are heavily obscured AGNs with quasar-like luminosities. In chapter 6 the X-ray spectrum of the ULIRG galaxy 'The Superantennae' has been studied. Its spectrum is hard, $\Gamma \sim 1.03$. The flattening of the spectrum is due to absorption. The Superantennae are obscured by a Compton thick medium with $N_H > 5 \times 10^{24} \text{ cm}^{-2}$. *Chandra* and *XMM-Newton* observations will determine both the starburst and AGN contribution to the X-ray spectra of ULIRGs. In addition the high redshift ULIRGs will be detected in X-rays and an insight in their X-ray properties will be provided.

8.4 Composite galaxies – Mrk609

Finally in chapter 7 the X-ray spectrum of the composite galaxy Mrk609 has been studied. These galaxies bear close resemblance to the narrow-line X-ray galaxies detected in large numbers in deep *ROSAT* surveys. These NLXGs again have spectra composite of Seyfert and starburst galaxies with luminosities $L_{2-10\text{keV}} \sim 10^{42-43} \text{ erg s}^{-1}$. Unfortunately the

faint fluxes of these NLXGs do not allow their detailed study in either optical or X-ray wavelength. Therefore, it is quite likely that the study of composite galaxies could provide an indirect insight in the spectra of the *ROSAT* NLXGs. Therefore *BeppoSAX* data from Mrk609 were analysed. X-ray variability in the soft and hard bands was detected, pointing towards an AGN origin of the emission in both bands. The X-ray spectrum is flat ($\Gamma \sim 1.4$), flatter than that of the Seyfert 1 galaxies. The upper limit of the equivalent width of the line at 6.4 keV (~ 350 eV) rules out the Compton thick hypothesis for this object. If the *ROSAT* NLXGs have spectra similar to that of Mrk609, then they should play an important role in the production of the hard XRB.

8.5 Future Prospects

It is apparent that there is a lot to be learnt about the spectrum of the galaxies harbouring an AGN. The *ROSAT*, *ASCA* and *BeppoSAX* data used in this work do not allow to derive firm conclusions regarding the nature of the hard X-ray background. However, it is becoming evident that all the sources studied in this thesis – broad line quasars, obscured active galaxies, ULIRGs and NLXGs– could contribute significantly to the XRB emission. The combination of high spectral resolution, high spatial resolution, high sensitivity and broad bandwidth coverage, provided by *Chandra* and *XMM-Newton* will shed light to the X-ray spectrum of the individual AGNs, especially the absorbed AGNs. At the same time they will allow for population studies to be conducted. Therefore in the near future the nature of the sources producing the XRB will be identified and the evolution of the black holes will be probed.

In particular, *Chandra* with its unique spatial resolution (HPD for the PSF of ≤ 0.5 arcsec) and excellent image quality will allow direct imaging of the sources making up the XRB, whereas *XMM-Newton* with its high effective area (1620 cm² at 6 keV and 2485 cm² at 1.5 keV) will allow spectral studies of faint sources. It is estimated that a 10^{-15} erg cm⁻²s⁻¹ source will yield ~ 1000 counts in the 0.1-10 keV band, in the EPIC pn alone, sufficient for spectral analysis to be carried out. Therefore it is expected that within the

next few years we will be able to better determine the X-ray spectrum of all types of AGNs, and quantify the different components contributing to their X-ray spectrum. In addition we will be able to determine the average QSOs spectrum with luminosity and redshift and establish the origin of the flattening of the QSO spectrum towards fainter fluxes. Moreover the QSO luminosity function will be constructed, thus allowing the estimate of the contribution of this class of objects to the XRB.

On a longer scale, the optical/near IR Next Generation Space telescope (*NGST*; Mather, Seery & Belly 1996) and the far IR *SIRFT* (Werner 1998) and *FIRST* (Pilbratt 1993, Genzel 1997) will revolutionise our knowledge of the FIR properties of AGNs and galaxies. Information obtained from the optical, far- and near IR observations together with X-ray observations, will determine the relative contributions from AGN and star-formation activity in different classes of objects. In the future a multiwavelength approach will be vital in order to test the predictions of the obscured X-ray synthesis models, determine the nature of the sources contributing to the XRB emission, and above all comprehend the nature of the sources in our universe.

References

Akiyama M., *et al.* , 2000, ApJ, 532, 700

Allen S. W., Di Matteo T., Fabian A. C., 2000, MNRAS, 311, 493

Almaini O., Shanks T., Griffiths R.E., Boyle B.J., Roche N., Georgantopoulos I., Stewart G.C., 1997, MNRAS, 291, 55

Almaini O., Boyle B.J., Griffiths R.E., Shanks T., Stewart G.C., Georgantopoulos I., 1995, MNRAS, 277, L31

Almaini O., 2000, astro-ph/000109

Almaini O., Shanks T., Boyle B.J., Griffiths R.E., Roche N., Stewart G.C., Georgantopoulos I., 1996, MNRAS, 282, 295

Alonso-Herrero A., Ward M. J., Kotilainen J. K., 1997, MNRAS, 288, 977

Antonucci R., 1993, ARA&A, 31, 473

Antonucci R., Hurt, T., Miller J., 1994, ApJ, 430, 210

Aretxaga I., Terlevich R., 1994, MNRAS, 269, 462

Baldwin J. A., Phillips M. M., Terlevich R., 1981, PASP, 93, 5

Barger A. J., Cowie L. L., Sanders D. B., Fulton E., Taniguchi Y., Sato Y., Kawara K., Okuda H., 1998, Nature, 394, 248

Bassani L., Dadina, M., Maiolino, R., Salvati, M., Risaliti, G., della Ceca, R., Matt, G., Zamorani, G., 1999, ApJS, 121, 473

Blair A.J., Stewart G.C., Georgantopoulos I., Boyle B.J., Griffiths R.E., Shanks T., Almaini O., 2000, MNRAS, 314, 138

Blandford R. D., Levinson A., 1995, ApJ, 441, 79

Blandford R. D., Begelman M. C., 1999, MNRAS, 303, L1

Blundell K. M., Beasley A. J., Lacy M., Garrington S. T., 1996, ApJ, 468, L91

Boldt E., 1987, IAUS, 124, 611

Boyle B.J., McMahon R.G., Wilkes B.J., Elvis, M., 1995, MNRAS, 272, 462

Boyle B.J., McMahon R.G., Wilkes B.J., Elvis, M., 1995, MNRAS, 276, 315

Boyle B.J., Staveley-Smith L., Shanks T., Georgantopoulos I., Stewart G.C., Griffiths R. E., 1995, Obs, 115,10

Boyle, B.J., Staveley-Smith L., Stewart G. C., Georgantopoulos I., Shanks T., Griffiths R. E., 1993, MNRAS, 265, 501

Boyle B.J., Almaini O., Georgantopoulos I., Blair A.J., Stewart G.C., Griffiths R.E., Shanks T., Gunn K.F., 1998a, MNRAS, 297, 53L

Boyle B.J, Georgantopoulos I., Blair A.J., Stewart G.C., Griffiths R.E., Shanks T., Gunn K.F., Almaini O., 1998b, MNRAS, 296, 1

Brandt W.N., Fabian A.C., Takahashi K., Fujimoto R., Yamashita A., Inoue H., Ogasaka Y.,1997, MNRAS, 290, 617

Brandt W.N., Boller T., Fabian A. C., Ruszkowski M., 1999, MNRAS, 303, L53

Cagnoni I., della Ceca R., Maccacaro T., 1998, ApJ, 493, 54

Cid Fernandes R., Terlevich R., Aretxaga I., 1997, MNRAS, 289, 318

Collin-Souffrin S., 1987, ApJ, 179, 60

Colina L., Lipari S., Macchetto F., 1991, ApJ,379, 113

Comastri A., Setti G., Zamorani G., Hasinger G., 1995, A&A, 296, 1

Comastri A., 2000, astro-ph/0003437

Condon J., Cotton W.D., Greisen E.W., Yin Q.F., Perley R.A., Taylor G.B., Broderick J.J., 1998, AJ, 115, 1639

- David L. P., Jones C., Forman W., 1992, ApJ, 388, 82
- DeGrijp M.H.K, Keel W.C, Miley G.K, Goudfrooij P., Lub J., 1992, A&A, 96, 389
- Della Ceca R., Castelli G., Braitto V., Cagnoni I., Maccacaro T., 1999, ApJ, 524, 674
- De Vaucouleurs G., de Vaucouleurs A., Corwin J.R., Buta R.J., Paturel G., Fouque P.,
Third reference catalogue of Bright galaxies, 1991, New York : Springer-Verlag.
- di Matteo T., Allen S. W., 1999, ApJ, 527, L21
- Dickey J.M., Lockman F.J., 1990, ARA&A, 28, 215
- Draine B.T. & Salpeter E.E., 1979, ApJ, 231, 438
- Duc P.A., Mirabel I.F., Maza J., 1997, A&ASS, 124, 533
- Ehle M., Pietsch W., Beck R., 1995, A&A, 295, 289
- Elvis M., *et al.* , 1994, ApJS, 95, 1
- Fabbiano G., Feigelson E., Zamorani G., 1982, ApJ, 256, 397
- Fabbiano G., 1989, ARA&A, 27, 87
- Fabian A.C., Barcons X., 1992, ARA&A, 30, 429
- Fabian A.C., Rees M.J., 1995, MNRAS, 277, 55
- Fabian A.C. *et al.* , 1994, ApJ, 436, L51
- Fabian A.C., Barcons X., Iwasawa T., Almaini O., 1998, MNRAS, 297, L11
- Fanaroff B. L., Riley J. M., 1974, MNRAS, 167, 31
- Filippenko A.V., Ho L. C., Sargent W. L. W., 1993, ApJ, 410, L75
- Fiore F., Laor A., Elvis M., Nicastro F., Giallongo E., 1998, ApJ, 503, 607

Fiore F., *et al.* 1999, MNRAS, 306, L55

Fiore F., *et al.* 2000, astro-ph/0007118

Freedman W. L., *et al.* , 1994, ApJ, 427, 628

Gendreau K.C. *et al.* , 1995, PASJ, 47, L5

Georgantopoulos I., Stewart G.C., Shanks T., Boyle B.J., Griffiths R.E., 1996, MNRAS, 280, 276

Georgantopoulos I., *et al.* , 1997, MNRAS, 291, 203

Georgantopoulos I., Almaini O., Shanks T., Stewart G.C., Griffiths R.E., Boyle B.J., Gunn K.F., 1999a, MNRAS, 305, 125

Georgantopoulos, I., Papadakis, I., Warwick, R.S., Smith, D.A., 1999, MNRAS, 307, 815

Georgantopoulos, I., 2000, MNRAS, 315, 77

George I.M., Fabian A. C., 1991, MNRAS, 249, 352

George I.M., Turner T.J., Netzer H., Nandra K., Mushotzky R.F., Yaqoob T., 1998, ApJS 114, 73

Giacconi R., *et al.* , 1962, Phys. Review Letters, 9, 439

Giacconi R., *et al.* , 2001, ApJ, 551, 624

Gilli R., Risaliti G., Salvato M., 1999, A&A, 347, 424

Gilli R., Comastri A., Brunetti G., Setti G., 1999, NewA, 4, 45

Giommi P., Perri M., Fiore F., 2000, A&A, 362, 799

Goodrich R. W., Miller J. S., 1994, ApJ, 434, 82

Griffiths R. G., Warwick R. S., Georgantopoulos I., Done C., Smith D. A., 1998, MNRAS, 298, 1159

Griffiths R. E., Georgantopoulos I., Boyle B. J., Stewart G. C., Shanks T., della Ceca R., 1995, MNRAS, 275, 77

Guainazzi M., Matt G., Brandt W. N., Antonelli L. A., Barr P., Bassani L., 2000, A&A, 356, 463

Guainazzi M., *et al.*, 1998, MNRAS, 301, L1

Guilbert P. W., Rees M. J., 1988, MNRAS, 233, 475

Gunn K. F., Shanks T., 1998, AN, 319, 66

Haardt F., Maraschi L., 1991, ApJ, 380, L51

Haardt F., Maraschi L., 1993, ApJ, 413, 507

Haardt F., Maraschi L., Ghisellini G., 1997, ApJ, 476, 620

Halpern J. P., Eracleous M., Forster K., 1998, ApJ, 501, 103

Halpern J. P., Turner T. J., George I. M., 1999, MNRAS, 307, L47

Hasinger G., Burg R., Giacconi R., Hartner G., Schmidt M., Trumper J., Zamorani G., 1993, A&A, 275, 1

Hasinger G., Burg R., Giacconi R., Schmidt M., Trumper J., Zamorani G., 1998, A&A, 329, 482

Heckman T. M., 1980, A&A, 87, 152

Heisler C.A, Lumsden S., Bailey J., 1997, Nature, 385, 700

Ho L.C., Filippenko A.V., Sargent W.L.W., 1996, ApJ, 455, 614

Ho L.C., Filippenko A.V., Sargent W.L.W., Peng, C.Y., 1997, ApJS, 112, 391

Hughes D. H. *et al.*, 1998, Nature, 394, 241

Iwasawa K., Fabian A.C., Brandt W. N., Crawford C. S., Almaini O., 1997, MNRAS, 291, L17

Iwasawa K., Comastri A., 1998, MNRAS, 297, 1219

Iwasawa K., Fabian A.C., Nandra K., 1999, MNRAS, 307, 611

Jourdain E., *et al.* , 1992, A&A, 256, L38

Kaaret P., Prestwich A.H., Zezas A., Murray S.S., Kim D.-W., Kilgard R.E., Schlegel E.M., Ward M. J., 2001, MNRAS, 321, L29

Kennicutt R. C. Jr, 1983, ApJ, 272, 54

Kennicutt R. C. Jr, Tamblyn P., Congdon C. E., 1994, ApJ, 435, 22

Kim D.-C, Sanders D.B., Veilleux S., Mazzarella J.M., Soifer, B.T., 1995, ApJS, 98, 129

Komossa S. & Bade N., 1998, A&A, 331, L49

Kraft R. P., Burrows D. N., Nousek J. A., 1991, ApJ, 374, 344

Laor A., Draine B.T., 1993, ApJ, 402, 441

Laor A., Fiore F., Elvis M., Wilkes B. J., McDowell J.C., 1997, ApJ, 477, 93

Lawrence A., Papadakis I., 1993, ApJ, 414, L85

Lawson A.J., Turner M.J.L., 1998, MNRAS, 288, 920

Lightman A. P., White T. R., 1988, ApJ, 335, 57

Lira P., Lawrence A., Johnson R. A., 2000, MNRAS, 319, 17

Lutz D., Veilleux S., Genzel R., 1999, ApJ, 517, 13

Madau P., Ghisellini G., Fabian A. C., 1994, ApJ, 433, L53

Maiolino R., Salvati M., Bassani L., Dadina M., Dela Ceca R., Matt G., Risaliti G., Zamorani G., 1998, A&A, 338, 781

Maiolino R., Rieke G.H., 1995, ApJ, 454, 95

Maiolino R., Ruiz M, Rieke G.H., Keller L.D., 1995, ApJ, 446, 561

Maiolino R. *et al.* , 2000, A&A, 355, L47

Maisack M, *et al.* , 1993, A&A, 407, L61

Makishima K., Ohashi T., Kondo H., Palumbo G.G.C., Trinchieri G., 1990, ApJ, 365, 159

Malkan M. A., Sargent W. L. W., 1982, ApJ, 254, 22

Malkan M. A., Gorjian V., Tam R., 1998, ApJS, 117, 25

Marshall F., Boldt E.A., Holt S.S., Miller R.B., Mushotzky R.F., Rose L.A., Rothschild R.E., Serlemitsos P.J., 1980, ApJ, 235, 4

Marston A.P., Elmegreen D., Elmegreen B., Forman W., Jones C., Flanagan K., 1995, ApJ, 438, 663

Mather J. C., *et al.* , 1994, ApJ, 420, 439

Matt G., Guainazzi M., Frontera F., Bassani L., Brandt W. N., Fabian A. C., Fiore F., Haardt F., Iwasawa K., Maiolino R., Malaguti G., Marconi A., Matteuzzi A., Molendi S., Perola G. C., Piraino S., Piro L., 1997, A&A, 325, 13

Matt G., Guainazzi M., Maiolino R., Molendi S., Perola G. C., Antonelli L. A., Bassani L., Brandt W. N., Fabian A. C., Fiore F., Iwasawa K., Malaguti G., Marconi A., Poutanen J., 1999, A&A, 341, 39

Matt G., Fabian A.C., 1994, MNRAS, 267, 187

Matt G., Fiore, F., Perola, G.C., Piro, L., Fink, H.H., Grandi, P., Matsuoka, M., Oliva, E., Salvati, M., 1996, MNRAS, 281, L69

Matt G., 2000, A&A, 355, L31

Matt M.J., 1998, MNRAS, 298, 537

Melnick J. & Mirabel I.F., 1990, A&A, 231, L19

Miller J.S. & Goodrich R.W., 1990, ApJ, 355, 456

Mirabel I.F., Lutz D., Maza J., 1991, A&A, 243, 367

Miyaji T., Hasinger G., Schmidt M., 2000, A&A, 353, 25

Miyoshi M., Moran J., Herrnstein J., Greenhill L., Nakai N., Diamond P., Inoue M., 1995, Nature, 373, 127

Moran E., Halpern J. P., Helfand D. J., 1996, ApJS, 106, 341

Morrison R. & McCammon D., 1983, ApJ, 270, 119

Mulchaey J. S., Koratkar A., Ward M. J., Wilson A. S., Whittle M., Antonucci R. R. J., Kinney A. L., Hurt T., 1994, ApJ, 436, 586

Murayama T., Mouri H., Taniguchi Y., 2000, ApJ, 528, 179

Mushotzky R.F, Done C., Pounds K., 1993, ARA&A, 402, 432

Mushotzky R. F., Cowie L. L., Barger A. J., Arnaud K. A., 2000, Nature, 404, 459

Nandra K. & Pounds K., 1994, MNRAS, 268, 405

Nicastro F., 2000, ApJ, 530, L65

Ogasaka Y. *et al.* , 1997, PASJ, 49, 179

Ogasaka Y., *et al.* , 1998, AN, 319, 430

Ohta K., Yamada T., Nakanishi K., Ogasaka Y., Kii T., Hayashida K., 1996, ApJ, 458, 57

Osterbrock D. E., 1981, ApJ, 249, 462

Page M., Mason K. O., McHardy I. M., Jones, L. R., Carrera F. J., 1997, MNRAS, 291, 324

Palumbo G.C.C., Fabbiano G., Trinchieri G., Fransson C., 1985, ApJ, 298, 259

- Parmar A.N., Guainazzi M., Oosterbroek T., Orr A., Favata F., Lumb D., 1999, *A&A*, 345, 611
- Peterson B. M., 1997, "An Introduction to Active Galactic Nuclei", Cambridge University Press
- Piccinotti G., Mushotzky R. F., Boldt E. A., Holt S. S., Marshall F. E., Serlemitsos P. J., Shafer R. A., *ApJ*, 253, 485
- Pietsch W., Trinchieri, G., Vogler, A., 1998, *A&A*, 340, 351
- Polletta M., Bassani L., Malaguti G., Palumbo G.G.C., Caroli E., 1996, *ApJS*, 106, 399
- Ptak A., Yaqoob T., Serlemitsos P. J., Kunieda H., 1996, *ApJ*, 459, 542
- Ptak A., Serlemitsos P. J., Yaqoob T., Mushotzky R., 1999, *ApJS*, 120, 179
- Ptak A., Yaqoob T., Mushotzky R., Serlemitsos P., Griffiths R., 1998, *ApJ*, 501, 37
- Read A.M., Ponman T.J., Strickland D.K., 1997, *MNRAS*, 286, 626
- Rees M.J., 1984, *ARA&A*, 22, 471
- Reeves J.N, 1999, PhD thesis, University of Leicester
- Reeves J.N, Turner M., 2000, *MNRAS*, 316, 234
- Reichert G.A., Mushotzky R. F., Filippenko A. V., AIP Conference Proceedings 313, New York: American Institute of Physics (AIP), 1994, edited by Eric M. Schlegel and Robert Petre., p.85
- Rephaeli Y., Gruber D., Persic M., 1995, *A&A*, 300, 91
- Reynolds C.S., Ward M.J., Fabian A.C., Celotti A., 1997, *MNRAS*, 291, 403
- Reynolds C.S., 1997, *MNRAS*, 286, 513
- Risaliti G., Maiolino R., Salvati M., 1999, *ApJ*, 522, 157
- Roberts T. P., Warwick R. S., 2000, *MNRAS*, 315, 98

Romero-Colmenero E., Branduardi-Raymont G., Carrera F. J., Jones L. R., Mason K. O., McHardy I. M., Mittaz J. P. D., 1996, MNRAS, 282, 94

Rudy, R. J., Cohen R. D., Ake T. B., 1988, ApJ, 332, 172

Rush B., Malkan M. A., Fink H. H., Voges W., 1996, ApJ, 471, 190

Sandage A. & Tammann G.A., 1981, A Revised Shapley-Ames Catalog of Bright Galaxies (Washington: Carnegie Institution of Washington)

Sandage A. & Bedge J., 1994, The Carnegie atlas of galaxies (Washington: Carnegie Institution of Washington)

Sanders D.B., Phinney E. S., Neugebauer G., Soifer B. T., Matthews K., 1989, ApJ, 347, 29

Sanders D.B., 1998, AAS, 192, 6206

Sanders D.B. & Mirabel I.F., 1996, ARA&A,34, 749

Sanders D.B., Soifer B. T., Elias J. H., Madore B. F., Matthews K., Neugebauer G., Scoville N. Z., 1988, ApJ, 325, 74

Sanders D.B., Soifer B.T., Elias J.H., Neugebauer G., Matthews K., 1988b, ApJ, 328,L35

Schartel N., *et al.* , 1996, MNRAS, 283,101

Schmidt M., *et al.* , 1998, A&A, 329, 495

Schmitt H. R., Kinney A.L., Storchi-Bergmann T., Antonucci R., 1997, ApJ, 485, 434

Schulz H., Komossa S., Berghofer T. W., Boer B., 1998, A&A, 330, 823

Setti G., Woltjer L., A&A, 224, 21L

Shanks T., Georgantopoulos I., Stewart G. C., Pounds K. A., Boyle B. J., Griffiths R. E., 1991, Nature, 353, 315

Smith D., Done C., 1996, MNRAS, 280, 355

Soifer B.T. *et al.* , 1984, ApJ, 278, L71

Stark A.A, Gammie C. F., Wilson R. W., Bally J. Linke R. A., Heiles C., Hurwitz M., 1992, ApJS, 79, 77

Tanaka Y., Inoue H., Holt S., 1994, PASJ, 46, L37

Tanaka Y., Nandra K., Fabian A. C., Inoue H., Otani C., Dotani T., Hayashida K., Iwasawa K., Kii T., Kunieda H., Makino F., Matsuoka M., 1995, Nature, 375, 659

Terashima Y., Ptak A., Fujimoto R., Itoh M., Kunieda H., Makishima K., Serlemitsos P.J, 1998, ApJ, 496, 210

Terlevich R., Tenorio-Tagle G., Franco J., Melnick J., 1992, MNRAS, 255, 713

Terlevich R., Melnick J., 1985, MNRAS, 213, 841

Tran H.D, 1995, ApJ, 440, 565

Trumper J., in "High resolution X-ray spectroscopy of cosmic plasmas", Cambridge, England and New York, Cambridge University Press, 1990, p. 291-294.

Turner T.J. & Pounds K.A., 1989, MNRAS, 240, 833

Turner T. J., Urry C. M., Mushotzky R. F., 1993, ApJ, 418, 653

Turner T.J., George, I.M., Nandra K., Mushotzky R., 1997, ApJS, 113, 23

Ueda Y., Takahashi Y., Ohashi T., Makishima K., 1999, ApJ, 524, 11

Ueno S., Law-Green S.D, Awaki H., Koyama K., 1998, IAUS, 188, 432

Ueno S., Mushotzky R., Koyama K., Iwasawa K., Awaki H., Hayashi I., 1994, PASJ, 46, L71

Urry M., Padovani P., 1995, PASP, 107, 803

Uttley P., McHardy I. M., Papadakis I. E., Cagnoni I., Fruscione A., 2000, MNRAS, 312, 880

- Vecchi A., Molendi S., Guainazzi M., Fiore F., Parmar A.N., 1999, A&A, 349, 73
- Veilleux S., Goodrich R., Hill G. J., 1997, ApJ, 477, 631
- Veilleux S., Osterbrock D.E., 1987, ApJS, 63, 295
- Veron P., Goncalves A. C., Veron-Cetty M.-P., 1997, A&A, 319, 52
- Vignali C., Comastri A., Cappi M., Palumbo G.G.C., Matsuoka M., Kubo H., 1999, ApJ, 516, 582
- Vignali C., Mignoli M., Comastri A., Maiolino R., Fiore F., 2000, MNRAS, 314, L11
- Vignati P., *et al.* , 1999, A&A, 349, L57
- Vikhlinin A., Forman W., Jones C., Murray S., 1995, ApJ, 451, 564
- Ward M.J., Done, C., Fabian, A.C., Tennant A.F., Shafer R.A, 1998, ApJ, 324, 767
- Weaver K. A., Nousek J., Yaqoob T., Mushotzky R. F., Makino F., Otani C., 1996, ApJ, 458, 160
- Wilman R. J., Fabian A. C., Cutri R. M., Crawford C. S., Brandt W. N., 1998, MNRAS, 300, L7
- Witt H.J., Czerny B., Zycki P.T., 1997, MNRAS, 286, 848
- Wood K.S., *et al.* , 1984, ApJS, 56, 507
- Wright E. L., Smoot G. F., Bennett C. L., Lubin P. M., 1994, ApJ, 436, 443
- Yaqoob T., 2000, astro-ph/0008142
- Zdziarski A. A., Ghisellini G., George I. M., Fabian A. C., Svensson R., Done C., 1990, ApJ, 363, L1
- Zezas A.L., Georgantopoulos I., Ward M.J., 1998, MNRAS, 301, 915